



The University of
Nottingham

UNITED KINGDOM • CHINA • MALAYSIA

Fabric Forming Simulation and Process Optimisation for Composites

By

Shuai Chen

MSc. (Hons.)

Thesis submitted to the University of Nottingham

for the degree of Doctor of Philosophy

September 2016

Abstract

The development and optimisation of automated fabric preforming processes is critical for the adoption of composite materials for low cost, high volume applications. This thesis presents the development of a numerical material model to simulate the forming of 2D fabric plies into complex 3D shapes. The material model has been used to evaluate the feasibility of using matched-tool forming and double diaphragm forming, to manufacture low cost fabric preforms suitable for liquid moulding processes. The research has focused on two main aspects: (I) fabric characterisation and modelling and (II) process simulation and optimisation. The forming behaviour of woven fabrics and non-crimp fabrics (NCF) has been investigated to understand the deformation mechanisms and the cause of defects, in order to seek feasible solutions for defect reduction. A non-orthogonal constitutive relation has been developed to capture the nonlinear material behaviour, which was implemented in an explicit finite element model and used to refine the forming process.

Results from the material model indicate that pillar stitched NCFs are not as compliant as woven fabrics of the same areal mass. The likelihood of defects is therefore higher for the NCF and the shear behaviour is axisymmetric due to the influence of the stitch yarn. The NCF material exhibits two types of wrinkling during matched tool forming; out-of-plane wrinkling at the ply level (macro-scale wrinkling) induced by excessive shear, and in-plane wrinkling at the bundle level (meso-scale wrinkling) caused by fibre compression. Stitch rupture can also occur at high shear angles, which can lead to further localised wrinkling. Fabric bridging is the dominant defect in large curvature regions when using double diaphragm forming (DDF), and wrinkling was found to be generally lower than in matched-tool forming. The model has been used to successfully identify the cause of all of these defects in NCF preforms manufactured by DDF, and has been used to optimise preform geometry and process parameters to mitigate these problems. Darts were added to preforms to alleviate fabric bridging and improve surface conformity, using the tensile stress in the yarns to identify suitable positions and orientations, minimising the effect on the mechanical performance of the component.

An optimisation methodology has been developed for placing local inter-ply stitches on multi-ply preforms, by coupling the FE analysis with a genetic algorithm. The stitches enable

multiple plies to be joined together to aid robotic handling and the optimisation routine ensures that the placement of the stitches does not adversely affect the formability of the preform. Results indicate that whilst the inter-ply stitches affect the shear distribution at a global level, the formability of a multi-ply preform can be improved compared to the unstitched counterpart by optimising the pattern of through-thickness stitches.

A two-step optimisation method was also developed to optimise the boundary conditions for a matched tool forming scenario. Spring-loaded clamps were used to provide in-plane tension in the fabric plies during forming, rather than using a blank holder to induce tension through friction, providing an opportunity to reduce preform size and therefore waste. The optimisation algorithm was used to determine the location and size of the clamps around the blank perimeter and the stiffness of the attached springs. It was shown that this method can effectively homogenise the global shear angle distribution, reducing the peak shear angle compared to using a segmented blank holder.

List of Publications

The following papers have been produced as a result of this research on fabric forming simulation and process optimisation.

Journal papers

- (1) Chen S, McGregor O P L, Endruweit A, Elsmore M T, De Focatiis D S A, Harper L T, Warrior N A. Double diaphragm forming simulation for automotive composite structures [J]. Submitted to Composites Part A: Applied Science and Manufacturing. (Under review)
- (2) Chen S, McGregor O P L, Harper L T, Endruweit A, Warrior N A. Defect formation during preforming of a bi-axial non-crimp fabric with a pillar stitch pattern [J]. Composites Part A: Applied Science and Manufacturing, 2016, 91: 156-167.
- (3) Chen S, Harper L T, Endruweit A, Warrior N A. Formability optimisation of fabric preforms by controlling material draw-in through in-plane constraints [J]. Composites Part A: Applied Science and Manufacturing, 2015, 76: 10-19.
- (4) Chen S, Endruweit A, Harper L T, Warrior N A. Inter-ply stitching optimisation of highly drapeable multi-ply preforms [J]. Composites Part A: Applied Science and Manufacturing, 2015, 71: 144-156.

Conference papers

- (5) McGregor O P L, Chen S, Endruweit A, Harper L T, Warrior N A. Defect Characterisation and selective stitch removal in non-crimp fabrics [C]. in International Conference SAMPE Europe 2015: Amiens, France.
- (6) Chen S, Harper L T, Endruweit A, Warrior N A. Optimisation of forming process for highly drapeable fabrics [C]. in 20th International Conference on Composite Materials, 2015: Copenhagen, Denmark.
- (7) Chen S, Endruweit A, Harper L T, Warrior N A. Forming simulations of multi-layered woven preforms assembled with stitch yarns [C]. in 16th European Conference on Composite Materials, 2014: Seville, Spain.

Acknowledgements

The author would like to express his gratitude to his academic supervisors, Professor Nicholas Warrior and Dr Lee Harper, for their kind support and sustained encouragement. It was a great honour to carry out this PhD research under their professional, patient and kind supervision.

Special thanks go to Dr Andreas Endruweit and Dr Oliver McGregor for their professional support. Their theoretical and experimental support was invaluable for this project. It was a fantastic experience to work with the other team members on this interesting topic and to share ideas to make progress together. Thanks also go to all of the technicians for their technical assistance, and all other colleagues and friends for their support.

The author is grateful for the financial support from The Faculty of Engineering in The University of Nottingham and Innovate UK under the “Affordable Lightweighting Through Pre-form Automation” (ALPA) project and technical support from the project partners: McLaren Automotive, Hexcel, the Advanced Manufacturing Research Centre and the Manufacturing Technology Centre.

Last but not least, the author’s parents and grandparents have offered him selfless love, generous support and uninterrupted encouragement, which have given the author the confidence to achieve this milestone.

Contents

Abstract	i
List of Publications	iii
Journal papers	iii
Conference papers.....	iii
Acknowledgements.....	iv
Contents	v
Chapter 1 Introduction.....	1
1.1 Background.....	1
1.2 Theme definition.....	2
1.3 Outline of thesis.....	3
Chapter 2 Literature Review.....	5
2.1 Introduction.....	5
2.2 Fabric reinforcements	5
2.2.1 Fabric Architecture	5
2.2.2 Forming mechanisms	7
2.2.2.1 In-Plane shear	8
2.2.2.2 In-Plane tension	10
2.2.2.3 Out-of-plane bending	11
2.2.3 Defect mechanisms.....	12
2.2.4 Material characterisation.....	14
2.2.4.1 In-plane shear test.....	14
2.2.4.2 Biaxial tensile test.....	17

2.2.4.3	Bending test	18
2.3	Fabric forming processes	19
2.3.1	Matched tool forming	20
2.3.2	Diaphragm forming	21
2.3.2.1	Single versus double diaphragm forming	22
2.3.2.2	Diaphragm forming defects	22
2.4	Forming simulation framework	24
2.4.1	Kinematic models vs. finite element methods	24
2.4.2	Implicit vs. explicit algorithms	26
2.4.3	FE modelling scale	27
2.5	Fabric forming simulations	32
2.5.1	NCF forming simulations	32
2.5.2	Multi-ply forming simulations	33
2.5.3	Simulating the effect of inter-ply stitches	34
2.5.4	Diaphragm forming simulations	35
2.5.5	Forming optimisation	36
2.5.6	Validating forming simulations	37
2.6	Chapter summary	38
Chapter 3	Fabric material characterisation	40
3.1	Introduction	40
3.2	Non-orthogonal constitutive framework	40
3.2.1	Homogenisation	40
3.2.2	Coordinate definition	41
3.2.3	Coordinate transformation	43
3.2.4	Implementation of material model	45

3.3	Woven fabric modelling and validation	47
3.4	Non-crimp fabric (NCF) modelling and validation	51
3.4.1	NCF Materials	51
3.4.2	NCF Picture frame shear testing	51
3.4.3	NCF Forming experiment	52
3.4.4	NCF Modelling approach	54
3.4.5	NCF model validation	57
3.5	Hemisphere forming simulations	59
3.5.1	NCF forming validation	59
3.5.2	Defect detection in bi-axial NCF	63
3.6	Chapter summary	67
Chapter 4	Inter-Ply Stitching Optimisation	69
4.1	Introduction	69
4.2	Modelling of multi-ply fabric with localised inter-ply stitches	69
4.2.1	Inter-ply stitch model	69
4.3	Methodology of stitching optimisation	73
4.3.1	Implementation of genetic algorithm	74
4.3.2	Fitness function	75
4.3.3	Adaptive programming strategy	78
4.4	Results and discussion of inter-ply stitching optimisation	79
4.5	Chapter summary	86
Chapter 5	Material Draw-In and Optimisation	88
5.1	Introduction	88
5.2	Modelling of fabric preforming using in-plane constraints	89
5.2.1	Validation for forming model using in-plane constraints	89

5.3	Methodology of in-plane constraint optimisation	90
5.3.1	General strategy	90
5.3.2	Step I: Clamping arrangement optimisation	91
5.3.3	Step II: Spring stiffness optimisation	94
5.3.4	GA stability analysis	95
5.4	Results and discussion of in-plane constraint optimisation.....	96
5.4.1	Clamping arrangement optimisation from Step I.....	96
5.4.2	Stiffness optimisation from Step II	100
5.4.3	Comparison with constraint application through blank holders	103
5.5	Chapter summary	105
Chapter 6	Double Diaphragm Forming	107
6.1	Introduction.....	107
6.2	Process design and experiment.....	107
6.2.1	Double diaphragm forming process	107
6.2.2	Non-crimp fabric.....	109
6.2.3	Diaphragm characterisation	109
6.3	Double diaphragm forming process simulation	110
6.3.1	DDF modelling approach.....	110
6.3.2	NCF material model	112
6.3.3	Diaphragm material model	112
6.4	DDF results and discussion	115
6.4.1	Net shape forming	115
6.4.2	DDF defect detection	115
6.4.3	Scenarios for bridging reduction	121
6.5	Chapter summary	124

Chapter 7	Conclusions.....	125
7.1	Fabric characterisation and modelling.....	125
7.2	Process simulation and optimisation	126
References	127

Chapter 1 Introduction

1.1 Background

Historically, structural applications for carbon fibre composites have been limited to high-end sports cars and certain niche applications, where the limiting factor has been the high cost of raw materials and manufacturing [1-4]. Currently the use of high performance carbon-epoxy composites is well-established in racing and road cars such as the McLaren MP12-4C [5]. Mainstream OEM applications are generally limited to secondary components such as roof panels (e.g. BMW M3 [6]), closures (e.g. Ford Focus [7]) and cosmetic panels and fitments such as door mirrors. However, the recent introduction of the BMW i3 electric vehicle has seen the first carbon fibre intensive vehicle produced and sold for less than £30,000 [8]. This has been achieved by creating a composite upper structure manufactured from relatively simple resin transfer moulded (RTM) panels.

The launch of the BMW i3 has started a revolution in the way vehicles are designed and manufactured from composite materials. BMW have since adopted carbon fibre for structural components on the new 2016 7-series, including the B-pillar, cant rails, sills and header rail [2], which has an annual production volume in excess of 70,000ppa. This increase in composites consumption is being driven predominantly by fuel efficiency and low carbon emissions regulations, requiring lightweight composite parts to replace metal components. It is reported that the North American automotive composite materials market will reach US\$7.2 billion by 2019, growing at more than 4% CAGR. Research efforts in this area will open up the market to wider applications by reducing the cost point at which advanced composite materials become viable. A conservative estimate would be that by 2020, 50,000 vehicles per year could contain up to 500 Euros of structural composite material each (Jaguar Land Rover predict 300,000 conventional vehicles per year in the near future) at a value of 12 million Euros, and 5 million vehicles with 100 Euros of composite by the year 2030, a total in excess of 500 million euros. This would be consistent with the Automotive Council UK's lightweight vehicle and powertrain roadmap which predicts carbon composite materials in bodies-in-white ramping up from 2017 to 2030 [9].

Currently, wider application of composite materials in the automotive industry is limited by the long manufacturing cycle times required to produce finished components. Research into carbon fibre production has reduced the cost of raw materials by reducing the amount of energy consumption [10, 11] and by using lower cost precursors [12]. The development of “snap-curing” liquid epoxies has also facilitated rapid moulding cycles, using high pressure resin transfer moulding [13]. However, the main production bottle-neck remains to be the preforming cycle, which is required to convert flat 2D fibre fabrics into complex 3D shapes. Whilst highly automated fibre deposition processes for preform production exist, these are generally only suitable for large, simple curvature components typically found in the aerospace industry [14, 15], rather than the more geometrically complex, intricate components found in the automotive sector. This project aims to understand the challenges faced when trying to form composite parts for medium volume applications (30,000ppa). The outcomes from this project will also enable cost reductions through reduced material wastage and increased structural optimisation through efficient material utilisation.

1.2 Theme definition

The aim of this project is to simulate and optimise advanced preforming technologies for producing high-quality 3D preforms using automated processes. Numerical simulation is employed to assist in the understanding of fabric material behaviour during forming, in order to predict the onset of defects, such as wrinkles. This information will be used to drive process developments in an attempt to produce a net-shape 3D preform, with zero wastage and no touch labour.

The primary objectives of this project focus on two aspects:

- I. Material characterisation and modelling: Characterise the drapeability of different fabric types (including woven fabric and non-crimp fabric (NCF)) and develop corresponding constitutive relations to take account of either symmetric or asymmetric behaviours.
- II. Process simulation and optimisation: Design processing scenarios and optimise forming parameters to either improve forming quality, or facilitate automated fabric handling, for different types of fibre architecture.

1.3 Outline of thesis

This project was implemented to develop an effective and efficient methodology for predicting the forming behaviour of different fabric architectures and to refine the preforming manufacturing process.

A literature review (in Chapter 2) is conducted to summarise the milestones on fabric forming research. A range of typical fabrics are investigated to understand the dominant forming mechanisms and the cause of defects. In addition, state-of-the-art preforming processes are compared to understand their different capabilities and limitations on fabric preforming. A series of key factors and parameters are identified for automated manufacturing, in order to control forming quality and improve robot handling. This chapter provides an overview of the gaps in the current knowledge and an outline of the approach to be taken in this thesis to meet the aims and objectives.

Chapter 3 presents and validates a constitutive model for describing the deformation behaviour of a pillar-stitched NCF, accounting for the rotation of the carbon fibre yarns and the direction-dependent contribution of the intra-ply stitches. Its implementation in explicit Finite Element (FE) simulations enables the prediction of meso-scale defect formation during preforming based on macro-scale observations. The model is first validated using data from the literature for a plain weave commingled glass/PP material to verify that the constitutive relation is correct for bi-axial fabrics.

Chapter 4 seeks to understand the opportunities offered by locally stitching multiple fabric plies together to create a single preform blank, which can be formed into a complex 3D shape. This aims to reduce preform assembly time in the tool and aid automated deposition of the ply stack. A genetic algorithm is implemented to determine the optimum position of local stitches, in order to improve preform quality for multiple-ply with different orientations.

Chapter 5 aims to optimise the draw-in of the blank during forming, using spring-loaded clamps around the perimeter to control in-plane tension. This arrangement enables the blank to be heated more easily prior to forming and offers more flexibility in terms of controlling material draw-in, as the spring-loading for each clamp can be controlled independently. It also provides an opportunity to reduce preform size and therefore waste. The optimisation

procedure seeks to determine the optimum location and size of each clamp and the stiffness of each spring to minimise the global in-plane shear angle of the fabric.

A novel double diaphragm forming process is introduced in Chapter 6 to form dry fabrics. This creates an opportunity to form parts quickly (about 5 minutes) using low cost tooling and at low pressures. The diaphragms create tension in the fabric, therefore mechanical blank holders can be avoided and net-shaped parts can be created with no wastage. Numerical simulation is employed to understand and optimise the diaphragm forming process, using experimental data to validate the model and confirm defect observations.

Conclusions are drawn to summarise the primary discoveries for this research and to provide guidelines for design, analysis and optimisation for industrial application (Chapter 7).

Chapter 2 Literature Review

2.1 Introduction

This Chapter reviews the literature for a range of common fabric architectures and forming methods, in order to understand the dominant forming mechanisms and the cause of critical defects in formed composite components. Recent forming simulation developments have also been reviewed to understand the challenges faced when trying to predict the forming behaviour of technical textiles over complex 3D geometries. A summary at the end of this chapter provides an overview of the gaps in the current knowledge and an outline of the approach to be taken to meet the aims and objectives defined in Chapter 1.

2.2 Fabric reinforcements

2.2.1 Fabric Architecture

The term “fabric” employed here describes an interlaced architecture mainly constructed by yarns and sometimes assembled by stitches. Fibre convertors are capable of delivering high-quality fabrics at production rates of up to several hundred kg/hr using modern machinery from automated processes such as weaving and knitting [16]. Driving down cost is the primary driver for adopting off-the-shelf fabric products from commercial suppliers, which are relatively easy to handle and form into complicated geometries. Fabrics offer a good balance in terms of the cost of raw materials and ease of manufacture, although material wastage can be as high as 40%, due to poor utilisation for complex components [17, 18]. Whilst there are many different kinds of fabrics [19], only 2D woven fabrics and non-crimp fabrics (NCF) are of interest in the current work, as they are widely used in industry to produce 3D components.

As shown in Figure 2.1, the architecture of a woven fabric is established by interlacing yarns, enabling necessary deformation during forming. The yarns undulate over/under each other creating crimp, which reduces the reinforcement efficiency of the fibres when moulded. Gaps can also form at fibre cross-overs, which can be the cause of stress raisers, but also provide possible spaces for the tows to deform during fabric shearing. The formability of a woven fabric is therefore affected by its weave pattern [20]. Although plain weaves (see Figure 2.1

(a)) produce a more stable architecture to facilitate material handling, the side effect is reduced formability because of the greater number of fibre-fibre interactions (see Figure 2.1(b)) [20].

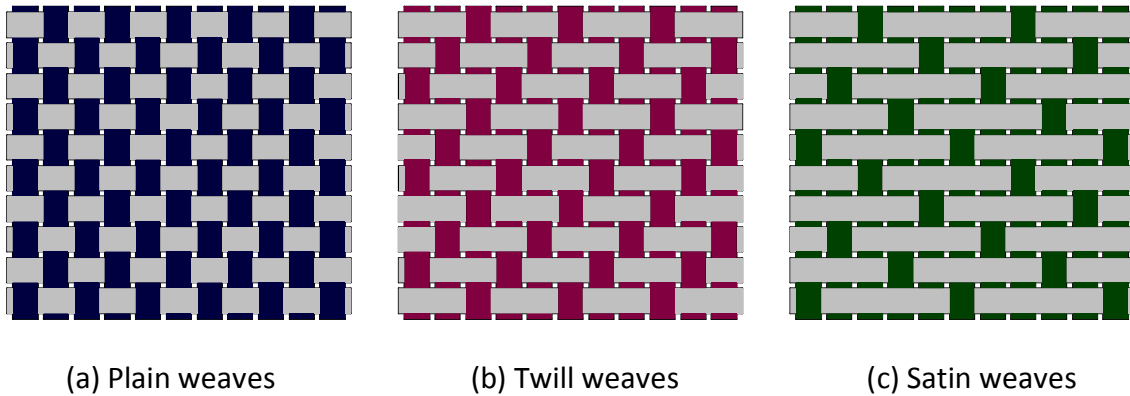


Figure 2.1: Typical woven fabrics

Non-crimp fabrics (NCF) are produced by assembling UD crimp-free fibre plies through stitching, sewing, knitting and/or chemical bonding. As shown in Figure 2.2, there is no crimp of the main reinforcing fibres, which offers improved in-plane stiffness compared with a woven fabric and mechanical properties approaching those of unidirectional materials [21]. In general, NCFs are not as formable as woven fabrics, but they are of particular interest for automated preforming processes, as they are very stable during handling [20]. NCFs are often constructed as multi-axial materials (i.e. 0°/90° or 45°/0°/-45°), as it is an efficient way of depositing a large areal density of fibre in the minimum number of plies.

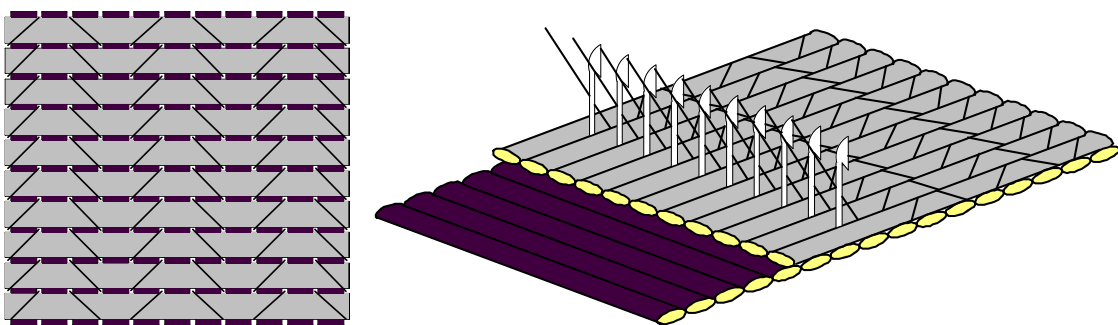


Figure 2.2: Typical non-crimp fabrics (NCFs).

Biaxial NCFs are the main interest in this thesis. Biaxial NCF reinforcements are composed of two layers of fibres, typically at 0°/90° or $\pm 45^\circ$, which are connected together by through-thickness stitches. The intra-ply stitch pattern can be selected to improve stability, by preventing unwanted shear deformation during handling. The dominant forming mechanism

of a biaxial NCF fabric is in-plane shear deformation, similar to other bi-directional materials (such as woven fabrics). However, the mechanisms of shear are different, as the mesoscopic architecture of an NCF is established by introducing intra-ply stitches rather than interlacing the primary yarns. Both straining of the in-plane segments of the intra-ply stitches and rotation of the primary yarns contributes to the shear behaviour of the NCF at the macroscale. Inter-yarn friction provides some resistance to shear deformation during yarn rotation. The orientation of the in-plane segments of the stitches relative to the primary yarn direction can lead to asymmetric shear behaviour, which may be undesirable for real components, as it may be difficult to avoid defects during forming [22]. Positive and negative shear terms are commonly referred to in the literature to indicate when the in-plane segment of the stitch yarn is in tension or compression respectively [23], as shown in Figure 2.3. The influence of the intra-ply stitches on the shear stiffness can be significant (for $\pm 45^\circ$ fabrics) under positive shear, as it is dominated by the tensile properties of the stitch yarn. The in-plane segments of the stitch are likely to fail at high strains (induced by large shear angles), causing irreversible damage to the fabric and a sudden reduction in the shear stiffness [14]. In negative shear, NCFs tend to exhibit the same phenomena as woven fabrics when the in-plane segments of the stitch are loaded in the compressive direction [21]. In general, there is low shear stiffness up to shear angles of $\sim 30^\circ$ when the main shear resistance mode is friction between the primary yarns, followed by a rapid increase of the shear stiffness with the onset and intensification of the lateral compression of the fibre bundles.

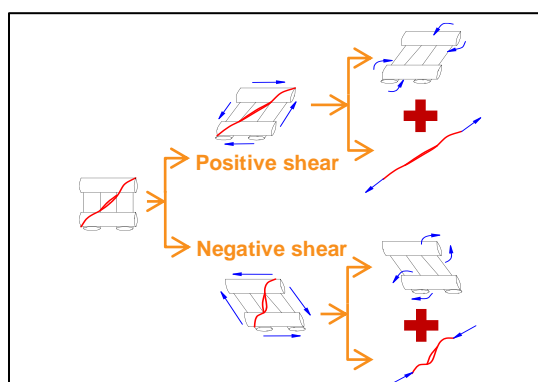


Figure 2.3: Schematic showing the difference between positive and negative shear.

2.2.2 Forming mechanisms

Fabrics undergo large deformations to conform to the target geometry during the forming process. The formability of fabric materials is mainly derived from the deformation of the

reinforcement, which can be primarily represented by in-plane tension, in-plane shear and out-of-plane bending in macro scale. The macro-scale behaviour of the representative material cell indicates typical nonlinearity and irreversibility in the form of nominally equivalent stress-strain curves, which indicate the complex interaction mechanism of the internal meso-/micro-structure. The equivalent tensile modulus is significant along both primary fibre directions, but is negligible in terms of the out-of-plane bending resistance. Additionally, the shear modulus is also quite small and therefore large deformation is possible. Rotation of the yarns occurs until the locking angle is achieved, which corresponds to the onset of wrinkling.

2.2.2.1 In-Plane shear

The in-plane shear modulus G of the fabric is much smaller than the tensile modulus E ($E/G < 0.001$); therefore the in-plane shear mode dominates the formability. Forming 2D fabric preforms into complex 3D shapes requires large shear deformations, which occur due to fibre reorientation. The yarns rotate and slip, and simultaneously, intersecting yarns compact each other at their crossovers as shown in Figure 2.4. The shear rigidity is therefore dependent on the changes in mesoscale geometry (yarn compaction) and the intra-ply yarn-yarn slippage (including warp-weft, warp-warp and weft-weft) during yarn rotation, which can cause yarn spreading and bunching.

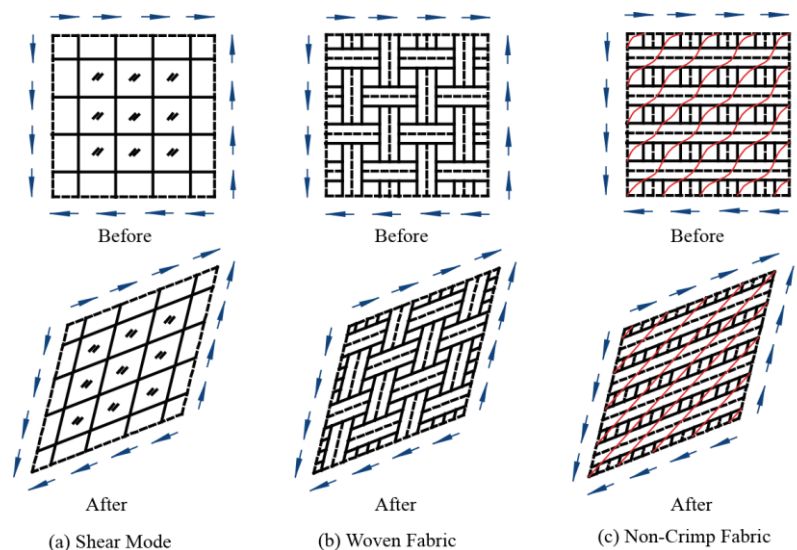
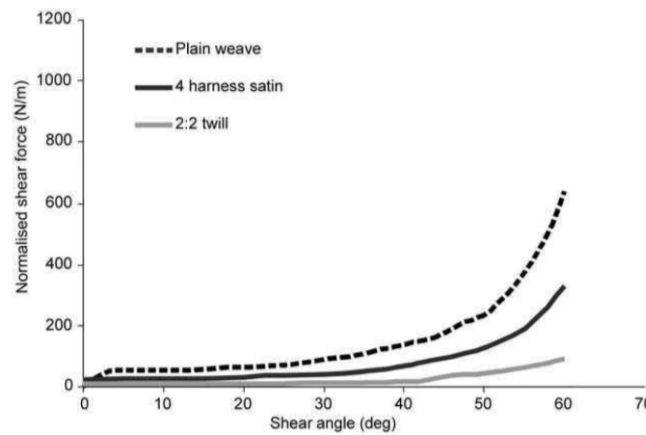


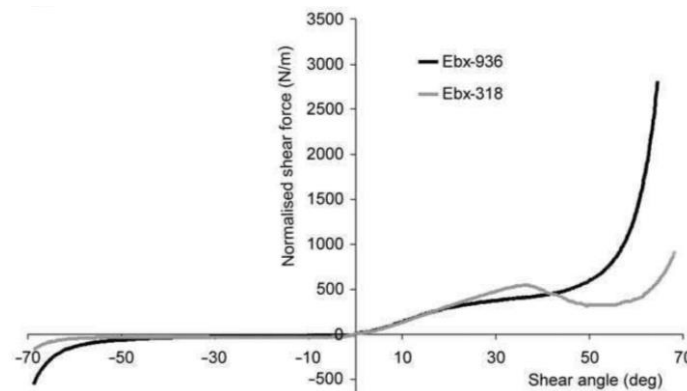
Figure 2.4: In-plane shear mode and mechanisms respectively for woven fabric and NCF.

For 2D woven fabrics, the interlaced yarn structure and intra-ply slippage between yarns provides the shear resistance during forming (see Figure 2.4(b)), where the former starts

dominating the shear behaviour after a certain shear deformation (about 50° for the specific fabrics as shown in Figure 2.5(a)), namely shear locking. The shear stress-strain curve is symmetric; therefore only one test is required in either the positive or negative shear directions.



(a) Three woven fabrics with superficial density 800 g/m^2



(b) NCFs retained with tricot (Ebx-936) and chain (Ebx-318) stitch oriented at 45° to the tows

Figure 2.5: Shear behaviour curves for fabrics. Negative shear angle represents deformation perpendicular to the stitch. [24]

For NCFs, both the intra-ply slippage between primary yarns and the stretching of fixture stitches (intra-ply) may contribute to the shear resistance (see Figure 2.4(c)). The stitches provide an orientation-dependent contribution to the equivalent shear modulus of the fabric. The compressive stiffness of the stitch is negligible, but the tensile component dominates the shear response at the macroscale. However, the tensile stiffness of the stitch only influences the shear compliance of the fabric in one direction, which may lead to asymmetric shear behaviour of NCFs as shown in Figure 2.5(b) depending on the stitch pattern. The stitches used to fix the fibre architecture are the primary cause of shear locking on NCFs, since they

are able to constrain the inter-tow movement and enhance the resistance after a certain shear angle, by locking up the yarns. The failure of stitches along the axial direction can alleviate the shear locking effect, but may lead to other defects such as laddering. For example, the threshold value for the NCF materials in positive shear in Figure 2.5(b), (about 50°) is smaller than the one in negative shear (about 60°) due to local stitch failures.

Compared to the tensile modulus, the equivalent shear resistance is very small before locking, which then increases dramatically to exhibit the mesoscopic shear locking mechanism, as shown in Figure 2.5.

2.2.2.2 In-Plane tension

The macroscopic in-plane tensile mode is determined by the redistribution and elongation of yarns at the meso/micro scale, as shown in Figure 2.6. The stress-strain curve along the fibre direction may show a nonlinear relationship, which varies with the ratio of tensile forces between two fibre orientations, as shown in Figure 2.7. For 2D woven fabrics, this nonlinearity is derived from the undulation of yarns (see Figure 2.6(b)); while, for NCFs, this feature is mainly generated from the undulated stitch yarns, which are less significant due to their non-crimp mesoscopic architecture (see Figure 2.6(c)).

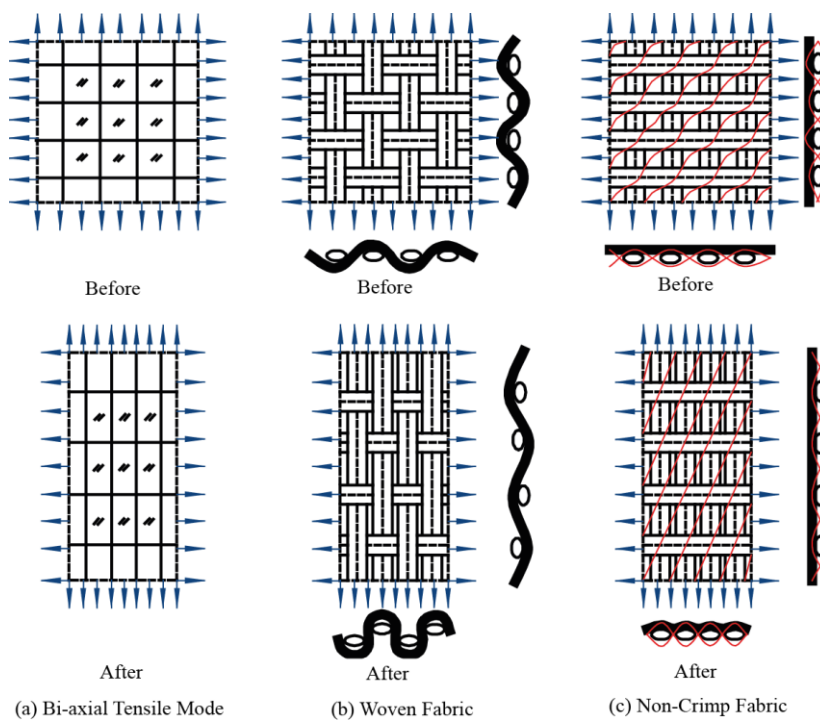


Figure 2.6: In-plane tensile/compression mode and mechanisms respectively for woven fabric and NCF.

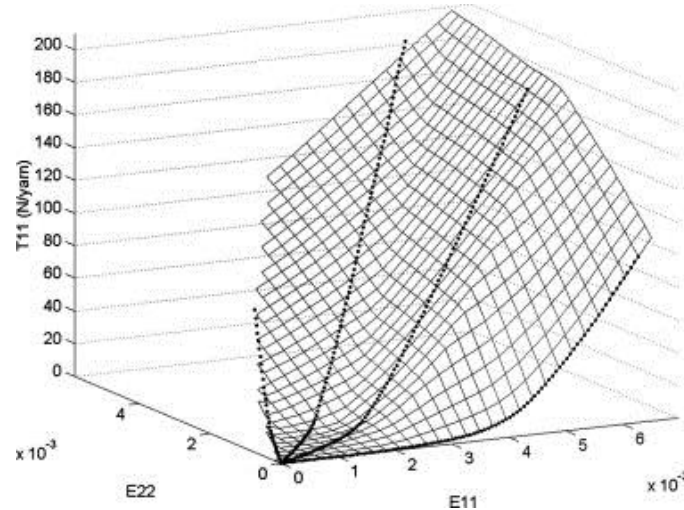


Figure 2.7: Biaxial tensile behaviour surface for a balanced glass plain weave fabric obtained from experimental results. [25]

When a fabric is loaded in tension, the undulating yarns (or stitch yarns in NCFs) tend to straighten, resulting in a characteristic J-shape to the stress-strain curve (i.e. only nonlinear at the beginning) (see Figure 2.7). However, this is a bi-axial phenomenon, because as the undulation decreases in one direction it tends to increase in the other direction (see Figure 2.6), which can lead to some difficulties in modelling fabric forming. However, this nonlinearity can generally be ignored when the material is flat (i.e. small undulation of primary yarns) so that the Young's modulus along the fibre direction can be assumed to be linear without significantly compromising precision [26].

2.2.2.3 Out-of-plane bending

The out-of-plane bending stiffness is significantly lower than the in-plane stiffness, as yarns can slide relative to each other (i.e. intra-ply slippage) [24]. Although the equivalent macroscopic deformation is almost the same for different fabrics, their bending mechanisms are slightly different, as shown in Figure 2.8. The bending stiffness for 2D woven fabrics is derived from the elongation of the undulated yarns, which is independent of the direction of bending (see Figure 2.8(b)). The bending stiffness of NCFs depends on the direction of bending however (see Figure 2.8(c)), as the ply is effectively unbalanced due its construction.

Although the bending stiffness is necessary to predict realistic wrinkling features [27], the membrane assumption is still suitable for thin fabrics [28], since the onset of wrinkling defects primarily depends on compressive and in-plane shear stiffnesses rather than bending stiffness [29].

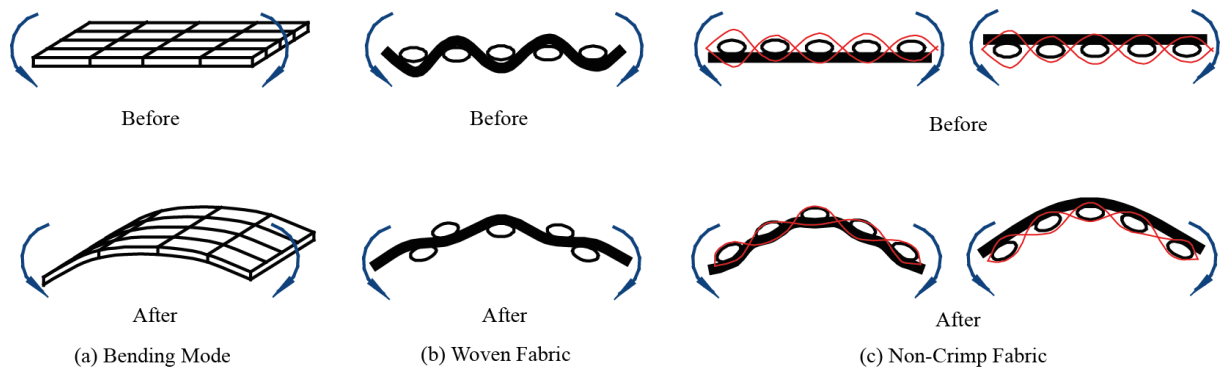


Figure 2.8: Out-of-plane bending mode and mechanisms respectively for woven fabric and NCF.

2.2.3 Defect mechanisms

Defects which occur during fabric forming may significantly reduce the mechanical performance of the final product. Wrinkling is one of the most common defects that occurs during forming; others include fibre misalignment and local variations in local fibre volume fraction due to fibre spreading or bunching [30]. In particular, stitch damage is an additional defect mode for NCFs, but this may not be critical if the primary yarns are unaffected. The main defect modes for woven and NCF fabrics are summaries in Table 2.1.

Table 2.1: Typical defect modes derived from fabric forming.

Defect mode	Macro-scale wrinkling (ply folds)	Meso-scale wrinkling (bundle loops)	Gaps/voids (Laddering)	Stitch damage
Phenomena				
Mechanism	Transverse yarn compaction (shear locking)	Longitudinal yarn compression (yarn buckling)	Intra-ply yarn spacing (intra-ply over-slippage)	Longitudinal stitch extension (stitch failure)
Measure	Shear angle (locking angle)	Fibre compressive stress/strain/energy (critical buckling strain/energy)	Fibre tensile strain/stress (fibre spacing)	Stitch stress (stitch strength)
Applicable materials	Woven Fabric & NCF			NCF only

Shear deformation is the most important mechanism governing the forming of a fabric reinforcement [19, 24, 31, 32]. The shear angle can be employed as a measure of wrinkle initiation, induced by the compaction of intersecting yarns in the transverse direction. As the

shear angle increases, the local in-plane shear and compressive energies increase. Once the locking angle is exceeded, additional energy is stored by ply wrinkling or yarn buckling. However, in-plane tension may alter wrinkling onset angle, which depends on the type of fabric. For woven fabrics, the in-plane tension may change the undulation of the yarns, resulting in the variation of yarn rotational constraint; while, for NCFs, the yarns are not crimped and the in-plane tension do not significantly affect the shear angle corresponding to the initiation of wrinkling.

The spreading and opening of yarns (laddering) is a defect induced by tensile deformation. At the mesoscale, the tension along one fibre direction leads to the redistribution of load to crossing transverse fibres. The tensile strain/stress at the macroscale can be used as an appropriate measure of this defect. Its occurrence relies on the meso-geometry of the fabric (i.e. the width, spacing and undulation of yarns), interfacial properties (i.e. fibre-fibre/yarn-yarn friction and slippage) and constituent properties (i.e. tensile/buckling resistance of yarn and tensile resistance of stitches).

The fundamental difference in the fibre architecture caused by the inclusion of the stitch yarn means that the mechanisms for defect formation in NCFs are somewhat different to those in woven materials. In-plane fibre buckling [22] and out-of-plane fibre wrinkling [33] are still the most common mechanisms as with woven fabrics, but fibre pull-out, stitch thread failure and inter-layer sliding have also been reported [34]. The change in fabric surface area during shear means that the spaces between the yarns decrease. When adjacent yarns make contact, further compaction is restricted when the locking angle is reached, causing compressive stresses that are released by out-of-plane wrinkling [33]. Most wrinkles occur where large shear deformation occurs. However, in actual forming scenarios, where fabric draw-in is controlled through blank holders, wrinkles have been reported in regions where the local shear angle was small and therefore the locking angle had not been reached [22]. This is related to the magnitude of the blank holder force, which affects the level of local shear deformation. However, if the stitches are in compression, the stitches become loose during fabric shear, removing the restriction placed on the yarn. The yarns are therefore free to move and the sample increases in thickness as the test area decreases, rather than buckling. Lomov et al. [21] showed that the thickness of the sheared fabric generally increases following the assumption of a constant volume. Bias extension testing of NCF has shown that additional

deformation mechanisms can occur during fabric shear, such as fibre sliding [34, 35]. Hemisphere tests indicate that inter-yarn sliding leads to ply deterioration, with only one primary fibre direction remaining in some regions. The slip distance is dependent on the stiffness and pre-tension of the stitching thread. If the stiffness is high, the slip distance is negligible and the NCF deformation resembles that of a woven fabric. Fibre slippage is not observed during picture frame testing however, due to different boundary conditions.

2.2.4 Material characterisation

Non-standard test methods are available to characterise the properties of fabric materials [36]. The outcome of the material characterisation phase is to provide ready-to-use data that can be directly implemented in numerical models, for supporting the development of preforming techniques.

2.2.4.1 In-plane shear test

Picture frame tests and bias extension tests are different testing methods to characterise the shear behaviour of fabrics, providing the nonlinear shear modulus and locking angle.

- (1) The picture frame test is implemented using a square pin-jointed frame as shown in Figure 2.9(a) and Figure 2.10(a). The fabric sample is placed with bi-directional yarns parallel to the frame arms respectively and all ends are clamped by the frame. A vertical displacement is applied to the top vertex of the frame via the crosshead of the testing machine and the corresponding force is recorded by a load cell. A well-understood relationship between the force and shear angle has already been established to characterise the homogeneous shear behaviour based on the geometric parameters of frame and sample. Three different normalisation methods have been introduced to compare the testing data from different groups using different sizes of picture frames, using energy-based methods (including length normalisation, area normalisation and a modified length normalisation) [19, 36, 37]. Peng et al [36, 38] concluded that the modified length normalisation method can provide a more consistent material behaviour if tests are performed using different specimen sizes.
- (2) The bias extension test is conducted on a rectangular sample as shown in Figure 2.9(b) and Figure 2.10(b). The length/width ratio should be no less than 2 and both warp and weft yarns should be initially placed at $\pm 45^\circ$ to the tensile loading direction. A

displacement is imposed perpendicular to the clamped edge and the driving force is recorded by a load cell. The shear angle has to be measured by image analysis, such as DIC (Digital Image Correlation) [39-41]. However, unlike the picture frame test, the shear force from bias extension is calculated from an iteration equation [36] rather than an explicit expression.

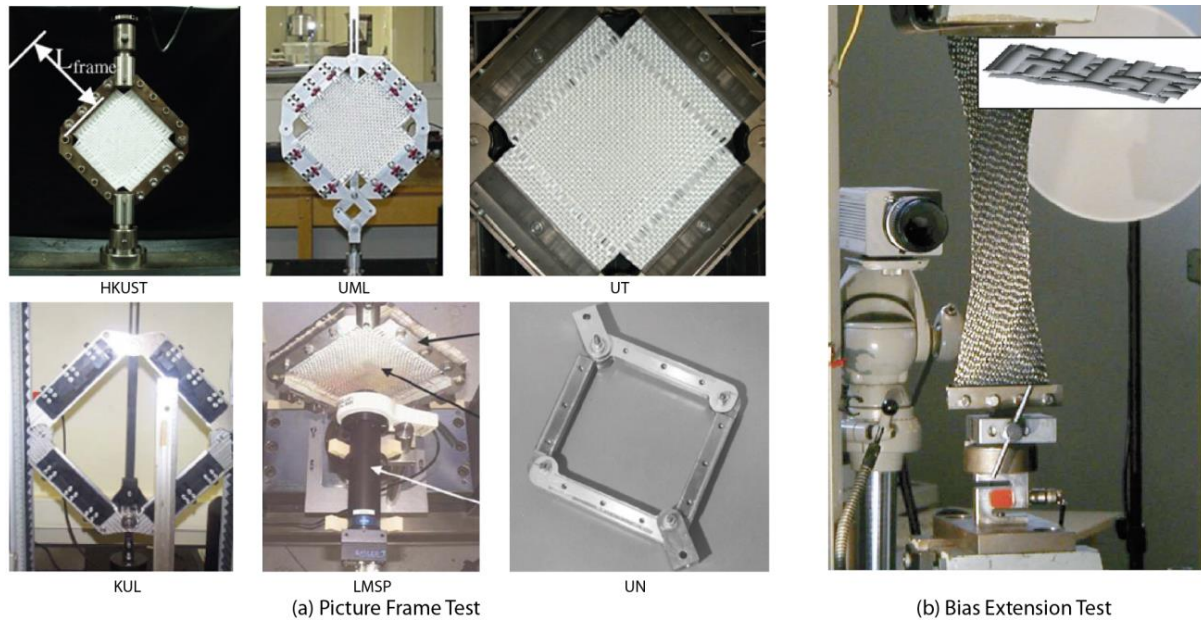


Figure 2.9: Testing rigs of in-plane shear behaviour. (a) Picture frame test rigs from different groups (left) [36]: Hong Kong University of Science and Technology (HKUST), University of Massachusetts Lowell (UML), University of Twente (UT), Katholieke Universiteit Leuven (KUL), Laboratoire de Mécanique des Systèmes et des Procédés (LMSP), University of Nottingham (UN); (b) Bias extension test rig (right). [39]

The rig design for shear testing is aimed at replicating the boundary condition of pure shear imposed on an equivalently homogenised media. The picture frame test takes account of the whole material region; where the test curve indicates an overall behaviour of the material field (see Figure 2.10(a)). For the bias extension sample, there are three typical regions undergoing different loading statuses and only the middle area (see Figure 2.10(b)) is subjected to pure shear [41]. As shown in Figure 2.10, the areas in red are the regions expected to undergo pure shear for both approaches and all the homogenised material points in these regions are expected to be under the same shear conditions. However, for NCFs, this condition is not always satisfied, since stitches start failing locally and this propagates as the shear deformation increases. Once the failure of any stitch occurs, the deformation is not uniformly distributed and the subsequent curve represents the average response. Thus, the material behaviour recorded after stitch failure may be spurious.

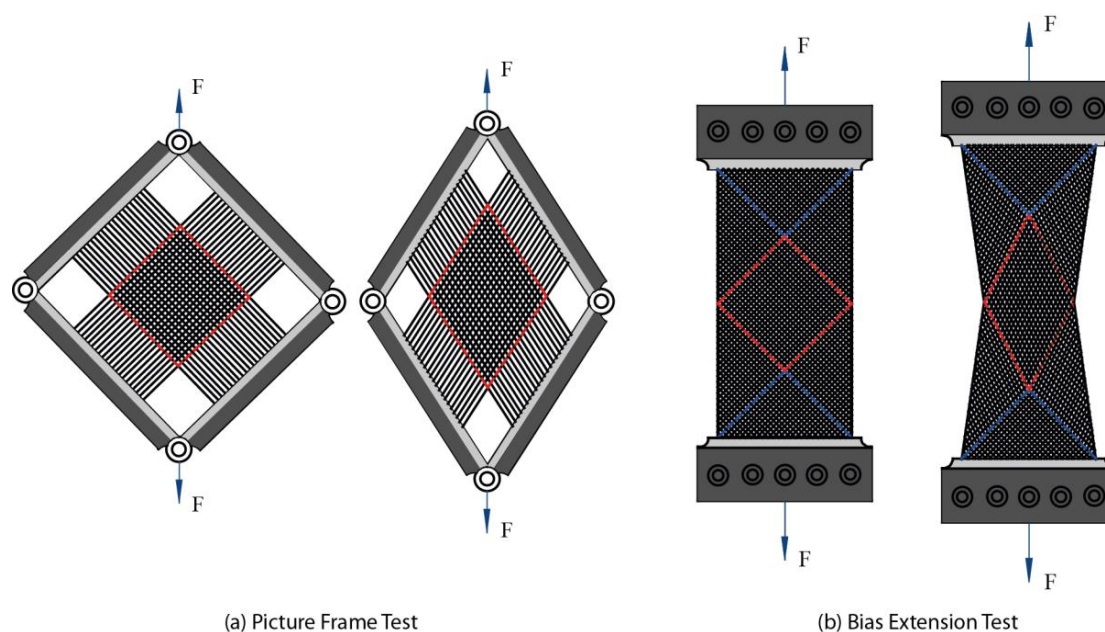


Figure 2.10: Testing mechanism of in-plane shear behaviour for fabric materials. (a) Picture frame test (left); (b) Bias extension test (right). The area of the red frame is the material region under pure shear.

There is much debate in the literature as to which test method should be adopted to characterise the in-plane shear compliance of biaxial NCFs. The choice is more obvious for other NCF formats, with bias extension testing used for triaxial NCFs [42] and the picture frame test for UD materials [43]. Comparisons of the picture frame test and bias extension test have been performed for a range of biaxial NCFs with different stitch patterns (tricot or chain) [33]. There is an initial difference (at low shear angles) in the shear compliance between the two tests when the stitches are in tension, which can be attributed to different strain levels generated in the stitch. Strains are applied directly to the stitches in the bias extension test for positive shear, as they run between the grips of the test fixture. Whereas the strain is applied indirectly in the picture frame test, as the stitches do not run between the frame edges if the samples are prepared correctly (fibres parallel to grips are removed from the grip region to minimise fibre bending [21]). In compression, the shear force is generally higher for the picture frame test compared to the bias extension test [33]. This discrepancy is independent of the stitches and can be attributed to misalignment of the primary fibres in the picture frame test. Fixed clamping at the frame edges can lead to local yarn bending at the boundary, whereas the fibre ends are unclamped in the central pure shear zone of the bias extension sample, so are free to rotate. The picture frame is also more likely to produce a pure shear situation because of the boundary conditions, whereas bias extension can highlight fibre slip. The picture frame test is more difficult to standardise, as small

misalignments can lead to large variability, but the results are more easily interpreted [21]. The difference between the shear of the fabric and the shear of the frame in a picture frame test can be considered to be negligible, as the local variability in local shear angle was measured to be less than $\pm 2^\circ$ [21]. However, the shear resistance of the fabric strongly depends on the pretension applied by the frame [14], but this value is rarely reported. Multi-axial test methods have been developed for biaxial and multi-axial fabrics, in order to explore effects such as shear-tension coupling [44, 45]. Biaxial bias extension tests demonstrate that shear-tension coupling exists, but the data reduction from this test is non-trivial and difficult to interpret for forming simulation purposes.

2.2.4.2 Biaxial tensile test

According to the deformation mechanism, woven fabrics indicate larger levels of nonlinearity under tension than NCFs due to considerable undulation of the yarns. In general, NCFs exhibit linear behaviour in bi-axial tension, since the primary yarns are parallel to the ply surface [19]. Therefore, the biaxial testing rig (see Figure 2.11(a)) is more applicable for woven materials. As shown in Figure 2.11(b), either the force ratio (F_{t1}/F_{t2}) or the displacement ratio (λ_1/λ_2) can be controlled in the test to achieve different testing conditions.

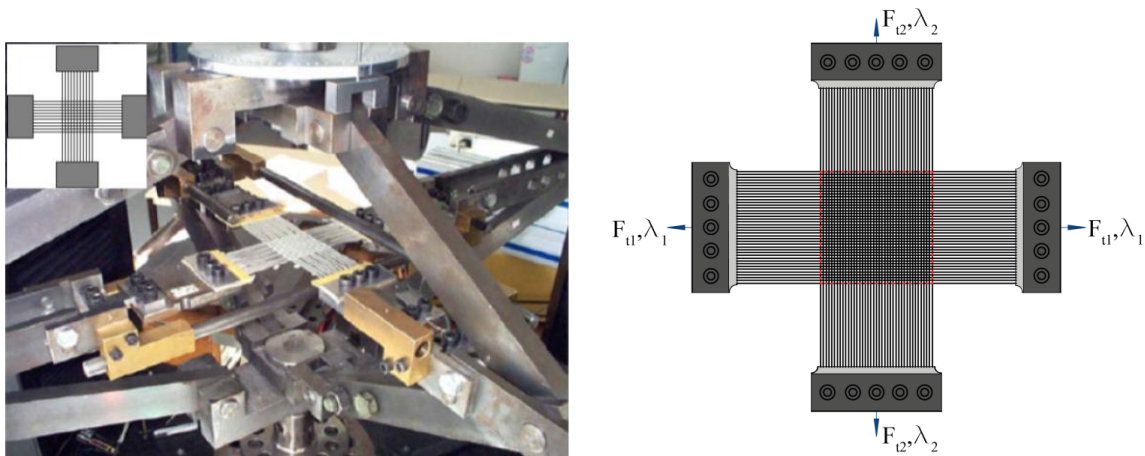


Figure 2.11: Biaxial tensile testing rig and mechanism for fabric materials. (a) Bi-axial tensile testing rig (left) [40, 46]; (b) Mechanism of testing rig (right). The area of the red frame in (b) is the material region under testing.

As shown in Figure 2.12, the stress-strain curves of woven fabric exhibit a J-shape, which is different from the individual yarn. Due to the variation of undulation, the tensile modulus is almost zero at the beginning and gradually increases to the equivalent modulus of the individual yarns. The nonlinear segment ends around 0.4% strain, which is quite low

compared to the large shear deformation during fabric forming. Boisse et al [26] investigated the influence of these fibre undulations on the forming behaviour of woven fabrics, using both an FE simulation and experiments. It was concluded that the influence of this tensile nonlinearity is negligible when the deformed area is larger than the area of the undulation-influenced domain. The tensile behaviour was assumed to be linear in [40, 47, 48] and the simulation results were in agreement with experiments, although this point is still openly debated in the literature.

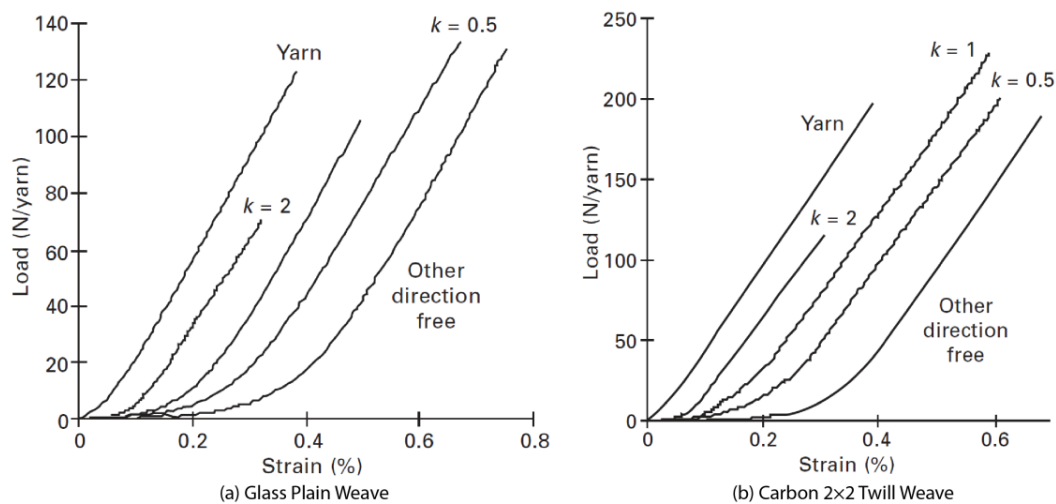


Figure 2.12: Bi-axial testing data of different woven fabrics. (a) Glass plain weave (left); (b) Carbon 2×2 twill weave (right). $k = \varepsilon_1/\varepsilon_2$ is the strain ratio, where 1 is the investigated fibre direction which could be either warp or weft. [19]

2.2.4.3 Bending test

Usually, the tensile stiffness of fabric is much higher than the bending stiffness so that a membrane assumption is widely employed in fabric forming simulations. However, it is important to include the bending stiffness for simulating realistic wrinkling shape during preforming [49]. Results based on the membrane assumption can only indicate the occurrence of wrinkling defects but are unable to replicate detailed wrinkling features.

There are two different devices to measure the representative bending stiffness for fabrics, i.e. KES-FB system [50] and ASTM cantilever bending system [51-53] (see Figure 2.13(a)), where the gravity is employed to generate the bending moment. The curvature of each deformed status is calculated from the geometry of the specimen. Therefore, the bending stiffness EI is obtained from the relationship between the bending moment M at the cross-section and the corresponding curvature κ (i.e. $EI = M/\kappa$) using the measured curves as shown in Figure 2.13(b).

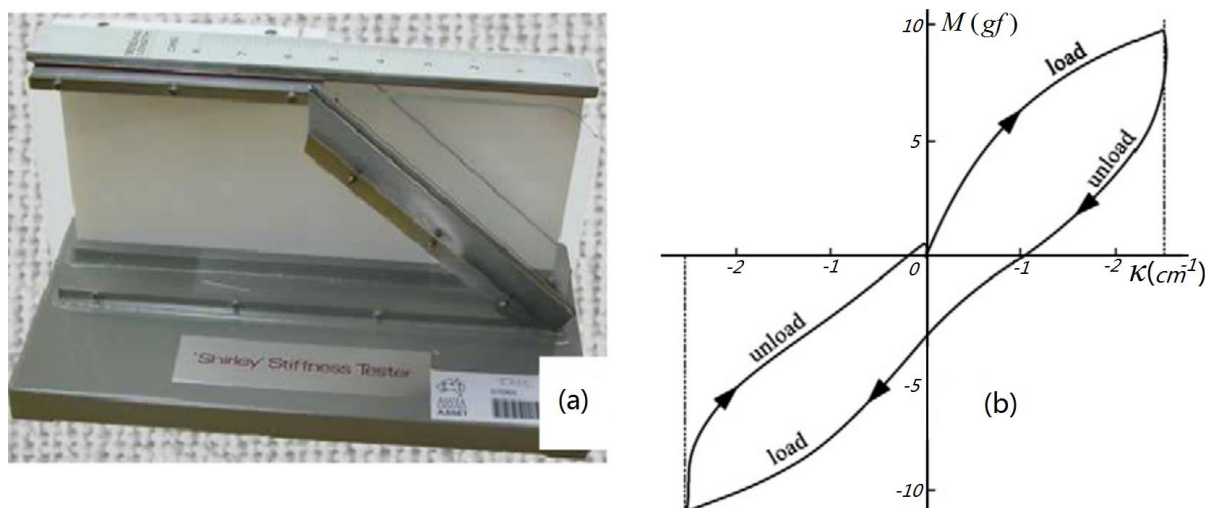


Figure 2.13: Measurement of woven fabric bending properties. (a) ASTM, Standard test method for bending stiffness of fabrics [51]; (b) a representative curve from fabric bending test [53].

2.3 Fabric forming processes

Reducing manufacturing costs and cycle times, whilst maintaining component quality, is key to wider application of composite materials in the aerospace and automotive sectors. One of the major bottlenecks in any manufacturing process for composite components is forming flat 2D fibre broad goods into doubly-curved 3D shapes. To improve efficiency, manual labour must be minimised and automation implemented, but a geometrically complex component that is formable by manual layup is not necessarily formable using an automated process. Manual layup enables an optimised sequence of forming operations to be followed for each individual ply [54]. This can be difficult to replicate in an automated process, particularly if all plies are formed at once to minimise cycle time. Complex inter-ply interactions due to friction increase the risk of defects, such as in-plane fibre waviness or out-of-plane ply wrinkling, to occur in multi-ply formings. When the geometry to be formed comprises single curvature, such as a prismatic C-channel, the dominant deformation mode for multi-ply preforms is inter-ply slip [1]. However, as the complexity of the geometry increases, a combination of in-plane and out-of-plane deformation is required and the likelihood of defects increases.

Complex 3D preforms can be produced from 2D flat configurations using either matched tooling or single-sided tooling processes. The selection of the process type is dependent on expected production volumes, cycle times, component cost and component size. This thesis will primarily focus on single-sided tooling processes, but simulation and experimental results will be benchmarked against a matched-tooling solution.

2.3.1 Matched tool forming

In matched tool forming, a matched set of male and female tools are located in a hydraulic press and used to force the fabric plies into the cavity. A punch, die and blank holder are the primary elements of a matched tool forming system, and the process is conducted in four stages, as shown in Figure 2.14.

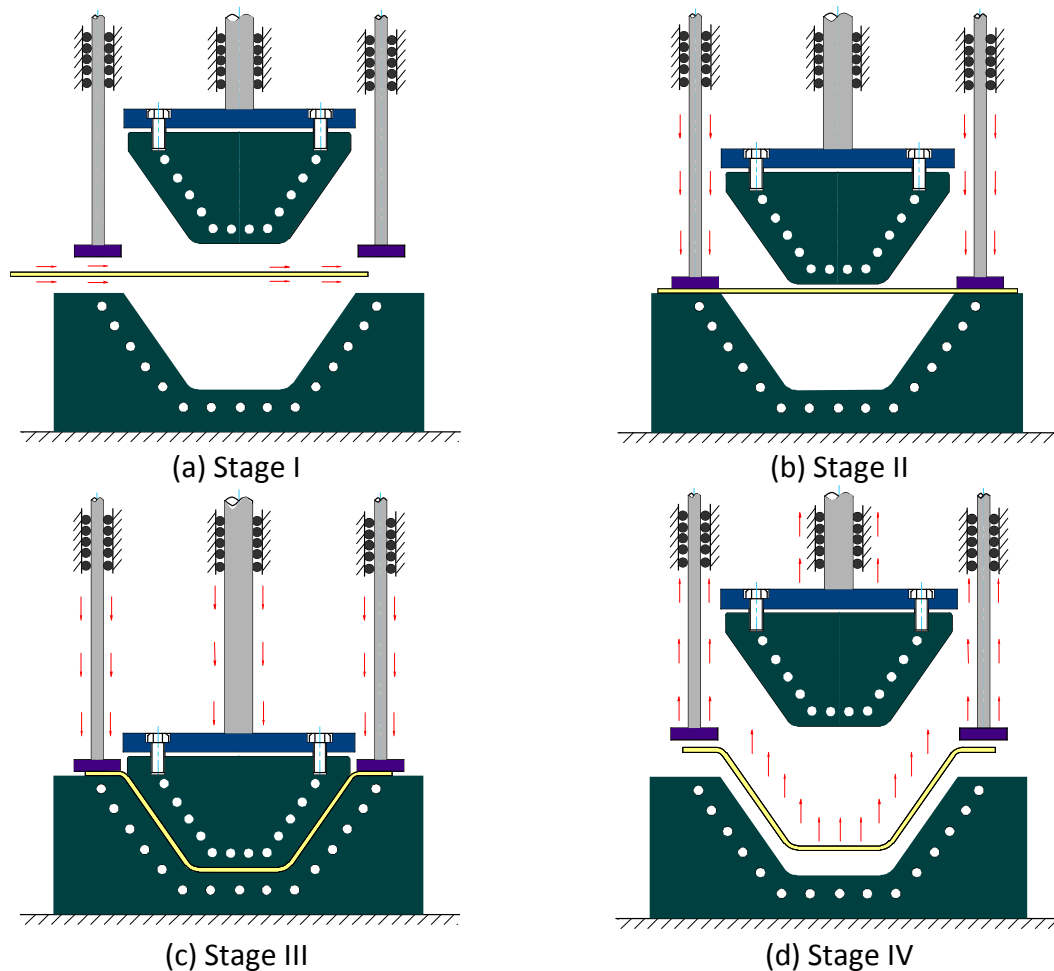


Figure 2.14: Typical matched tool forming process.

- Stage I Preparation: The matched tool is opened, release agent is applied on the surfaces of the tools, and then the prepared material with thermoset or thermoplastic binder is transferred to the mould.
- Stage II Constrain material: The blank holder is employed to clamp the fabric stack around the edge of the cavity.
- Stage III Stamping: The punch is driven by the hydraulic press until reaching a scheduled stroke length and the tool together the preform is heated to activate the binder powder.

Stage IV Mould releasing: The matched tool is opened again after cooling down the tool and then the produced preform is released from the mould.

The implementation of a matched tool process requires a series of tools to be designed and manufactured, where the male (i.e. punch) and the female (i.e. die) moulds closely control the forming quality. However, the capital expenditure for this type of process is extremely high, which limits its application to high volumes (~100,000ppa+).

2.3.2 Diaphragm forming

Diaphragm forming (or hot drape forming) is one potential method for automating the production of low cost preforms for high volume applications (30,000+ ppa). It offers lower capital investment compared to matched-tool forming. The forming process applies a hydrostatic pressure to the fabric stack via a membrane, and is commonly used as a preforming step for autoclave cure cycles in the aerospace industry [55]. It is typically associated with thermoplastic composite materials [56-58], but more recently has been used to process thermoset prepregs [55, 59-61] and produce binder-stabilised dry fabric preforms for liquid moulding [62-65] routes. As shown in Figure 2.15, this process is carried out in four stages.

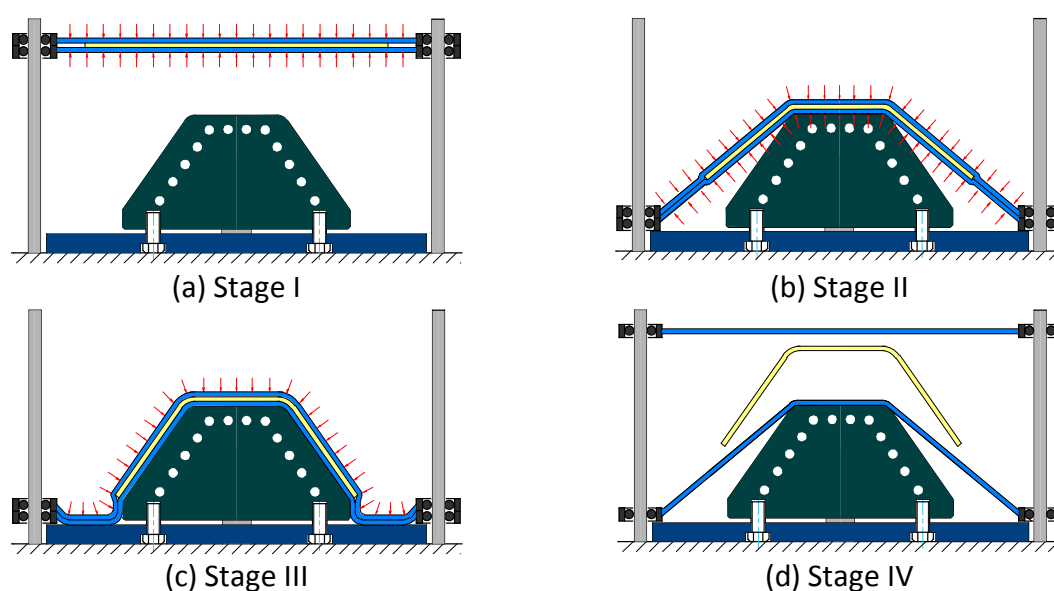


Figure 2.15: Typical diaphragm forming process.

Stage I Preparation: The prepared material with thermoset or thermoplastic binder powder is transferred to mould and the whole system is sealed carefully to create isolated spaces.

- Stage II Forming: The diaphragm is constrained around the perimeter to a gliding frame and then the fabric stack is driven by this frame to approach the mould.
- Stage III Vacuuming: The vacuum is created in the closed space, which is used for reducing the clearance between the mould and the material, and then the preform in mould is heated to activate the binder powder.
- Stage IV Mould releasing: Air re-enters the vacuum space after cooling down the tool and then the produced preform is released from the mould.

2.3.2.1 Single versus double diaphragm forming

There are two diaphragm forming options; using either a single membrane (Single Diaphragm Forming, SDF) or two membranes (Double diaphragm forming, DDF). In DDF, material plies are sandwiched between two deformable membranes, which are deep-drawn over a rigid tool by applying a pressure differential normal to the surface. Multi-axial in-plane tension is applied to the plies through friction on the membrane surfaces, which can be controlled by the pressure between the diaphragms to avoid fibre wrinkling and buckling and control in-plane shear. DDF is used to form the full ply stack in one operation, as the presence of the lower diaphragm prevents subsequent operations. SDF offers more process flexibility, enabling the preform to be constructed from multiple plies which can be formed sequentially. However the single diaphragm, does not constrain the ply stack relative to the tool, particularly for complex geometries which can result in greater variation.

2.3.2.2 Diaphragm forming defects

Defects in the fibre architecture caused by diaphragm forming are different to those caused by matched tool forming. At the end of the stroke of a matched tool process, both sides of the preform are in contact with tool surfaces. Therefore, any local changes in thickness are smoothed out, as the material undergoes transverse extension (UD materials), inter- and intra-ply slip and inter-ply rotation. Comparison of matched tool forming and DDF [66] shows that DDF constrains the material movement much less and allows some thickening of the material as it shears, rather than inducing out-of-plane buckling. The quality of the formed component is also influenced by the tool design, depending on whether the fabric is draped over a male tool, or drawn into a female tool [67]. The shape of the tool controls the magnitude of the compression force during diaphragm forming, and therefore in-plane fibre

tension. The clamping forces and the forming forces are independent for a matched tool process, and are provided by the blank holder and the punch/die respectively. However, both of these functions are provided simultaneously by the membranes in diaphragm forming, which results in reduced process control. For a male tool, the diaphragm/preform initially makes contact with the highest point of the tool and tension is generated, stretching the diaphragms. Compressive stresses occur due to the effect of Poisson's ratio, resulting in severe out-of-plane buckling in the diaphragms. For a female tool, the diaphragm/preform initially makes contact with the large flat region surrounding the perimeter, creating a frictional force, affecting the tension in the preform. This can help to prevent compressive stresses (hence wrinkling) from occurring, but can also cause fabric bridging. The forming forces are unable to overcome the large frictional forces, therefore preventing the fabric from drawing into the tool. A DDF process study by Krebs et al. [67] showed that for a hemisphere geometry, reduced wrinkling was seen when deep drawing into a female mould compared with draping over a male tool. Vacuum-only pressure is commonly used for thermosets, but a positive hydrostatic pressure (0.1 MPa - 1.7 MPa) is commonly used for forming thermoplastics, as the diaphragms tend to be thicker and stiffer in order to prevent wrinkling [68]. Bersee and Beukers [69] conclude that there is no real benefit to hydrostatic pressures above 1 bar, which significantly reduces capital costs and makes the process scalable for larger structures.

The deformation mode and the onset of defects are also dependent on the diaphragm material type. Disposable vacuum bag materials like modified urethane films or polyimide elastomers are often used to preform pre-impregnated materials ready for the autoclave cure cycle. The low thickness of these materials can cause problems with wrinkling [55], and thicker, stiffer diaphragms are therefore commonly used in commercial processes to alleviate shear-induced out-of-plane buckling [70]. The deformation of the upper diaphragm can also be significantly different to the lower diaphragm, depending on the heating arrangement.

Material wastage is difficult to avoid when using a matched tool forming process, as excess material must remain in the blank holder region in order to maintain tension to the end of the forming step. There is an opportunity for producing net-shape preforms using diaphragm forming, as in-plane tension is provided by the frictional forces at the diaphragm/preform interface. Krebs et al. [67] showed the importance of optimising the ply shapes to reduce

waste, but also to avoid redundant areas of fabric which can lead to instabilities, such as wrinkling, buckling and fabric bridging. Hallander et al. [71] showed the influence of the ply stacking sequence on the formability, with different fibre types influencing the local friction and inter-ply shear. The final formed shape is sensitive to the initial fibre architecture and minimising the number of transitions from $\pm 45^\circ$ plies to 0° plies can help to reduce the overall level of wrinkling [72].

2.4 Forming simulation framework

2.4.1 Kinematic models vs. finite element methods

There are two primary approaches for drape simulation: (1) kinematic method and (2) finite element method. Kinematic drape simulation codes [73, 74] use a purely geometrical approach to compute fabric drape patterns. Whilst this method is computationally relatively inexpensive, there is no accounting for realistic mechanical material properties or process conditions. Conversely, Finite Element (FE) simulations enable the physics of the forming problem to be modelled and are becoming an increasingly viable choice as computing resources improve. This approach enables the influence of process parameters, including contacts and friction between components to be studied, but more importantly can be used to indicate the likelihood of defects occurring during forming.

The kinematic approach models the fabric as a pin-jointed net of rigid bars representing fibre sections between cross-over points. The connected fibre sections are then placed sequentially on the geometry of the preform. As shown in Figure 2.16, a deformed pattern is obtained by mapping the network to the target geometry using the kinematic relation [75].

This model is developed under the assumption that the forming mechanism is 100% derived from the rotation of the warp and weft yarns (i.e. trellis shear) [77-79]. Thus, it does not introduce other mechanisms (for instance fibre elongation, yarn undulation and yarn slippage etc.) which makes the result independent of the fibre/fabric type. Also, it only utilises ideal interactions with the tool and between plies, such as zero-frictional effects. The kinematic analysis compares the local shear angles against the defined locking angle to establish whether the 3D geometry is formable or not, but it is unable to explicitly predict the occurrence of all forming defects (such as out of plane wrinkles or laddering) [30].

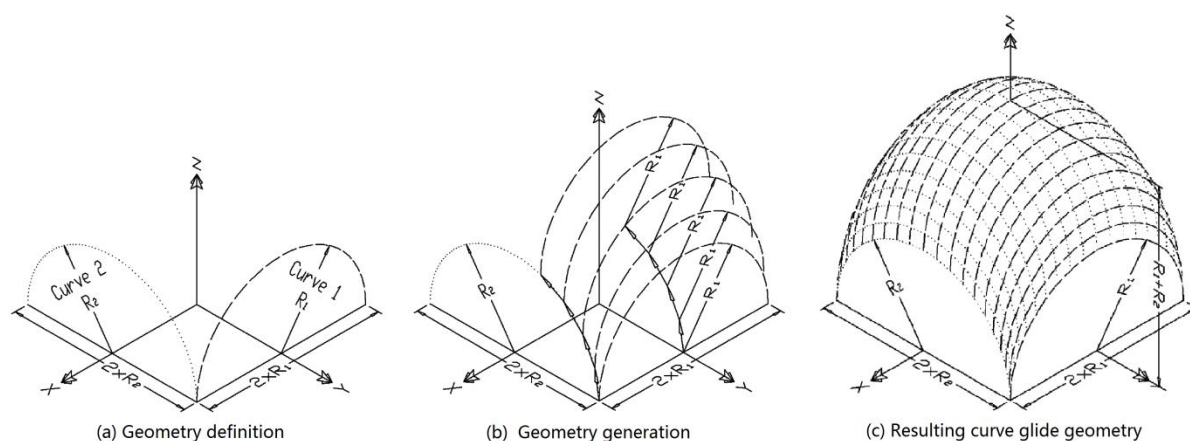


Figure 2.16: Generation of draping pattern using kinematic method. [76]

Many attempts have been made to extend the capability of this modelling algorithm, mainly for complicated geometries [76, 80-82] and different fabric types [83, 84]. However, due to its fundamental assumptions on deformation mode, the kinematic method is still not always a reliable way to simulate fabric forming processes. Consequently, this method is usually employed during the conceptual design stage to obtain some basic understanding of fabric forming, but a more realistic model is required for process optimisation. For this reason, kinematic models have been discounted for the work in this thesis.

Only the FE method is adopted herein due to its precise and comprehensive prediction on mechanical performances. Although a meso-scale FE model is considered to be more realistic to capture deformation details at the bundle level, the computational costs are still impractical for many industrial applications [85-87]. A macro-scale FE model may be a more suitable option [63] for the modelling requirements in this thesis. The material is considered to be a continuum and the constitutive relation is defined for the macroscopic element based on a homogenisation scheme [88]. The material behaviour is highly dependent on the fibre orientation and the fabric may be subject to large deformation during forming process to receive enough formability [89-91]. It is essential to define the constitutive law under a non-orthogonal coordinate framework to deliver more realistic result [92].

As shown in Table 2.2, the finite element method is superior to the kinematic method for providing more realistic and comprehensive prediction of fabric forming behaviour, including modes of deformation and defects. However, there is still no universally recognised FE model to precisely capture fabric forming behaviour [28, 91] for different material types [93].

Table 2.2: Comparison between kinematic and finite element approaches.

Approach	Advantages	Disadvantages
Kinematic method	Easy to setup the model	Only consider in-plane shear mode as forming mechanism
	Efficient to run the simulation	
	Commercial codes directly available	Unable to fully demonstrate material differences
Finite element method	Precise behaviour prediction	Difficult to prepare the FE model (geometry, contact and properties)
	Various result formats and comprehensive analysis	Computationally costly
	High flexibility for application	Require expertise on modelling

The finite element approach can therefore account for considerable nonlinear effects derived from anisotropic nonlinear material behaviour [19, 26, 28, 85, 88-90, 93, 94], large deformations [26, 40, 47], complex contacts and friction [87, 95-98]. Current issues are related to the experimental determination of the effective material input parameters, and to the computational cost for generating a numerical solution. Composite forming is very similar to metal sheet forming, the main difference being that there is a need to know the fibre orientations and fabric density during and after forming, as this information is a measure of the success of the forming process.

2.4.2 Implicit vs. explicit algorithms

The fabric forming process is a quasi-static process. It can be simulated using both implicit and explicit algorithms. An implicit algorithm is an iterative method, while an explicit algorithm is a kind of time-marching method based on numerical integration.

An implicit algorithm does not strictly require a very small time increment, as the size of the increment relies on the required precision and convergence time. An explicit algorithm requires a very small time increment to satisfy the stability requirement. Although a typical time increment in most implicit calculations is larger than the ones used in an explicit analysis, a much larger number of iterations may be required using implicit solver. Consequently, the computational cost of an implicit algorithm may be extremely high compared to an explicit algorithm. Additionally, an implicit algorithm can occupy more computational resources (such as CPU, disk space and memory) during iterations due to the nonlinearity of fabric material

properties as well as the complex contact in preforming. Hence, the maximum capability of an implicit simulation mainly depends on the performance of computer rather than the running time. Explicit algorithms were initially developed for solving high-speed dynamic problems, which may be extremely time-consuming using an implicit algorithm. There are no convergence problems when using an explicit solver and this is particularly relevant for composite forming simulations where complex contacts are used. Providing the time increment is small enough, an explicit algorithm is much more efficient for dealing with quasi-static forming problems.

2.4.3 FE modelling scale

Fabric reinforcements are subject to large deformation in producing complex 3D preforms. Their fibrous architectures imply the existence of mechanical interaction between fibres as well as between yarns. The rotation of yarns leads to the redistribution of material and a local change in stiffness. The fabric has a high resistance to extension along the fibre orientation, but low resistances to compression, shear and bending, etc. These enable large deformations to occur, which may lead to considerable distortion of the fabric architecture. A fabric is intrinsically a multi-scale material [28], therefore choosing an appropriate FE modelling scale is dependent on the application of the model (microscale, mesoscale and macroscale). It is impractical to directly apply the microscale model for process simulation, due to an impractical number of degrees of freedom. The fabric forming process is typically modelled at the meso-scale or macro-scale, with some multi-scale models now being adopted [27, 86, 91, 99-102].

Mesoscale modelling is conducted at the scale of the yarn. For woven fabrics for example, each yarn is modelled as an individual component in the fabric assembly, as shown in Figure 2.17. Similarly for NCFs, stitches are also modelled as individual yarns, as shown in Figure 2.18. The simulation demonstrates the interactive behaviour between the constituents, which provides a high level of detail about the deformation modes and therefore the onset of defects [87].

The difficulty of mesoscale modelling is in establishing complicated geometries, defining appropriate contacts, generating high-quality meshes (see Figure 2.19) as well as applying realistic loads and boundary conditions (see Figure 2.20). Since a typical yarn is only several

millimetres wide and an arbitrary piece of fabric used in preforming may contain an enormous number of yarns, the quantity/scale of elements required may easily surpass the CPU capacity. Modelling the whole component at the mesoscale may result in extremely high computational costs [85], particularly for large-scale geometries. Historically, this method has only been employed for small and simple configurations at the laboratory scale [86, 87], although several attempts have been carried out to simplify the mesoscopic model [25]. The major benefit of using a mesoscale model is that the deformation of the meso-structure clearly highlights the forming mechanism, enabling manufacturing defects to be directly correlated to the mechanical behaviour of the meso-components, rather than relying on a homogenised average result obtained from macroscale model.

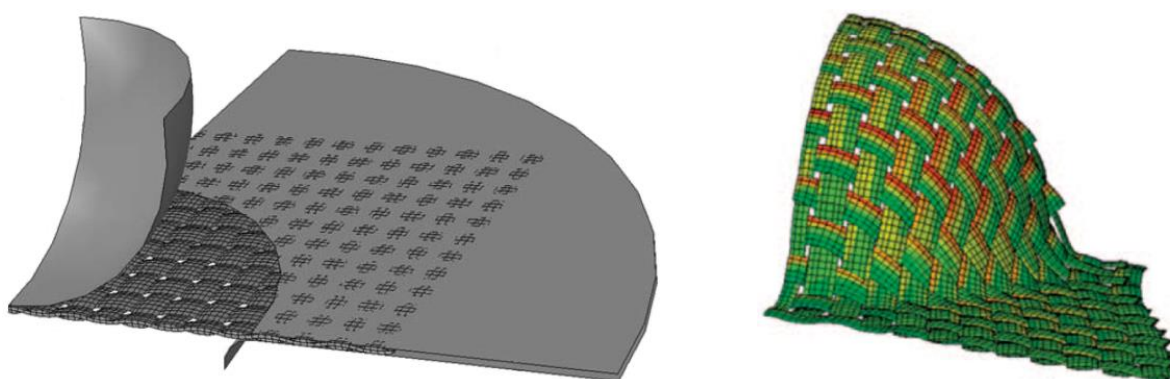


Figure 2.17: Meso-scale model for woven fabric forming. [86]

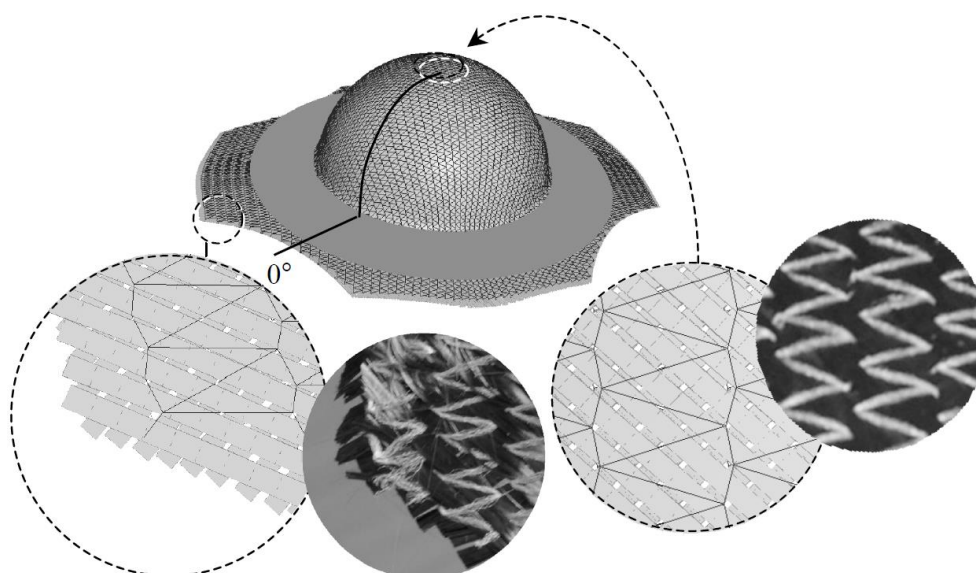
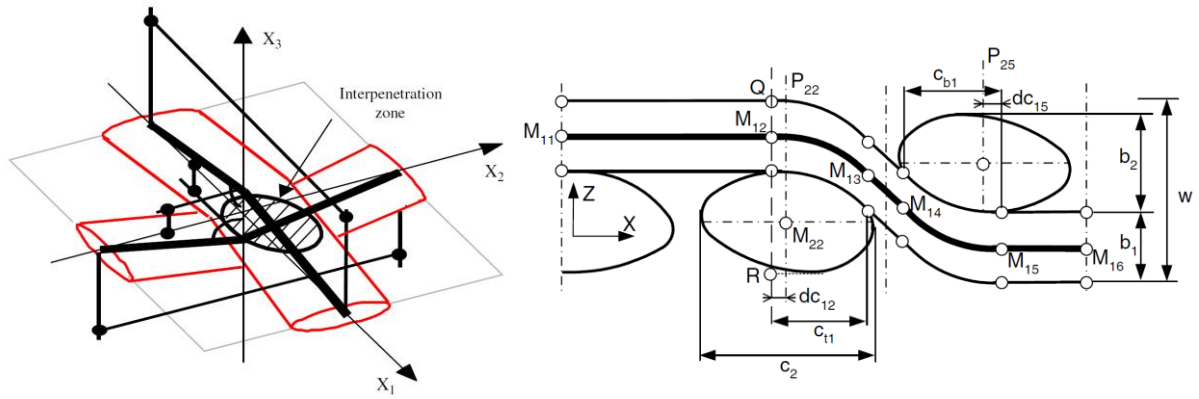
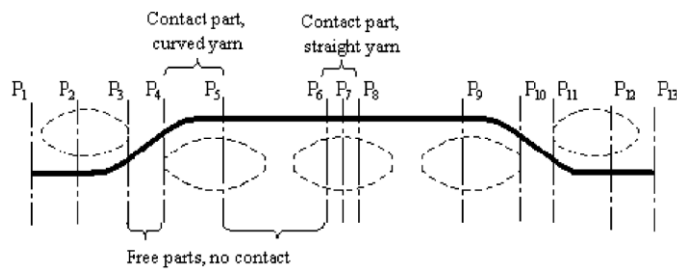


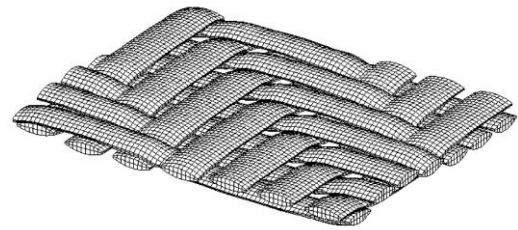
Figure 2.18: Meso-scale model for non-crimp fabric (NCF) forming. [103]



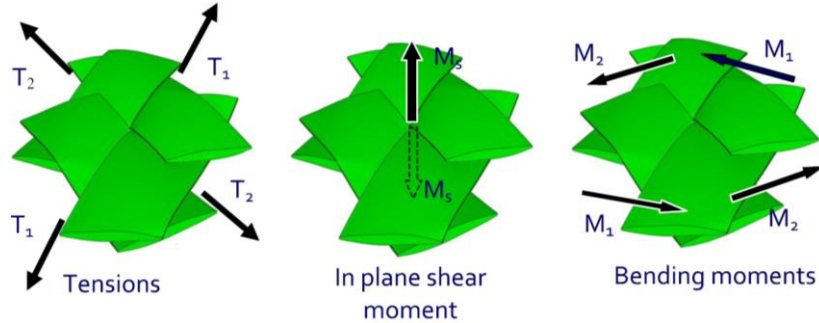
(a) Geometry modelling



(b) Contact modelling



(c) Meshing

Figure 2.19: Meso-scale modelling of fabric material. [25]**Figure 2.20: Load resultants on a unit woven cell. [104]**

Macroscale modelling treats the structured fibrous material as a continuum, as shown in Figure 2.21, which requires some form of homogenisation. Effective properties are obtained from material testing, which are then directly utilised in the macro FE model according to mechanical equivalence. The most difficult decision is how to homogenise the material and how to calculate the effective material properties for large strain analysis. The main advantage of this approach is that other features, such as geometry and contacts, can be addressed relatively simply and conveniently at this scale. Macro-scale modelling is the most commonly employed technique reported in the literature [28]. It provides the most promising way for evaluating and optimising the preforming process based on FE analyses [63].

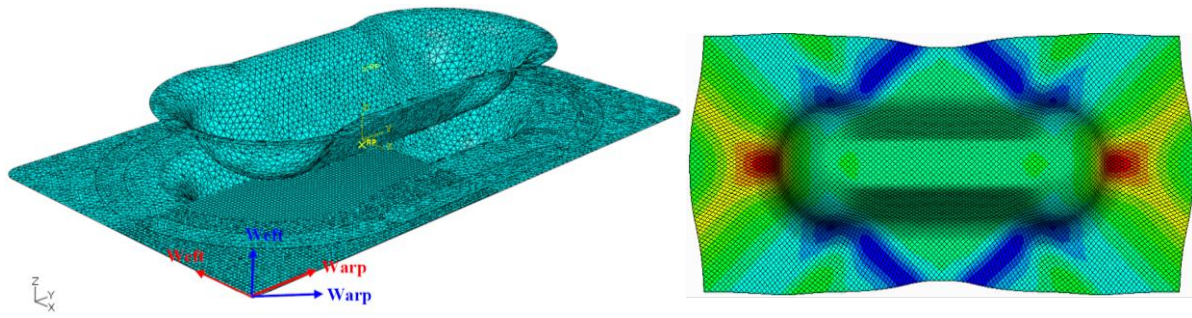


Figure 2.21: Macro-scale model for fabric forming. [40, 47]

The constitutive relation for the macro-scale model is typically defined in an orthogonal coordinate system. With this classical definition, the constitutive tensor possesses some particular and preferential characteristics, such as symmetry and sparsity [88, 105, 106]. However, a regular orthogonal model is unable to capture the mechanical behaviour of the fabric since the primary yarns are likely to rotate, therefore they do not remain mutually perpendicular. The orthogonal relation is based on average rotations of the homogenised continuum, and is therefore unable to precisely follow the deformation of both yarns [48], which may result in a discrepancy when large deformations are anticipated during preforming. A non-orthogonal constitutive model is considered to be more suitable for describing fabric forming behaviour [92] (see Figure 2.22), with the two coordinate axes at the same orientation as the primary yarns following deformation. The primary axes of the fabric do not remain perpendicular to each other throughout the forming process, therefore defining the material properties in a current fibre-coordinate system is more preferential for producing realistic simulations of the fabric forming behaviour [90].

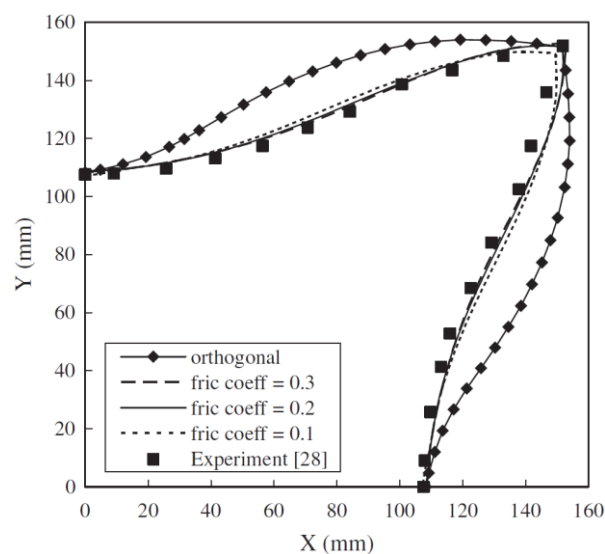


Figure 2.22: Comparison between orthogonal and non-orthogonal constitutive models [92].

The material behaviour can be defined as either hyper-elastic [107-109] or hypo-elastic [40, 47, 48, 110] in the non-orthogonal coordinate system. A hyper-elastic constitutive relation is generally defined in the initial undeformed configuration rather than the current deformed configuration, so that the provided material properties referring to fibre direction cannot be directly used which make it inconvenient for simulating large strain problems in preforming [48]. In consequence, a hypo-elastic relation is more frequently adopted for macroscale models, although there is no clear evidence showing the superiority over the other until now.

A multi-scale modelling technique combines mesoscale and macroscale modelling techniques. It is used to establish a mapping relation between the mesoscopic mechanisms and macroscopic modes, as shown in Figure 2.23. The former is used to characterise material properties, while the latter is responsible for replicating structural behaviour during the forming process.

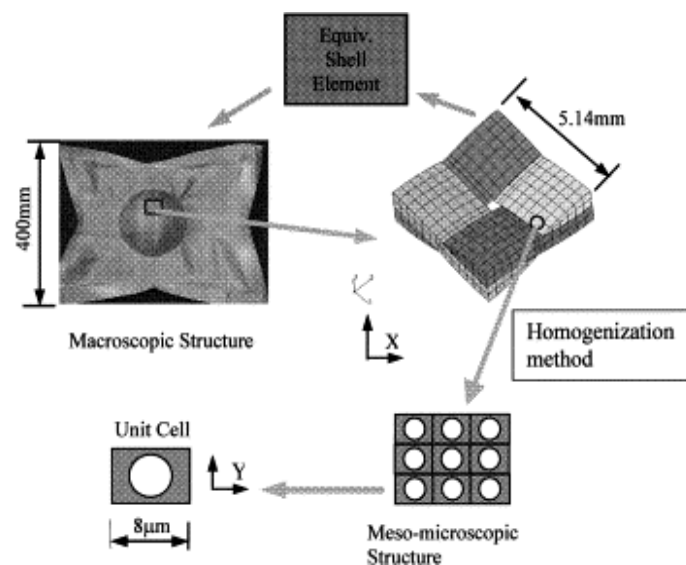


Figure 2.23: Multi-scale modelling for fabric forming. [88]

A mesoscale model is only employed to analyse a representative unit cell of the fabric, rather than the entire material, which can dramatically reduce the requirements on computational resources. As shown in Figure 2.24, effective properties (such as tensile modulus and shear modulus) are obtained from the unit cell analysis, which directly feed into the macro-scale model [99]. The macro-scale model accelerates the run time of the preforming simulation. Macroscopic deformation behaviour is used to inform the formability and demonstrate the occurrence of possible defects, and it can be traced back to the mesoscale unit cell to establish the deformation/defect mechanisms [102].

A semi-discrete model has been developed as a variant of the multi-scale model [27, 28, 91, 101]. Features are considered at the mesoscale (such as yarns, stitches, etc.), which require strain energies to be calculated. These discrete components are treated as part of the finite element, where their strain energy in the interpolated displacement field results in the interior loads applied to the elemental nodes as a continuum. The required input material data is quite straightforward and can be obtained directly from classical tests (i.e. tensile and bias extension tests). This model has been confirmed as an alternative to an experiment [111], but developing an automatic scheme for geometry and contact preparation is necessary to accelerate the modelling process. A semi-discrete model may be a potential option for investigating the influence of stitches, by considering the stitches as additional reinforcements to the homogenised continuous media.

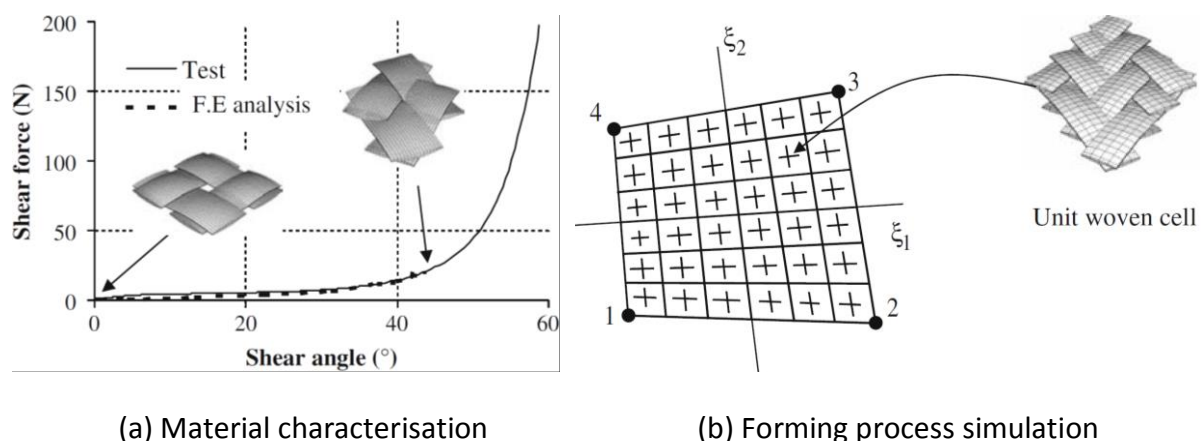


Figure 2.24: Unit cell analysis provides material properties for forming process simulation. [99]

2.5 Fabric forming simulations

2.5.1 NCF forming simulations

Finite Element (FE) simulations are generally well developed for understanding the forming behaviour of woven fabrics, as defining the material as a continuum at the macroscale is straightforward. Fewer studies however, have been presented on the constitutive modelling and numerical forming of NCFs, despite their potential advantages in terms of manufacturing and performance over woven materials. Mesoscopic constitutive models are the most common [23, 33, 112] but are not practical for investigating industrial scale components. Macroscopic NCF models have been presented [93], but in general, are unable to capture the inter-ply fibre sliding when considering the material as a continuum. Semi-discrete

approaches have also been developed [34], where the two fibre layers are modelled separately with shell elements, and 1D beam elements are used to connect them together to account for the influence of the stitch. Fibre slippage is controlled by a Coulomb friction law with a sliding threshold. This approach is computationally expensive as it involves additional degrees of freedom and complex contact constraints. It appears there is currently no universal approach for modelling the deformation of biaxial NCFs. Differences in the mesoscale architecture can significantly influence the forming behaviour and therefore the choice of modelling route. For example, the shear behaviour of a biaxial NCF using a chain stitch with high stitch stiffness may be very similar to that of a woven material and therefore a macroscale continuum approach may be appropriate. Conversely, a mesoscale approach may be required for an NCF using a tricot stitch that exhibits high levels of slippage, in order to capture the high levels of fibre sliding.

The chosen modelling scale will ultimately determine how the contribution of the NCF stitch is accounted for in the model. A macroscale model for woven materials was adapted in [93] to account for the asymmetric behaviour of the NCF, using a non-orthogonal constitutive law. Asymmetric shear curves (different curves for positive and negative shear) were produced using the picture frame test. The apparent shear stiffness was dependent on both the in-plane shear deformation of the fibre yarns and the tensile deformation of the stitch. The compressive stiffness of the stitch was assumed to be negligible. Comparisons with experimental hemisphere formings demonstrate that a macroscale approach can suitably capture the contribution of the stitch for some biaxial NCFs. The contribution of the stitch yarn in a mesoscale model is more difficult to define, as assumptions have to be made regarding the properties of the stitch, in terms of either friction parameters for contact constraints [34] or the mechanical properties of beam element [33, 64]. A bias extension test was used in [112] to characterise the contribution of the stitch, by using an inverse method to calibrate the stitch data empirically. The stiffness of the stitch yarns was calculated in [34] based on the diameter and the stiffness of the polyester thread. The influence of friction and the shear stiffness of the stitch were determined by an inverse law from bias extension testing.

2.5.2 Multi-ply forming simulations

Previous research on reinforcement forming has generally addressed the simulation of components consisting of a single fabric ply [19, 26], or preforms of multiple plies with

identical orientation [113, 114], where the difference in draw-in between plies and inter-ply friction is not as significant as in heterogeneous multi-ply preforms [40, 115]. However, little work has been reported on forming of complex stacking patterns or multi-ply preforms containing localised stitch-bonds.

One approach for simulation of multi-ply forming is to use multi-layered finite elements (FE), where one layer of elements represents multiple fabric layers, for more efficient simulation [115]. However, this method ignores relative sliding between plies, which is one of the main forming modes for multi-ply systems. In order to account for sliding, each ply needs to be modelled independently as a separate element layer. Cheruet et al. [116] modelled forming of a Z-shaped component consisting of 10 pre-impregnated plies and found that predicted relative inter-ply sliding agreed well with experimental data. Harrison et al. [117] conducted forming simulations for two cross plies ($0^\circ/90^\circ$ UD) of thermoplastic prepreg, assuming a biaxial constitutive relationship. The viscous nature of the matrix material ensured that the main in-plane deformation mode was trellising (shear), similar to a woven material. However, when the fibres are dry, the deformation mechanism changes, and intra-ply sliding of loosely fixated yarns becomes more important, particularly for multi-ply forming of non-crimp fabrics (NCF) [34]. Experimental results show that NCFs experience high levels of slip within each layer of the bi-directional material, as the stitches provide less restraint than interweaving of warp- and weft-yarns. This phenomenon was captured in simulations by using bar elements to represent the stitch between UD plies modelled as shell elements. Good agreement was shown between numerical simulations and experimental results for forming of a hemisphere, but sliding was limited to the fibre direction, which may be an oversimplification for more complex geometries.

2.5.3 Simulating the effect of inter-ply stitches

Investigations into the influence of stitches have been generally limited to studying intra-ply stitches in NCFs [34] or single woven plies [113], to understand how they can be used to control local yarn angles. Molnar et al. [114] investigated the influence of inter-ply stitching experimentally. Local stitch-bonds were found to affect shear deformation in the formed fabric. It was concluded that it is possible to transfer shear forces into un-sheared regions of the ply during forming. Through-thickness stitching in multi-ply preforms has been simulated in explicit finite element analyses using spot weld constraints [113, 118]. Whilst only multi-

ply stacks with identical ply orientations were studied, for certain cases, redistribution of strains within the fabric through use of stitches was proven feasible to avoid wrinkling. Duhovic et al. [113] studied the force-displacement relationship for stitches in detail. It was found that stitches did not restrict the fabric shear behaviour when a strain offset was defined to account for slack in the thread during tensile loading, and was set to a value obtained from experiments. Bel et al. [119] investigated the influence of local stitch-bonds on preforming of commercial components, using beam spring elements to model the stitches in explicit FE studies.

Margossian et al. [64] found that the contribution of stitches to the in-plane mechanical properties of a ply is almost negligible compared to that of the yarns in the fabric. Assembly stitches behave as additional local inter-ply constraints, providing connecting forces to decrease the relative local inter-ply displacement. This effect becomes much more significant for adjacent plies with different initial fibre orientations, since the relative inter-ply displacement is greater under these circumstances. As their in-plane influence can be ignored, each through-thickness stitch can be considered in isolation (in-plane stitch path can be overlooked).

Shear deformation in the fabric plies caused by the introduction of stitch bonds may negatively affect the properties of the finished component. A mathematical algorithm is required to determine optimised stitching patterns, to minimise local fabric shear. While there is no published work on the optimisation of inter-ply stitching, several suitable approaches have been identified from other optimisation problems. For optimisation based on large numbers of non-linear FE analyses, the enumeration approach is unsuitable, as the total computation time is unfeasibly long. Also, gradient/sensitivity-based search methods are inapplicable due to the lack of explicit relationships between the stitching patterns and the shear angle distribution. On the other hand, heuristic algorithms are an effective way to solve problems with large numbers of variables, and consequently genetic algorithms (GAs) have been chosen for this work.

2.5.4 Diaphragm forming simulations

Matched-tool forming is well-understood, with a range of macroscale [93] and mesoscale [23, 112] constitutive relationships available for describing the deformation behaviour of woven

and non-crimp fabrics. Material models have been developed for diaphragm forming [63, 64, 120, 121], but capturing the behaviour of the diaphragms is complex. Leutz et al [63] simulated the SDF process, and Margossian et al [64] simulated the DDF process, but neither reported details of the material models used for the membranes. The diaphragm was modelled using a plastic material model by Sorrentino and Bellini [121], based on an isotropic nonlinear viscoelastic shell element of the Maxwell type. A rubber diaphragm was modelled using a hyperelastic Mooney-Rivlin material model by Sjölander [120], which was also calibrated using uniaxial tensile tests and assumed to be incompressible. Similar to sheet metals, the biaxial deformation of the diaphragms can be characterised by the bulge forming test or the bubble forming test [58].

2.5.5 Forming optimisation

To successfully drape a reinforcement without encountering unwanted wrinkles and defects, the main challenge is identifying optimum forming conditions. Among the processing parameters affecting fabric press forming, the distribution of the blank holder force (BHF) and the blank shape are two essential properties in matched tool forming that should be optimised to improve the quality of the formed shape [93, 122]. In diaphragm forming, the influence of forming temperature has been reported [59, 123] and forming at higher temperatures generally yields better tool conformity by reducing the diaphragm stiffness. To date, most FE forming studies have focused on capturing the deformation of fabrics accurately through implementation of suitable constitutive material models [90, 94], rather than focusing on optimising the forming process.

Procedures for optimisation of the forming process can be classified as direct or indirect. Indirect methods refer to trial and error approaches, which require experience to interpret the results and can be time consuming. Nonetheless, they are likely to be used for optimising composite forming processes, since the complex relationship between wrinkling strain and clamping force does not need to be formulated. Indirect methods have previously been used to optimise fabric blank size [122] and BHF distribution [93], in order to minimise wrinkle formation. The probability for wrinkles to occur was shown to increase as the blank size is reduced relative to the size of the punch, since the tension in the blank is released during the latter stage of the forming process [122]. A uniform BHF distribution produced the least wrinkles in forming a hemisphere. However, it was concluded that a segmented blank holder

is required to further reduce the level of wrinkling, to vary the local pressure distribution as a function of intra-ply shear and compressive forces [93].

Direct optimisation methods rely on mathematical relationships between the processing parameters (BHF, blank shape, fabric pre-shear) and the objective function (describing shear angle, wrinkling etc.) to be formulated, and have been used extensively for optimising metal forming problems. They commonly employ Genetic Algorithms (GA) [124-127], which mimic natural selection processes to enable the strongest permutation of design variables to evolve, and inferior ones to fade out. GAs are not widely used for optimising composite forming problems, because they are computationally expensive. A GA was coupled with a kinematic drape model by Skordos et al. [74], where the drape start point, drape direction and the pre-shear angle of the fabric were defined as design parameters. Employing the GA reduced the CPU time to 30 % of that required for an exhaustive search [74]. Alternatively, a simplified FE model was used in conjunction with a GA to optimise the BHF around the perimeter of the blank, with the objective of minimising wrinkling [128]. Results indicated that optimising the BHF successfully eliminated concentrated buckling of tows around the base of the hemisphere, without affecting the in-plane shear angle distribution.

2.5.6 Validating forming simulations

Composite forming models are often validated by comparing local shear angles and ply perimeters from the simulation with experimentally formed shapes. A number of real-time full-field vision systems have been developed to automate the process control of fibre preforms [129]. Imaging is performed during manufacturing which can be used to establish a quality assurance system, thereby closing the quality control loop. The ITA drape test is an instrumented hemisphere forming rig which combines the measurement of the forming force with an optical analysis of small-scale defects such as gaps and loops [130]. Errors are typically identified subjectively, not in an objective and holistic way. Other optical methods are available to compare 3D formed preforms to the target shape [44], which can be used to identify out-of-plane defects such as wrinkling or fibre bridging. EuroPAS [64], Falcon and Apodius are examples of automated systems for measuring filament angles and gaps in formed fabric preforms. The data collected can be mapped back onto the 3D formed shape to help identify the source of defects.

2.6 Chapter summary

The forming behaviour of biaxial NCFs is quite different to woven materials due to the influence of the stitch yarn. Straining of the in-plane segments of the intra-ply stitches and rotation of the primary yarns contributes to the shear behaviour of the NCF at the macroscale. The orientation of the in-plane segments of the stitches relative to the primary yarn direction can lead to asymmetric shear behaviour, which is significant and needs to be accounted for during process simulation.

In-plane fibre buckling and out-of-plane fibre wrinkling are the most common defect mechanisms for fabrics, but fibre pull-out, stitch thread failure and inter-layer sliding are additional mechanisms observed for NCFs. The shear angle can be employed as a measure of wrinkle initiation, induced by the compaction of intersecting yarns in the transverse direction. There is a threshold shear angle value, namely the 'locking angle', corresponding to the onset of wrinkling.

Diaphragm forming is of interest in this work because of the lower capital costs compared to matched tool forming and shorter cycle times compared to hand-layup. Historically, diaphragm forming has been used for consolidation of hand-layup parts, but this study will investigate the feasibility of using this process for forming complex 3D structures. It is important to note that the defect mechanisms are different to matched tool forming, which need to be captured in the forming simulation. Comparisons of matched tool forming and double diaphragm forming shows that double diaphragm forming constrains the material movement much less and allows some thickening of the material as it shears, rather than inducing out of plane buckling. The clamping forces and the forming forces are separate for a matched tool process, which are provided by the blank holder and the punch/die respectively. However, both of these functions are provided simultaneously by the diaphragm, which can result in additional defects.

A macroscale finite element model will be used to simulate the forming process, as the computational costs of a mesoscale bundle level model are still impractical for industrial-scale applications. This approach enables the influence of process parameters to be studied, including contacts and friction between components, but more importantly can be used to indicate the likelihood of defects occurring during forming. Constitutive models for NCF

materials are not as widely reported as woven materials, so a new model will be developed for a pillar-stitched biaxial NCF to capture the asymmetrical shear behaviour. The finite element model will be coupled with a genetic algorithm to identify optimum forming conditions, in order to drive future material and process developments.

Chapter 3 Fabric material characterisation

3.1 Introduction

This Chapter presents and validates a constitutive model for describing the deformation behaviour of a pillar-stitched NCF in preforming, accounting for the rotation of the carbon fibre yarns and the direction-dependent contribution of the intra-ply stitches. Its implementation in explicit Finite Element (FE) simulations enables the prediction of meso-scale defect formation during preforming based on macro-scale observations. The model is first validated using data from the literature for a plain weave commingled glass/PP material to verify that the constitutive relation is correct for bi-axial fabrics.

Preforming experiments using a biaxial carbon fibre NCF indicate that the local distribution of defects is significantly different on both sides of each bi-axial ply, with two different defect mechanisms observed. Correlation with simulation results indicates that one defect type is caused by excessive shear, inducing out-of-plane wrinkling in regions of positive shear (macro-scale wrinkling). The other defect type is caused by fibre compression, inducing in-plane wrinkling in regions of negative shear (meso-scale wrinkling). Local distributions of shear angle and wrinkling strain have been used to determine the wrinkling mode and to confirm the corresponding defect mechanism.

3.2 Non-orthogonal constitutive framework

3.2.1 Homogenisation

All fabrics are modelled at the macro-scale as continuums using an explicit FE method. Meso-/micro-scale details are implicitly embodied in the continuous elements by homogenisation [88]. Unlike consolidated composite products, the fabric yarns may be subjected to large deformations to conform to the target surface, particularly in regions with large and complex curvatures, resulting in significant fibre re-orientation. The equivalent properties at each material point following homogenisation are highly dependent on the local fibre orientations, which should be defined at each time increment. As shown in Figure 3.1 for a bi-axial fabric material, the local fibre orientations are coupled with the element deformation and the two

primary fibre axes are not always perpendicular to each. A non-orthogonal coordinate system is therefore more sensible than the classic orthogonal system to construct the constitutive framework [92].

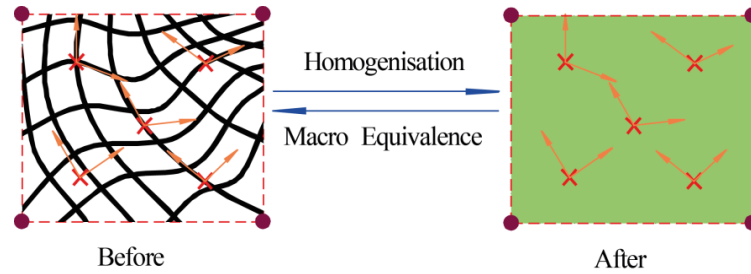


Figure 3.1: Homogenisation for fabric material in preforming.

For an arbitrary material integration point (shown in Figure 3.2), the constitutive relation is defined using a local fibre coordinate system, which always follows the fibre orientation at the local material/integration point throughout the deformation. The deformation behaviour at other points is obtained by numerical interpolation using elemental shape functions.

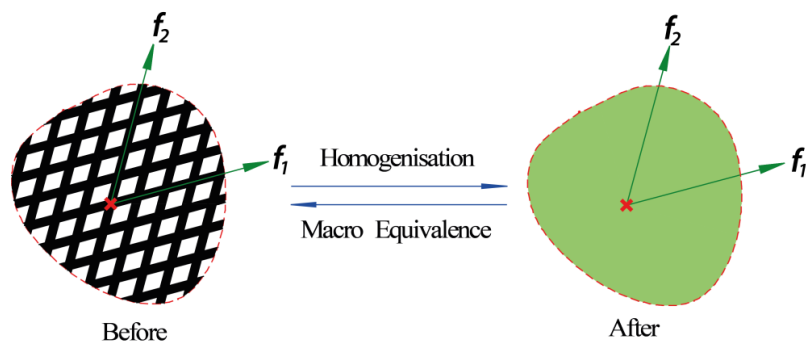


Figure 3.2: Material point of fabric.

3.2.2 Coordinate definition

A non-orthogonal coordinate system is defined locally at an arbitrary point as shown in Figure 3.3, where $\underline{f}_1, \underline{f}_2$ are two base vectors along local fibre orientations at this point defining the local material plane. The normal vector of this plane, \underline{f}_3 , is introduced to represent the out-of-plane axis of the 3D non-orthogonal fibre coordinate system according to the right hand rule. Since vectors $\underline{f}_1, \underline{f}_2$ are tied to the fibre orientations, the proposed coordinate system is changing with the deformation of the homogenised finite element. In particular, shear deformation is a primary cause of the fibre non-orthogonality rather than rigid rotation of the element.

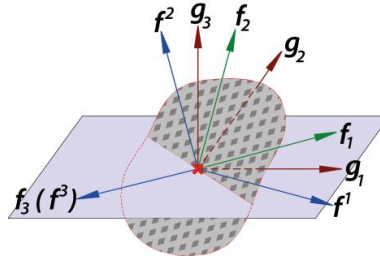


Figure 3.3: Coordinate definition at material Point.

According to polar decomposition, the deformation gradient tensor $\underline{\underline{F}}$ yields to

$$\underline{\underline{F}} = \underline{\underline{R}} \cdot \underline{\underline{U}} \quad (3.1)$$

where $\underline{\underline{R}}$ is the polar rotation tensor and $\underline{\underline{U}}$ is the right stretch tensor.

Since $\underline{\underline{U}}$ is positive definite, the polar rotation tensor $\underline{\underline{R}}$ can be expressed as

$$\underline{\underline{R}} = \underline{\underline{F}} \cdot \underline{\underline{U}}^{-1} \quad (3.2)$$

The material co-rotational coordinate system (MCCS) is usually employed in FE analyses for large deformation issues, where its three base axes are defined by \underline{g}_1 , \underline{g}_2 and \underline{g}_3 , i.e.

$$\begin{cases} \underline{g}_1 = \underline{\underline{R}} \cdot {}^0\underline{g}_1 \\ \underline{g}_2 = \underline{\underline{R}} \cdot {}^0\underline{g}_2 \\ \underline{g}_3 = \underline{\underline{R}} \cdot {}^0\underline{g}_3 \end{cases} \quad (3.3)$$

where, ${}^0\underline{g}_1$, ${}^0\underline{g}_2$, ${}^0\underline{g}_3$ are unit base vectors (UBVs) of initial MCCS and \underline{g}_1 , \underline{g}_2 , \underline{g}_3 are UBVs of current MCCS. For a $0^\circ/90^\circ$ fabric ply, ${}^0\underline{g}_1 = \{1,0,0\}^T$, ${}^0\underline{g}_2 = \{0,1,0\}^T$, ${}^0\underline{g}_3 = \{0,0,1\}^T$. This corotational coordinate system is an orthogonal system, i.e.

$${}^0\underline{g}_1 \perp {}^0\underline{g}_2 \perp {}^0\underline{g}_3 \text{ or } {}^0\underline{g}_1 \cdot {}^0\underline{g}_2 = {}^0\underline{g}_2 \cdot {}^0\underline{g}_3 = {}^0\underline{g}_3 \cdot {}^0\underline{g}_1 = 0 \quad (3.4)$$

And

$$\underline{g}_1 \perp \underline{g}_2 \perp \underline{g}_3 \text{ or } \underline{g}_1 \cdot \underline{g}_2 = \underline{g}_2 \cdot \underline{g}_3 = \underline{g}_3 \cdot \underline{g}_1 = 0 \quad (3.5)$$

Since the homogenised material properties are highly dependent on the fibre orientations, it is more appropriate to define the constitutive relation at the bi-axial fibre coordinate system (BFCS) which is constructed by three base vectors \underline{f}_1 , \underline{f}_2 and \underline{f}_3 . It is a non-orthogonal coordinate system, unlike MCCS.

The current fibre orientations (\underline{f}_1 and \underline{f}_2) are traced by

$$\underline{f}_1 = \frac{\underline{F} \cdot {}^0\underline{f}_1}{\|\underline{F} \cdot {}^0\underline{f}_1\|} \quad (3.6)$$

$$\underline{f}_2 = \frac{\underline{F} \cdot {}^0\underline{f}_2}{\|\underline{F} \cdot {}^0\underline{f}_2\|} \quad (3.7)$$

where, ${}^0\underline{f}_1$ and ${}^0\underline{f}_2$ are the initial fibre orientation vectors. Vectors ${}^0\underline{f}_1$, ${}^0\underline{f}_2$, \underline{f}_1 and \underline{f}_2 are first order covariant tensors. Then, the corresponding contravariant tensors are

$$\underline{f}^1 = \frac{\underline{f}_1 - (\underline{f}_1 \cdot \underline{f}_2) \underline{f}_2}{\|\underline{f}_1 - (\underline{f}_1 \cdot \underline{f}_2) \underline{f}_2\|} = \frac{\underline{F} \cdot {}^0\underline{f}_1 - (\underline{F} \cdot {}^0\underline{f}_1 \cdot \underline{f}_2) \underline{f}_2}{\|\underline{F} \cdot {}^0\underline{f}_1 - (\underline{F} \cdot {}^0\underline{f}_1 \cdot \underline{f}_2) \underline{f}_2\|} \quad (3.8)$$

$$\underline{f}^2 = \frac{\underline{f}_2 - (\underline{f}_2 \cdot \underline{f}_1) \underline{f}_1}{\|\underline{f}_2 - (\underline{f}_2 \cdot \underline{f}_1) \underline{f}_1\|} = \frac{\underline{F} \cdot {}^0\underline{f}_2 - (\underline{F} \cdot {}^0\underline{f}_2 \cdot \underline{f}_1) \underline{f}_1}{\|\underline{F} \cdot {}^0\underline{f}_2 - (\underline{F} \cdot {}^0\underline{f}_2 \cdot \underline{f}_1) \underline{f}_1\|} \quad (3.9)$$

Then, normal vectors of fabric surface at the corresponding material point, \underline{f}_3 and \underline{f}^3 , can be determined as

$$\underline{f}_3 = \underline{f}^3 = \frac{\underline{f}_1 \times \underline{f}_2}{\|\underline{f}_1 \times \underline{f}_2\|} = \frac{\underline{f}^1 \times \underline{f}^2}{\|\underline{f}^1 \times \underline{f}^2\|} = \frac{\underline{f}_1 \times \underline{f}_2}{\|\underline{f}_1 \times \underline{f}_2\|} = \frac{\underline{f}^1 \times \underline{f}^2}{\|\underline{f}^1 \times \underline{f}^2\|} \quad (3.10)$$

where

$$\underline{f}_1 \perp \underline{f}_2 \perp \underline{f}_3 \quad \text{or} \quad \underline{f}_1 \cdot \underline{f}_2 = \underline{f}_2 \cdot \underline{f}_3 = \underline{f}_3 \cdot \underline{f}_1 = 0 \quad (3.11)$$

and

$$\underline{f}^1 \perp \underline{f}^2 \perp \underline{f}^3 \quad \text{or} \quad \underline{f}^1 \cdot \underline{f}^2 = \underline{f}^2 \cdot \underline{f}^3 = \underline{f}^3 \cdot \underline{f}^1 = 0 \quad (3.12)$$

Thus, \underline{f}_1 , \underline{f}_2 and \underline{f}_3 define an orthogonal coordinate system with respect to the warp yarn, called the uniaxial fibre coordinate system-I (UFCS-I). Similarly, \underline{f}^1 , \underline{f}^2 and \underline{f}^3 define another orthogonal coordinate system with respect to the weft yarn (called UFCS-II). Consequently, the non-orthogonal constitutive relation defined in BFCS is decomposed into two parts, defined in UFCS-I and UFCS-II. The contribution of each yarn to the fabric properties can be assigned in its own orthogonal coordinate system individually and then transferred to a global coordinate system (either MCCS or BFCS) to synthesise the overall property matrix of the fabric reinforcement.

3.2.3 Coordinate transformation

In finite element analysis, most macro-scale quantities (such as stresses and strains, etc.) are usually supplied and stored in the co-rotational coordinate system, called MCCS for short (i.e.

Green-Naghdi system used in Abaqus). A coordinate transformation scheme is compulsory to associate the non-orthogonal and orthogonal constitutive relations.

The transformation matrices between MCCI and UFCS-I $\mathbf{Q}_{I \rightarrow M}$ and $\mathbf{Q}_{M \rightarrow I}$ yield

$$\mathbf{Q}_{I \rightarrow M} = \begin{bmatrix} \underline{g}_1 \cdot \underline{f}_1 & \underline{g}_1 \cdot \underline{f}_2 & \underline{g}_1 \cdot \underline{f}_3 \\ \underline{g}_2 \cdot \underline{f}_1 & \underline{g}_2 \cdot \underline{f}_2 & \underline{g}_2 \cdot \underline{f}_3 \\ \underline{g}_3 \cdot \underline{f}_1 & \underline{g}_3 \cdot \underline{f}_2 & \underline{g}_3 \cdot \underline{f}_3 \end{bmatrix} = \mathbf{Q}_{M \rightarrow I}^T \quad (3.13)$$

where, the subscript $I \rightarrow M$ denotes transform coordinate from UFCS-I to MCCI, the subscript $M \rightarrow I$ denotes transform coordinate from MCCI to UFCS-I, the superscript T denotes transposition. Both $\mathbf{Q}_{I \rightarrow M}$ and $\mathbf{Q}_{M \rightarrow I}$ are orthogonal matrices.

Similarly, the transformation matrices between MCCI and UFCS-II $\mathbf{Q}_{II \rightarrow M}$ and $\mathbf{Q}_{M \rightarrow II}$ yield to

$$\mathbf{Q}_{II \rightarrow M} = \begin{bmatrix} \underline{g}_1 \cdot \underline{f}^1 & \underline{g}_1 \cdot \underline{f}^2 & \underline{g}_1 \cdot \underline{f}^3 \\ \underline{g}_2 \cdot \underline{f}^1 & \underline{g}_2 \cdot \underline{f}^2 & \underline{g}_2 \cdot \underline{f}^3 \\ \underline{g}_3 \cdot \underline{f}^1 & \underline{g}_3 \cdot \underline{f}^2 & \underline{g}_3 \cdot \underline{f}^3 \end{bmatrix} = \mathbf{Q}_{M \rightarrow II}^T \quad (3.14)$$

where, the subscript $II \rightarrow M$ denotes transform coordinate from UFCS-II to MCCI, the subscript $M \rightarrow II$ denotes transform coordinate from MCCI to UFCS-II, the superscript T denotes transposition. Both $\mathbf{Q}_{II \rightarrow M}$ and $\mathbf{Q}_{M \rightarrow II}$ are orthogonal matrices.

Since MCCI, UFCS-I and UFCS-II are orthogonal coordinate systems, $\mathbf{Q}_{I \rightarrow M}$, $\mathbf{Q}_{M \rightarrow I}$, $\mathbf{Q}_{II \rightarrow M}$ and $\mathbf{Q}_{M \rightarrow II}$ possess orthogonality, i.e.

$$\mathbf{Q}_{M \rightarrow I}^{-1} = \mathbf{Q}_{M \rightarrow I}^T = \mathbf{Q}_{I \rightarrow M} \quad (3.15)$$

$$\mathbf{Q}_{I \rightarrow M}^{-1} = \mathbf{Q}_{I \rightarrow M}^T = \mathbf{Q}_{M \rightarrow I} \quad (3.16)$$

$$\mathbf{Q}_{M \rightarrow II}^{-1} = \mathbf{Q}_{M \rightarrow II}^T = \mathbf{Q}_{II \rightarrow M} \quad (3.17)$$

$$\mathbf{Q}_{II \rightarrow M}^{-1} = \mathbf{Q}_{II \rightarrow M}^T = \mathbf{Q}_{M \rightarrow II} \quad (3.18)$$

In Abaqus/Explicit, the strain tensor and strain increment tensor are supplied in MCCI at each time increment, which can be converted into fibre coordinate systems as

$$d\underline{\underline{\epsilon}}^I = \mathbf{Q}_{M \rightarrow I} \cdot d\underline{\underline{\epsilon}}^M \cdot \mathbf{Q}_{M \rightarrow I}^T \quad (3.19)$$

$$d\underline{\underline{\epsilon}}^{II} = \mathbf{Q}_{M \rightarrow II} \cdot d\underline{\underline{\epsilon}}^M \cdot \mathbf{Q}_{M \rightarrow II}^T \quad (3.20)$$

Individual yarns are equivalently considered as transversely isotropic at each point where the mechanical properties are equal in all directions of local cross-sectional plane. Hence, the relation between the increments of stress and strain can be obtained as

$$d\underline{\underline{\sigma}}^I = \underline{\underline{C}}^I : d\underline{\underline{\varepsilon}}^I \quad (3.21)$$

$$d\underline{\underline{\sigma}}^{II} = \underline{\underline{C}}^{II} : d\underline{\underline{\varepsilon}}^{II} \quad (3.22)$$

where $\underline{\underline{C}}^I$ and $\underline{\underline{C}}^{II}$ are respectively stiffness tensors (4th order) of warp and weft yarns. In each time increment, the material is assumed to behave linearly so that the principle of superposition can be applied. In order to superimpose both contributions from warp and weft yarns to stress increment, they are transformed into MCCS by

$$d\underline{\underline{\sigma}}^{MI} = \underline{\underline{Q}}_{I \rightarrow M} \cdot d\underline{\underline{\sigma}}^I \cdot \underline{\underline{Q}}_{I \rightarrow M}^T \quad (3.23)$$

$$d\underline{\underline{\sigma}}^{MII} = \underline{\underline{Q}}_{II \rightarrow M} \cdot d\underline{\underline{\sigma}}^{II} \cdot \underline{\underline{Q}}_{II \rightarrow M}^T \quad (3.24)$$

Thus, the resultant stress increment $d\underline{\underline{\sigma}}^{MR}$ defined in MCCS can be obtained by

$$d\underline{\underline{\sigma}}^{MR} = d\underline{\underline{\sigma}}^{MI} + d\underline{\underline{\sigma}}^{MII} \quad (3.25)$$

Hence, the stress tensor after each increment (i.e. $\underline{\underline{\sigma}}^{new}$) is calculated by adding the stress increment tensor (i.e. $d\underline{\underline{\sigma}}^{MR}$) to the stress tensor at the beginning of this increment $\underline{\underline{\sigma}}^{old}$ as

$$\underline{\underline{\sigma}}^{new} = \underline{\underline{\sigma}}^{old} + d\underline{\underline{\sigma}}^{MR} \quad (3.26)$$

Similarly, all the tensors can be transformed into any desired coordinate systems. In consequence, the non-orthogonal constitutive relation can be defined and converted to update stresses.

3.2.4 Implementation of material model

The material model is implemented in a user-defined subroutine in Abaqus/Explicit based on the non-orthogonal fibre coordinate system, where the axes coincide with the current orientations of yarns at any material point. The non-orthogonal constitutive relation captures anisotropic behaviour of biaxial composite materials under large shear deformation more accurately than an orthogonal model [88, 89]. A VFABRIC subroutine has been developed to define the mechanical constitutive relations of the fabrics under investigation. The VFABRIC routine is valid for materials that exhibit two structural directions, which may not remain orthogonal following deformation.

The non-orthogonal material model is summarised in Figure 3.4. The in-plane engineering strains at the beginning of each time increment in the explicit time integration scheme ($\varepsilon_{f_1}^{old}$,

$\varepsilon_{f_2}^{old}, \gamma_{12}^{old}$ i.e. $[\varepsilon]_{f_1 f_2}^{old}$) and the corresponding strain increments ($d\varepsilon_{f_1}, d\varepsilon_{f_2}, d\gamma_{12}$ i.e. $[d\varepsilon]_{f_1 f_2}$) are calculated internally. The raw material data are transformed to the current non-orthogonal fibre coordinate system. For each fibre direction in the non-orthogonal system, material properties ($[C]_{f_1}^{ort}, [C]_{f_2}^{ort}$) are defined in an orthogonal system, where one base vector is parallel to the fibre direction. For the fabric forming process, the shear deformation can be large, and the two yarn orientations may no longer be perpendicular to each other during forming. Material properties are transformed into the non-orthogonal fibre coordinate system ($[C]_{f_1 f_2}^{non-ort}$) using the current coordinate transformation matrix, $[Q]$. Finally, the initial stress tensor ($[\sigma]_{f_1 f_2}^{old}$) can be updated to be $[\sigma]_{f_1 f_2}^{new}$ by superimposing it with the stress increment tensor ($[d\sigma]_{f_1 f_2}$), which is calculated from the current constitutive matrix in the non-orthogonal fibre coordinate system. This is subsequently returned to Abaqus/Explicit for further processing. Using the VFABRIC subroutine, the coordinate systems have been defined automatically by Abaqus/Explicit as well as the coordinate transformation, which is more convenient than using VUMAT subroutine. However, the stress tensor in non-orthogonal fibre coordinate system has to be updated by means of superimposing the contributions from both yarns.

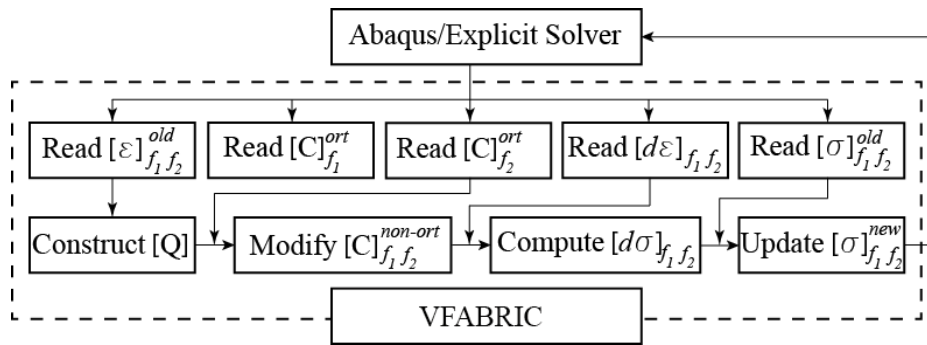


Figure 3.4: Flow chart of user-defined VFABRIC material model.

Although material properties along the fibre directions (such as E_{11}) can be applied directly in VFABRIC, other properties (such as E_{12}) need to be transformed into the non-orthogonal fibre coordinate system (i.e. the system defined by the warp-fibre vector \underline{f}_1 , the weft-fibre vector \underline{f}_2 and the out-of-plane vector \underline{f}_3) using the current coordinate transformation matrix. Only very minor modifications are required in the VFABRIC sub-routine to establish a non-orthogonal constitutive matrix compared with the more generalised VUMAT approach in

Abaqus/Explicit. Implementing a VFABRIC routine therefore reduces the number of tensor operations and results in a more computationally efficient model.

3.3 Woven fabric modelling and validation

Numerical tests have been performed to verify that the constitutive relation used in the current VFABRIC subroutine is correct for bi-axial fabrics, using experimental and numerical data from the International Forming Benchmark study [131] for a double dome geometry as shown in Figure 2.21. The choice of material parameters is consistent with published data [36, 40, 47, 132] for a balanced plain weave glass/polypropylene commingled fabric. The value of Young's modulus was taken to be constant (35.4 GPa) in each fibre direction, ignoring any initial non-linearity in the stress-strain curve due to fibre crimp. Including the influence of fibre crimp in the material model was found to have an insignificant effect on the forming behaviour of a woven glass fabric in hemisphere forming simulations by Boisse et al [26]. The shear modulus G_{12} was described by the polynomial

$$G_{12} = (6.7135|\gamma_{12}|^4 - 9.8228|\gamma_{12}|^3 + 6.3822|\gamma_{12}|^2 - 1.5928|\gamma_{12}| + 0.1948) \text{ MPa} \quad (3.27)$$

where γ_{12} is the in-plane shear angle in radians, defined in the range of $\left(-\frac{\pi}{2}, \frac{\pi}{2}\right)$.

At first, the validation has been implemented by elementary tests (such as uniaxial tension and simple shear), indicating a consistent element behaviour as expectations. Subsequently, this constitutive relation was employed to replicate the benchmark forming for the double dome geometry. Each ply was discretised into 5076 square membrane elements (Abaqus/Explicit element type M3D4R). All parts of the tooling were considered to be rigid bodies. A penalty contact algorithm was used to define the behaviour at all interfaces. An isotropic Coulomb friction model was adopted for both the tooling-material and material-material contacts with a constant coefficient of 0.2 [40, 47]. Displacement boundary conditions were applied to the punch and a force of 100 N was applied to the blank holder to control blank slippage. Two material configurations were studied during the validation stage; forming of a single $0^\circ/90^\circ$ ply and a single $\pm 45^\circ$ ply.

The run time of the model is extremely important for successful implementation of the process optimisation, as large numbers of iterations need to be run to determine the optimum pattern. Both mass scaling (MS) and time scaling (TS) have been evaluated in this

study to reduce CPU time using an automatic scaling scheme provided by Abaqus/Explicit. Figure 3.5 indicates that there is a very strong correlation between experimental forming results from the literature [28, 40, 47, 132] and numerical forming results based on the VFABRIC model developed here, and that TS or MS do not compromise the validity of the simulation results. Both shear angle distribution and material draw-in are very closely matched when adopting MS or TS. The local shear angle has been checked at 10 discrete points (see Table 3.1 and Figure 3.6) and compared quantitatively against experimental data [40, 47]. The peak shear angles differ by about 3% (1.26°) between the MS and TS models.

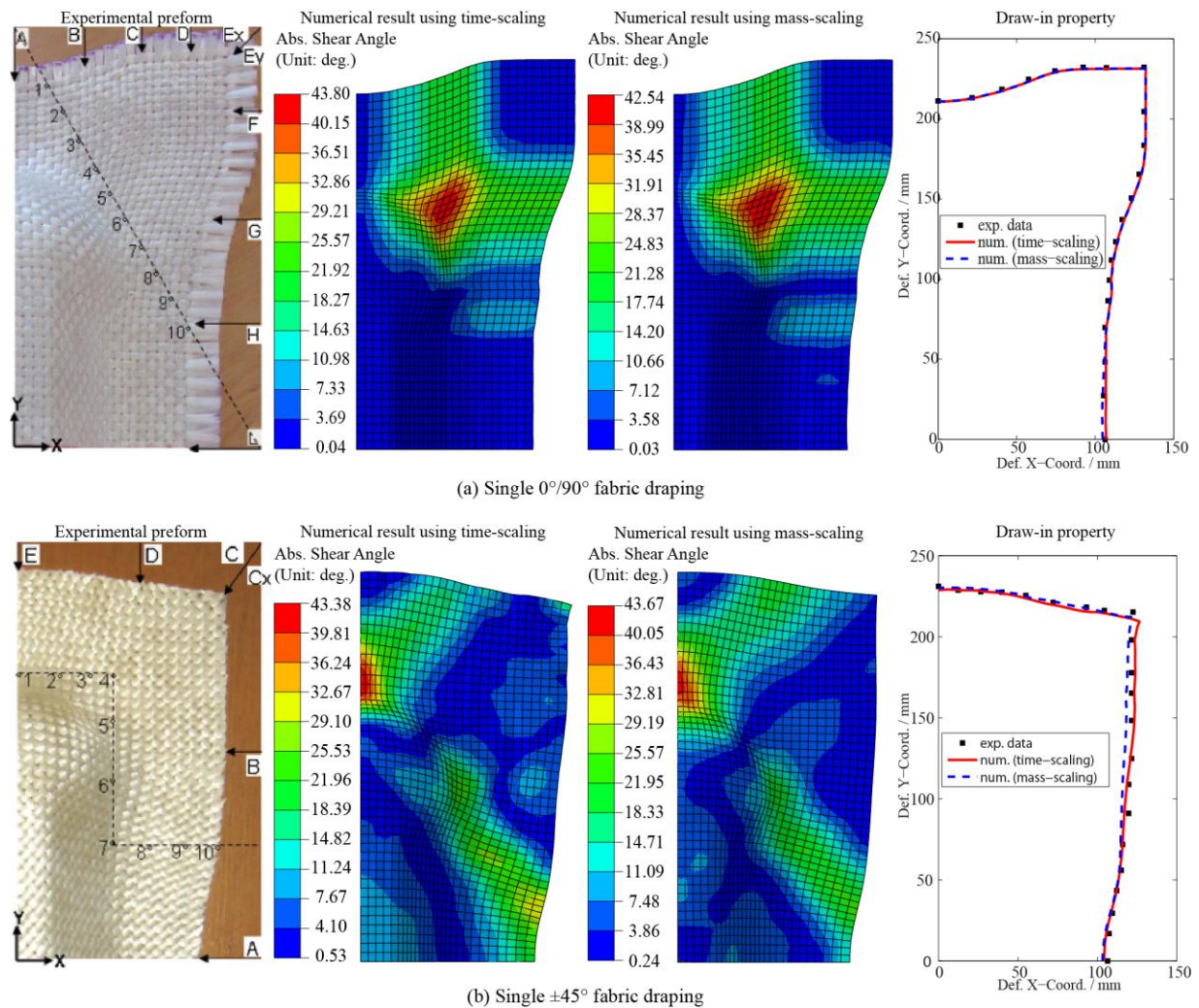


Figure 3.5: Comparison of Abaqus/Explicit VFABRIC model using time-scaling and mass-scaling against experimental results from literature [40, 47]; (a) plain weave fabric at 0°/90°; (b) plain weave fabric at ±45°.

The element edges in the mesh for each ply are aligned with the geometry axes, rather than with the fibre orientations. A sensitivity analysis has been performed to assess the potential issue of finite element shear locking for cases where the material directions are not aligned

with the element edges, which is discussed in the literature [133, 134]. Simulation results for local shear angle distributions in $0^\circ/90^\circ$ and $\pm 45^\circ$ fabric plies at different mesh orientations are plotted in Figure 3.7. The shear angle distributions for the $0^\circ/90^\circ$ ply appear to be insensitive to the mesh orientation, with maximum shear angles of 42.54° (aligned) vs 43.54° (misaligned) respectively. For the $\pm 45^\circ$ ply, differences in local shear angle distributions for different mesh alignment are more significant than for the $0^\circ/90^\circ$ case, but the difference between maximum shear angles, 44.89° (aligned) and 43.67° (misaligned), is still small. Since global ply deformation patterns appear to be unaffected, a slight reduction in accuracy of results for plies with misalignment between material orientations and mesh orientations is considered acceptable here.

Table 3.1: Comparison of shear angle data from Abaqus/Explicit VFABRIC model using time-scaling (TS) and mass-scaling (MS) against experimental results from literature [40, 47]; left: plain weave fabric at $0^\circ/90^\circ$; right: plain weave fabric at $\pm 45^\circ$.

0°/90° Plain Weave Fabric						± 45° Plain Weave Fabric					
ID	Coord. (mm)		Shear Angle (deg.)			ID	Coord. (mm)		Shear Angle (deg.)		
	Def. X	Def. Y	Exp.	Num. (TS)	Num. (MS)		Def. X	Def. Y	Exp.	Num. (TS)	Num. (MS)
1	19	209	7.84	7.33	7.69	1	1	169	42.16	42.36	42.75
2	29	194	14.48	14.55	14.25	2	25	168	23.61	22.17	23.05
3	38	177	22.61	21.50	21.63	3	43	168	9.67	9.78	10.59
4	49	161	33.66	34.22	32.89	4	57	168	0.00	0.42	3.13
5	58	147	38.94	39.28	38.91	5	56	141	8.87	8.52	5.96
6	67	132	26.53	24.22	26.42	6	56	106	14.82	16.01	16.00
7	77	116	16.62	16.05	15.46	7	56	69	22.82	20.34	21.93
8	86	101	3.21	3.76	3.31	8	78	66	21.79	23.12	20.53
9	95	86	7.06	7.96	7.77	9	99	67	17.83	17.79	17.33
10	105	69	0.00	1.08	1.64	10	118	66	7.77	6.06	8.56
Avg. Abs. Error						Avg. Abs. Error					
$\frac{1}{N} \sum \gamma_{12}^{num} - \gamma_{12}^{exp} $			0.80°		0.59°	$\frac{1}{N} \sum \gamma_{12}^{num} - \gamma_{12}^{exp} $			0.93°		1.28°
CPU Time			419 sec		77 sec	CPU Time			386.9 sec		93.4 sec

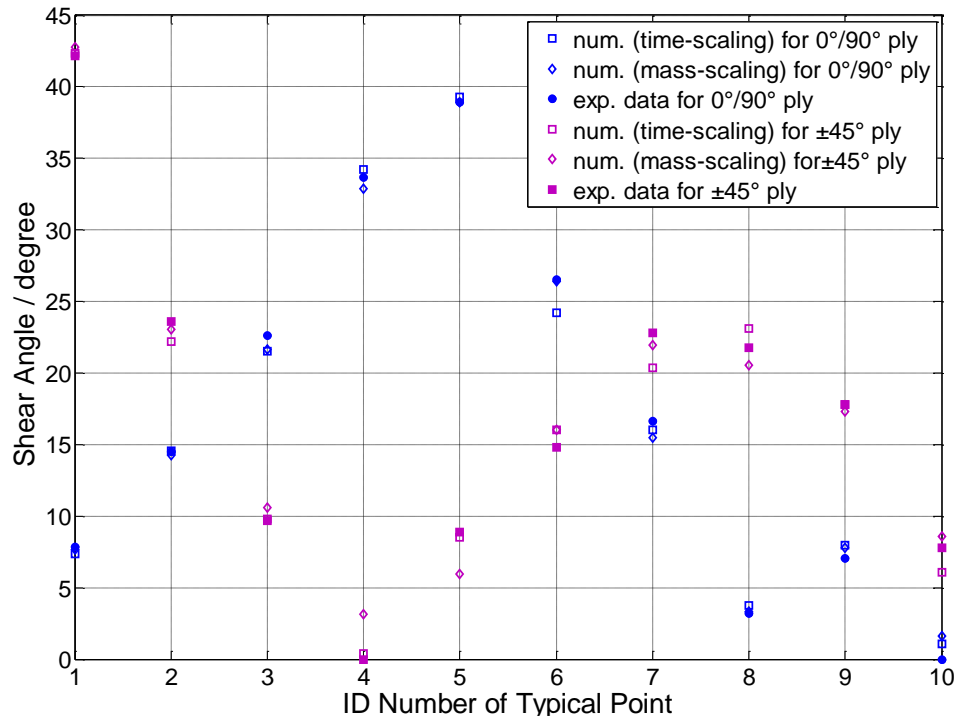


Figure 3.6: Comparison of shear angle data from Abaqus/Explicit VFABRIC model using time-scaling (TS) and mass-scaling (MS) against experimental results from literature [40, 47].

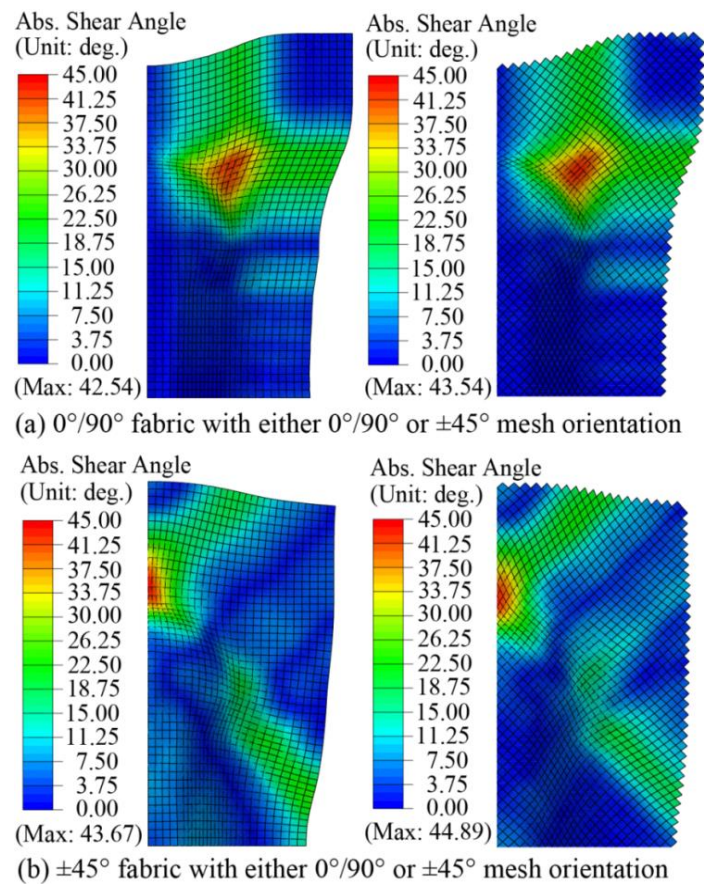



Figure 3.7: The effect of mesh orientation relative to material orientations on the shear angle distribution for both 0°/90° and ±45° plies.

3.4 Non-crimp fabric (NCF) modelling and validation

3.4.1 NCF Materials

A bi-axial $\pm 45^\circ$ carbon fibre NCF with a pillar stitch at 0° (Hexcel FCIM359) has been used during this study, as described in Table 3.2. The lay-up for all simulations and experiments was $[0^\circ/90^\circ]_2$, to enable both 0° and 90° fibres to be visible on the formed surfaces of the hemisphere. A small amount (6 %wt) of reactive binder (Momentive Epikote 620) was applied between the layers of the experimental samples to stabilise the formed shape. The uncompressed thickness of each ply was measured to be 0.4 mm, which is an average value by measuring three different positions using a calliper.

Table 3.2: Summary of NCF material parameters (Photo shows both surfaces of NCF ply).

Material designation	FCIM359	
Supplier	Hexcel	
Fibre type	Toray T620 – 50C	
Fibre areal weight (gsm)	440	
Fibre orientation ($^\circ$)	± 45	
Fibre tow size (K)	24	
Stitch yarn	Polyester	
Stitch pattern	Pillar	
Stitch gauge (GG)	6	
Stitch length (mm)	2.12	
Stitch linear density (dtex)	78	
Stitch areal weight (gsm)	9	

3.4.2 NCF Picture frame shear testing

Since only two short edges of the specimen are constrained during bias extension test, fibre pull-out (i.e. intra-ply yarn sliding) usually occurs inducing significant errors in shear curve testing. The in-plane shear behaviour of the NCF was characterised by picture frame shear tests on cruciform fabric specimens, in order to provide the input shear stiffness data for the modelling, using the methodology outlined by Harrison et al. [37]. Additional care has been taken to rule out the influence of high variability induced by yarn misalignment during picture frame test. The edge length of the testing frame, l_{frame} , was 145 mm, and the length of the central region of shear deformation, l_{fabric} , was 110 mm. The shear tests were carried out on a universal testing machine at a cross-head speed of 100 mm/min. The shear force, F_s , was determined from the force measured at the load cell, and the shear angle was calculated from

the cross-head displacement, using equations presented elsewhere [36]. The normalised force, F_{norm} , is defined as

$$F_{norm} = \frac{F_s \cdot l_{frame}}{l_{fabric}^2} \quad (3.28)$$

Two video cameras, positioned on either side of the test specimen, were used to record the specimen surface topography during each test and to identify the onset of defects. This qualitative information was related to the corresponding shear angle calculated from the cross-head displacement.

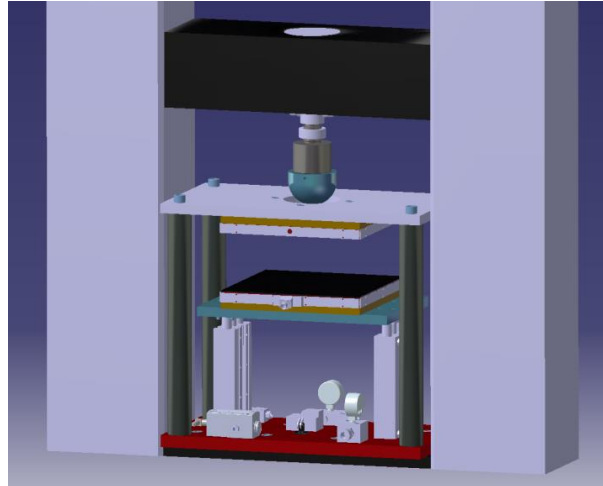
For selected specimens, stitches were removed from the NCF to isolate the contribution of the stitches on the in-plane shear behaviour from that of the primary yarns. The stitches were removed after the samples had been loaded into the picture frame. A soldering iron was used to melt the stitching thread, which avoided disturbing the underlying fibre architecture.

3.4.3 NCF Forming experiment

A laboratory-scale hemisphere forming tool, which was integrated into a universal testing machine, was used for preforming carbon fibre NCFs, as shown in Figure 3.8. Two 300 mm × 300 mm square heated platens with central holes with 104 mm diameter were used to clamp the fabric plies. A clamping force of 1200 N was applied to the blank holder, which was much higher than the one normally used in forming woven fabrics. This force was determined by experiment using a series of ascending magnitudes respectively. Once the NCF was not able to lift the blank holder, the corresponding force was selected as the clamping force. A hemispherical punch with a diameter of 100 mm was attached to the crosshead of the machine via a 25 kN load cell, which allowed the forming force to be monitored. A punch speed of 100 mm/min was used to form the plies. Each forming experiment was performed at ambient temperature, before the temperature of punch and square platens was ramped to 165 °C and held for 10 minutes to cure the binder.

The visible surfaces of the NCF layers were marked with a square grid with a line spacing of 10 mm prior to forming (Figure 3.9(a)). The grid lines were aligned with the directions of the primary yarns. Grid strain analysis (GSA) [135] was used to determine the level of shear deformation in the formed hemispheres. As shown in Figure 3.9(b), the 3D coordinates of grid intersection points were digitised using a coordinate measuring machine (CMM), and the

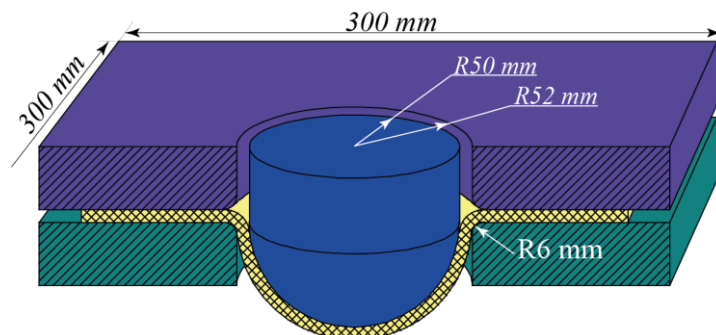
angles between the gridlines were calculated using GSA. A Matlab script was written to process the Cartesian coordinate data generated by the CMM, which was presented as a 3D surface plot. The experimental repeatability associated with the CMM measurements was found to have a Root Mean Square Error (RMSE) of less than 3 %, as one of the formed parts was independently measured 3 times (Figure 3.9(c)).



(a) Tool design

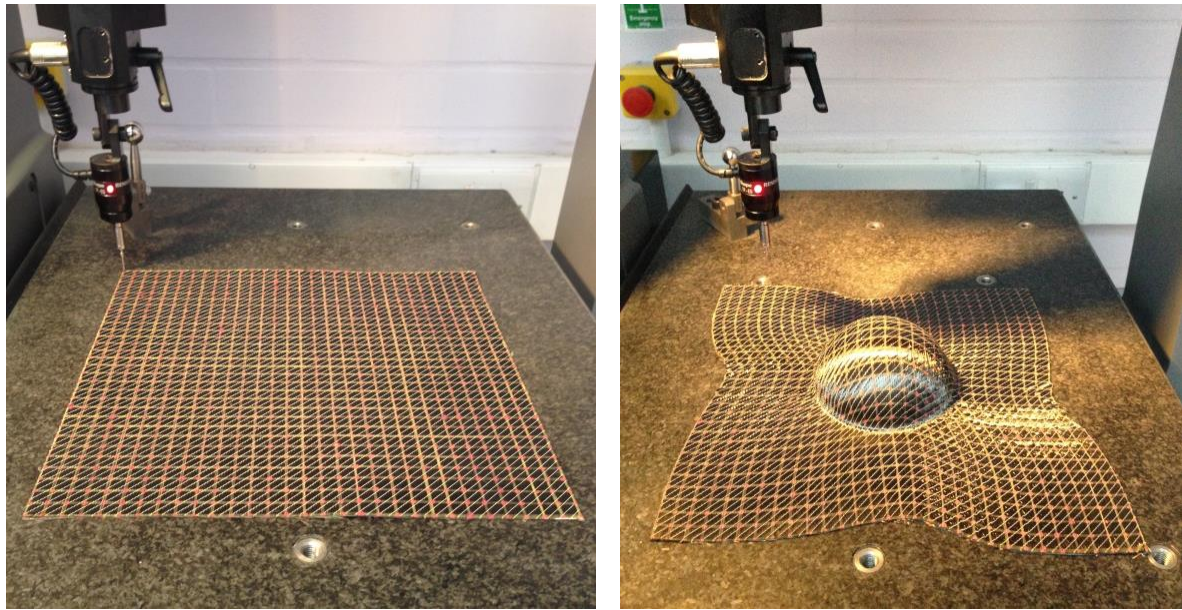


(b) Tool setup



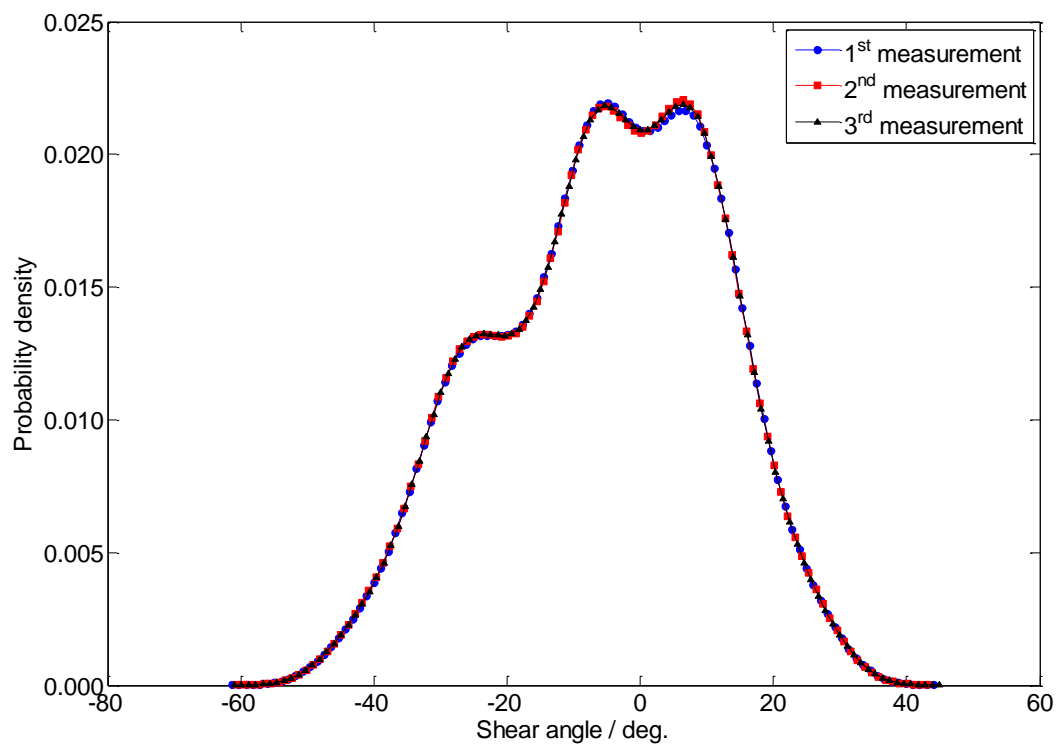
(b) Dimensions

Figure 3.8: Hemisphere forming tool.



(a) Undeformed fabric

(b) Deformed fabric



(c) Probability density of shear angles measured three times independently on a preform at a displacement of the hemispherical punch of 50 mm

Figure 3.9: Grid measurement for NCF preforms using a coordinate measuring machine (CMM).

3.4.4 NCF Modelling approach

The same non-orthogonal constitutive model has been implemented for the NCF material as previously described for woven fabrics in Section 3.3. Figure 3.10 shows the fundamental differences in shear behaviour between the NCF and a twill weave fabric of the same areal

density from picture frame test. The shear response of the woven material is symmetrical about the origin, and the normalised shear force is shown to increase steadily until the locking angle is reached. The shear behaviour of the NCF is asymmetric due to the stitch contribution. The normalised shear force rises linearly to a peak at approximately 1 N/mm, as the stitch is loaded in tension. This peak corresponds to a shear angle of 0.5 rad, where the first stitches start to rupture. Then the shear force reduces progressively as other stitches fail successively. All stitches have failed at a shear angle of approximately 0.75 rad. There is no evident peak in the negative shear direction in Figure 3.10, as the stitches are in compression (see Figure 2.3). The shape of the negative shear response for the NCF is similar to that of the woven material.

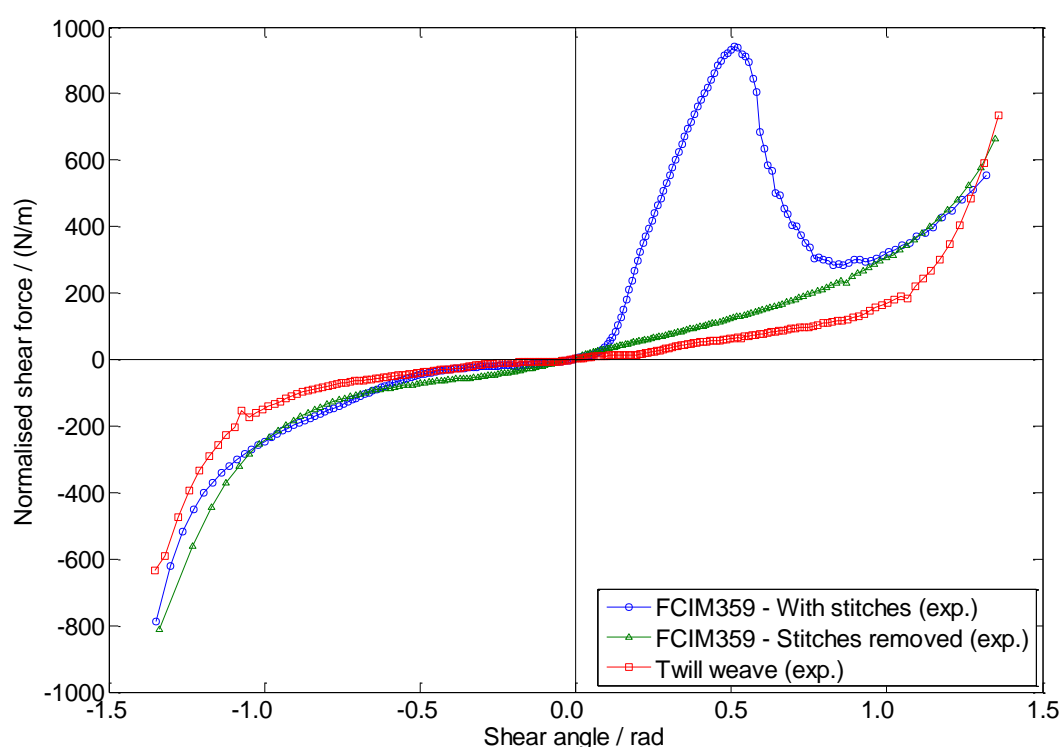


Figure 3.10: Experimental picture frame shear results for FCIM359 bi-axial NCF. Testing was performed in two directions, placing the stitch yarn in tension (positive shear) and compression (negative shear). Stitches were fully removed in some samples. Results for a 400 gsm twill weave fabric are shown for comparison.

Experimental results from picture frame shear tests (Figure 3.10) have been used to separate the contribution of the stitches, by conducting tests with and without removing stitches. Figure 3.10 indicates that the shear stress-strain response during negative shearing (<0.0 rad) is very similar for both scenarios. There is also very good agreement between the two curves for large positive shear angles (>1.0 rad), beyond the point where all stitches have failed in the stitched sample. This implies that the large peak in the positive shear curve at 0.5 rad is

dominated by the tensile contribution of the stitches, but the shear behaviour outside this region is dominated by the rotation of the primary yarns.

A combination of the two shear curves presented in Figure 3.10 has been used to derive the constitutive behaviour of stitched and unstitched NCFs, using the principle of superposition based on the piecewise linear assumption of material behaviour. As shown in Figure 3.11, the contribution of the primary yarn rotation was extracted from the curve for the stitched material by fitting the shear curve only to data points that exhibited a RMSE of less than 10 % compared to the unstitched curve in Figure 3.10. The remaining data represents the contribution of the stitches to the shear stiffness, which has been approximated by a bilinear relation. According to this model, there is slack in the stitches up to shear angles of approximately 0.06 rad (i.e. approximately 1.5°), the starting point of stitch damage is 0.50 rad (i.e. approximately 28.6°), and complete stitch failure occurs at 0.75 rad (i.e. approximately 43.0°). Thus, the stitches are active between 0.06 rad and 0.75 rad. As shown in Figure 3.12, the material shear curve can be obtained by superimposing the yarn rotation and stitch components, which agrees with the original experimental testing data, with an RMSE of less than 5 %.

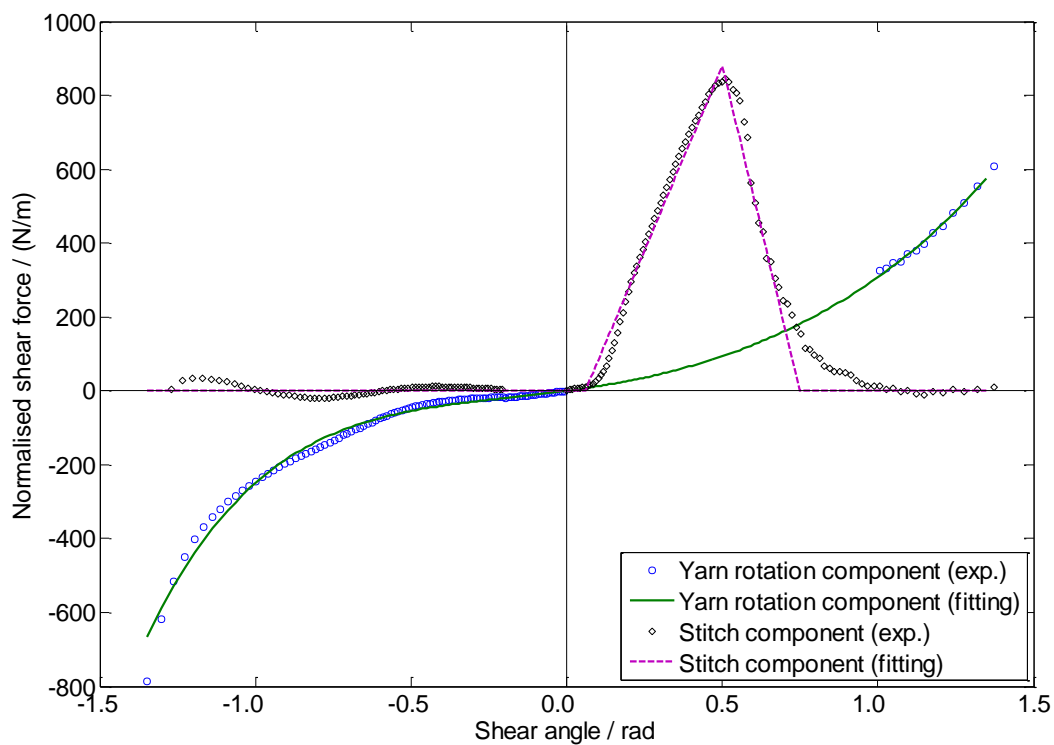


Figure 3.11: Shear resistance curve of FCIM359 (taken from Figure 3.10) separated into two components: Primary yarn rotation and stitch contribution.

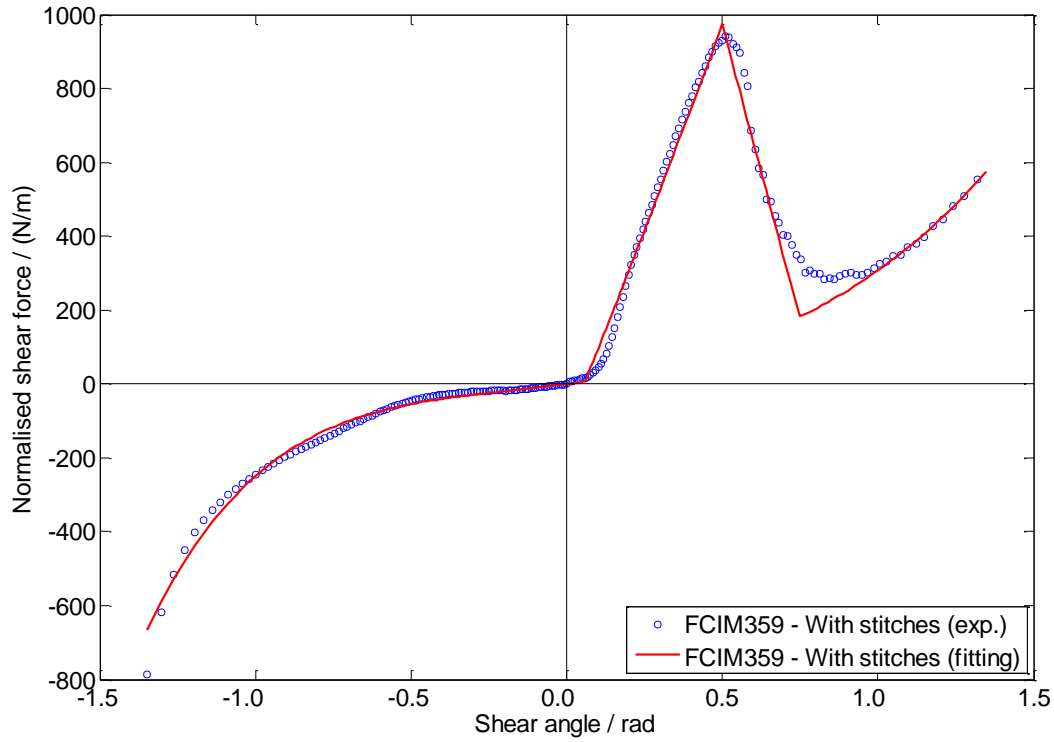


Figure 3.12: Summary of the shear resistance curve for fully stitched FCIM359 bi-axial NCF. Red line shows the numerical fit.

From the shear resistance curves presented in Figure 3.10 and Figure 3.12, the shear force can be described as

$$F_{norm} = F_{norm}^{yarn\ rotation} + F_{norm}^{stitch} \quad (3.29)$$

where, the contribution of the yarn rotation is

$$F_{norm}^{yarn\ rotation} = (29.56\gamma_{12}^5 - 65.56\gamma_{12}^4 + 137.06\gamma_{12}^3 + 94.73\gamma_{12}^2 + 112.19\gamma_{12})\text{N/m} \quad (3.30)$$

where γ_{12} is defined in the range of $\left(-\frac{\pi}{2}, \frac{\pi}{2}\right)^T$; and the contribution of the stitches is

$$F_{norm}^{stitch} = \begin{cases} (2000\gamma_{12} - 120)\text{N/m} & , \quad 0.06 \leq \gamma_{12} < 0.50; \\ (-3520\gamma_{12} + 2640)\text{N/m} & , \quad 0.50 \leq \gamma_{12} \leq 0.75; \\ 0 \text{ N/m} & , \quad \text{else.} \end{cases} \quad (3.31)$$

where γ_{12} is the shear angle in radians.

3.4.5 NCF model validation

Numerical tests have been performed to verify that the constitutive relation used in the current user subroutine is representative of the shear behaviour of a bi-axial NCF. The material model for the stitched NCF has been implemented into a picture frame shear simulation. The picture frame shear test was simulated using the same size and shape of specimens as in the experiments (Section 3.4.2). The primary yarns were parallel to the frame

edges in all cases. In positive shear, the pillar stitches were aligned with the direction of crosshead travel and subjected to elongation, whilst they were perpendicular to the direction of crosshead travel for the negative shear direction. As shown in Figure 3.13, a 4-bar linkage mechanism was modelled to replicate the motion of the frame. The fabric was modelled using square membrane elements (M3D4R) with a size of $2\text{ mm} \times 2\text{ mm}$.

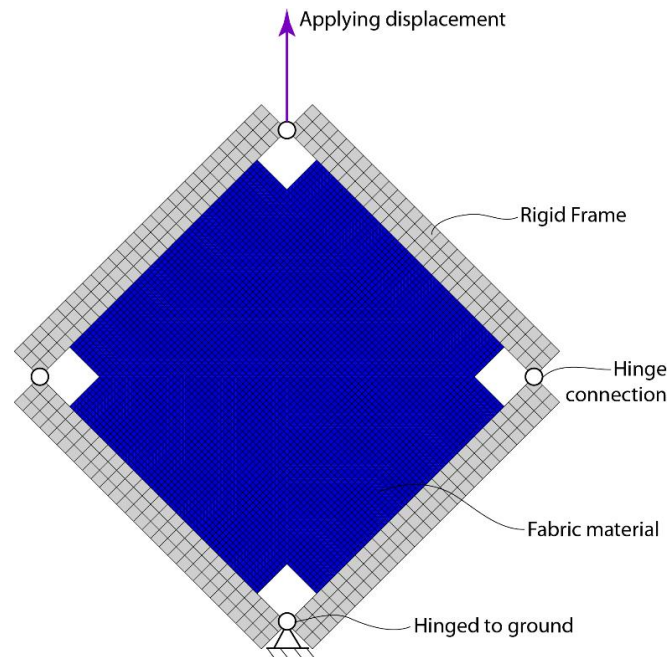


Figure 3.13: Finite element model of picture frame test.

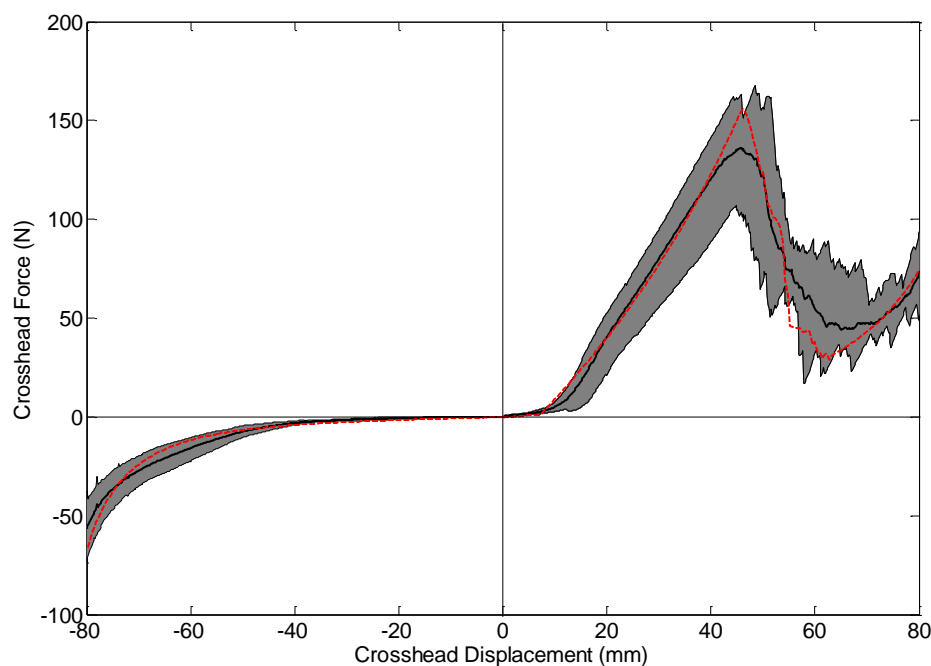


Figure 3.14: Comparison of shear resistance curves from picture frame shear experiments (black: average; grey: range of results from 12 tests) and simulations (red).

Force-displacement data from the simulation are compared against experimental picture frame shear data in Figure 3.14. Although there is a negative gradient in shear curve as shown in Figure 3.11 and Figure 3.12, no significant influence was observed in the simulation of picture frame test using Abaqus/Explicit. There is good agreement (approximately 5 % RMSE) between the two data sets, with the simulation curve falling within the bounds of the experimental data. However, the required time increment decreased to ensure the simulation kept on running stably due to this negative feature in positive shearing.

3.5 Hemisphere forming simulations

3.5.1 NCF forming validation

The forming simulation was validated by comparing the results for a hemisphere against the grid strain data and perimeter shape from experimental trials. Each 300 mm × 300 mm ply was discretised into square membrane elements (M3D4R) with dimensions of 2 mm × 2 mm.

The tooling was modelled using the geometry in Figure 3.8, with all parts considered to be rigid bodies. A penalty contact algorithm was used to define the behaviour at all interfaces. An isotropic Coulomb friction model was adopted, assuming a constant friction coefficient. The tooling-fabric friction coefficient was measured to be 0.23 and the fabric-fabric contact was 0.36 (plies at same orientation), according to experiments performed to ASTM D1894, ISO8295. Displacement boundary conditions were applied to the punch to control the stroke. A force was applied to the blank holder to control fabric slippage, which was varied during the stroke from 1200 N to 600 N depending on the displacement of the punch. This accounted for a reduction in blank holder pressure related to compression of the pneumatic cylinders in the (upstroke) set-up, which was measured during the experiments.

In forming experiments, preforms were produced using the hemispherical punch. Experiments were stopped at punch displacements of 30 mm (hemisphere partially formed) and 50 mm (hemisphere fully formed). The coordinates of the grid intersection points were measured three times for each preform. The average of these experimentally determined coordinates are compared with the simulation results. As shown in Figure 3.15, the simulated grid intersections are a close match to the measured points, which indicates that the model is able to predict the forming behaviour of the NCF with good accuracy. The error for the 50 mm punch displacement is larger than for the 30 mm displacement, i.e. the accuracy reduces

with increasing punch displacement. The largest differences between measured and simulated coordinates at grid points (1.79 mm for the 30 mm case and 2.87 mm for the 50 mm case) occur at points in the positive shear regions (i.e. top-right and bottom-left quadrant in Fig. 8), which exhibit the highest degree of wrinkling. These regions show the largest difference in data measured for different specimens (while the reproducibility of measurements for each specimen is high, see Figure 3.9) using the GSA approach, as the tension of the stitches and the initial orientation of the primary yarns may vary, affecting the level and position of local wrinkling. In addition, the macro-scale model used here neglects the change in fabric thickness and out-of-plane bending stresses. Therefore, the accuracy of the predicted local response of the fabric may be compromised at the finite element scale, but the global response is still representative.

The shear angle at each grid intersection has been calculated from both experimentally determined and predicted coordinates using GSA. The shear angles at all 961 grid intersections in the entire specimen have been compared to validate the numerical model. As shown in Figure 3.16, the overall shear angle distributions from the simulation are a good representation of the corresponding experimental data. The difference in local shear angle is less than 5° . More accurate prediction of shear deformation is obtained for the case using a smaller punch displacement (30 mm), since there are fewer wrinkling defects. However, deviations increase with increasing punch displacement, as larger shear deformations are required to achieve the final formed shape, which in turn induces more wrinkles. The largest differences in shear angle are limited to relatively small areas around the wrinkle regions and near the edge of the blank, which are a result of the density of the grid used on the experimental samples.

Further analysis has been conducted by comparing probability density curves of the experimentally determined and predicted shear angle distributions for two punch displacements (Figure 3.17). The corresponding pairs of curves show good agreement with each other. The difference between curves derived from the experiment and simulation for the 30 mm punch displacement is small (RMSE $< 5\%$). The peak shear angles in the negative and positive regions are predicted with high accuracy. There is some uncertainty in the range of small shear angles (i.e. around zero degree), which may be related to the very small difference in shear angles between neighbouring elements at the beginning of the simulation.

The difference increases for the 50 mm punch displacement due to the instabilities caused by the increase in wrinkling defects, where it is approximately 7 % (RMSE). The largest discrepancy appears in the range of small shear angles, which is similar to the 30 mm case.

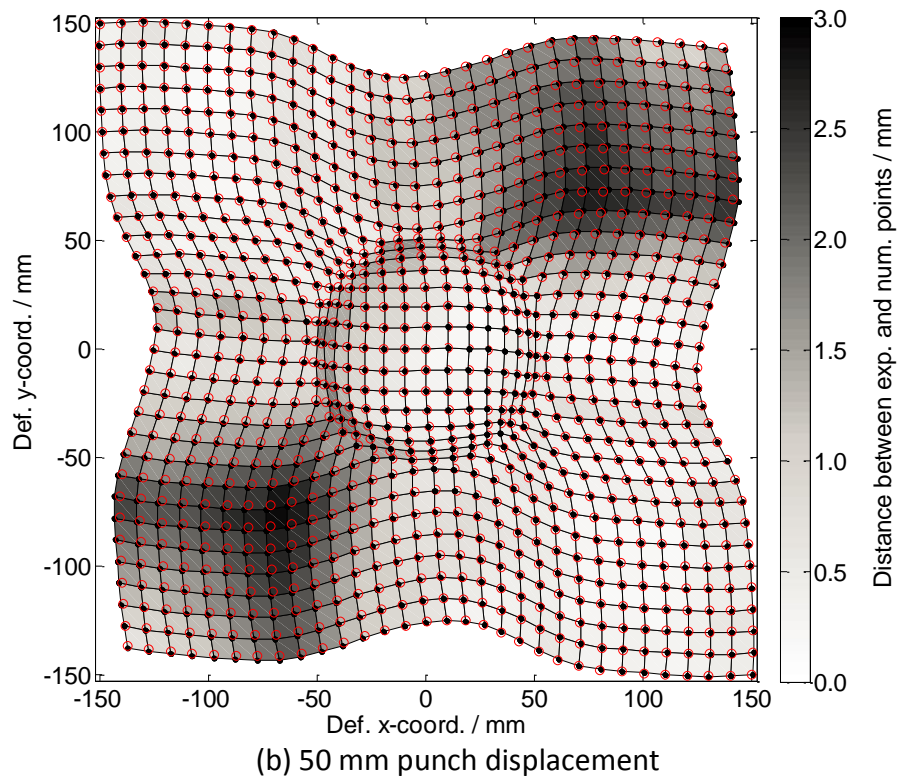
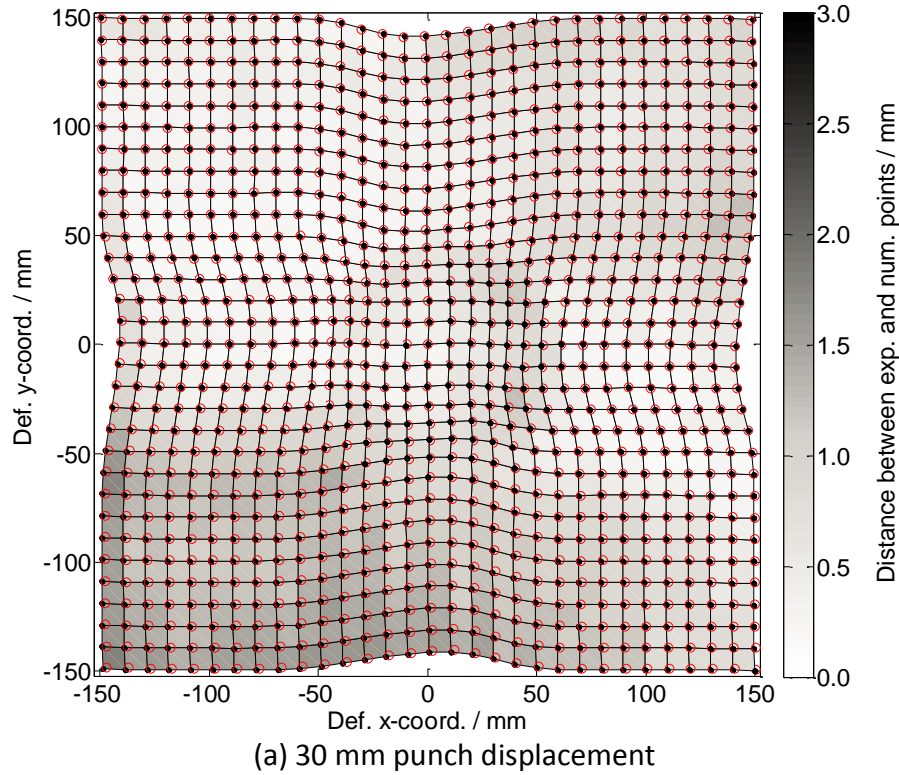
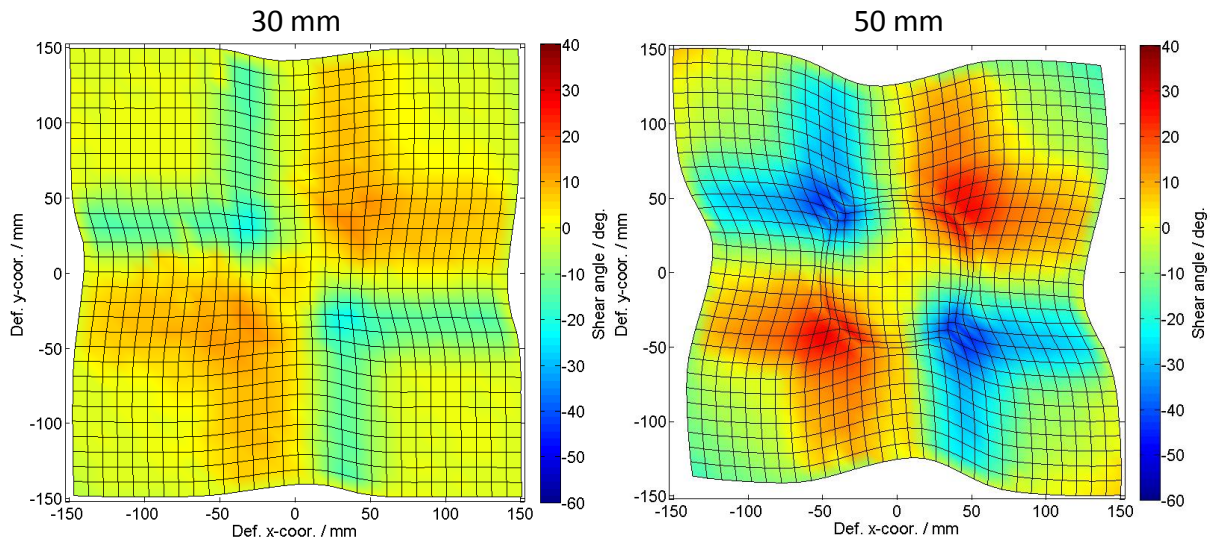
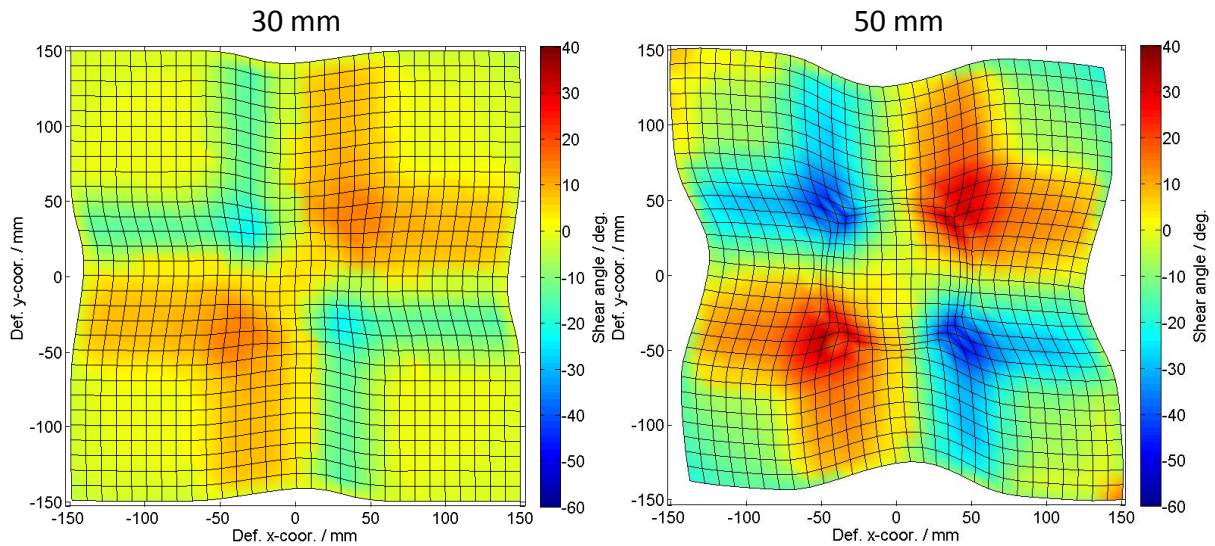


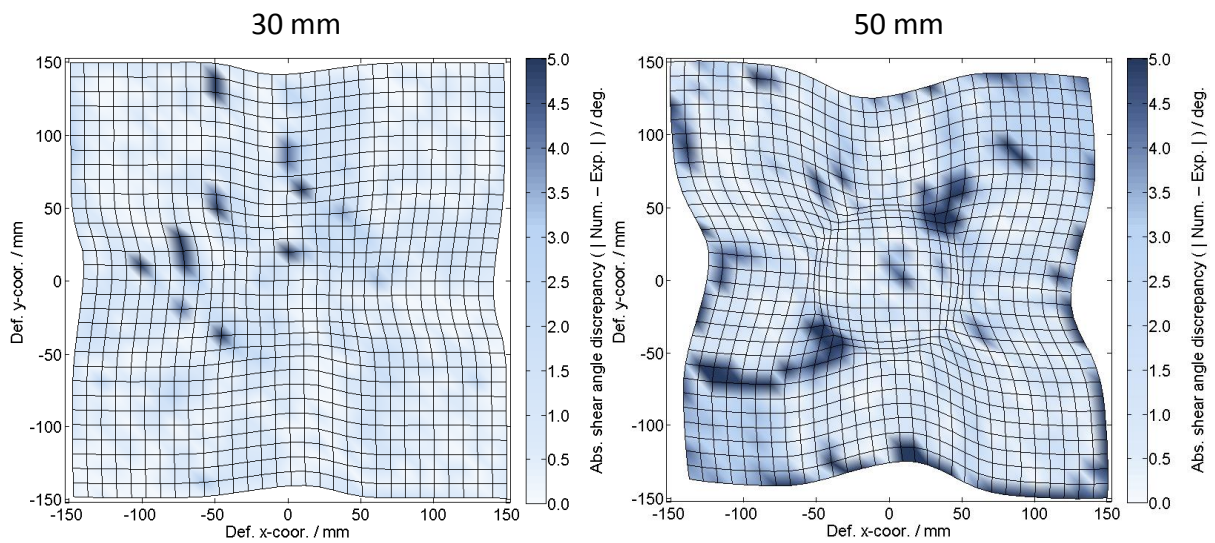
Figure 3.15: Comparison of experimental (red circles) and numerical (black solid dots) grids. The contour shows the distance between the grid intersections obtained from experiment and simulation.



(a) Shear angle distribution from experiment



(b) Shear angle distribution from simulation



(c) Difference of shear angle distributions from simulation and experiment

Figure 3.16: Comparison of shear angle distributions from experiment and simulation determined using GSA.

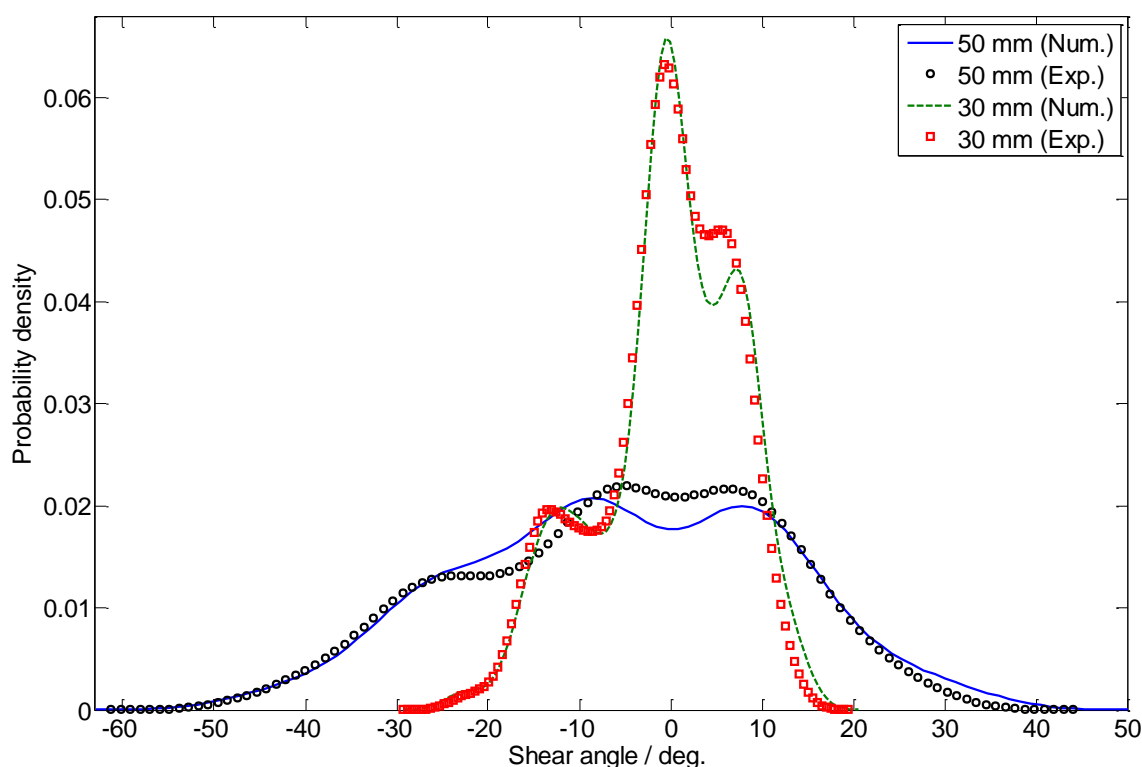


Figure 3.17: Probability density of shear angle from simulation and experiment using punch displacements of 30 mm and 50 mm.

3.5.2 Defect detection in bi-axial NCF

A single ply was preformed to a hemisphere at a punch displacement of 50 mm to quantify the level of intra-ply yarn slip. Figure 3.18 confirms that the level of intra-ply slip is negligible in the matched tool forming process, as the difference in grid strains between the convex and concave sides of the formed hemisphere is less than 3 %. This is within the systematic uncertainty for the coordinate measurement reported in Figure 3.9. There was also no significant difference in grid deformation (including perimeter shape), and no visible sign of ply deterioration. This supports the decision to use a macro-scale non-orthogonal constitutive model to describe the forming behaviour of this bi-axial NCF.

Unlike for woven fabrics, only one principal yarn orientation is visible from each side of a bi-axial NCF ply. Thus, wrinkling defects may appear differently on the concave and convex side of the hemisphere. Here, yarns on the convex side were initially orientated at 0° (aligned with the positive x-axis in Figure 3.18), and therefore wrinkling defects are indicated by the compressive strain along the first fibre orientation (i.e. E_{f11}). The fibres on the concave side of the hemisphere were orientated at 90° (aligned with the positive y-axis in Figure 3.18) before preforming, and local wrinkling on this side is highlighted by the compressive strain along the

second fibre orientation (i.e. E_{f22}). Figure 3.19 confirms that wrinkling defects occur at different positions on different sides of the bi-axial NCF ply.

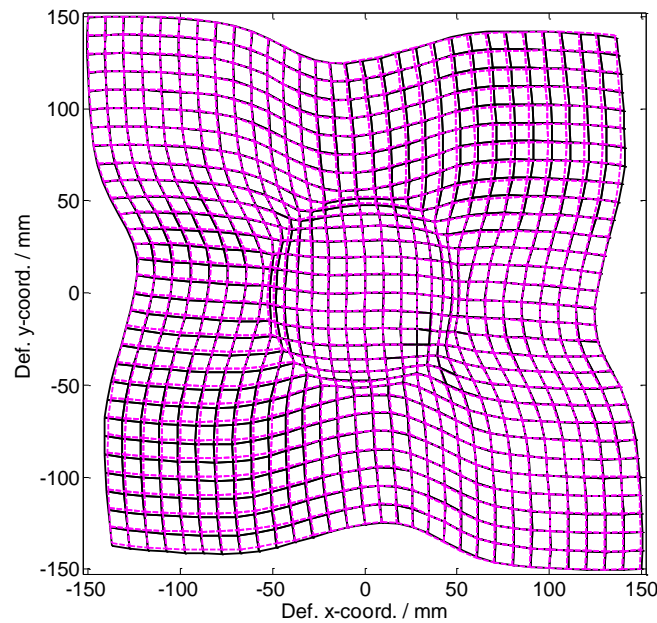


Figure 3.18: Comparison of grids measured from both sides of preforms at a punch displacement of 50 mm. Black solid grid: measured on hemisphere concave side (yarns initially along 90°); purple dashed grid: measured on hemisphere convex side (yarns initially along 0°).

Comparing the shear angle distributions (Figure 3.16) and wrinkling strain distributions along both fibre orientations (Figure 3.19) confirms that the majority of wrinkling defects occur within the highly sheared regions. There is a positive correlation between the shear deformation and the compressive strain, indicating the likelihood of wrinkles.

In order to investigate the onset and evolution of wrinkles, hemispheres were preformed at increasing punch displacement (10 mm, 30 mm and 50 mm) as shown in Figure 3.20. Two different kinds of wrinkling defects were observed; at the macro-scale, in the form of out-of-plane ply folds, and at the meso-scale, in the form of in-plane bundle waviness. These are easily distinguishable, and therefore these observations provide an effective way to trace the cause of the defects by comparing against observations from the simulations.

Positive and negative shear terms are commonly referred to in the literature to indicate when the in-plane segment of the stitch yarn is in tension or compression respectively [23], as shown in Figure 2.3. Out-of-plane macro-scale wrinkling, which results in a very uneven surface finish, can be observed mainly where positive shear dominates (Figure 3.20(a)). Since intra-ply stitches provide additional constraints on yarn rotation in these regions, shear

locking occurs at smaller shear angles than in regions with negative shear. Compressive in-plane strain then results in out-of-plane wrinkling as shown in Figure 3.20(a), which can be observed on both sides of the ply. Figure 3.16 indicates that some shear angles in the positive shear regions (for both 30 mm and 50 mm cases) have exceeded a shear angle of 0.5 rad (i.e. 28.6°) when individual intra-ply stitches start to fail (Figure 3.12). This indicates that the predicted wrinkling defects around this area (Figure 3.20(a)) can be attributed to excessive shearing, which is in agreement with the experiment.

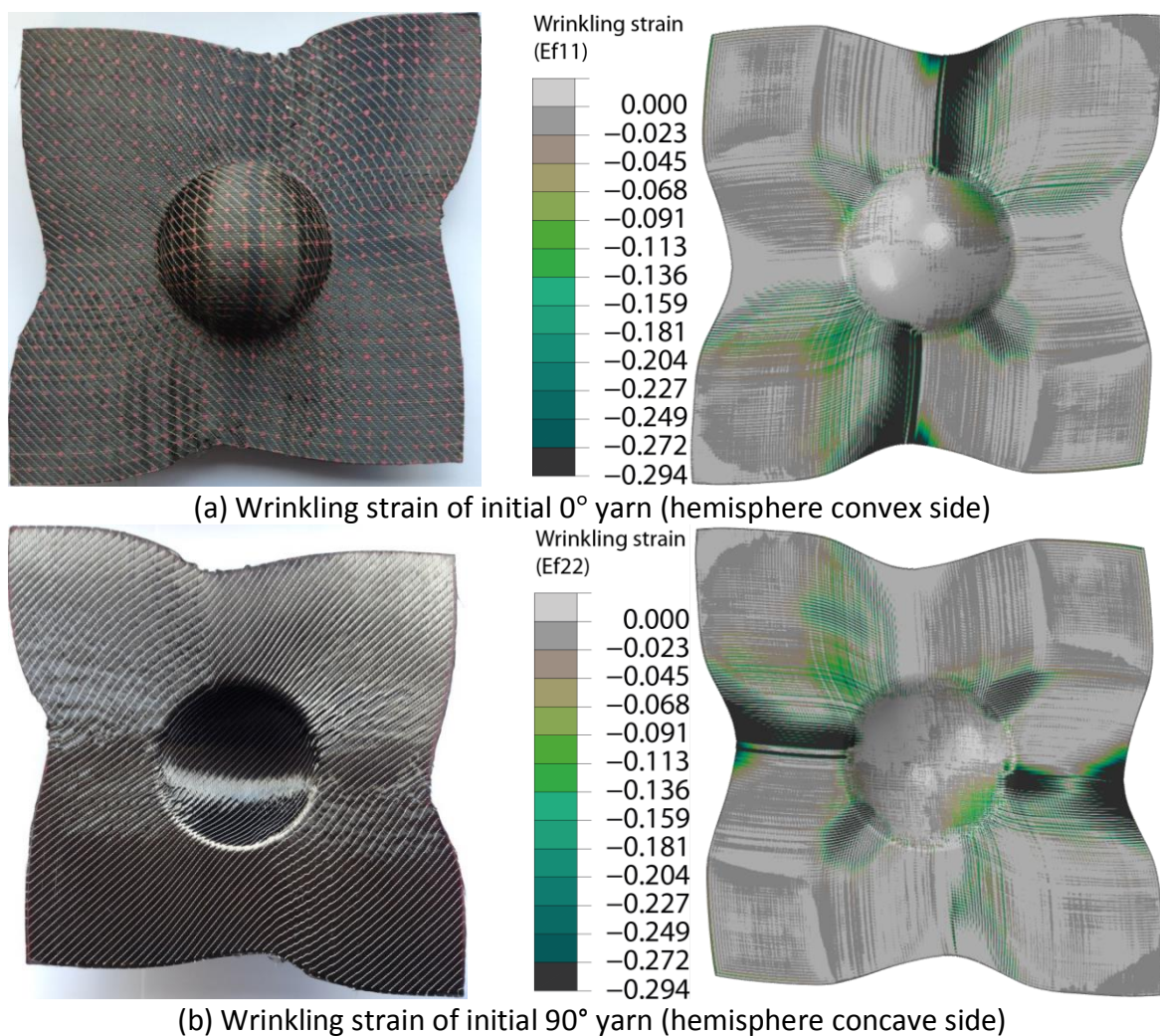
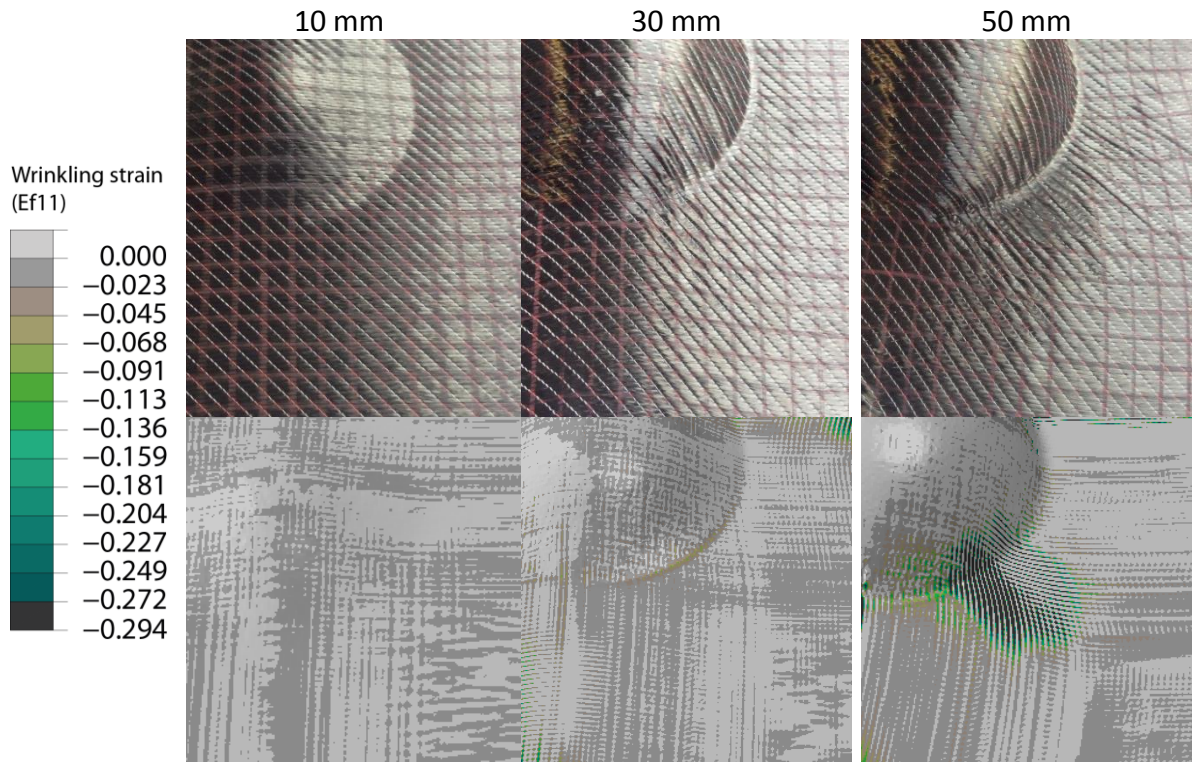


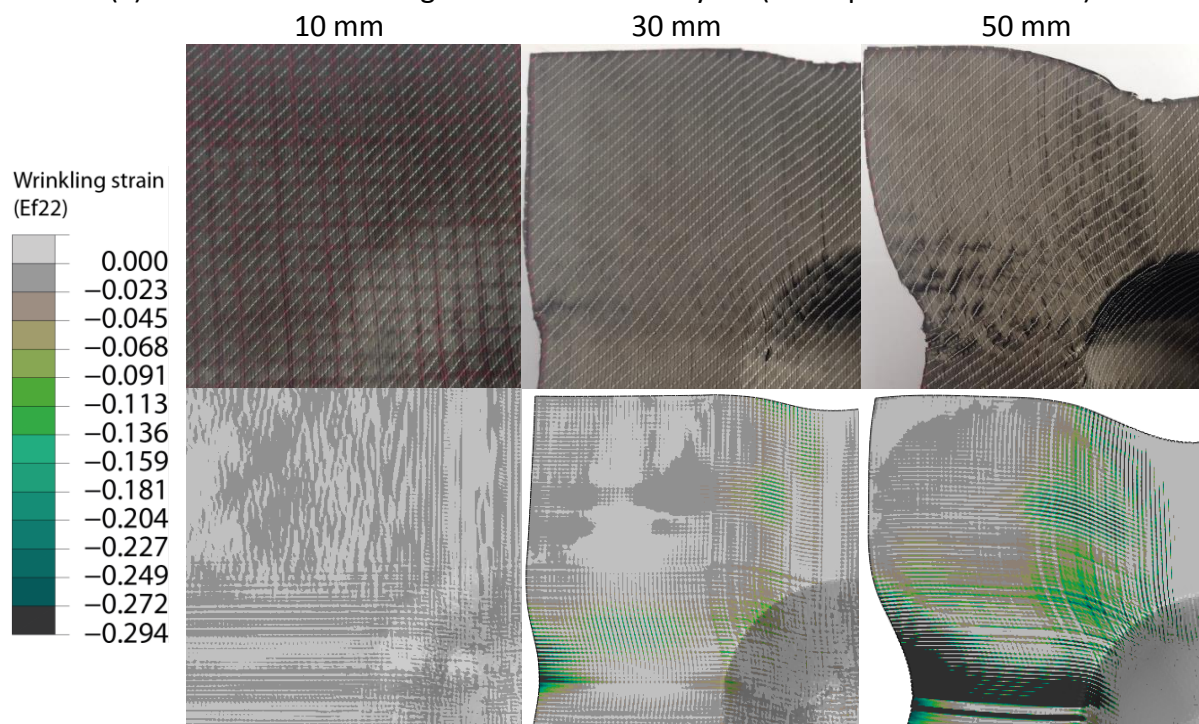
Figure 3.19: Wrinkling defect induced in NCF hemisphere forming process at a punch displacement of 50 mm.

Meso-scale wrinkling occurs mainly in the negatively sheared region of the part (Figure 3.20(b)). The surface roughness is unaffected, but in-plane fibre waviness is visible on the surface of the ply. The primary yarns can rotate more freely in-plane under negative shear, as the shear resistance is derived from in-plane friction between yarns and lateral yarn compression. Therefore in-plane fibre buckling occurs. As shown in Figure 3.16, the maximum absolute shear angles in the negative shear region are less than 60° for all cases. Visual

observation of the picture frame shear tests (Section 3.4.2) has indicated that no defects occur in negative shear within this range of angles. Hence, it can be concluded that defect formation in these regions is not related to excessive shearing.



(a) Macro-scale wrinkling defects of initial 0° yarn (hemisphere convex side)



(b) Meso-scale wrinkling defects of initial 90° yarn (hemisphere concave side)

Figure 3.20: Evolution of wrinkling defects with increasing punch displacement.

According to Figure 3.19 and Figure 3.20, wrinkling occurs at a compressive strain of approximately 0.03 in fibre direction, indicating some resistance to fibre buckling at lower strains. Defect formation can therefore be identified with good accuracy from simulation results, by combined evaluation of the shear angle and wrinkling strain distributions. The latter predicts potential areas for meso- and macro-scale wrinkling, without distinguishing type, whilst the former indicates defects related to macro-scale wrinkling only.

3.6 Chapter summary

A non-orthogonal constitutive framework has been developed to describe the macroscale properties of a biaxial fabric based on a homogenisation scheme. It has been employed for a benchmark material (plain weave commingled glass/PP fabric) from the literature, demonstrating that it realistically captures the forming behaviour.

The model is first validated using data from the literature for a plain weave commingled glass/PP material to verify that the constitutive relation is correct for bi-axial fabrics. The misalignment between material orientations and mesh orientations has been proven to be negligible, which may facilitate the implementation of process optimisation by simply adopting consistent meshes in the FE models for multi-ply fabric forming. Also, the FE simulation can be dramatically accelerated by selecting appropriate scaling factors (either time scaling or mass scaling) without significantly compromising precision (about 3%) using the developed constitutive model.

Intra-ply stitches, which are used to assemble two layers of yarns to produce one ply of bi-axial NCF, can introduce asymmetry to the fabric shear behaviour. In particular, pillar stitches in bi-axial NCFs make a significant directional contribution to the NCF shear resistance and affect the defect formation mechanisms in preforming. A constitutive model has also been developed and implemented in FE simulations to predict this behaviour, using the developed non-orthogonal constitutive framework to track the orientation of primary yarns at the macro-scale. Picture frame shear testing has been performed to capture the asymmetric shear behaviour of the bi-axial NCF, providing input data in the form of shear stiffness as a function of shear angle. Results indicate that the stable architecture of the NCF (with pillar stitches) is more difficult to form than a comparable plain weave fabric, with additional manufacturing defects likely during forming.

In order to identify the mechanisms of defect formation in detail, the shear stiffness was decomposed into two constituents, primary yarn rotation and tension in the stitching thread. The fibre rotation was described using a low-order polynomial, and the stitch behaviour was represented by a bilinear relation. A deviation of approximately 5 % was observed between the simulation and experimental data when the model was applied to a planar shear case. The simulation curve generally falls within the bounds of the experimental data for 12 experimental repeats.

A detailed study has been conducted to investigate the onset and propagation of defects for a bi-axial NCF with a pillar stitch, formed over a hemisphere tool. Grid strain analysis was employed to validate the simulation, and it was found that both sets of local shear angles differed by less than 5° at maximum punch displacement.

The model predicts different local distributions of forming defects on both sides of a NCF ply. Two types of defect mechanism have been identified in hemisphere forming. Comparisons with the simulation results indicate that one is caused by excessive shear, inducing out-of-plane wrinkling (macro-scale wrinkling), another is caused by fibre compression, inducing in-plane wrinkling (meso-scale wrinkling). By correlating the local distributions of shear angle and wrinkling strain, it is possible to determine the wrinkling mode and confirm the corresponding defect mechanism. Results show that the predicted wrinkling position and defect mechanism correlate well with the experiments, which further supports the validity of the NCF material model and the FE forming process simulation.

Chapter 4 Inter-Ply Stitching Optimisation

4.1 Introduction

This Chapter seeks to understand the opportunities offered by locally stitching multiple fabric plies together to create a single preform blank, which can be formed into a complex 3D shape. The explicit FE forming model developed in Chapter 3 is used to simulate the effect of local stitch-bonds in multi-ply preforms with different ply orientations. Results from a numerical study of a simple hemisphere geometry demonstrate the capability of simulating the forming behaviour of a multi-ply stack in a single operation. A genetic algorithm has been developed to determine the optimum position of local stitches, in order to improve preform quality and ultimately facilitate automated component manufacture. Two different criteria have been implemented to assess the forming outcome; the maximum value criterion (MAXVC) and the Weibull distribution quantile criterion (WBLQC). The convergence rates and optimum solutions for both criteria have been compared to understand the compromise between accuracy and computational efficiency.

4.2 Modelling of multi-ply fabric with localised inter-ply stitches

The proposed material model in Chapter 3 captures the dominant factors in woven fabric forming, including in-plane shear, fibre elongation and inter-tow/inter-ply slipping. A macro-scale homogenisation scheme has been adopted to avoid modelling discrete tows, which means the model runs quickly (about 90 seconds per hemisphere simulation). This enables a genetic algorithm to be implemented for the stitch optimisation, to analyse a large number of iterations within a sensible time. The model is insensitive to mesh orientation, which facilitates the placement of localised stitches by using a consistent mesh for all plies.

4.2.1 Inter-ply stitch model

Assembly stitches have been modelled as inter-ply connections by constraining coincident nodes using a user-defined 1D cable-spring element in Abaqus/Explicit, as shown in Figure 4.1. Both ends of each stitch element have unconstrained rotational degrees of freedom, and the compression modulus is set to zero, hence providing tensile stiffness only. A degree of ‘slack’

is built into the model by enabling the stitch elements to extend under zero tensile load (see Figure 4.2). The behaviour of the stitch is defined by the tensile stiffness along the axial direction and the initial slack length. The presence of the stitch does not influence the friction between the fabric plies, since the spring element represents a constraint of nodal mobility without physical surface properties. The constraining forces are calculated based on the distance between the connected nodes. The stitch in slack does not mean it is broken, it can be activated once the distance surpassing the threshold distance and also be deactivated when the distance indicating a slack status as long as the stitch has not been totally ruptured.

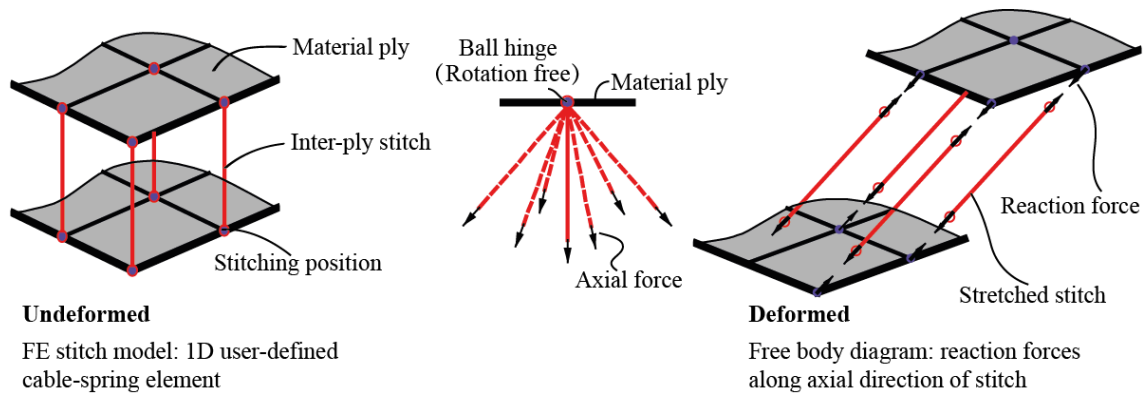


Figure 4.1: Inter-ply stitch model defined in Abaqus/Explicit using 1D user-defined cable-spring element.

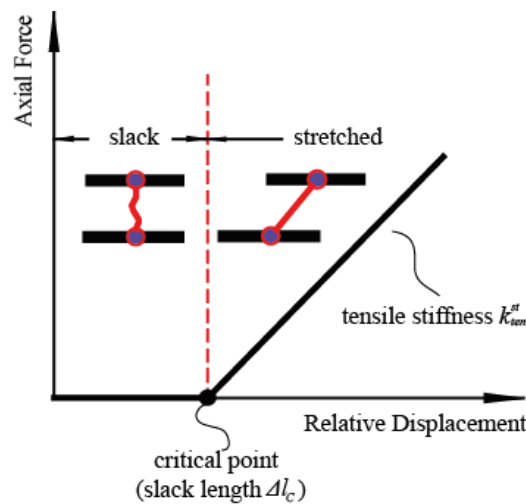


Figure 4.2: Definition of axial behaviour for stitch element.

The stitch constrains nodal displacement, as shown in Figure 4.1. The magnitude of the reaction force is equal to the axial stitch force. For an arbitrary inter-ply stitch element connecting nodes i and j (see Figure 4.3), the relative displacement Δl_{ij} can be calculated as

$$\Delta l_{ij} = |\vec{l}_{ij}| - |\vec{l}_{ij}| \quad (4.1)$$

$$\vec{l}_{i'j'} = \vec{l}_{oj'} - \vec{l}_{oi'} = (x_{j'}, y_{j'}, z_{j'}) - (x_{i'}, y_{i'}, z_{i'}) \quad (4.2)$$

$$\vec{l}_{ij} = \vec{l}_{oj} - \vec{l}_{oi} = (x_j, y_j, z_j) - (x_i, y_i, z_i) \quad (4.3)$$

where (x_i, y_i, z_i) and (x_j, y_j, z_j) are the initial nodal positions of a stitch element, while $(x_{i'}, y_{i'}, z_{i'})$ and $(x_{j'}, y_{j'}, z_{j'})$ are the current nodal positions of the same stitch element. All of these coordinates are calculated by Abaqus/Explicit at each time increment.

As shown in Figure 4.2, the axial stiffness of a stitch (i.e. k^{st}) is defined as

$$k^{st} = \begin{cases} 0 & , \quad \Delta l_{ij} \leq \Delta l_c \\ k_{ten}^{st} & , \quad \Delta l_{ij} > \Delta l_c \end{cases} \quad (4.4)$$

where the superscript “st” denotes properties associated with the stitch element, Δl_c is the critical relative displacement to identify whether the stitch element is slack or stretched, and k_{ten}^{st} is the tensile stiffness along the axial direction. These parameters can be obtained from material testing [113]. Values of $k_{ten}^{st} = 32.55 \text{ kN/m}$ and $\Delta l_c = 0.57 \text{ mm}$ [113] have been used throughout this study.

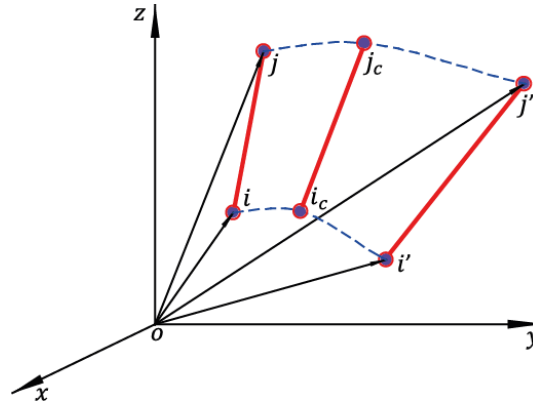


Figure 4.3: Motion of an arbitrary stitch element.

Hence, the axial force for each stitch element (i.e. F_{ij}^{st}) can be calculated as

$$F_{ij}^{st} = k^{st} \cdot \Delta l_{ij} \quad (4.5)$$

The stitch force is updated in each time increment by invoking the above 1D user-defined stitch element.

An example of a stitched preform stack is shown in Figure 4.4 for a hemisphere geometry. The preform consists of four plies with dimensions $320 \text{ mm} \times 320 \text{ mm}$ and a thickness of 1 mm in a $[(0^\circ/90^\circ) / \pm 45^\circ]_s$ configuration. The hemisphere has a diameter of 100 mm , and the

formed height is 50 mm. Stitch bonds have been applied at every node along the two diagonals from corner to corner.

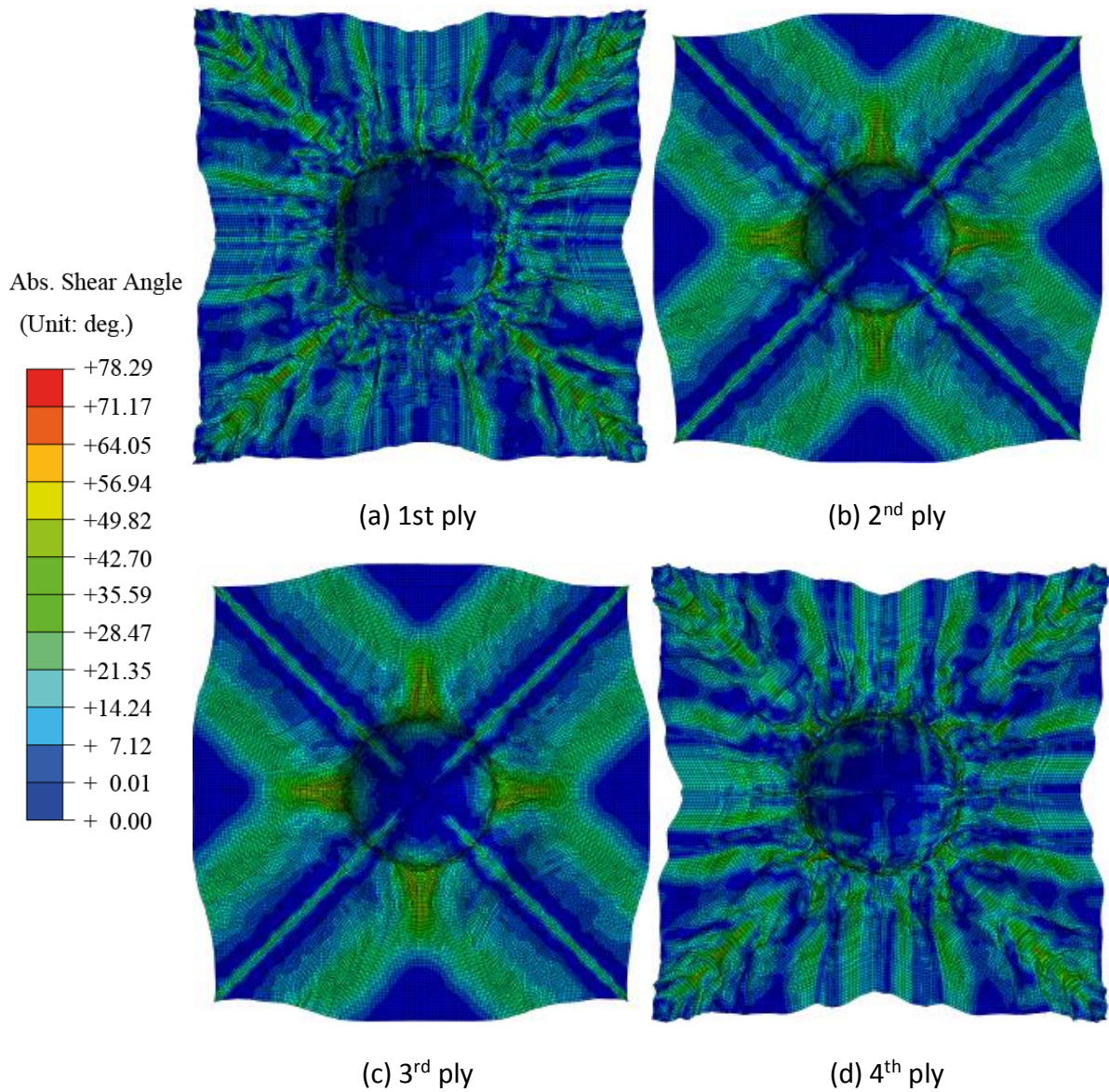


Figure 4.4: Results of forming simulation for a $[(0^\circ/90^\circ) / \pm 45^\circ]_s$ fabric stack with stitching from corner to corner along the two diagonals (maximum shear angle 78.29° in 4th ply at the bottom-left corner of the hemisphere).

The numerically calculated maximum shear angle for this case (78.29°) is significantly high, resulting in visible wrinkles on the formed hemispherical surface. This maximum shear angle exceeds the shear locking angle of the fabric (approximately 45° [36]). Unrealistically high values like this can occur as a consequence of the polynomial fit to the high shear modulus region of the experimental shear data [89]. Ideally, the shear angle cannot be larger than the shear locking angle and the shear stiffness has to converge to infinity due to the interference between yarns. But it can only converge to a finite value rather than infinity if a polynomial is

employed to fit the curve. Therefore, the shear modulus expressed in a polynomial is not stiff enough at high angles and extremely high shear angle may occur in the simulation inducing unrealistic deformation. The stitch paths go through the centre of the highest sheared regions in the $0^\circ/90^\circ$ plies, which results in the shear deformation being distributed more globally than in the unstitched case, since the mobility of the fibres along the diagonals is restricted. This can be seen clearly in Figure 4.5, which shows the local shear angles plotted along a diagonal path from the centre of the hemisphere to the top-right hand corner. Large deformations in the $\pm 45^\circ$ plies occur due to them being directly coupled to the $0^\circ/90^\circ$ plies. These results highlight the consequence of choosing a poor stitch pattern and emphasise the importance of developing a stitch optimisation routine to reduce excessive shear deformation.

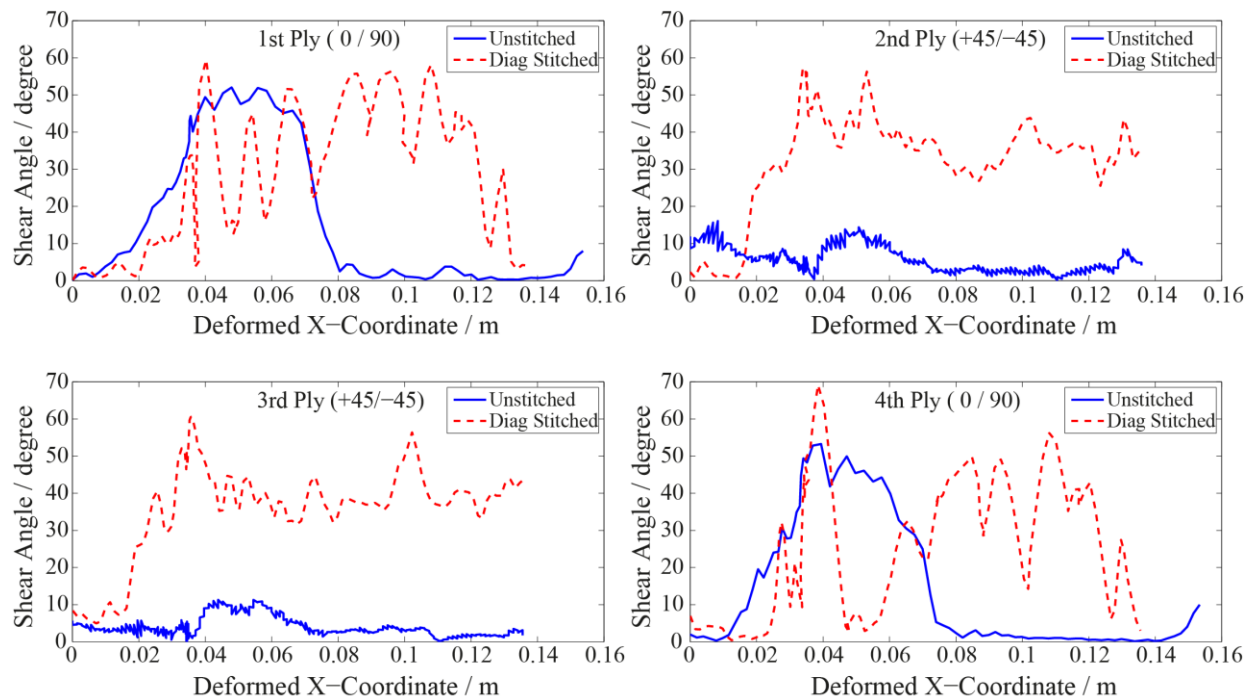


Figure 4.5: Local shear angles plotted along a diagonal path from the centre of the hemisphere to the top-right corner (see Figure 4.4).

4.3 Methodology of stitching optimisation

The stitching optimisation is implemented using Matlab, as shown in Figure 4.6. For each loop or “generation” in the GA, a group of stitching patterns called “individuals” is generated, and Abaqus/Explicit input files are produced. Abaqus/Explicit simulations are employed to determine the shear angle distribution for each individual, which is then returned to Matlab. For the returned shear angle data, the corresponding fitness value is determined individually to check for convergence. This loop repeats until the optimum is achieved.

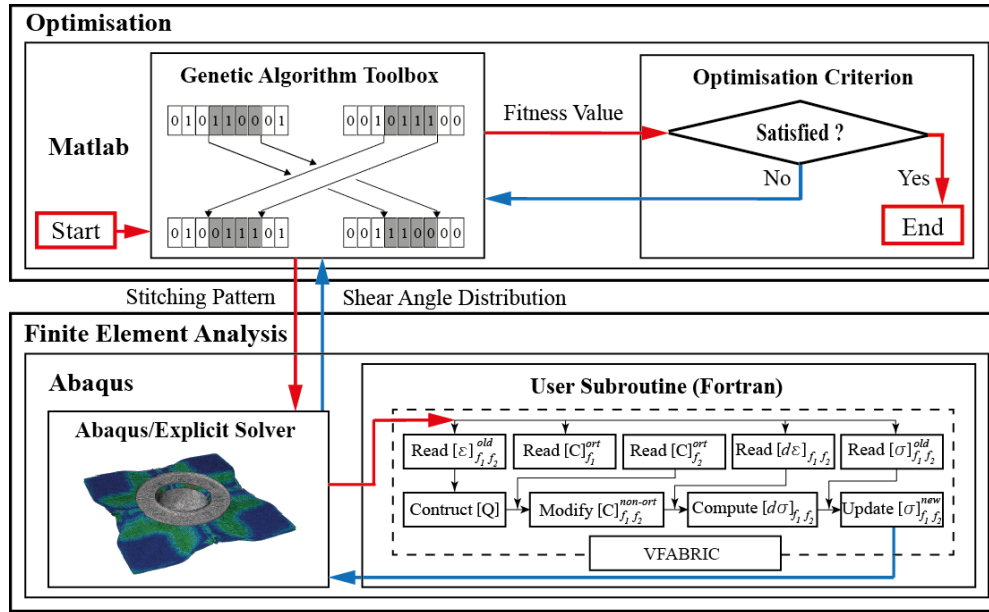


Figure 4.6: Implementation of localised stitching optimisation.

4.3.1 Implementation of genetic algorithm

A binary encoding method is applied to formulate each individual stitching pattern for the optimisation algorithm. Each stitching pattern represents a binomial-status series, which can be described numerically by the encoding scheme in Figure 4.7. Each bit in the binary code represents one potential stitching position and its value corresponds to a “stitched” or “unstitched” status. By using this encoding scheme, the physical problem can be converted into a mathematical problem to perform a series of GA manipulations to heuristically search for the optimum stitch pattern.

The stitching optimisation problem can be written as

$$\text{Minimise: } f\{p_1, p_2, \dots, p_n; \gamma_{12}(x, y, z)\} \quad (4.6)$$

$$\text{Subject to: } p_i = \begin{cases} 1, & \text{stitched} \\ 0, & \text{unstitched} \end{cases} \quad (i = 1, 2, \dots, n) \quad (4.7)$$

$$\gamma_{12}(x, y, z) \in [0^\circ, 90^\circ] \quad (4.8)$$

$$(x, y, z) \in \Omega_M \quad (4.9)$$

where, $f\{\cdot\}$ is the fitness function of the stitching optimisation in GA to describe the selection criterion, which is employed to assess the distribution of shear angles in the material field. p_i

($i = 1, 2, \dots, n$) is the i^{th} optimisation variable, which denotes the stitching status at the i^{th} potential stitching position. n is the total number of potential stitching positions.

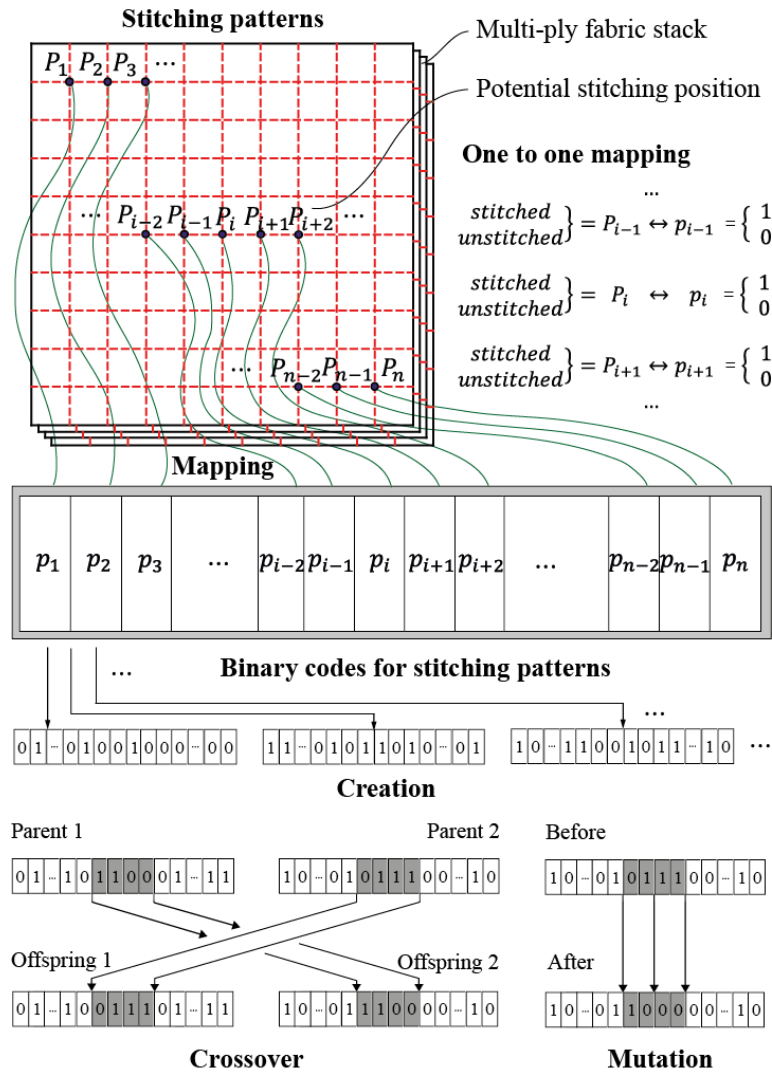


Figure 4.7: Binary encoding and manipulation scheme for stitching pattern.

4.3.2 Fitness function

The fitness function is used to assess how well each individual stitch pattern is adapted to the assessment criteria. Its value reflects the relative distance from the optimum solution, where a smaller value is preferential. During stitching optimisation, the aim is to optimise the shear angle distribution in the spatial material field. However, the shear angle is a field variable which it is too difficult to optimise directly. Hence, an appropriate fitness function is defined using a reduced mathematical expression, which is easier to manipulate numerically. Appropriate selection of the fitness function is important, as it dominates the convergence rate of optimisation and the accuracy of the optimum solution.

At the material level, characterisation of in-plane shear is assessed by measuring the non-linear mechanical response of the material during shear loading. A limit is often imposed on the level of deformation, in the form of a “locking angle” [19], which is the point at which tows are no longer able to rotate freely. The locking angle represents the maximum level of shear deformation that can be achieved before material wrinkling/buckling occurs, which is undesirable in a preformed reinforcement because of the influence on mechanical properties [36]. The objective is therefore to keep all local shear angles below the locking angle. Since the value of shear angle is limited by

$$|\gamma_{12}(x, y, z)| \in \left[0, \max_{(x,y,z) \in \Omega_M} \{|\gamma_{12}(x, y, z)|\}\right] \quad (4.10)$$

the optimisation objective can be reduced to minimise the maximum shear angle, referred to in this work as the maximum value criterion (MAXVC). The maximum can be derived from the finite element approximation for $|\gamma_{12}(x, y, z)|$. Thus,

$$f_{MAXVC}\{p_1, p_2, \dots, p_n; \gamma_{12}(x, y, z)\} = \max_{(x,y,z) \in \Omega_M} \{|\gamma_{12}(x, y, z)|\} \approx \max_{i=1,2,\dots,N} \{\gamma_i\} \quad (4.11)$$

where $f_{MAXVC}\{\cdot\}$ denotes the fitness function using MAXVC; Ω_M is the spatial material region; $\gamma_{12}(x, y, z)$ is the continuous shear angle distribution in the material region Ω_M ; N is the total number of material points; $|\cdot|$ is the absolute value of the variable; $\gamma_i = |\gamma_{12}(x_i, y_i, z_i)|$ is the absolute value of the shear angle at the i^{th} material point (x_i, y_i, z_i) . Since the stitching pattern determines the obtained shear angle distribution, the value of f_{MAXVC} is used for quantitative assessment of the fitness of the corresponding stitching pattern.

Although MAXVC is suitable for assessing the behaviour for most conditions, it can be somewhat conservative for achieving fast convergence. Additionally, the maximum shear angle only represents an upper bound and may not be representative of the overall distribution, resulting in an unfavourable stitch placement decision. For example, it may not be sensible to use this criterion when only a small number of elements exhibit extremely large shear angles, as these may be classed as outliers, and consequently the global shear angle distribution will be unaffected by the optimisation procedure [136]. Hence, a more global criterion is employed to summarise the shear angle data and a corresponding statistical criterion is proposed to assess the fitness of the stitching pattern. Since Extreme Value Theory

suggests that the Weibull distribution is suitable for modelling mechanical failure phenomena [137, 138], a two-parameter Weibull distribution is analogously employed here to characterise the stochastic behaviour of the shear angle distribution. The cumulative distribution function (CDF), $F(\gamma; \eta, \beta)$, is expressed as

$$F(\gamma; \eta, \beta) = 1 - e^{-\left(\frac{\gamma}{\eta}\right)^\beta}, \gamma \in [0, +\infty) \quad (4.12)$$

where η ($\eta > 0$) is the scale parameter and β ($\beta > 0$) is the shape parameter for the two-parameter Weibull distribution. Thus, their corresponding estimators, $\hat{\eta}$ and $\hat{\beta}$, can be determined by combining the following two equations obtained from the maximum likelihood method

$$\hat{\eta} = \left[\left(\frac{1}{N} \right) \sum_{i=1}^N \gamma_i^{\hat{\beta}} \right]^{\frac{1}{\hat{\beta}}} \quad (4.13)$$

$$\hat{\beta} = \frac{N}{\frac{1}{\hat{\beta}} \cdot \sum_{i=1}^N \left(\gamma_i^{\hat{\beta}} \cdot \ln \gamma_i \right) - \sum_{i=1}^N (\ln \gamma_i)} \quad (4.14)$$

where $\hat{\eta} > 0$ and $\hat{\beta} > 0$. The unknown parameters $\hat{\eta}$ and $\hat{\beta}$ are calculated by solving the above two equations numerically; based on $\gamma_1, \gamma_2, \dots, \gamma_N$, which are obtained from finite element analysis. If $\gamma_{1-\alpha}$ is the upper α quantile of the distribution, i.e. the probability to find a shear angle with a value greater than $\gamma_{1-\alpha}$ is α , then

$$F(\gamma_{1-\alpha}) = 1 - \alpha = 1 - e^{-\left(\frac{\gamma_{1-\alpha}}{\hat{\eta}}\right)^{\hat{\beta}}} \quad (4.15)$$

is the probability to find a shear angle smaller than $\gamma_{1-\alpha}$. When α has a small enough value (typically 0.05), and the distribution parameters have been estimated, the equation can be solved for $\gamma_{1-\alpha}$. This is considered to be the extreme value (i.e. the maximum shear angle) with a probability of $(1 - \alpha)$ [137].

Instead of using the maximum shear angle from all material points, the statistical extreme value is employed to represent the fitness score for each stitching pattern. The lower this value becomes, the better the stitching pattern. Hence, the fitness function using the Weibull distribution quantile criterion (WBLQC) can be written as

$$f_{\text{WBLQC}}\{p_1, p_2, \dots, p_n; \gamma_{12}(x, y, z)\} = \gamma_{1-\alpha} = \hat{\eta} \cdot \left(\ln \frac{1}{1 - \alpha} \right)^{\frac{1}{\hat{\beta}}} \quad (4.16)$$

4.3.3 Adaptive programming strategy

Due to the non-analytical relation between stitching pattern and shear angle distribution, shear angle data must be collected for every individual stitching pattern from FE analyses. Although the run time for each simulation has been reduced by mass scaling, processing a large number of FE jobs in series (Figure 4.8(a)) is not an efficient way to conduct the optimisation, because of considerable idling time of computational resources. It is also impractical to utilise a parallel algorithm to submit the jobs simultaneously (Figure 4.8(b)), since only a limited number of jobs can be submitted each time, due to typical constraints on the number of software licenses available and computing hardware. Thus, an adaptive hybrid algorithm has been developed for running the stitch optimisation as shown in Figure 4.8(c). It can manage and balance the computational resources and task allocation effectively, according to real-time feedback information. The model INP file for each case is directly modified by Matlab and then submitted to Abaqus solver. When FE jobs are running, the revision of INP files continues and they are managed by an adaptive job submission rather than being directly pre-allocated to a specific CPU. This can effectively and efficiently make use of all the computational resources, and it is also able to avoid unnecessary delay induced by the difference of CPU time between parallel submitted FE jobs.

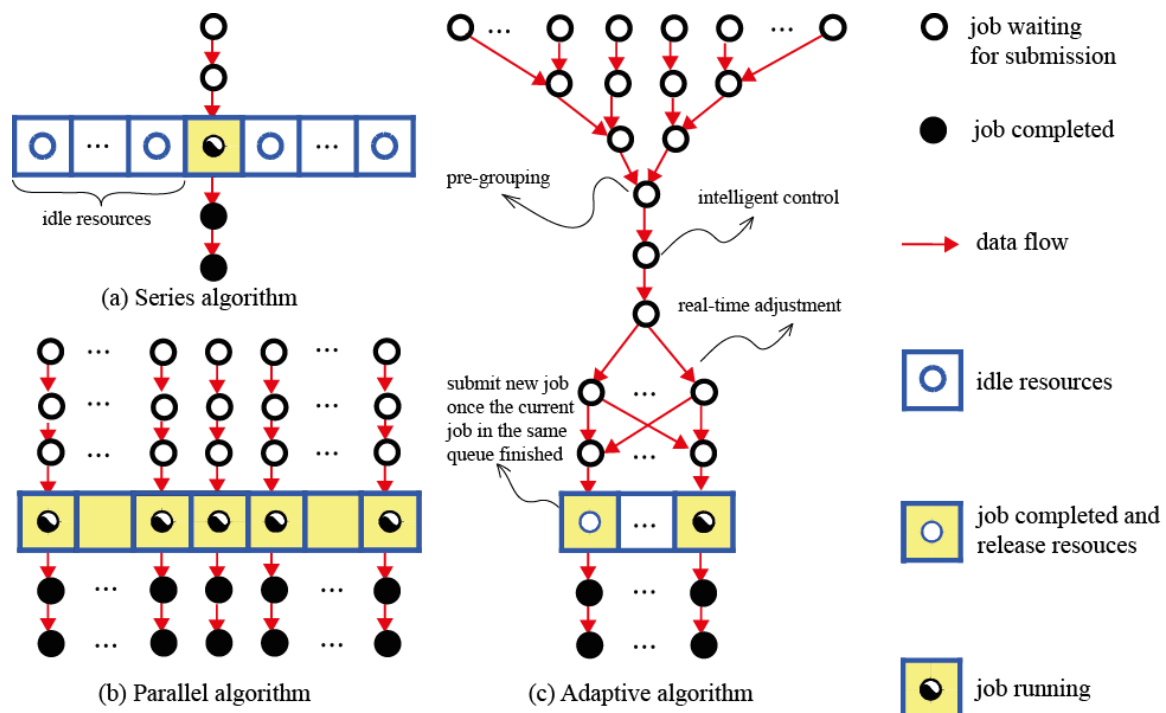


Figure 4.8: Processing strategy for stitching optimisation.

4.4 Results and discussion of inter-ply stitching optimisation

Stitching patterns were optimised for a hemisphere model with a diameter of 100 mm. The model consisted of a matched punch and die, with a planar blank holder applying normal pressure to the material to maintain tension in the tows throughout the forming process. The blank consisted of 4 plies of the same balanced woven fabric with the same properties as in Section 3.3, using a symmetric layup $[(0^\circ/90^\circ) / \pm 45^\circ]_s$. The plies were numbered in order from bottom to top as 1st ply to 4th ply. Each ply was 320 mm×320 mm×1 mm in size and discretised into 4096 square membrane elements (Abaqus/Explicit element type M3D4R). All parts of the tooling were considered to be rigid bodies. A penalty contact algorithm was used to define the behaviour at all interfaces. An isotropic Coulomb friction model was adopted for both the tooling-material and material-material contacts with a constant coefficient of 0.2. Displacement boundary conditions were applied to the punch and a force of 100 N was applied to the blank holder to control blank slippage.

The mechanical properties of stitches defined in Section 4.2.1 were assigned to every stitch element in each finite element model where applicable. In total, 81 potential positions, spaced at 40 mm intervals on a regular square grid, were considered as stitching variables. The population size was 100 in each generation and the tolerance for the fitness function was 0.05°. The crossover and mutation coefficients were 0.80 and 0.20 respectively, which specified the probabilities of applying the manipulations of crossover and mutation respectively to each gene in GA and these operations were conducted by Matlab GA toolbox.

To compare the natural selection criteria, both MAXVC and WBLQC were employed to execute the optimisation. Several typical generations have been selected to illustrate the optimisation evolutions using different fitness functions in Figure 4.9 and Figure 4.10. Each generation represents a summary of 100 individual stitch patterns, where the dots represent the locations for clusters of stitches, rather than individual stitches. The choice of the individuals in the initial population may influence the convergence speed, but not the final stitch pattern. The initial population of 100 patterns for the zeroth generation was generated randomly, which then evolve into subsequent generations according to the genetic algorithm. The number of individuals is chosen to be greater than the number of variables (81) to ensure a diverse population. The low tolerance for the fitness function ensures that the optimisation procedure is not terminated prior to achieving the optimum.

The frequencies for occurrence of each of the 81 stitch positions were equally represented in the zeroth generations in Figure 4.9 and Figure 4.10, as indicated by a relatively uniform red level for each dot. The shade of red changes as the stitch patterns evolve for each subsequent generation, where a darker red (tending towards black) represents a higher frequency for that stitch position and a lighter shade of red (tending towards white) represents a lower frequency. As the fitness function converges, all dots appear black, which indicates that all 100 stitch patterns for that generation are the same.

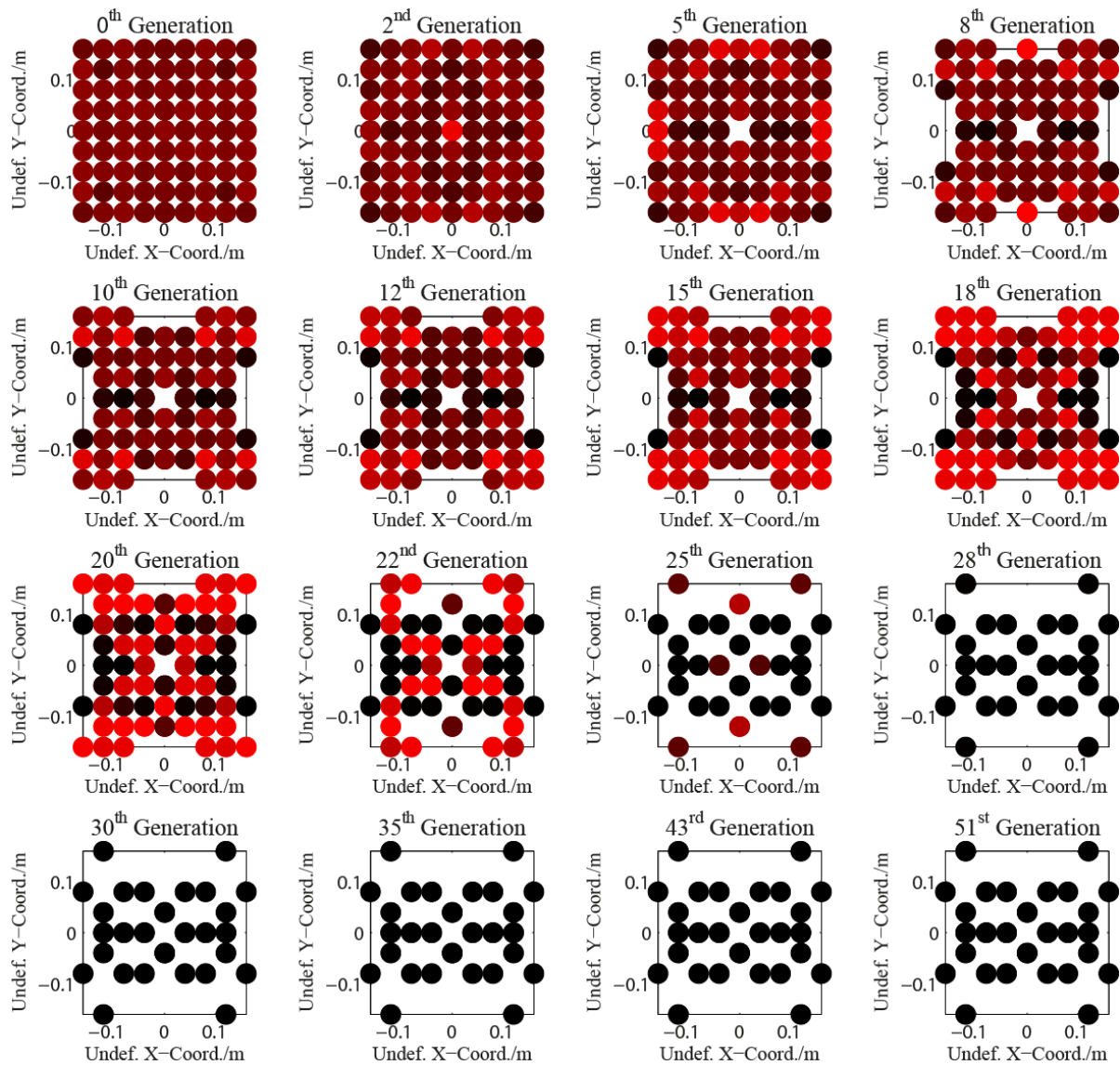


Figure 4.9: Optimisation evolution of stitching pattern based on MAXVC. Solid points represent stitching positions in the respective generation; red scale indicates the frequencies of occurrence within the respective generation.

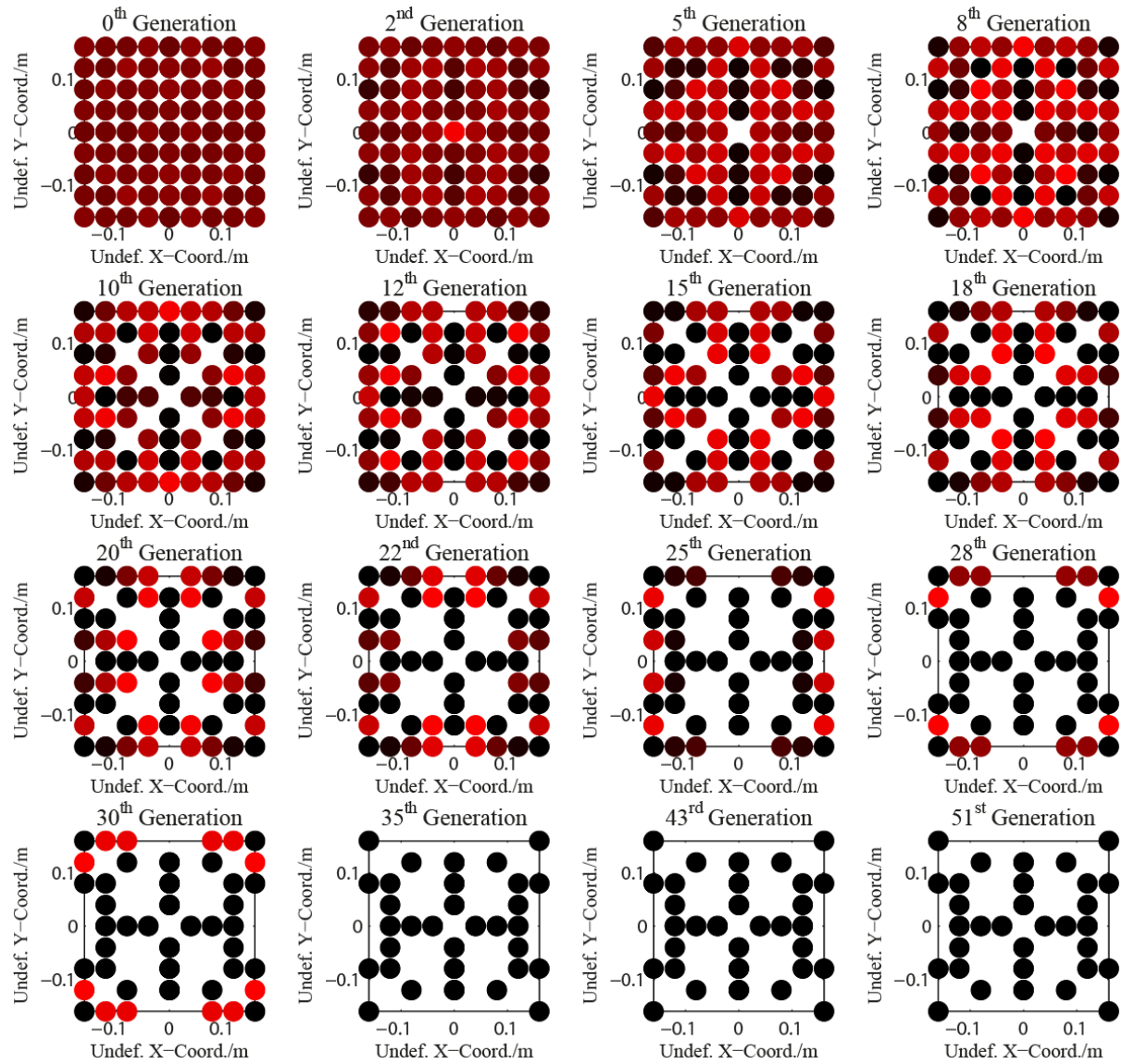


Figure 4.10: Optimisation evolution of stitching pattern based on WBLQC (Bottom). Solid points represent stitching positions in the respective generation; red scale indicates the frequencies of occurrence within the respective generation.

Figure 4.9 and Figure 4.10 indicates that: (1) both natural selection criteria converge to produce respective optimum solutions, even though their searching directions are different; (2) the final converged stitch positions are similar for both selection criteria. The basic patterns resemble a quadrilateral with a cross running through the centre and several additional stitches around the edges. However, their dimensions are different; (3) the convergence speed is faster for MAXVC (generation 28) than for WBLQC (generation 35). Whilst the shear angle distributions for the unstitched case are totally symmetrical, there are no symmetry conditions imposed during the optimisation process. Therefore the optimum stitch patterns are not always symmetrical, leading to asymmetric shear angle distributions.

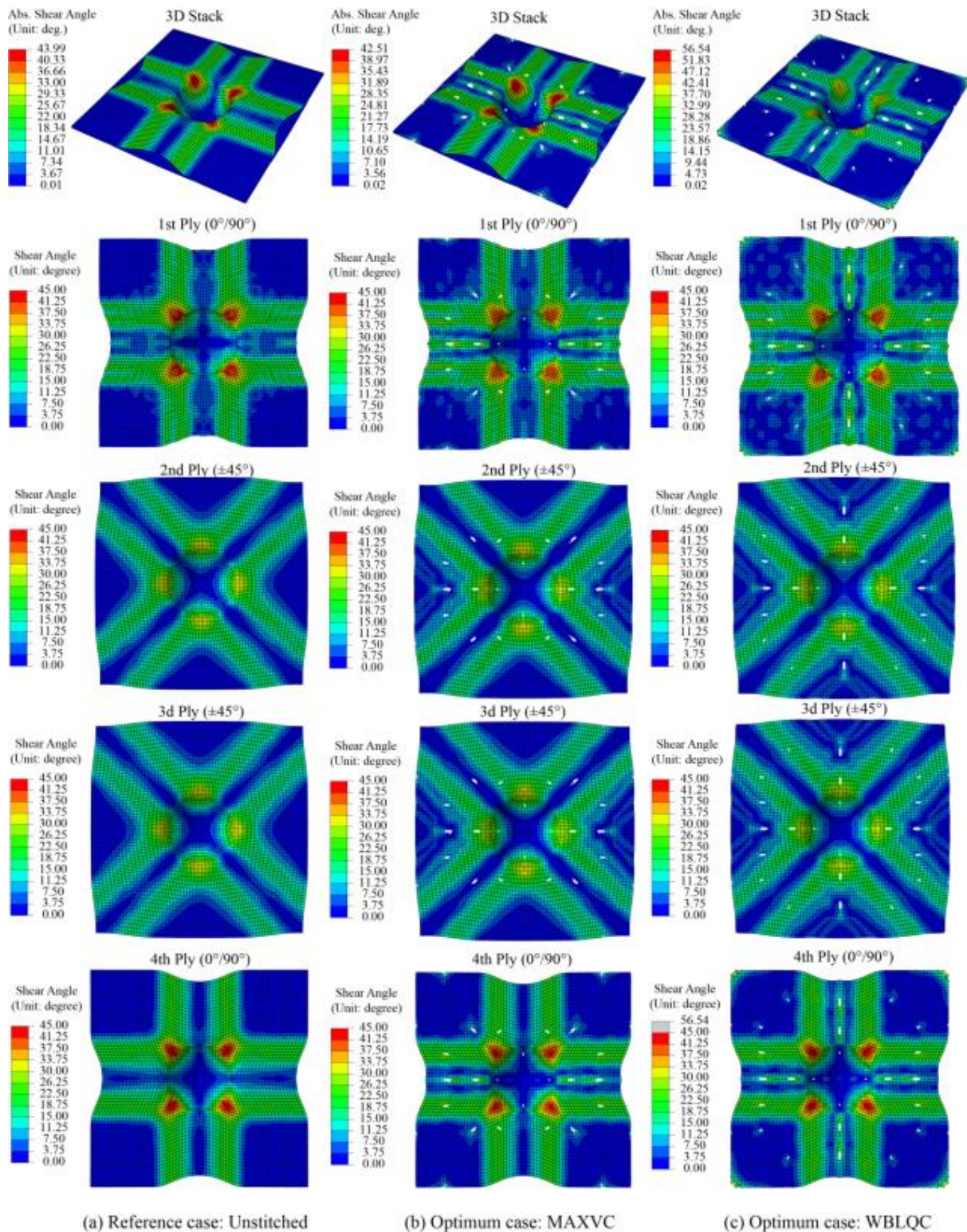


Figure 4.11: Shear angles and deformed configurations of preform assembly from MAXVC and WBLQC criteria compared against unstitched reference case; white points represent stitching positions; the maximum shear angles are 43.99° (unstitched), 42.51° (MAXVC) and 56.54° (WBLQC).

The unstitched case was taken as a reference case to evaluate the quality of the stitch optimisation. Figure 4.11 shows that the maximum shear angle of the optimum case using MAXVC (42.51°) is slightly smaller than for the unstitched case (43.99°). However, the

maximum shear angle from the WBLQC criteria (56.54°) is significantly higher than the maximum of the unstitched case. For this particular scenario, the shear angles of the 4 corner elements are extremely large and are far from the global average. Thus, they can be considered to be outliers. These severely sheared areas are small relative to the whole material field and are located at the perimeter of the blank away from the final formed surface. They will not influence the quality of the final component, but this outcome highlights the relevance of the statistical criterion. In addition, these distorted individual elements may be induced by numerical errors rather than realistic deformation so that Weibull distribution is employed to reduce the negative effect of outliers.

The global distribution of shear angles produced from the two criteria is almost identical as shown in Figure 4.11. Hence, both criteria appear to produce sensible solutions. Severely sheared regions (i.e. red) only occur in the $0^\circ/90^\circ$ plies (i.e. 1st and 4th plies), whilst the maximum shear angle for the $\pm 45^\circ$ plies (i.e. 2nd and 3rd plies) is smaller. This phenomenon is captured by both criteria.

The shear angle distributions have been plotted on the undeformed blank shape and normalised with respect to the unstitched configuration to make comparisons easier, as illustrated in Figure 4.12. The blue regions represent a reduction in shear angle compared with the unstitched case and red indicates an increase. For the $0^\circ/90^\circ$ plies (i.e. 1st and 4th plies), which were shown to have the highest sheared regions in Figure 4.11, the blue areas are larger and darker for the WBLQC case in Figure 4.12(b) than for the MAXVC case in Figure 4.12(a). Hence, the optimum stitch patterns that result from the WBLQC effectively homogenise the global shear angle distribution more than the MAXVC, as expected. Reduction in size and intensity of the blue regions is not so considerable for the $\pm 45^\circ$ plies (i.e. 2nd and 3rd plies) according to Figure 4.12.

There are also regions of increasing shear angle for both converged solutions, since load paths have been changed by placing localised stitches. These regions experience more deformation than in the unstitched case due to strain re-distribution through localised stitches, which flatten the shear profile in high deformation regions. The influence of these local increases depends on the affected area as well as its final absolute shear angle. If these increases occur on the formed surface of the final component then these effects can be considered to be negative. However, most of the darker red regions are concentrated around the edges of the

blank and are therefore not critical in this case. Figure 4.12 indicates that the increasing shear angle regions (red regions) do not reduce the overall quality of the preform, as the global shear angle is generally less than 30° , with only small discrete regions approaching 50° . Stitch patterns produced by WBLQC yield shear angle distributions closer to the unstitched benchmark solution and can provide better quality formed parts. However, the cost of using WBLQC is higher, taking more computational time to converge than MAXVC.

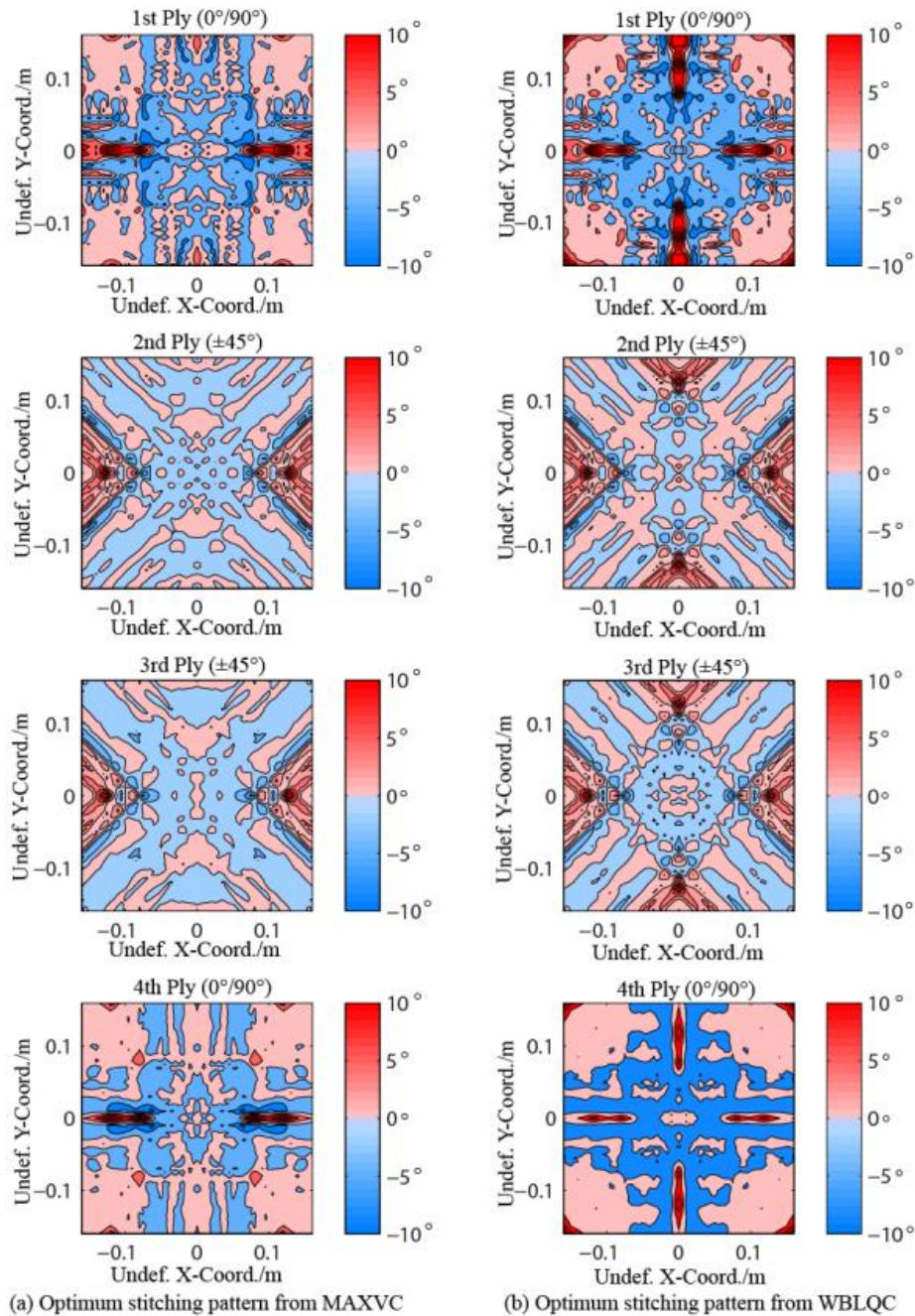


Figure 4.12: Shear angle distributions normalised with respect to the unstitched case, plotted on the undeformed blank shape; (a) using MAXVC; (b) using WBLQC; shear angle distributions are; blue regions indicate reduced shear angles and red indicates increased shear angles over the unstitched case.

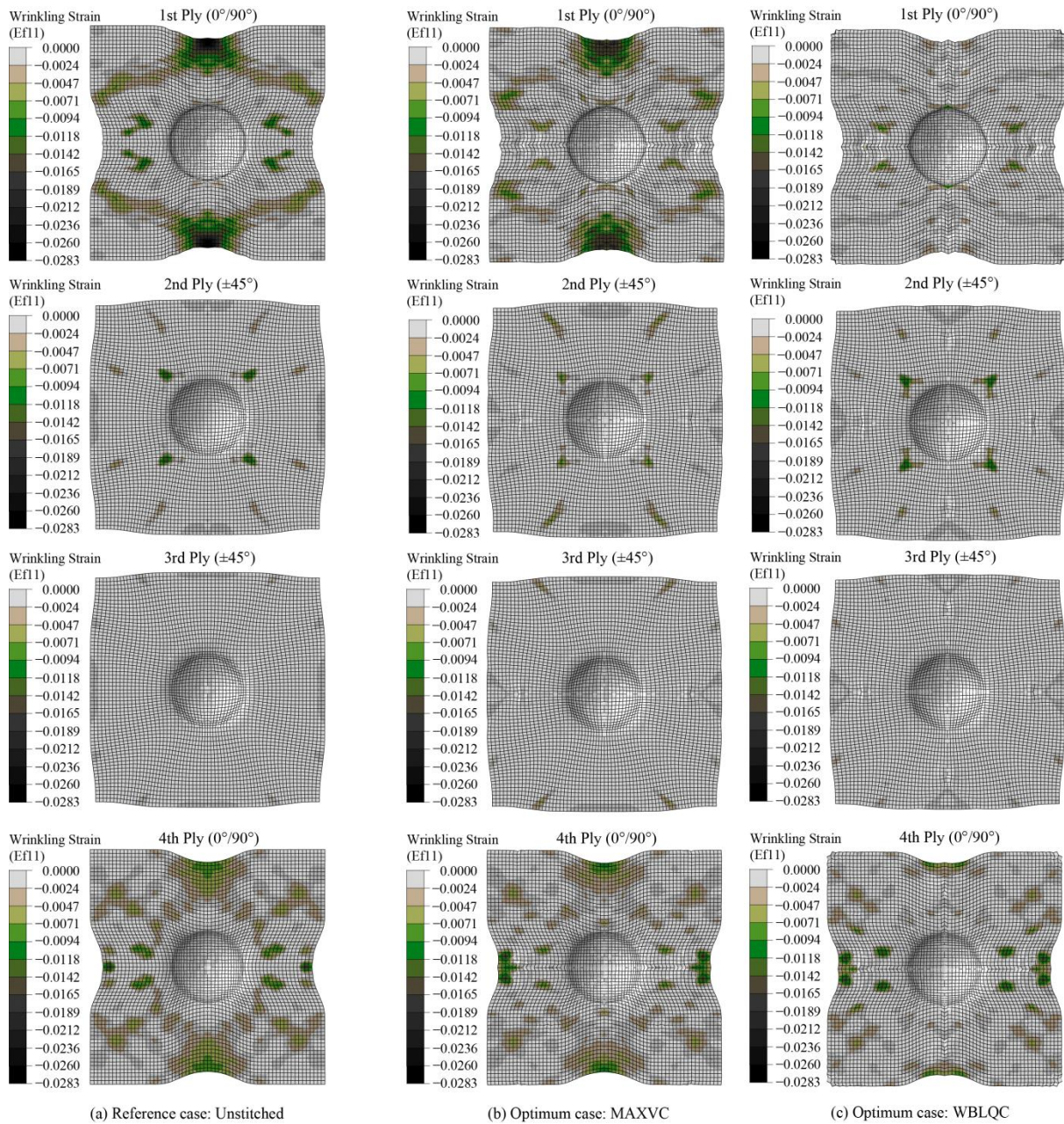


Figure 4.13: Wrinkling strain along 1st fibre orientation.

The optimisation procedure has successfully homogenised both the local and global shear angle distributions, using both criteria. However, it is important to avoid introducing additional defects when minimising the local shear angle. The compressive strains in the fibre direction (1-direction) have been plotted in Figure 4.13 to understand the likelihood of bundle wrinkling, as reported by Long et al. [139]. (Strain distributions in 2-direction are similar as shown in Figure 4.14). In general, there is a reduction in the magnitude of the compressive strains for the two optimised cases, with the WBLQC case indicating the lowest risk of bundle wrinkling. This provides further confidence in the optimisation results, but is only a qualitative

assessment that requires further experimental validation. The introduction of inter-ply stitches enable more interaction between plies. Since plies with different fibre orientations may slide along different directions, the wrinkling strain may be cancelled when applying inter-ply stitches.

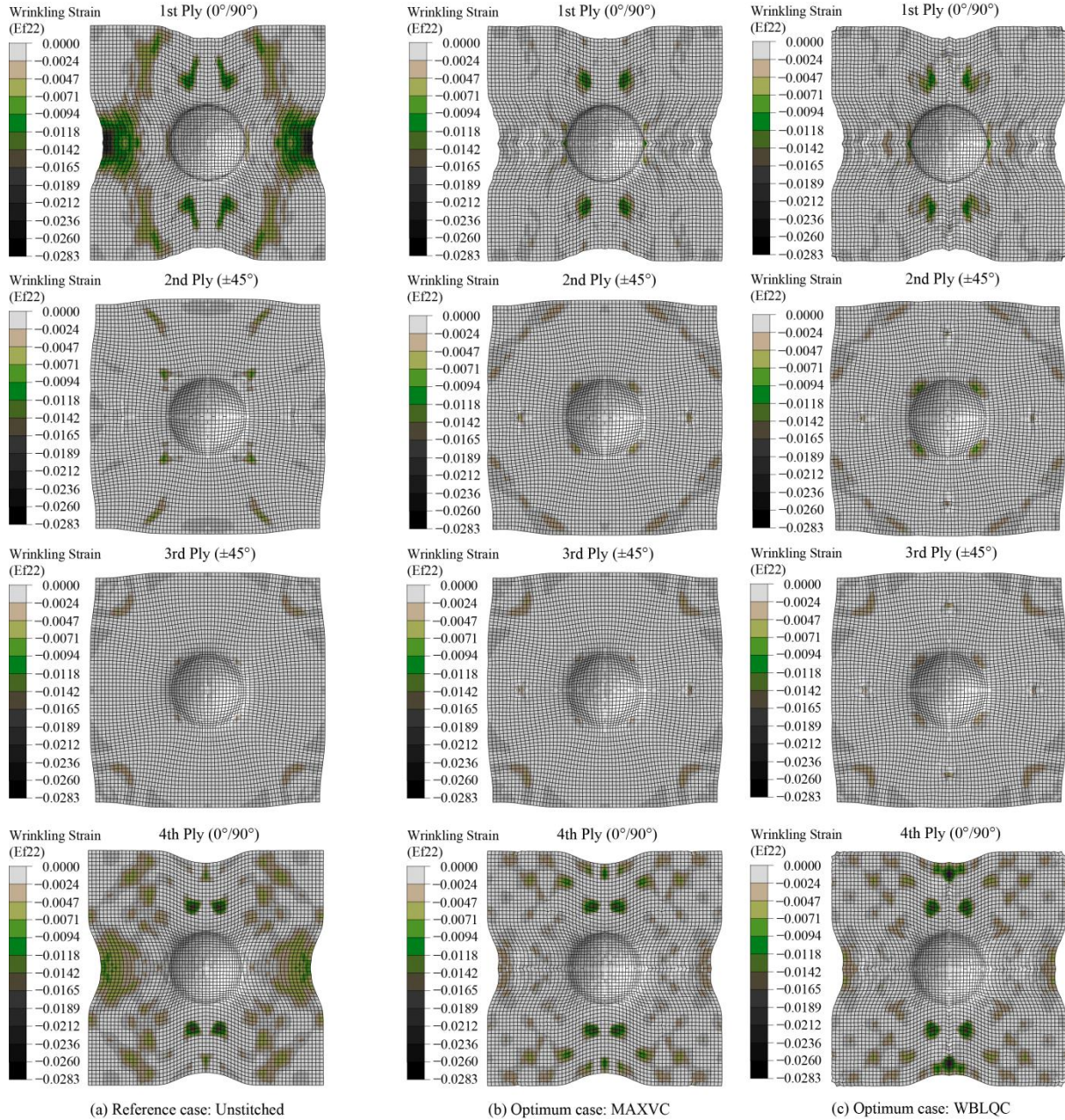


Figure 4.14: Wrinkling strain along 2nd fibre orientation.

4.5 Chapter summary

Assembly stitches have been modelled in an explicit FE model using user-defined 1D cable-spring elements. A simulation was performed for a balanced 4 ply preform with stitches applied in a diagonal configuration. Results indicated that the local maximum shear angle was

significantly higher than in the unstitched case, and local stitch-bonds influence the global shear angle distribution rather than having just a localised effect. It was concluded that placing stitch bonds is not an intuitive process and this highlighted the need for a stitch optimisation routine.

An optimisation methodology has been developed for placing local inter-ply stitches on multi-ply preforms, by coupling finite element analyses with a genetic algorithm. A binary encoding scheme has been employed and two different criteria have been proposed to assess the quality of the shear angle distribution for the optimised solution; the maximum value criterion (MAXVC) and the Weibull distribution quantile criterion (WBLQC). An adaptive hybrid processing strategy was designed to accelerate the optimisation by managing computational resources and task allocation efficiently.

Both MAXVC and WBLQC were found to be suitable criteria for local stitch optimisation, producing acceptable solutions towards the global optimum. The convergence speed is higher when adopting MAXVC compared with WBLQC, but WBLQC is more effective for finding a solution closer to the global optimum by eliminating the influence of outliers. The choice of criterion is therefore a compromise between optimisation quality and computational cost.

The shear angle distribution using the optimum stitching pattern has been homogenised rather than concentrating locally to induce localised forming defects, which indicates an effective improvement on formability. It can be concluded that using optimised patterns of through-thickness stitches can improve the formability of a multi-ply preform compared with an unstitched benchmark. Load paths are changed globally due to strain re-distribution through the localised stitches, which results in a more uniform shear angle distribution.

Chapter 5 Material Draw-In and Optimisation

5.1 Introduction

There are two scenarios to control material draw-in during fabric forming, as shown in Figure 5.1: The fabric is either constrained by a segmented blank holder or by spring-loaded clamps. Both methods generate in-plane tensile stresses in the fabric to minimise wrinkling.

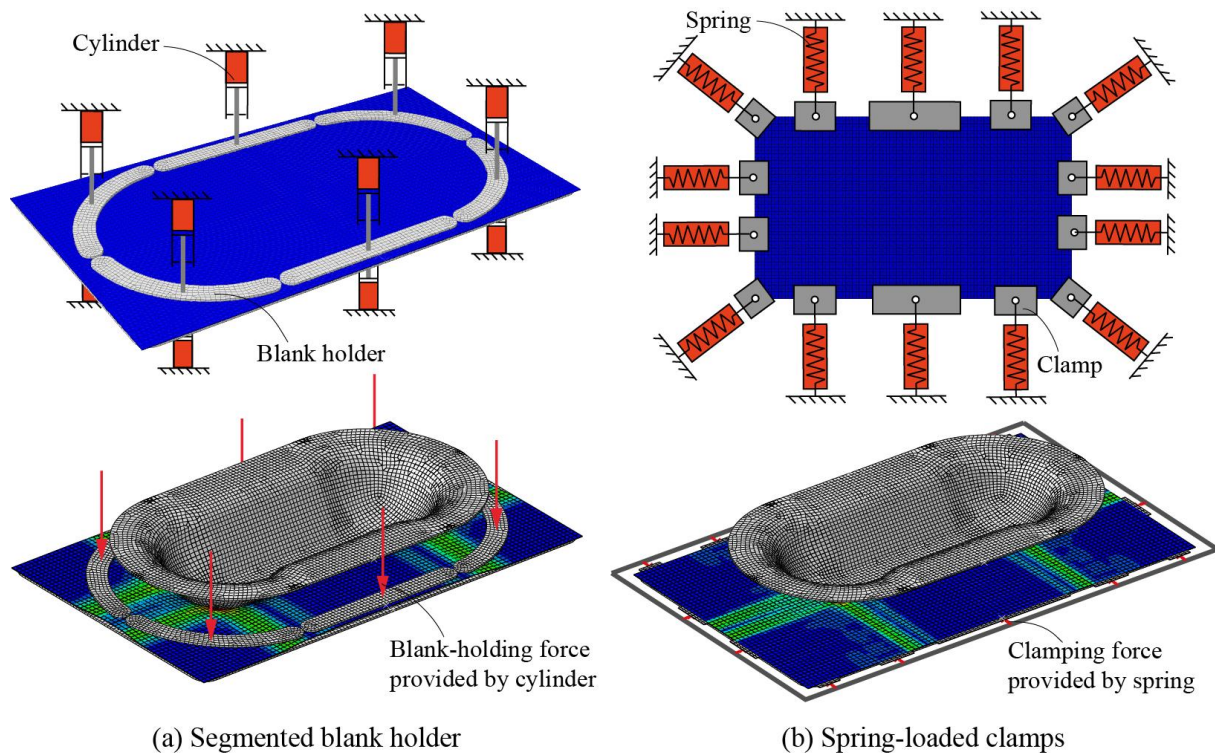


Figure 5.1: Two scenarios to material draw-in during fabric forming. (a) Segmented blank holder; (b) spring-loaded clamps.

This chapter presents a Genetic Algorithm (GA) coupled with the non-linear explicit FE model developed in Chapter 3 to optimise the draw-in of the blank using spring-loaded clamps during composite press-forming. Spring-loaded clamps are used to directly provide in-plane tension to the fabric (see Figure 5.1(b)), rather than applying a normal pressure (resulting in in-plane friction) through a blank holder (see Figure 5.1(a)). This technique has been discussed in the literature for thermoplastic forming [117, 140] and is currently used in the automotive industry in preforming of non-crimp fabric. It enables the blank to be heated more easily if the fabric is bindered or pre-impregnated, as the clamps are situated outside of the heated region of the press. This arrangement also offers more flexibility in terms of controlling

material draw-in, as the spring-loading for each clamp can be controlled independently, but leads to increased complexity. The optimisation procedure seeks to determine the optimum location and size of each clamp and the stiffness of each spring controlling the local draw-in. The objective is to minimise the global in-plane shear angle of the fabric.

5.2 Modelling of fabric preforming using in-plane constraints

The non-orthogonal constitutive model developed in Chapter 3 is employed in this optimisation study to describe the fabric behaviour during preforming. Comparisons against experimental data in Section 3.3 indicated high levels of accuracy for the simulation results, which was not significantly compromised by time-scaling or mass-scaling employed to reduce CPU time.

5.2.1 Validation for forming model using in-plane constraints

Numerical tests have been performed to validate the material model against experimental data for the case where in-plane constraints are used to provide tension in the fabric to control draw-in [117, 141], rather than out-of-plane blank-holders. Material parameters were consistent with the values in the literature [36, 40, 47, 132] for a balanced plain weave glass fibre/polypropylene commingled fabric, as previously presented in Section 3.3.

Validation was conducted using the same geometry and material properties as in the literature [117, 141]. The blank was a single $0^\circ/90^\circ$ ply at a thickness of 0.4 mm. The optimised blank shape described by Harrison et al. [117] was employed, and the ply was modelled using quadrilateral membrane elements (M3D4R). Tooling was considered to be rigid; Coulomb friction was adopted for both tooling-material and material-material contacts, with a coefficient of 0.2; displacement boundary conditions were applied to the punch, whilst in-plane spring elements were used to connect the edge of the blank to a rigid frame, in order to control blank slippage. The stiffness of the elastic 1D spring elements was 0.20 N/mm on the short edges and 0.27 N/mm on the long edges of the rectangular frame [117]. The clamping tabs were modelled as massless rigid bodies.

A comparison of the shear angle distributions is presented in Figure 5.2. Qualitatively, the outline shape of the final formed part from the simulation is in very close agreement with experimental data [117]. A quantitative analysis was performed by comparing the local shear angle at 20 discrete locations (Table 5.1). Two experimental repeats were performed [117],

and the measurements from each of the four quadrants were averaged for each repeat. Figure 5.2 indicates that the predicted shear angles from the numerical solution fall within the range of the experimental values, with deviations of generally less than 2° according to Table 5.1.

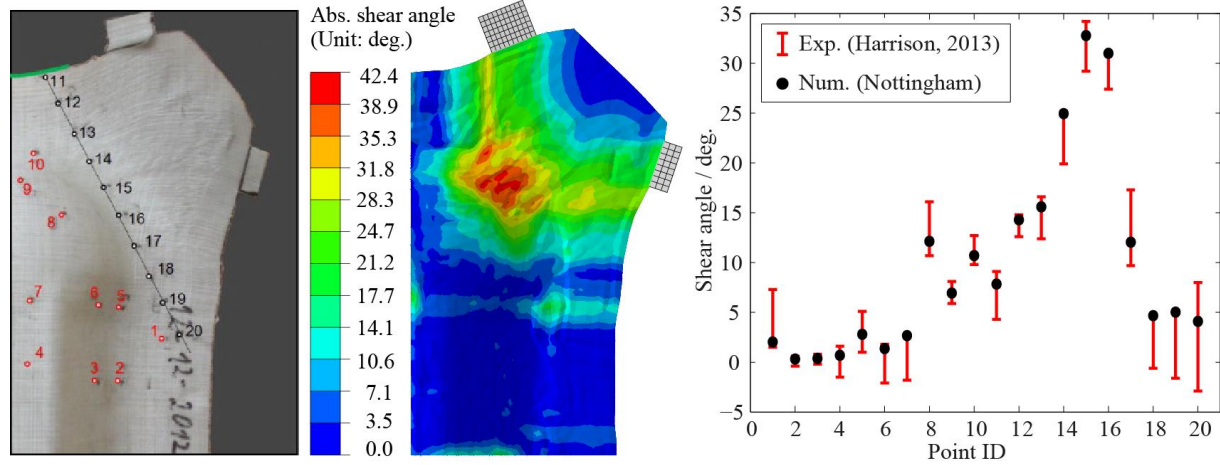


Figure 5.2: Comparison of fabric forming model using in-plane constraints against experimental results from literature [14]; fibre orientation is $0^\circ/90^\circ$.

Table 5.1: Comparison of shear angle data from Abaqus/Explicit VFABRIC model against two sets of experimental results from literature [117].

ID	Coord. (mm)		Shear angle (deg.)			ID	Coord. (mm)		Shear angle (deg.)		
	x	y	Exp. (case 1)	Exp. (case 2)	Num.		x	y	Exp. (case 1)	Exp.(case 2)	Num.
1	85	65	4.4 ± 2.9	3.3 ± 0.8	2.0	11	17.3	202.7	7.6 ± 1.5	6.2 ± 1.9	7.8
2	60	40	0.1 ± 0.5	0.1 ± 0.4	0.3	12	26	188	14.1 ± 0.7	13.7 ± 1.1	14.3
3	45	40	0.3 ± 0.3	0.3 ± 0.5	0.4	13	34.7	171.8	14.5 ± 2.1	15.2 ± 0.7	15.6
4	10	40	-0.4 ± 1.1	0.5 ± 1.1	0.7	14	44.6	155.9	22.3 ± 2.4	23.3 ± 1.9	25.0
5	60	80	3.7 ± 1.4	3.0 ± 2.0	2.8	15	52	142.1	31.5 ± 2.3	32.1 ± 2.1	32.8
6	45	80	0.5 ± 1.3	-0.5 ± 1.6	1.4	16	60	127.6	29.2 ± 1.8	29.1 ± 1.3	31.0
7	10	80	1.4 ± 1.4	-0.9 ± 0.9	2.7	17	68.9	112.6	15.8 ± 1.5	12.7 ± 3.0	12.1
8	25	120	11.9 ± 1.2	14.0 ± 2.1	12.1	18	77.1	97.2	4.0 ± 0.6	2.1 ± 2.7	4.7
9	5	140	7.0 ± 1.1	6.9 ± 0.4	7.0	19	84.9	83.4	4.1 ± 1.1	1.3 ± 2.9	5.0
10	15	160	10.4 ± 0.6	11.8 ± 0.9	10.7	20	94.4	67.4	5.5 ± 2.5	1.0 ± 3.9	4.1

5.3 Methodology of in-plane constraint optimisation

5.3.1 General strategy

The initial blank size for the double-dome forming study presented in this chapter is 470 mm \times 270 mm with a thickness of 0.4 mm, and the ply is discretised into 5076 square membrane elements (M3D4R). The initial fibre orientations in the blank are at $0^\circ/90^\circ$.

Springs are arranged around the perimeter of the preform to control material draw-in, providing in-plane constraints during draping. The optimum design of this system is dependent on the geometrical arrangement (number, position and size) of the springs and their mechanical properties (stiffness). The optimisation procedure is split into two stages as shown in Figure 5.3: (a) Step I: Clamping arrangement optimisation, (b) Step II: Spring stiffness optimisation. The first step determines sensible clamping positions to improve formability, by reducing the maximum global shear angle in the model. However, compromises have to be made as it is not practical to constrain every position. The second step determines optimum spring stiffnesses for the derived spring arrangement, therefore the final solution may not be the global optimum, but near-optimal.

This multi-stage approach makes the procedure independent of specific geometrical parameters, thus providing the flexibility for application to a variety of test geometries. Simultaneous optimisation could potentially be more cost-effective computationally and produce a more efficient solution, but only if a suitable mathematical description can be derived. However, this would require a specific new formulation of the optimisation problem for each forming task and would not enable routine application of the method.

5.3.2 Step I: Clamping arrangement optimisation

Each node around the perimeter of the blank is initially constrained by an individual spring element with the same initial stiffness (see Figure 5.3(a)). The other end of the spring is fixed to a fully constrained rigid frame. The force constraining movement of the blank is always oriented along the spring element axis, extending the spring as the material draws into the tool while forming. The status of each node (i.e. constrained or unconstrained) is determined by the optimisation algorithm. When it is unconstrained, the spring element is removed.

The clamping arrangement optimisation is implemented using Matlab, as shown in Figure 5.4. For each loop or “generation” in the GA, a group of constraint patterns called “individuals” is generated and Abaqus/Explicit input files are produced by modifying the sets definition of constrained nodes. The shear angle distribution in the deformed blank for each individual is determined from Abaqus/Explicit analyses and then returned to Matlab. A Matlab function has been developed to read the FE result files and then analyse the result data according to

the objective function. The corresponding fitness value is determined from this data to check for convergence. This loop repeats until the optimum is achieved.

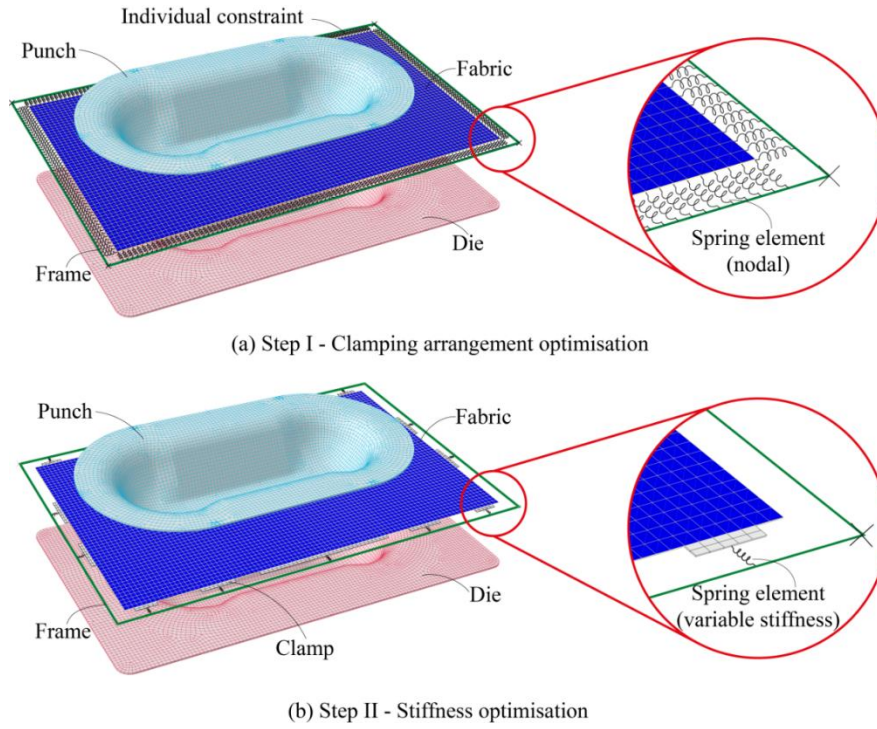


Figure 5.3: Finite element models for two-step in-plane constraint optimisation.

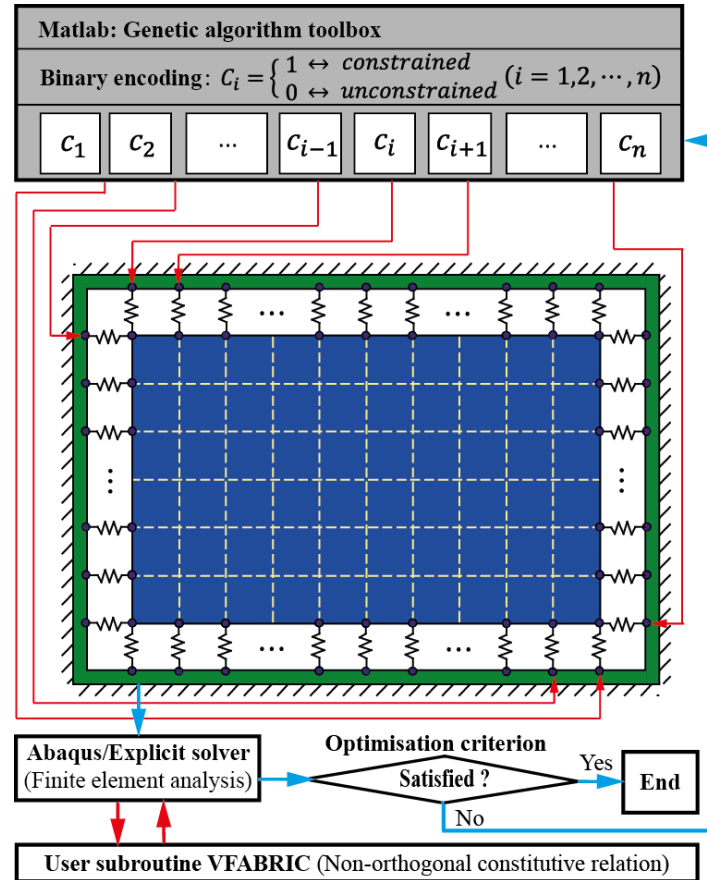


Figure 5.4: Implementation of Step I – Clamping arrangement optimisation.

A binary encoding method is applied to formulate each individual in-plane constraining pattern for the optimisation algorithm. Each pattern represents a binomial-status series, which can be described numerically by the encoding scheme in Figure 5.4. Each bit in the binary code represents one potential constraint position and its value corresponds to an “unconstrained” or “constrained” status (0 or 1). By using this encoding scheme, the physical problem can be converted into a mathematical problem to perform a series of GA manipulations to heuristically search for the optimum constraining pattern.

This geometry optimisation problem can be written as

$$\text{Minimise: } f\{c_1, c_2, \dots, c_n; \gamma_{12}(x, y, z)\} \quad (5.1)$$

$$\text{Subject to: } c_i = \begin{cases} 1, & \text{constrained} \\ 0, & \text{unconstrained} \end{cases} \quad (i = 1, 2, \dots, n) \quad (5.2)$$

$$\gamma_{12}(x, y, z) \in [0^\circ, 90^\circ] \quad (5.3)$$

$$(x, y, z) \in \Omega_M \quad (5.4)$$

where $f\{\cdot\}$ is the GA fitness function to describe the selection criterion of the constraining pattern, which is employed to assess the distribution of shear angles in the material field. The variable c_i ($i = 1, 2, \dots, n$) is the i^{th} optimisation variable, which denotes the constrained status at the i^{th} potential position. n is the total number of potential positions, i.e. the number of nodes on the blank perimeter.

The fitness function is used to assess how well each individual constraining pattern has adapted to the assessment criteria. Its value reflects the relative distance from the optimum solution, where a smaller value is preferred. A maximum value criterion (MAXVC) has been adopted here due to faster convergence compared with the Weibull distribution quantile criterion (WBLQC) previously used in Chapter 4, whilst maintaining acceptable accuracy. The objective is therefore to keep all local shear angles below the locking angle, by minimising the maximum shear angle. The maximum can be derived from the finite element approximation for $|\gamma_{12}(x, y, z)|$. Thus,

$$f_{MAXVC}\{c_1, c_2, \dots, c_n; \gamma_{12}(x, y, z)\} = \max_{(x,y,z) \in \Omega_M} \{|\gamma_{12}(x, y, z)|\} \approx \max_{i=1,2,\dots,N} \{\gamma_i\} \quad (5.5)$$

where $f_{MAXVC}\{\cdot\}$ denotes the fitness function using MAXVC, which aims to minimise the maximum shear angle; Ω_M is the spatial material region; $\gamma_{12}(x, y, z)$ is the continuous shear angle distribution in the material region, Ω_M ; N is the total number of integration points; $|\cdot|$

is the absolute value of the variable; $\gamma_i = |\gamma_{12}(x_i, y_i, z_i)|$ is the absolute value of the shear angle at the i^{th} material point, (x_i, y_i, z_i) . Since the constraining pattern influences the shear angle distribution, the value of f_{MAXVC} is used for quantitative assessment of the fitness.

The theoretical optimum positions from Step I cannot be directly used in Step II. It is impractical to constrain the end of each individual yarn around the perimeter of the blank in reality, thus neighbouring constraints need to be grouped together to form consolidated clamps. If the distance between two adjacent constrained positions is smaller than a threshold value, they are considered to be part of the same clamp. A minimum clamp size is also specified, and any isolated constraints are discarded. Additionally, clamps are removed or split if they generate excessive curvature around the perimeter of the blank or increase MAXVC. The stiffness of each constraint is directly obtained by summing the stiffnesses of all parallel springs associated with each individual clamp. These compromises are essential for successful industrial implementation, but their negative impact can be alleviated to some extent by optimising the spring properties in Step II. Here, these practical considerations have been implemented manually, which is facilitated by the two-stage optimisation approach. Whilst it would be feasible to include them in the optimisation code as additional constraints or regularisation terms, as previously discussed by Skordos et al. [128], this would increase the number of variables in the objective function. This would largely reduce the efficiency in automatically creating FE models, and the number of geometry variables may change during the optimisation, significantly increasing complexity. A potential solution would be to define a large enough number of variables and reserve sufficient memory, but this would be wasteful, causing computational resources to become redundant.

Since all nodes along the edges were initially connected to springs in Step I, it was necessary to choose a relatively low starting stiffness from the available range to avoid over-constraining the blank. In this step, the constraint stiffness was set to 0.03 N/mm at each applied position.

5.3.3 Step II: Spring stiffness optimisation

In-plane constraints are applied at the selected clusters of nodes identified in Step I (see Figure 5.3(b)). A subsequent optimisation step is performed using a GA to determine optimum stiffness values for each spring from a user-defined range.

For simplification, only linear behaviour is considered, which can be parameterised as

$$F_i^{ct} = k_i^{ct} \cdot d_i^{ct} \quad (i = 1, 2, \dots, m) \quad (5.6)$$

where m is the number of constrained clamping positions after refinement, k_i^{ct} is the stiffness of the i^{th} spring, d_i^{ct} is the in-plane displacement at the i^{th} constrained position, and F_i^{ct} is the corresponding constraining force. Consequently, the optimisation variables are converted into a stiffness k_i^{ct} ($i = 1, 2, \dots, m$). This method is also suitable for modelling non-linear behaviour, as the optimisation method is intrinsically the same, but the number of parameters increases.

The optimisation problem in Step II can be described as

$$\text{Minimise: } f\{k_1^{ct}, k_2^{ct}, \dots, k_m^{ct}; \gamma_{12}(x, y, z)\} \quad (5.7)$$

$$\text{Subject to: } k_i^{ct} \in [(k_i^{ct})^{low}, (k_i^{ct})^{upp}] \quad (i = 1, 2, \dots, m) \quad (5.8)$$

where $[(k_i^{ct})^{low}, (k_i^{ct})^{upp}]$ is the applicable stiffness range of the i^{th} constraint. Similarly, MAXVC is employed again as the fitness function to minimise the maximum shear angle in Step II

$$f_{MAXVC}\{k_1^{ct}, k_2^{ct}, \dots, k_m^{ct}; \gamma_{12}(x, y, z)\} = \max_{(x,y,z) \in \Omega_M} \{|\gamma_{12}(x, y, z)|\} \approx \max_{i=1,2,\dots,N} \{\gamma_i\} \quad (5.9)$$

In this step, optimisation is aimed at finding a near-optimal solution to reduce the negative influence induced by manually refining the constrained positions. A summary of the GA is presented in Figure 5.5.

5.3.4 GA stability analysis

The stability of a GA in delivering an optimum solution depends on the diversity of the population. This is determined by the population size, the initial population and probabilities for crossover and mutation. The population size has been chosen to be greater than the number of optimisation variables, for example using 100 for Step I (76 variables corresponding to 76 clamping positions per quarter model). The initial population is determined randomly to ensure sufficient diversity. The crossover probability (i.e. the proportion of each population where genes from individuals in the previous generation are recombined) was 0.8, a compromise between evolution rate and solution accuracy. The mutation probability enables a small random variation in the individuals of each generation

to create new genes, ensuring genetic diversity and enhancing the probability for an improved fitness score. Its value was determined adaptively for this study, based on the fitness scores from the previous generation.

It is important to ensure that the initial population is distributed across the entire solution space to avoid restricting the range for the optimum value. The distance between individuals in the solution space is therefore measured to quantify the diversity of the population. For the example of the 76 variables in Step I, the average distance between individuals must be less than the maximum value of 8.7 (i.e. $76^{1/2}$ for 76 binary variables). Furthermore, the average distance should progressively decrease for subsequent generations, indicating a reduction in search space and convergence towards the global optimum.

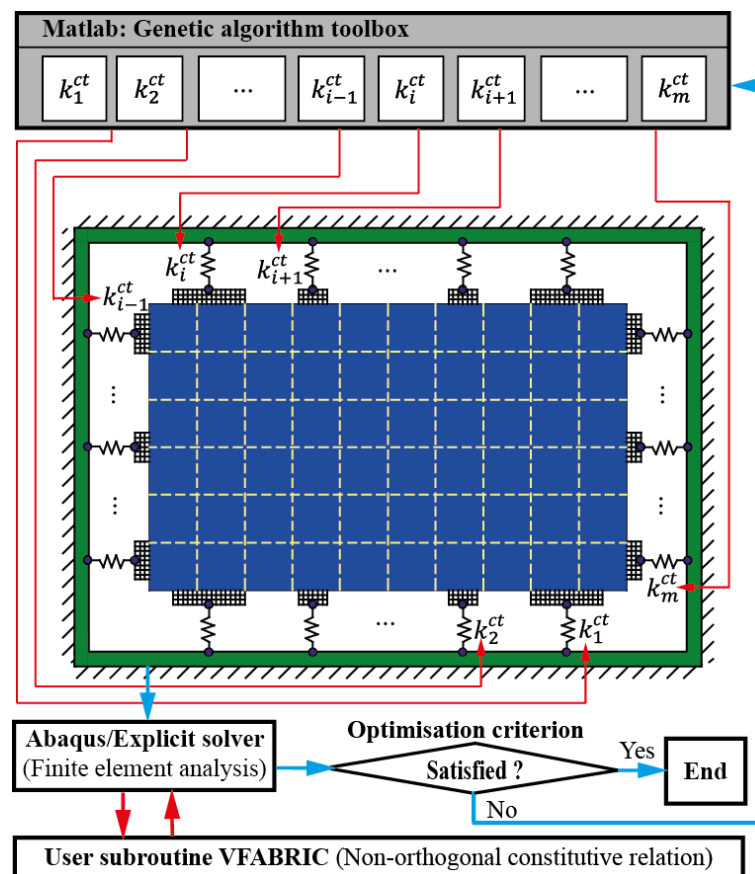


Figure 5.5: Implementation of Step II – Spring stiffness optimisation.

5.4 Results and discussion of in-plane constraint optimisation

5.4.1 Clamping arrangement optimisation from Step I

Several generations of clamping patterns have been selected to illustrate the optimisation evolution for Step I (Figure 5.6), indicating the reduction in number of constraints and the

evolution rate. Each generation represents a summary of 100 individual constraining patterns, where the bars represent constrained locations. The initial population of 100 patterns for the zeroth generation was generated randomly, which then evolved into subsequent generations according to the GA. In the figure, all bars are initially a shade of red, which indicates that all of the constraint positions are represented similarly across the 100 patterns. The shade of red changes as the constraining pattern evolves for each subsequent generation, where a darker red (tending towards black) represents a higher frequency for that constrained position. A lighter shade of red represents a lower frequency, where white indicates complete removal of the constraint. As the fitness function converges, all remaining bars appear black, which indicates that all 100 patterns for that generation are in agreement.

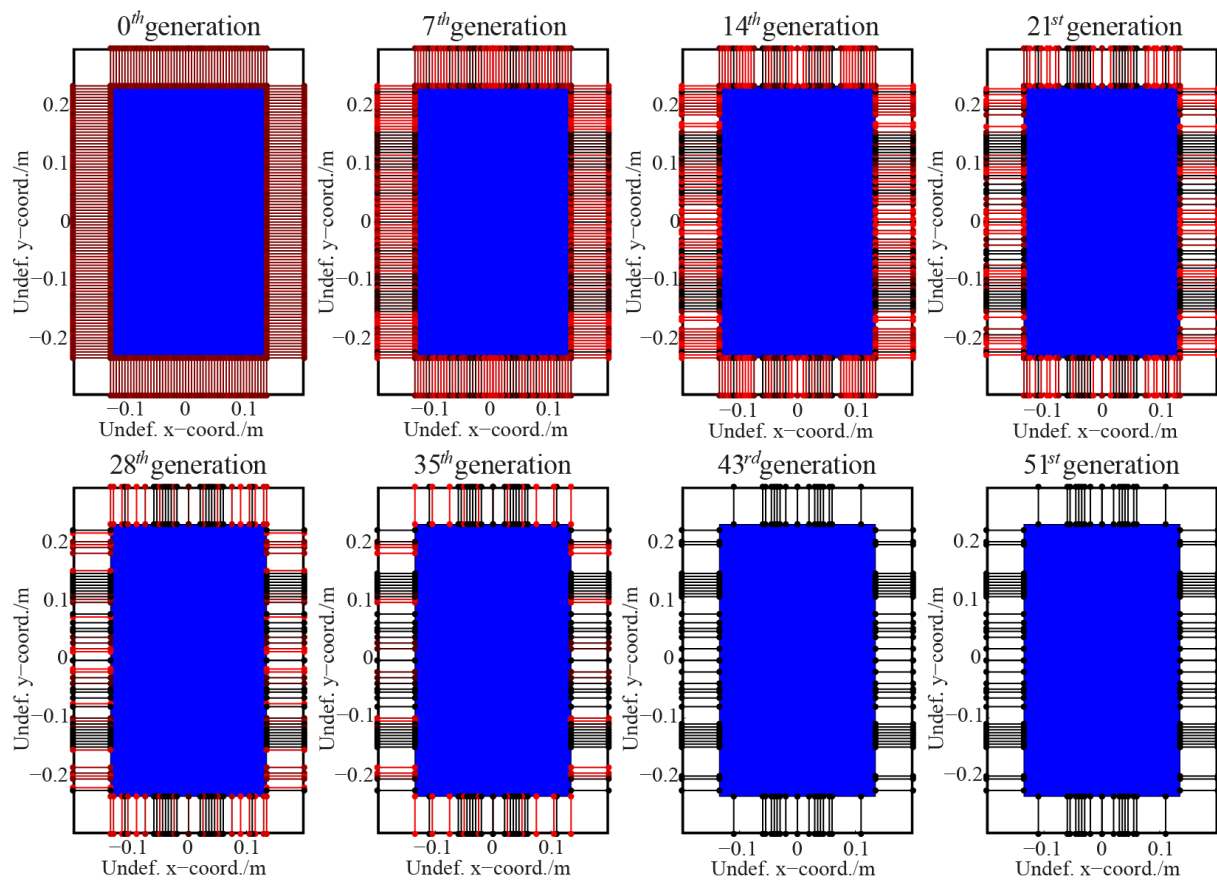


Figure 5.6: Optimisation evolution of constraining pattern in Step I; solid bars represent constrained positions in the respective generation; red scale indicates the frequencies of occurrence within the respective generation.

Figure 5.6 shows that some of the final constraint positions start to emerge as quickly as generation 7, with some bars already shown as black. By generation 14, some of the weaker bars are removed and a symmetrical clamping pattern starts to develop. By generation 35, there are very few red bars remaining, with the status of only 20 % of the clamping positions

uncertain at this stage. The final clamping pattern is determined after generation 43, which is confirmed by comparing with the outcome from generation 51.

The diversity of the population for each generation in Step I has been checked by evaluating the average distance between individuals, shown in Figure 5.7(a). For the first six generations the value is approximately 6, indicating that the initial population covers approximately 70 % ($6/8.7$) of the solution space. The average distance reduces by 1.6 % ($0.14/76^{1/2}$) for each subsequent generation, indicating that evolution is progressive, allowing sufficient opportunity for elite genes, (i.e. genes related to low fitness scores in terms of maximum shear angles), to survive during offspring creation.

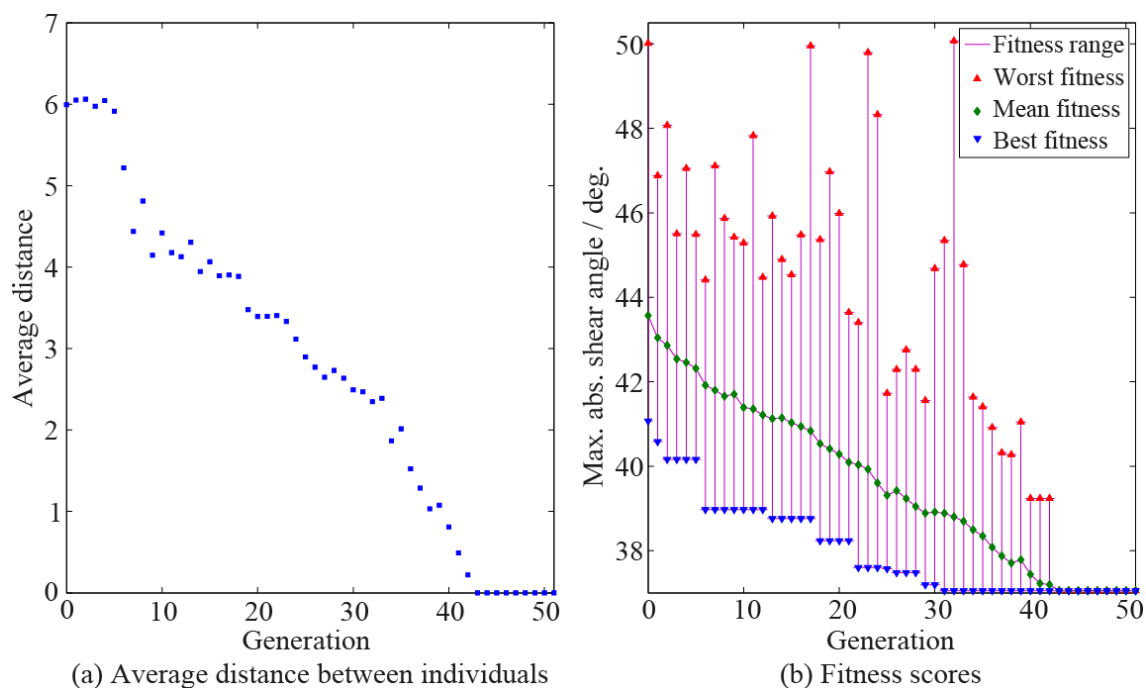


Figure 5.7: Population diversity and optimisation evolution for Step I.

Figure 5.7(b) shows the evolution of the fitness scores for Step I. The magnitude of the adaptive Fitness Range is similar for each generation until the Best Fitness converges, implying that a wide search range has been adopted throughout. The range of the fitness score varies due to adaptive mutation. The optimum solution (i.e. convergence of the Best Fitness) is achieved during generation 31. Perturbations induced by further mutations during the next 12 generations (indicated by a non-zero fitness range) appear to have no influence on the optimal solution. Furthermore, the mutation probability reduces to zero following generation 43, after the optimal solution has been determined. Therefore, Figure 5.7 confirms that the present diversity prevents local optimum solutions, random selection and instability.

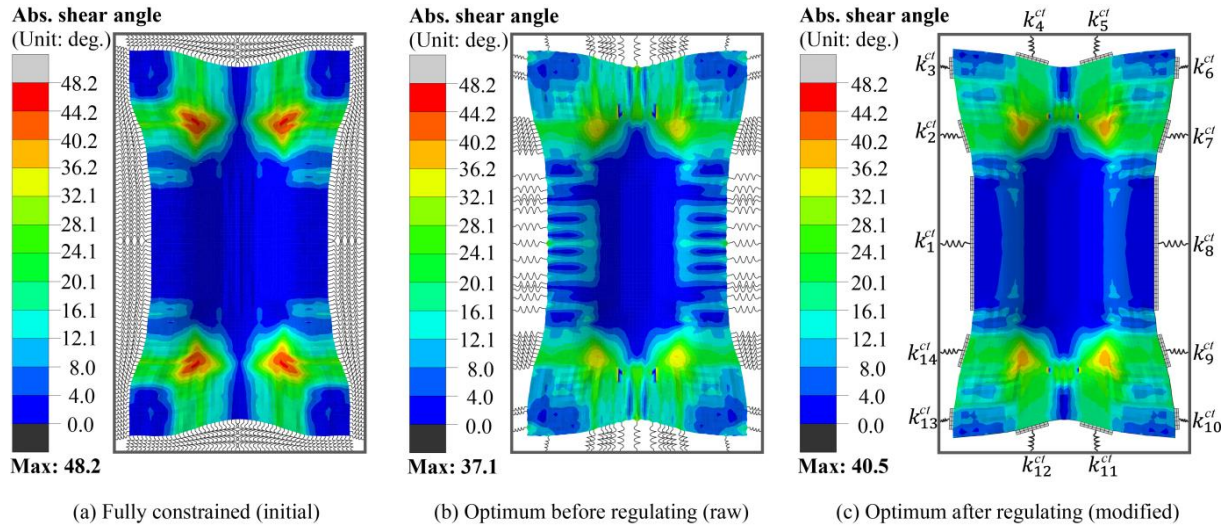


Figure 5.8: Step I – Clamping arrangement optimisation for a single 0°/90° ply.

The maximum shear angle decreases by 11.2°, from 48.2° for the fully constrained system (Figure 5.8(a)) to 37.1° after all unconstrained springs have been removed (Figure 5.8(b)). However, practical implementation of the optimum pattern in Figure 5.8(b) is not feasible, since too many individual springs are required to obtain the blank boundary conditions. Therefore, it is necessary to compromise and combine neighbouring clamps and eliminate isolated ones (see Figure 5.8(c)). The minimum threshold distance between clamps was chosen to be 25 mm (equivalent to the width of 5 finite elements), and the minimum clamp length was also assumed to be 25 mm. In addition, the spring located at the mid-point of the short edge (see Figure 5.8(b)) was removed, as this could not be combined into a single clamp due to the region of high curvature generated by the springs either side. Consequently, only two clamps were required along each of the short edges to maintain the optimum draw-in. The individual constrained positions from Figure 5.8(b) were combined and reduced to 14 clamps, as shown in Figure 5.8(c). The stiffness of each consolidated spring was directly obtained by summing the stiffness of all of the parallel springs belonging to each corresponding block. Table 5.2 provides a summary of the spring stiffnesses after Step I of the optimisation, including the length and position of the corresponding clamps.

Although the maximum shear angle increased by 3.4° in Figure 5.8(c) compared with the result in Figure 5.8(b), this still yields an overall reduction in peak shear angle of 7.7° compared with the unoptimised case. In addition, the shear angle distribution in Figure 5.8(b) indicates that wrinkling occurs along the long edges when constrained by individual springs, as there are local transitions in shear angle. However, these disappear in Figure 5.8(c) when

longer clamps are introduced along the edges. Constraining the blank using consolidated clamps homogenises the boundary constraints to eliminate undesirable wrinkling around the perimeter.

Table 5.2: Clamping parameters obtained from Step I and Step II (The origin of the undeformed coordinate system is the centre of the blank).

Clamp	Central edge position		Clamp length (mm)	Stiffness (N/mm)	
	Undef. x (mm)	Undef. y (mm)		Step I	Step II
k_1^{ct}	-135.0	0	160	0.39	0.21
k_2^{ct}	-135.0	130.0	40	0.27	0.21
k_3^{ct}	-135.0	212.5	25	0.09	0.19
k_4^{ct}	-40.0	235.0	40	0.21	0.28
k_5^{ct}	40.0	235.0	40	0.21	0.28
k_6^{ct}	135.0	212.5	25	0.09	0.19
k_7^{ct}	135.0	130.0	40	0.27	0.21
k_8^{ct}	135.0	0	160	0.39	0.21
k_9^{ct}	135.0	-130.0	40	0.27	0.21
k_{10}^{ct}	135.0	-212.5	25	0.09	0.19
k_{11}^{ct}	40.0	-235.0	40	0.21	0.28
k_{12}^{ct}	-40.0	-235.0	40	0.21	0.28
k_{13}^{ct}	-135.0	-212.5	25	0.09	0.19
k_{14}^{ct}	-135.0	130.0	40	0.27	0.21

5.4.2 Stiffness optimisation from Step II

The spring stiffnesses from the solution in Step I (Figure 5.8(c)) form the starting point of Step II. Half of the individuals for the zeroth generation used the same combination of constraint properties as the solution from Step I and the rest were generated randomly, which then evolved into subsequent generations according to the GA. The population size for the GA was 20 in each generation, and the tolerance for the fitness function was 0.05° . For the current work, the range of spring stiffnesses in this step was chosen to be from 0.03 N/mm to 0.50 N/mm. The stability of the optimisation for Step II was validated using the same methodology outlined for Step I. The fitness scores confirmed that the initial population was suitably diverse, and Figure 5.9(a) indicates that the solution was stable.

As shown in Figure 5.9(a), the maximum shear angle is reduced to 37.2° by optimising the spring stiffnesses. This value differs by 0.1° from the ideal optimum (37.1°) in Step I (see in Figure 5.8(b)). It indicates that the negative influence induced by artificially adjusting the constrained positions is minimised by seeking an optimal combination of clamp stiffnesses in

Step II, whilst making the solution more practical. Comparison of the maximum shear angles during each step therefore confirms that the two-stage optimisation does not significantly compromise the optimisation outcome. Using a more generic GA approach may enable both optimisation stages to be combined (e.g. assigning different sets of genes defining positions and stiffnesses) to further improve the accuracy of the solution. However, this would require variable encoding lengths to be used for the different parameters. Encoding the task as a single step optimisation problem may result in a more efficient solution in the longer term, but it would be more complex to implement and would only be applicable to this specific geometry.

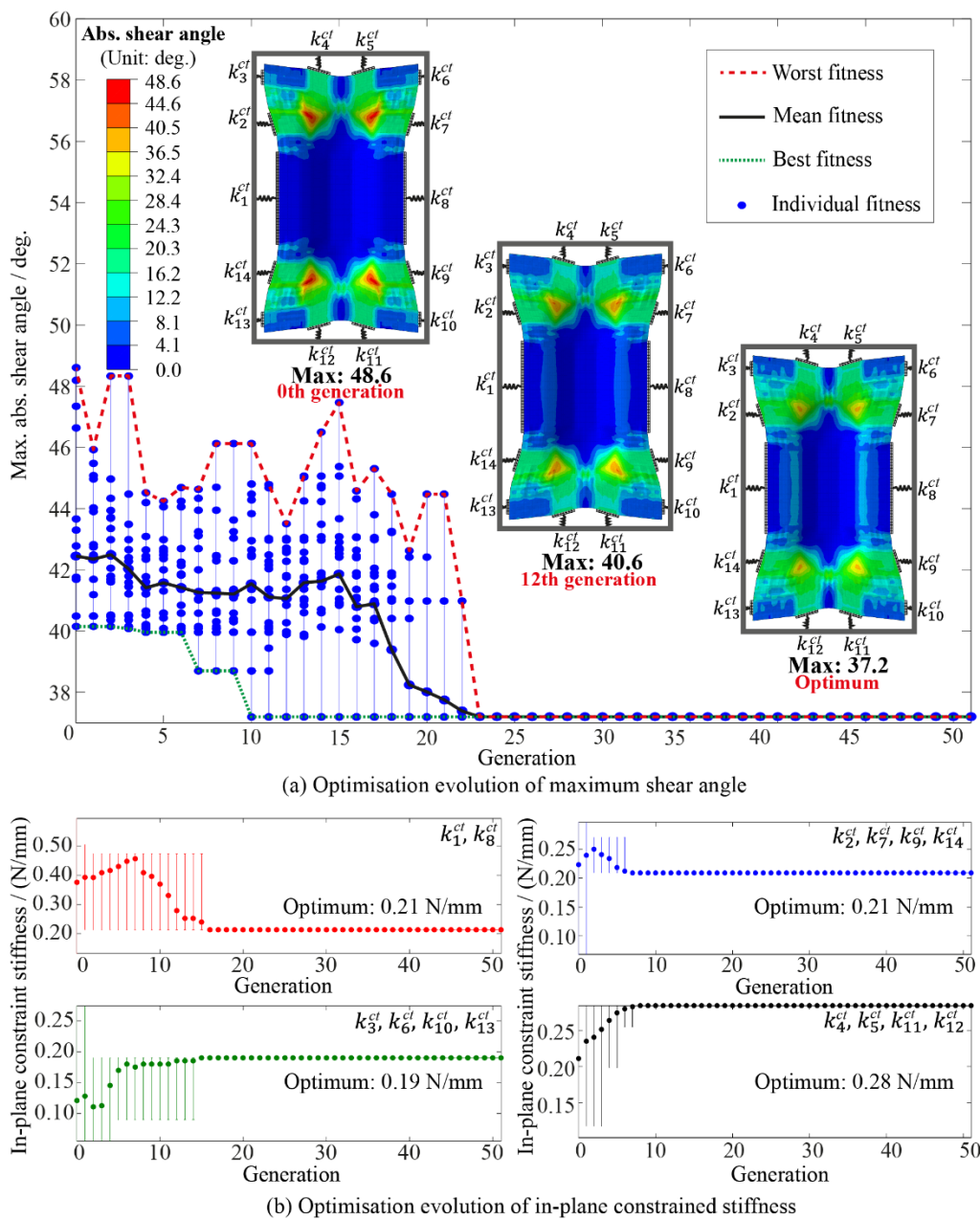


Figure 5.9: Step II – Stiffness optimisation for a single 0°/90° ply.

The convergence of the spring stiffnesses for Step II is presented in Figure 5.9(b). The optimum combination of spring stiffnesses is presented in Table 5.2 and illustrated schematically in Figure 5.10. This figure allows a general strategy for spring placement to be derived: At zones of the component geometry with small curvature, springs with relatively low stiffness are attached through long clamps to provide near uni-axial tension. Zones with a high degree of curvature require multiple springs with stiffnesses adapted to suit the fibre orientation, which are attached through short localised clamps, allowing for multi-axial tension to be applied to the blank. In general, springs attached to the clamps along the long edges have a stiffness of 0.20 N/mm, and springs along the short edges are approximately 0.30 N/mm for the current geometry. These are of similar magnitude to those used by Harrison et al. [117], where fewer clamps were used, and the stiffer springs were placed on the long edges.

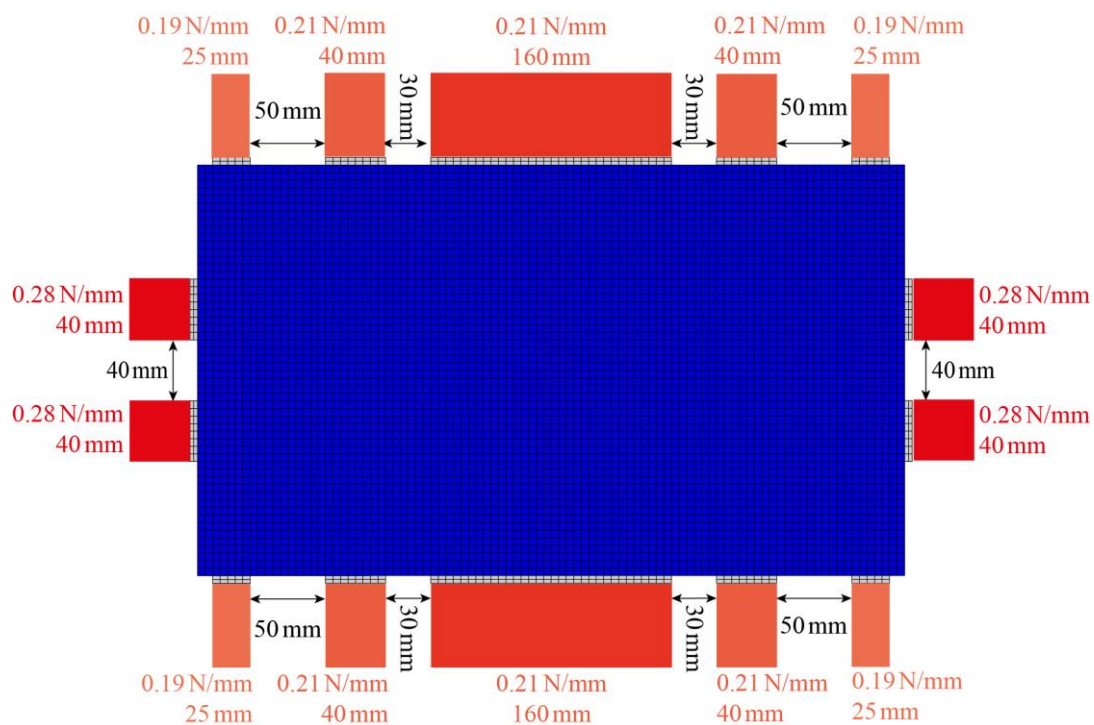


Figure 5.10: Schematic of locations and widths of clamps; spring stiffnesses are also indicated.

Figure 5.11 illustrates in-plane strains along the two principal fibre directions, where only negative strains are shown. These negative strains indicate fabric compression, which may result in localised wrinkles. The progression of the images implies that maximum strains along both fibre orientations have been reduced through strain homogenisation during optimisation, resulting in a reduction of potential regions of severe wrinkling. Whilst the shear

angle distribution was the optimisation objective, the distribution of wrinkling strain is simultaneously homogenised as previously seen in the inter-ply stitching optimisation in Chapter 4.

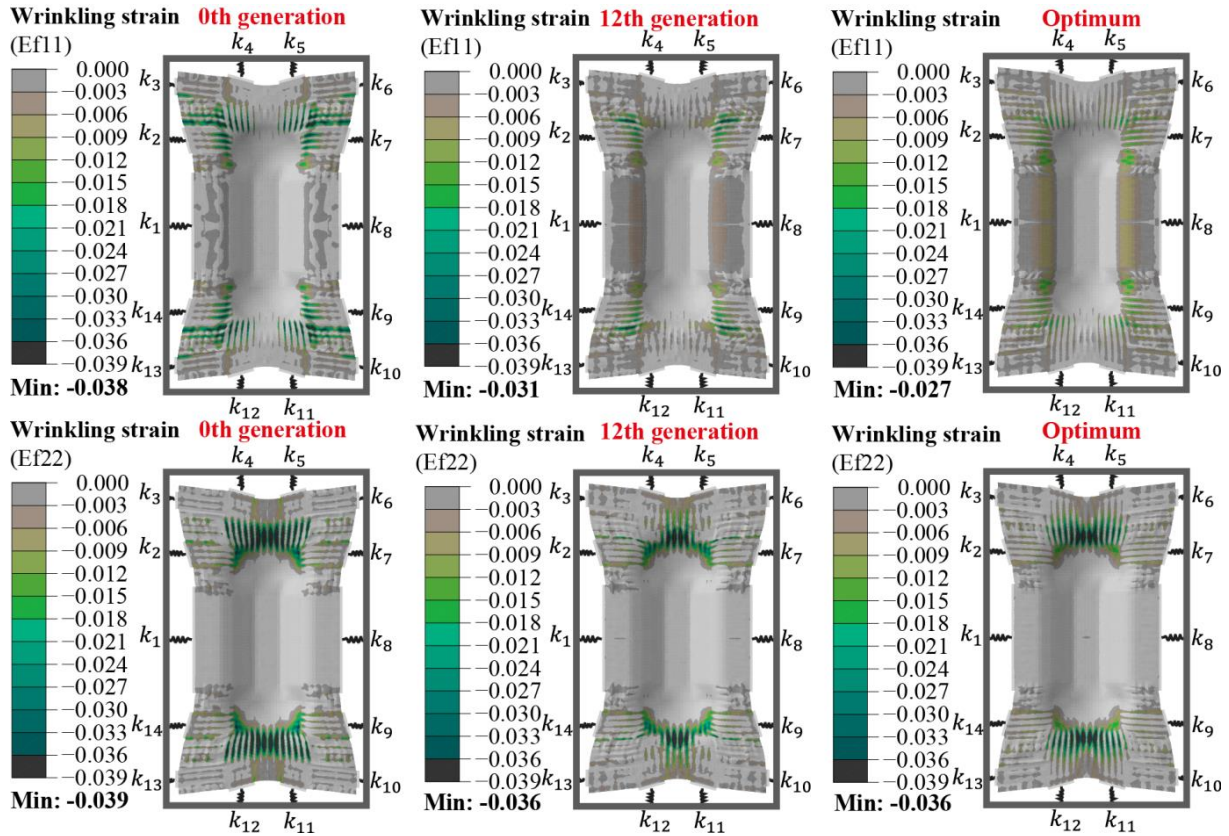


Figure 5.11: Wrinkling strain along both principal fibre orientations.

5.4.3 Comparison with constraint application through blank holders

Results from the two-stage spring/clamp optimisation have been compared against results from a segmented blank holder approach, for the same double hemisphere geometry. The geometry of the blank holder, which was taken from the International Forming Benchmark study [36, 40, 47, 132], is divided into six segments (Figure 5.1(a)). The force applied on each segment has been established using the same GA optimisation method as described above, where the range of the blank holder force was selected to be from 0.01 kN to 1.00 kN.

As shown in Figure 5.12, the maximum shear angle is reduced to 42.5° by optimising the forces applied to the blank holder segments. This is 4° smaller than the initial generation and is comparable to values reported in the literature [40, 47, 132]. The optimum solution in Figure 5.12 for the segmented blank holder constraint can be directly compared to the optimum distribution in Figure 5.9 for the spring-loaded clamp constraint. The spring-loaded

clamps appear to be a more effective way of reducing local shear angle, with the maximum value (37.2°) more than 5° smaller than for the blank holder approach (42.5°). However, Figure 5.9 indicates that there are more significant local transitions in shear angle for the spring-loaded clamps than for the blank holder, which may result in the onset of severe wrinkling.

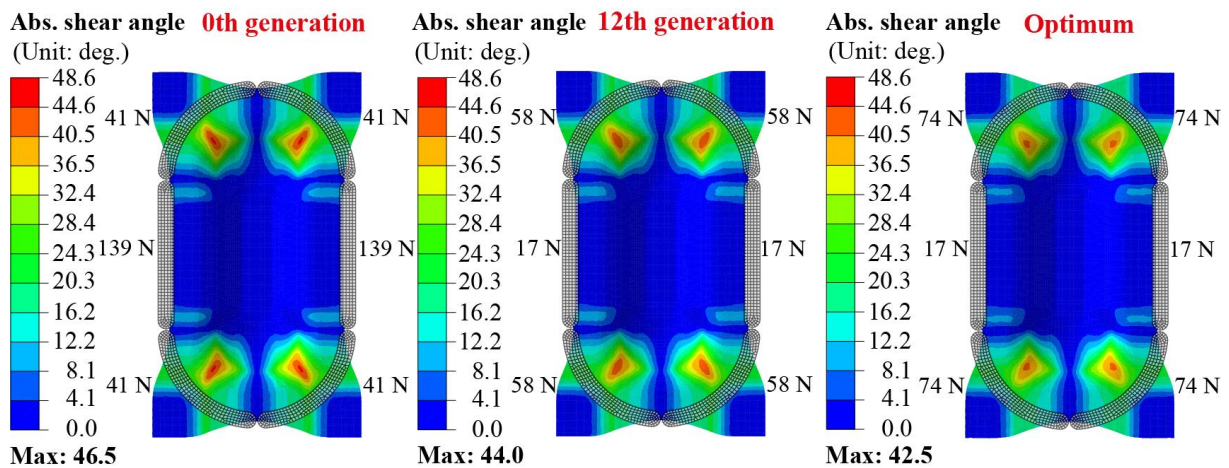


Figure 5.12: Evolution of shear angle distribution from segmented blank holder force optimisation.

Figure 5.13 illustrates in-plane strains along the two principal fibre directions using segmented blank holder to control material draw-in, where only negative strains are shown to indicate fabric compression, which may result in localised wrinkles. These results also indicate that the shear angle distributions and wrinkling strain are not independent objectives, as previously seen in the inter-ply stitching optimisation (Chapter 4).

According to Figure 5.9 and Figure 5.12, larger maximum shear strains for the case using spring-loaded clamps, (3.6%), while the wrinkling risk is higher than for the case using a segmented blank holder (2.2%) by comparing Figure 5.11 and Figure 5.13. This implies that using blank-holders applying a normal force to the fabric surface may help to control the occurrence of wrinkles, as they provide resistance to out-of-plane deformation of the blank whilst providing in-plane tension to control material draw-in.

Whilst smaller in-plane shear angles were achieved with the spring-loaded clamping arrangement, the segmented blank holder set-up can potentially be further improved through optimisation of shape and position of the segments to reduce the maximum shear angle.

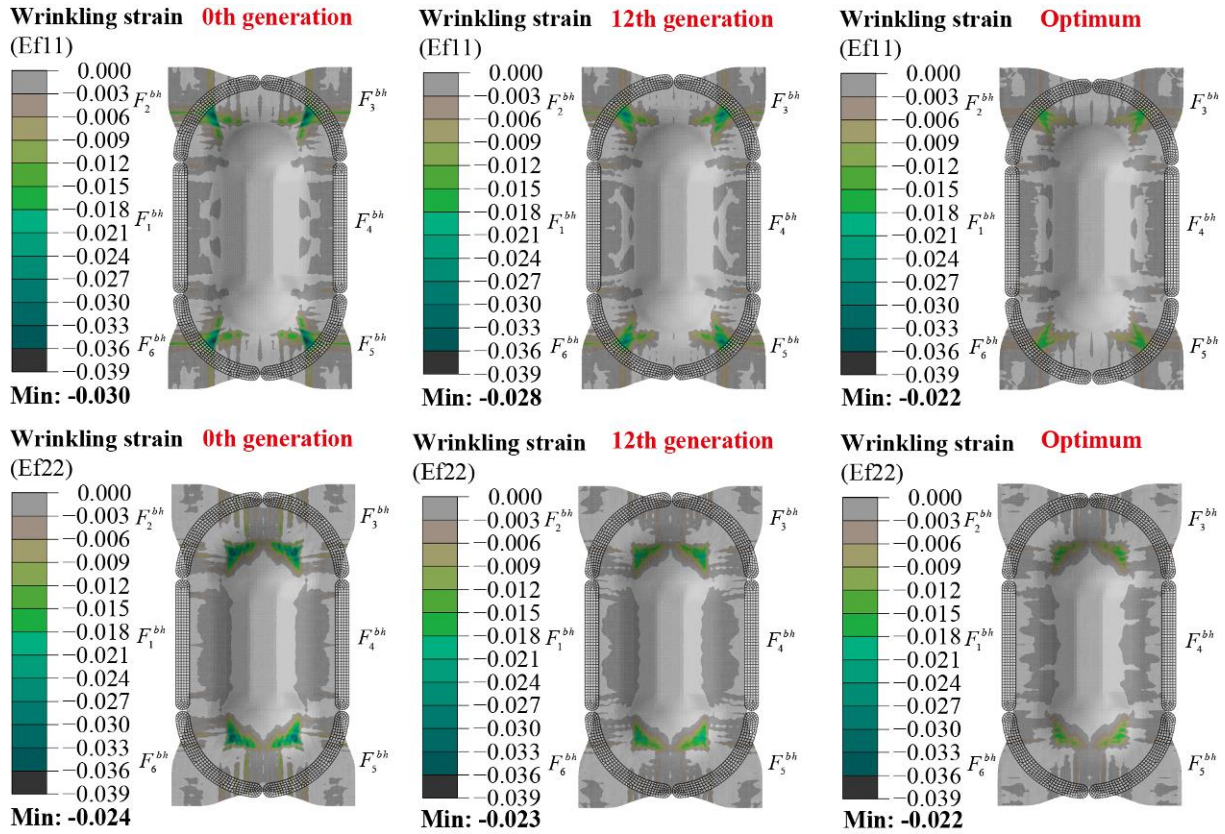


Figure 5.13: Evolution of wrinkling strain distribution along two principal fibre directions from segmented blank holder force optimisation.

5.5 Chapter summary

A scenario has been introduced for controlling material draw-in during reinforcement forming processes, using a series of in-plane springs to locally apply tension to the preform, rather than using a blank holder to compress the preform out-of-plane and apply constraints through friction. The in-plane constraints around the edges of the blank were modelled using spring elements connected to a fully constrained rigid frame, providing axial forces to control material slippage into the cavity.

An optimisation methodology has been developed by combining the explicit FE model with a genetic algorithm to optimise parameters associated with the in-plane constraints using spring-loaded clamps. It has been implemented in two stages: (a) Step I: Clamping arrangement optimisation, (b) Step II: Spring stiffness optimisation. Process optimisation has been demonstrated using a double-dome geometry from the literature. Results indicate that controlling material draw-in by constraining the blank in-plane around the perimeter is an effective way of homogenising the global shear angle distribution and minimising the local

maximum value. The peak shear angle was reduced from 48.2° to 37.2° following the two-stage optimisation process. Strains along the two principal fibre directions have also been reduced during the optimisation, through strain homogenisation, resulting in a reduction of potential regions of severe wrinkling.

However, whilst spring-loaded clamps can effectively control material draw-in and reduce local shear angles to an acceptable level, the peak compressive strains were found to be higher than when using a segmented blank holder constraint. Adopting blank holders can therefore help to reduce the occurrence of wrinkles (2.2 % wrinkling strain compared with 3.6 %) due to the normal force applied.

Chapter 6 Double Diaphragm Forming

6.1 Introduction

This chapter investigates the use of double diaphragm forming for producing geometrically complex fabric preforms suitable for liquid moulding processes. A material model has been developed to simulate diaphragm forming of non-crimp fabrics, in order to investigate the geometrical limitations of the process and the cause of defects. A generic geometry is studied and results are presented to show how the ply shapes are optimised to provide a net-shape preform without defects.

6.2 Process design and experiment

6.2.1 Double diaphragm forming process

A laboratory-scale diaphragm forming machine was developed at the University of Nottingham as part of the Innovate UK funded ALPA project, to preform binder-stabilised dry fabrics (see Figure 6.1). The membranes were 1.8m×1.5m. The lower membrane was clamped between a support frame and a rectangular picture frame and the upper membrane was fixed to the lower membrane using a vacuum-tight zipper seal. This arrangement was fixed to four pneumatic cylinders which were used to raise and lower the diaphragms relative to the forming tool.

A schematic of the process steps is shown in Figure 2.15. The fabric plies were placed on top of the lower diaphragm. The upper diaphragm was then added and the zipper seal was closed manually to encapsulate the fabric plies (Figure 2.15(a)). A vacuum was drawn between the two diaphragms to clamp the material. The diaphragm/picture frame arrangement was raised to within 150mm of the infrared heaters in order to melt the powdered binder at 90°C. Once the set-point was achieved, the diaphragm arrangement was quickly lowered and draped over the tool (Figure 2.15(b)). A second vacuum (independent to the first) was then drawn between the lower diaphragm and the tool to complete the forming process (Figure 2.15(c)). The preform was left to cool below the melting point of the binder before removing (Figure 2.15(d)). The vacuum was released between the diaphragms and the top membrane was

removed first, to prevent the preform from distorting or springing back. The vacuum between the lower diaphragm and the tool was released once the preform had been removed, enabling the lower diaphragm to recover before the next preforming cycle. The total cycle time was approximately 4 minutes for this laboratory setup. This time largely depends on the thickness of the ply stack and the chemistry of the binder, in order to ensure all binder has been activated. This could potentially be reduced further by implementing forced cooling and increasing the power density of the heaters.

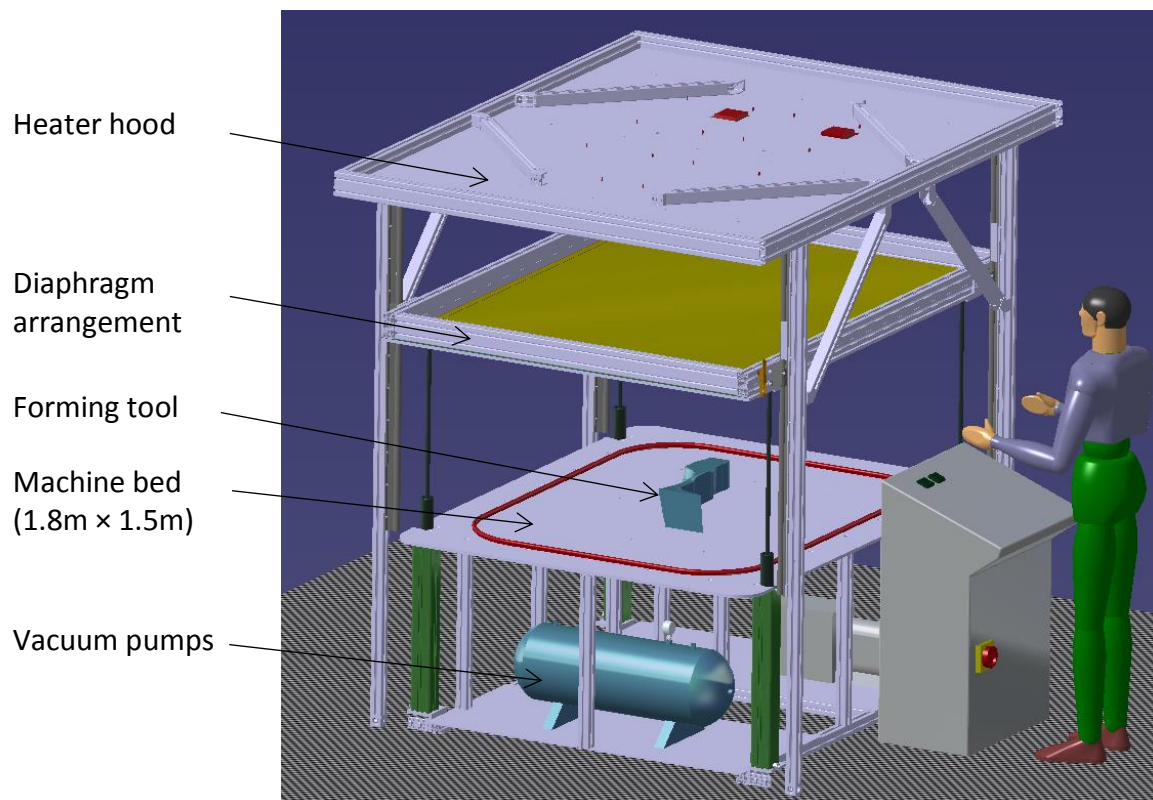


Figure 6.1: Details of diaphragm forming machine.

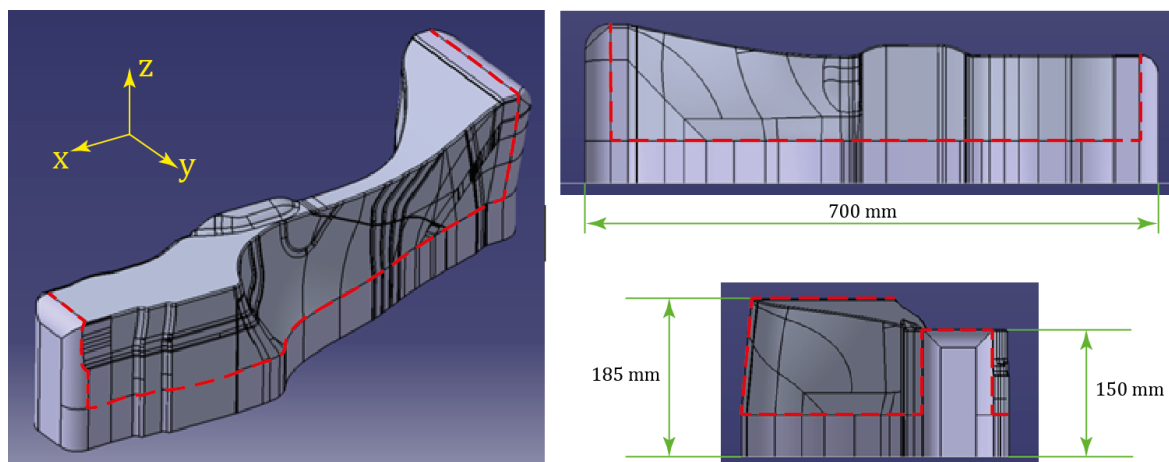


Figure 6.2: Tool geometry for case study component. Red lines indicate the trimmed edge of the final component.

A generic geometry was developed to represent a section from a complex automotive structure, as shown in Figure 6.2. The surface shape includes regions of single and double curvature and surface features which could lead to fabric bridging.

6.2.2 Non-crimp fabric

All preforms were produced using two plies of FCIM359 biaxial non-crimp fabric (NCF), supplied by Hexcel, Leicester, UK. Each ply consisted of 440gsm of carbon fibre with a 24K tow size, in a $\pm 45^\circ$ architecture [142, 143] with a pillar stitch at 0° . A small amount (6%wt) of Momentive Epikote 05390 binder was applied between layers to stabilise the post-formed shape. The thickness of each ply was measured to be 0.4mm, using a vernier caliper. The in-plane shear behaviour of the FCIM359 fabric has been previously characterised in Section 3.4. Flat ply outlines were exported from the simulation in DXF format and plotted to scale to provide a template, which was used as a guide to cut the fabric plies by hand.

6.2.3 Diaphragm characterisation

The diaphragms were made from Supervac silicone sheet with 50° Shore A hardness, supplied by Silex Ltd, UK. A series of mechanical tests were performed on coupons to characterise the in-plane behaviour of the diaphragm. Uniaxial tensile tests were performed on a universal testing machine at a strain rate of 0.03 s^{-1} . The tensile force was recorded by a 5kN load cell and balanced travelling extensometer was used to measure the axial strain (see Figure 6.3(a)). The cross-section of the sample was 5mm wide and 1.56mm and rubber faced jaws were used to avoid stress concentrations due to clamping.

A Flexible Biaxial Film Tester [144] was also used to perform both equibiaxial tensile tests and planar shear tests on the silicone diaphragms (see Figure 6.3(b)). The machine consisted of a horizontal biaxial frame driven by two independent leadscrews and controlled by a LabView interface. The biaxial specimen was 75mm×75mm, clamped by 7 miniature pneumatic grips along each edge. Load cells are integrated into the two central grips to record the forces, and strain was measured using a non-contact video tracking system which relied on a series of markers applied to the top surface of the specimen. The equibiaxial tensile tests were performed by applying the same displacement rate, corresponding to a strain rate of 0.03 s^{-1} to each grip. The pure shear test was performed by constraining one lead screw so that the

specimen width remained constant, whilst applying a displacement corresponding to a strain rate of 0.03 s^{-1} to the other lead screw.

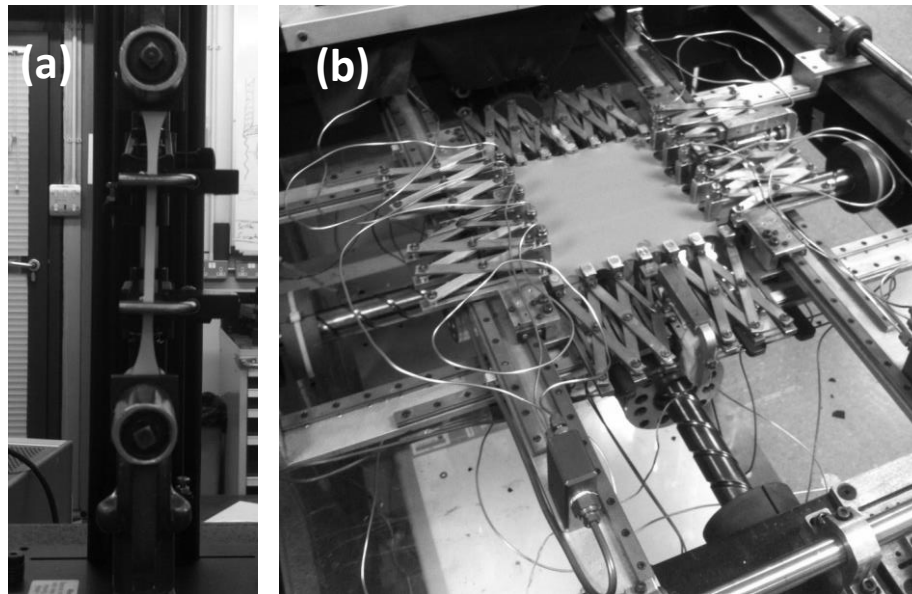


Figure 6.3: Photographs showing test rigs for (a) uniaxial tensile testing and (b) biaxial tensile testing of silicone diaphragms.

6.3 Double diaphragm forming process simulation

6.3.1 DDF modelling approach

A schematic of the simulation geometry is presented in Figure 6.4. Each fabric ply was modelled in Abaqus/Explicit using quadrilateral membrane elements (M3D4R), with a maximum edge length of 5 mm. The diaphragms were modelled using 10mm×10mm S4 shell elements, which were constrained in the xy-plane around the perimeter to replicate the constraints of the picture frame on the diaphragm forming rig. All parts of the tooling (tool and machine bed) were considered to be rigid bodies. A penalty contact algorithm was used to define the behaviour at the interfaces. An isotropic Coulomb friction model was adopted for tooling-diaphragm, diaphragm-material and material-material contacts, with measured constant coefficients of 0.67, 0.52 and 0.36 respectively, according to experiments performed to ASTM D1894, ISO8295.

Pressures were applied to the upper surface of the top diaphragm and the lower surface of the bottom diaphragm as shown in Figure 6.5. Initially both pressures were equal in magnitude but opposite in direction (A to B) to simulate the clamping force on the fabric plies generated by the vacuum between the diaphragms. Displacement boundary conditions were

then applied to the edge nodes of the diaphragms to simulate the picture frame being lowered to make contact with the bed of the machine. Subsequently, a pressure differential was created between the two diaphragm surfaces to simulate the vacuum being applied between the lower diaphragm and the tool. The pressure applied to the bottom diaphragm was reduced (B to C), drawing the diaphragm arrangement into contact with the surface of the tool.

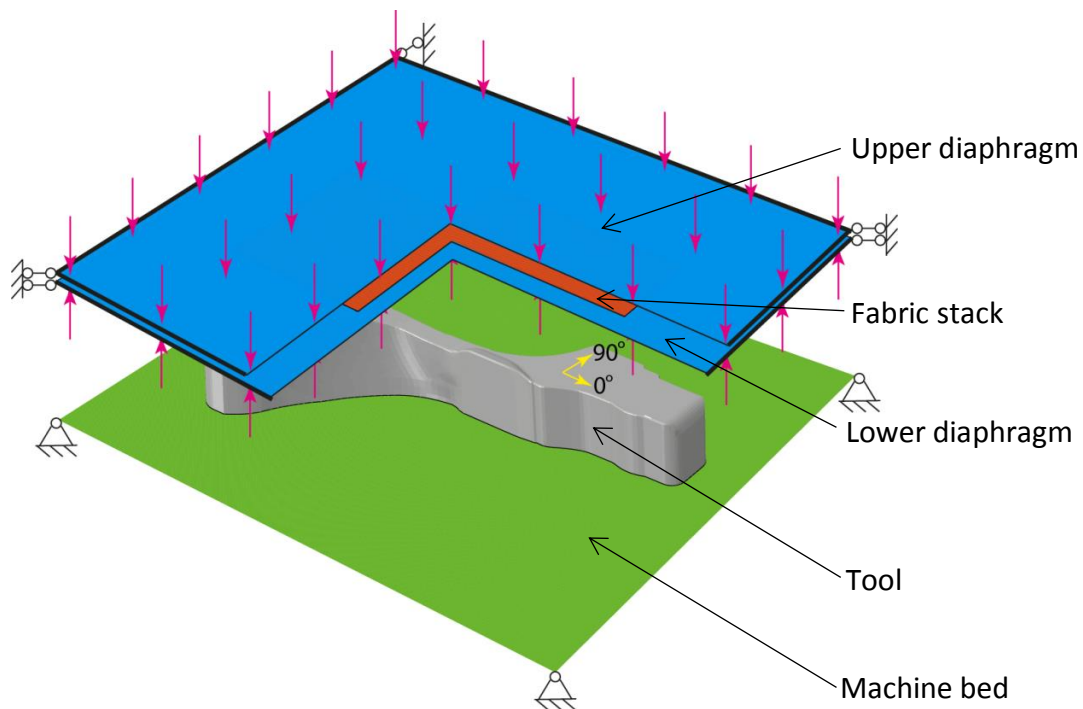


Figure 6.4: FE model of double diaphragm forming. A quadrant from the two diaphragms and the fabric stack has been removed for clarity. Arrows indicate the direction of the applied pressure.

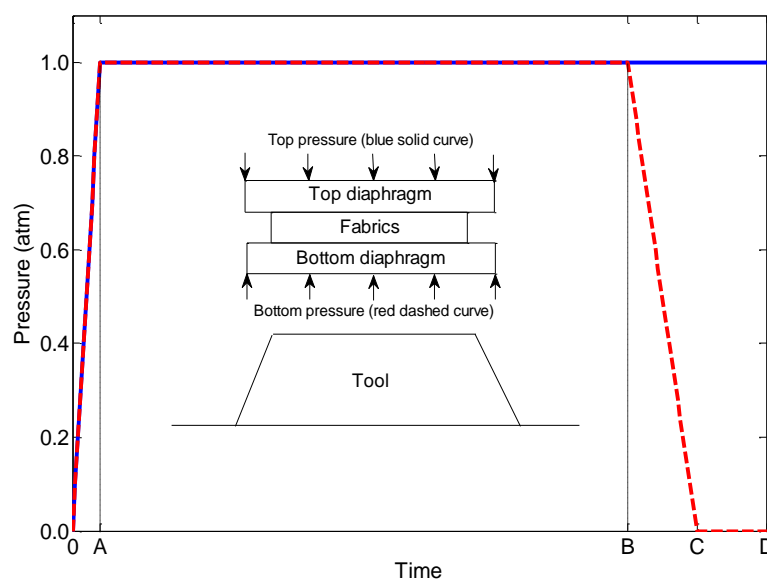


Figure 6.5: Definition of pressure applied to the diaphragms in the FE model.

6.3.2 NCF material model

The constitutive model for the NCF plies was developed in Section 3.4. A non-orthogonal constitutive relation was employed to define the asymmetric forming behaviour of NCF based on homogenisation. The shear compliance of the NCF is derived from two components: rotation of the principal fibre yarns and tension in the intra-ply stitches, which is described by superimposing these two contributions. This material model is implemented using a user-defined subroutine in Abaqus/Explicit. For validation, force-displacement data from the simulation of a picture frame test was shown to be within the bounds of the experimental data (the root mean square error was approximately 5%). Further validation was conducted for a hemisphere forming in Section 3.5, for which the constitutive relation for the NCF fabric plies was shown to suitably capture the onset of the main defect mechanisms, and local shear angles were predicted within $\pm 5^\circ$ of the experimental values.

6.3.3 Diaphragm material model

An Ogden model [145] was used to describe the hyperelastic, non-linear stress-strain behaviour of the silicone diaphragms. The model assumes that the material behaviour can be described by a strain energy density function expressed in terms of the principal stretches (λ_1 , λ_2 and λ_3) and the constitutive relationships are obtained from the derivative of the strain energy with respect to stretch and by applying appropriate boundary and symmetry conditions. The nominal stress-strain equations for the three load cases, uniaxial tension (subscript u), biaxial tension (subscript b) and pure shear (subscript s) are presented in Table 6.1, where T is the nominal stress, ϵ is the nominal strain (extension ratio), N is the order of Ogden model, and α_i and μ_i are material constants.

Table 6.1: Stress-strain relations for three load cases using the Ogden hyperelastic material model.

Mode	λ_1	λ_2	λ_3	T
Uniaxial	$1 + \epsilon_u$	$(1 + \epsilon_u)^{-\frac{1}{2}}$	$(1 + \epsilon_u)^{-\frac{1}{2}}$	$\sum_{i=1}^N \frac{2\mu_i}{\alpha_i} \left((1 + \epsilon_u)^{\alpha_i-1} - (1 + \epsilon_u)^{\frac{1}{2}\alpha_i-1} \right)$
Equibiaxial	$1 + \epsilon_b$	$1 + \epsilon_b$	$(1 + \epsilon_b)^{-2}$	$\sum_{i=1}^N \frac{2\mu_i}{\alpha_i} \left((1 + \epsilon_b)^{\alpha_i-1} - (1 + \epsilon_b)^{2\alpha_i-1} \right)$
Planar (pure) shear	$1 + \epsilon_s$	1	$(1 + \epsilon_s)^{-1}$	$\sum_{i=1}^N \frac{2\mu_i}{\alpha_i} \left((1 + \epsilon_s)^{\alpha_i-1} - (1 + \epsilon_s)^{\alpha_i-1} \right)$

A non-linear least-squares fit was performed on the uniaxial and equibiaxial test data to establish α_i and μ_i , using the built-in Marquard-Levenberg algorithm within Abaqus [146]. Assuming $m = 2N$ for the Ogden model, the coefficients ($a_i = \alpha_i$ or μ_i) are found by iteration as

$$a_i^{(r+1)} = a_i^{(r)} - \sum_{j=1}^m \sum_{k=1}^n [P_{ik}^{(r)} P_{jk}^{(r)} + \gamma \delta_{ij}]^{-1} P_{jk}^{(r)} E_k^{(r)} \quad (6.1)$$

where r is the iteration count, n is the number of data points, δ_{ij} is the Kronecker delta function, E_k is the vector of relative errors written as

$$E_k = \frac{T_k^{test} - T_k^{th}}{T_k^{test}} \quad (6.2)$$

and P_{ik} is the partial derivative of the vector of relative errors with respect to a_i

$$P_{ik} = \frac{\partial E_k}{\partial a_i} = -\frac{1}{T_k^{test}} \cdot \frac{\partial T_k^{th}}{\partial a_i} \quad (6.3)$$

After initialising $\alpha_i^{(0)}$, the parameters $\mu_i^{(0)}$ are found with a linear-least squares fit using the following derivatives

$$\frac{\partial T_k^{th}}{\partial \mu_i} = \frac{2}{\alpha_i} (\lambda^{\alpha_i-1} - \lambda^{c\alpha_i-1}) \quad (6.4)$$

$$\frac{\partial T_k^{th}}{\partial \alpha_i} = -\frac{2\mu_i}{\alpha_i^2} (\lambda^{\alpha_i-1} - \lambda^{c\alpha_i-1}) - \frac{2\mu_i}{\alpha_i} (\lambda^{\alpha_i-1} - c\lambda^{c\alpha_i-1}) \ln \lambda \quad (6.5)$$

where

$$c = \begin{cases} -0.5, & \text{if uniaxial} \\ -2.0, & \text{if biaxial} \\ -1.0, & \text{if planar} \end{cases} \quad (6.6)$$

A second order model was found to produce the best quality of fit, with virtually no improvement at higher orders. The constants from the least-squares fit are presented in Table 6.2 and a comparison of the model to the experimental data can be seen in Figure 6.6. The root mean squared error (RMSE) between the experimental data and the analytical Ogden model is 2.2% for the uniaxial case and 5.5% for the equibiaxial case. The pure shear data was excluded from the least-squares fit, and was used instead to further validate the model with a different mode of deformation.

Table 6.2: Material constants for Ogden hyperelastic model used to describe the deformation of the silicone diaphragm material.

Diaphragm material	μ_1 (Pa)	α_1	μ_2 (Pa)	α_2
1.56mm silicone	150904	3.0918	813392	0.18451

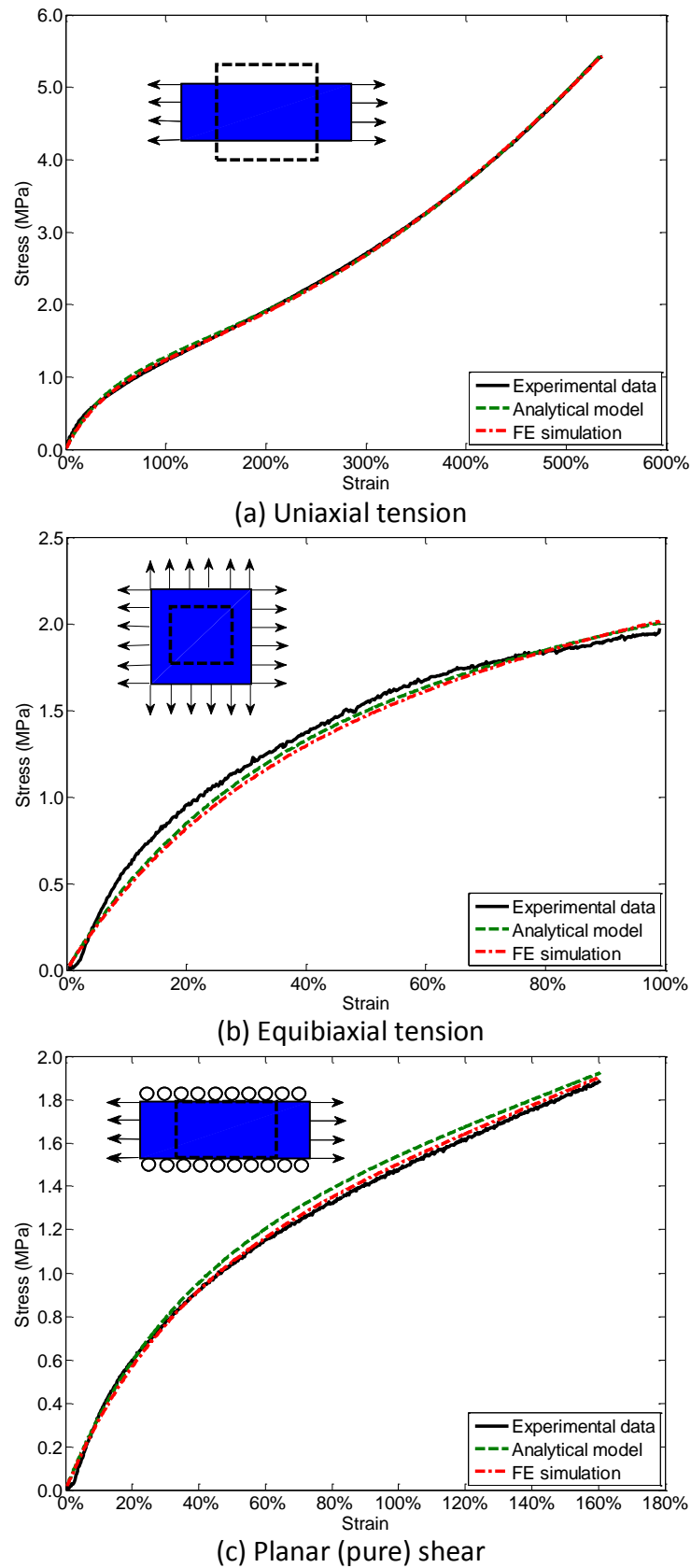


Figure 6.6: Data used to characterise the deformation behaviour of the silicone diaphragms. Experimental data is presented for three load cases and compared by predictions using the Ogden model.

Figure 6.6 shows that the Ogden model adequately captures the response of the silicone diaphragm when subjected to pure shear, with an RMSE of 5.5% compared to the experimental data. The Ogden parameters were implemented into an Abaqus/Explicit simulation using the built-in hyperelastic Ogden model to verify the numerical stability of the fitting parameters, considering the non-linear behaviour of the material. The model passed all of the internal stability checks within Abaqus/Explicit and the mechanical response in a 1-element simulation was identical to the analytical solution for each test case.

6.4 DDF results and discussion

6.4.1 Net shape forming

The initial ply outline of the 2D blank was determined for the geometry presented in Figure 6.2, in order to achieve a net-shaped component. The ply orientation was assumed to be $\pm 45^\circ$ from the NCF material roll (where the 45° fibre orientation was aligned with the x-axis called longitudinal direction and the -45° fibres were aligned with the y-axis called transverse direction in Figure 6.2), as this was the most challenging fibre architecture for the chosen geometry. The initial ply was rectangular (900mm×550mm, see Figure 6.7(a)) and the perimeter shape was revised iteratively according to the forming result obtained from the previous step. Elements positioned outside the final trim line on the formed ply were deleted and the simulation was run again. Multiple iterations were required, since the initial ply shape was too large and fabric bridging occurred around the base of the tool (Figure 6.7(a)). The fabric therefore did not make contact with the tool in all areas, which made it difficult to determine the trim line. Four iterations were required in total to achieve a near net-shaped preform, as shown in Figure 6.2.

The simulation results presented in Figure 6.7 demonstrate some of the forming defects that occur, such as out-of-plane wrinkling and excessive local shear, but the most dominant defect is fabric bridging due to the deformable diaphragms.

6.4.2 DDF defect detection

Fabric bridging is typically quantified in forming simulations as a measured distance between the formed surface and the tool, and is a characteristic of the conformity of the fabric. However, bridging may be detected at the same position on the component for a $0^\circ/90^\circ$ ply

and a $\pm 45^\circ$ ply, but different solutions may be required to improve the fabric conformity for the two cases. Hence, additional criteria are required to support the conventional distance measurement, in order to overcome fabric bridging.

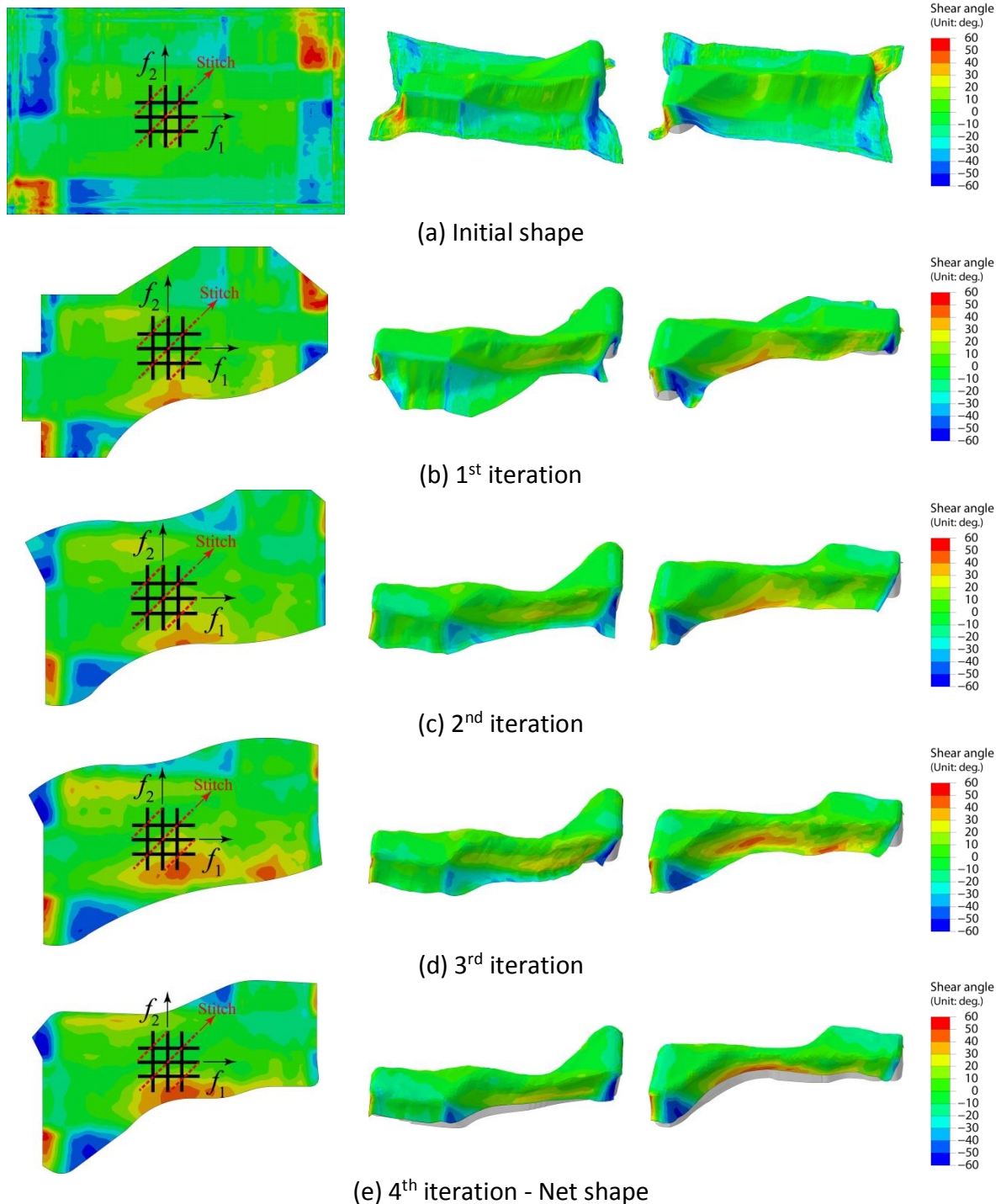


Figure 6.7: Iterations of net ply shape formed by DDF for biaxial $\pm 45^\circ$ ply with 0° stitches from NCF material roll. Undeformed ply shape (left column), different views of deformed ply shapes (middle and right column).

As shown in Figure 6.8, the resultant force from the pressure differential discussed in Figure 6.5 generates the forming forces to drive the fabric onto the tool surface. However, it also

simultaneously generates a friction force which constrains the material sliding. Whilst a high vacuum pressure increases the forming force, a corresponding increase in in-plane friction may make it difficult to overcome fabric bridging, particularly for deep concave features. If bridging occurs, the fibres carry the forming forces applied in the bridging area. Yarns are locally pinned and material movement becomes constrained, preventing draw into the cavity. This results in the generation of considerable local tensile stresses in the primary yarns around concave sections of the tool, and has therefore been defined here as the “bridging stress”. The bridging stress enables the cause of bridging to be identified, i.e. the location and direction of bridging yarns.

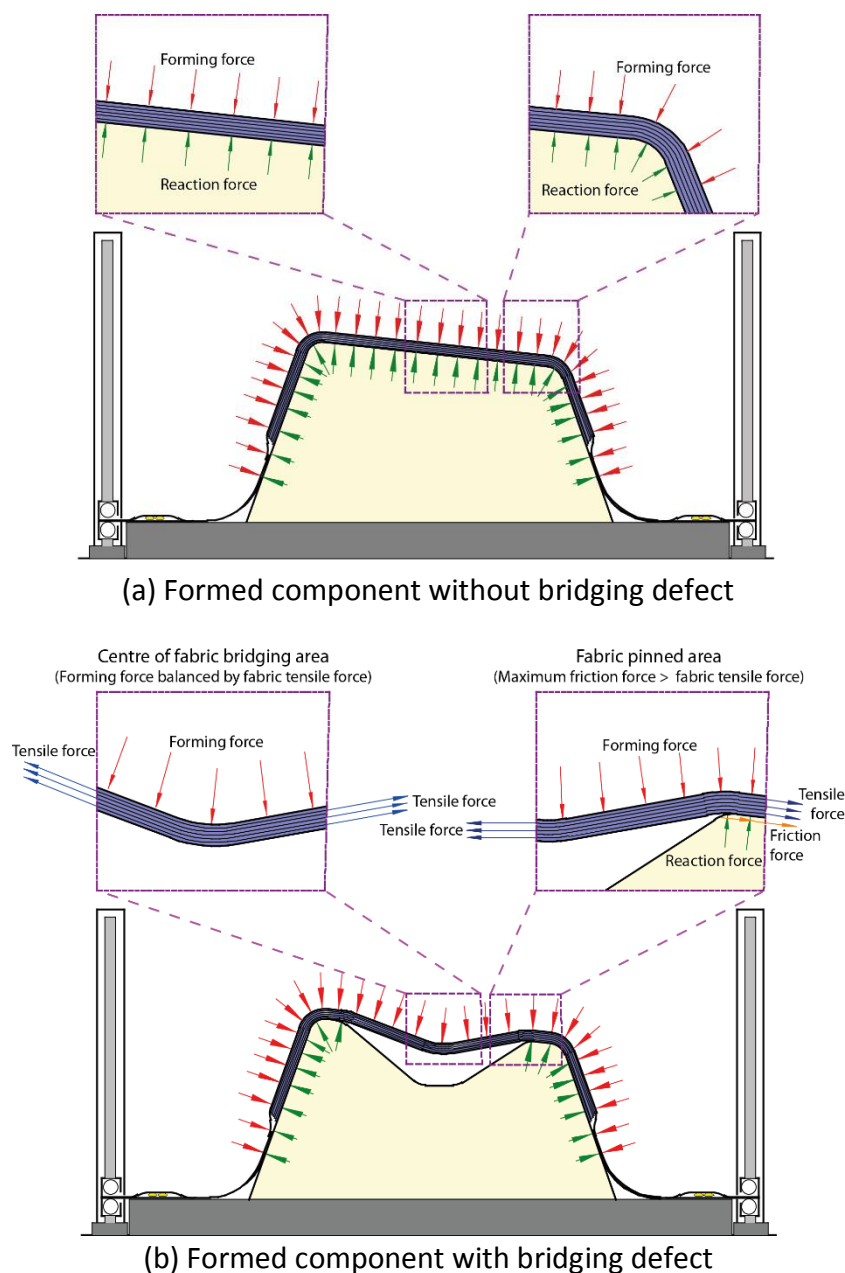
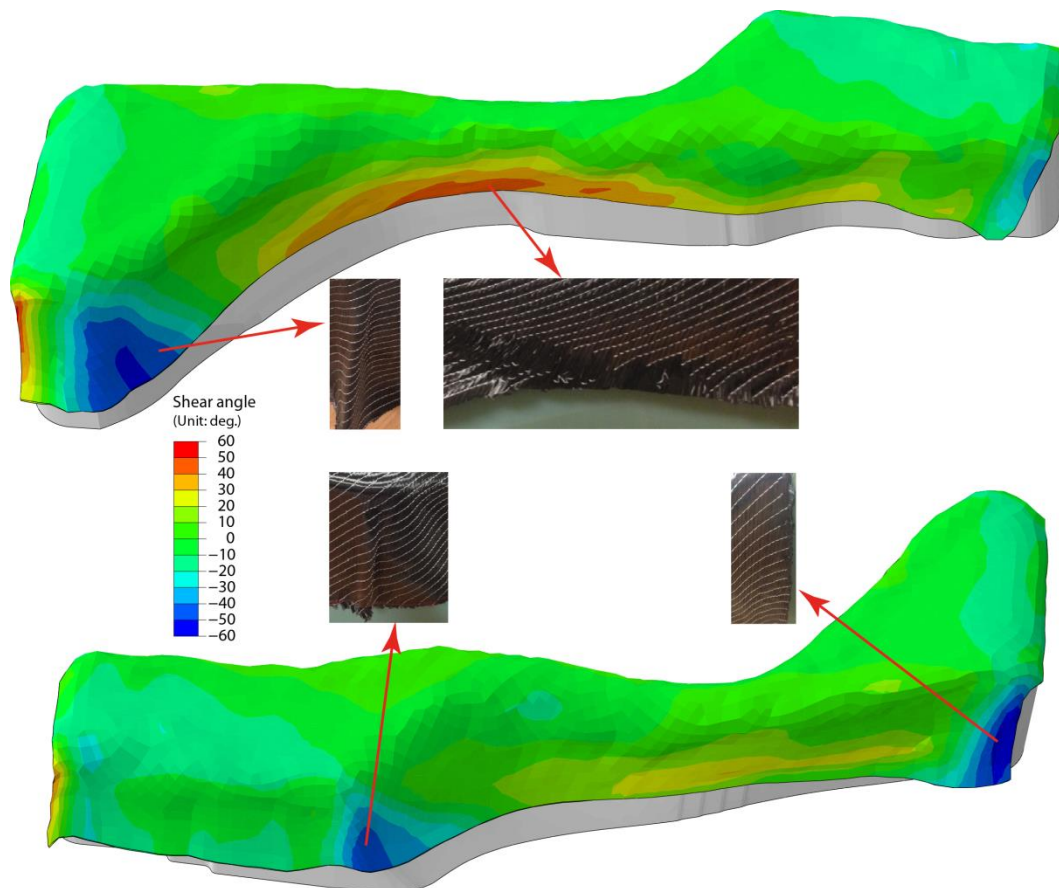


Figure 6.8: Roles of forming pressure and mechanism of bridging defect.

The laboratory diaphragm forming machine in Figure 6.1 has been used to validate the model, forming the case study component presented in Figure 6.2. Two plies of biaxial FCIM359 NCF were cut to the net-shape shown in Figure 6.7(e), with the 45° fibres aligned in the x-direction and the pillar stitches running at 45° . Figure 6.9 indicates that there is very good agreement between the simulation and experiment in terms of the formed shape, including the ply outline. Both include similar defects and three different field variables have been evaluated from the simulation to investigate their cause. These are defined as the local shear angle, the wrinkling strain (negative strains along the principal yarns) and the bridging stress (positive stresses along the principal yarns).

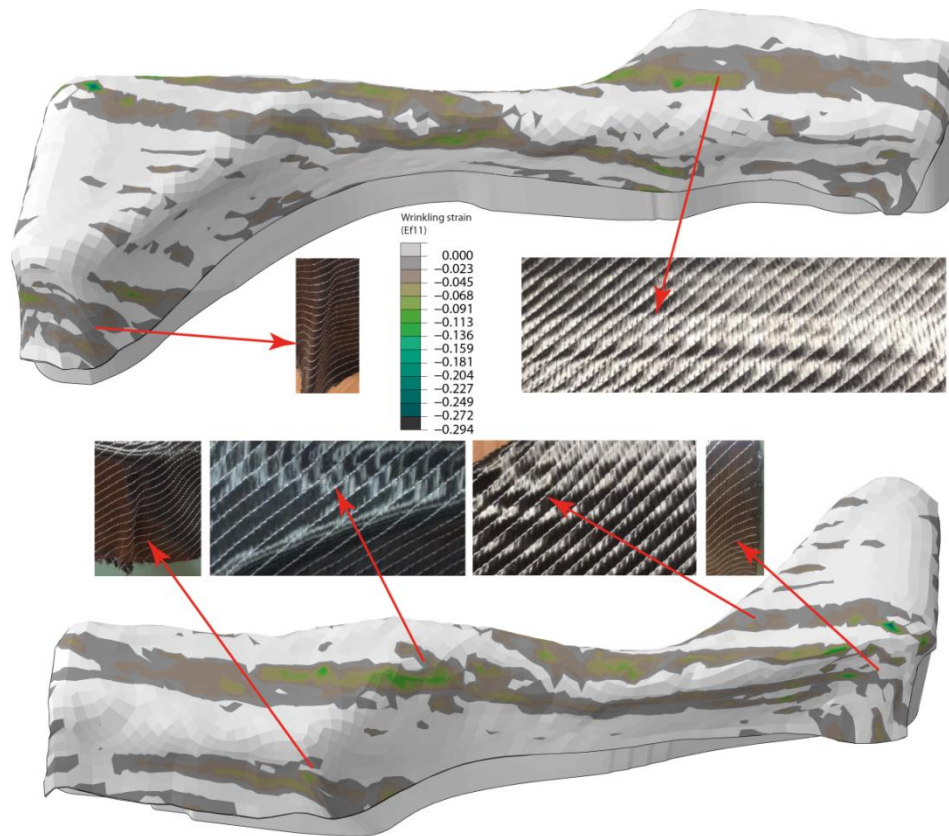


(a) Experiment

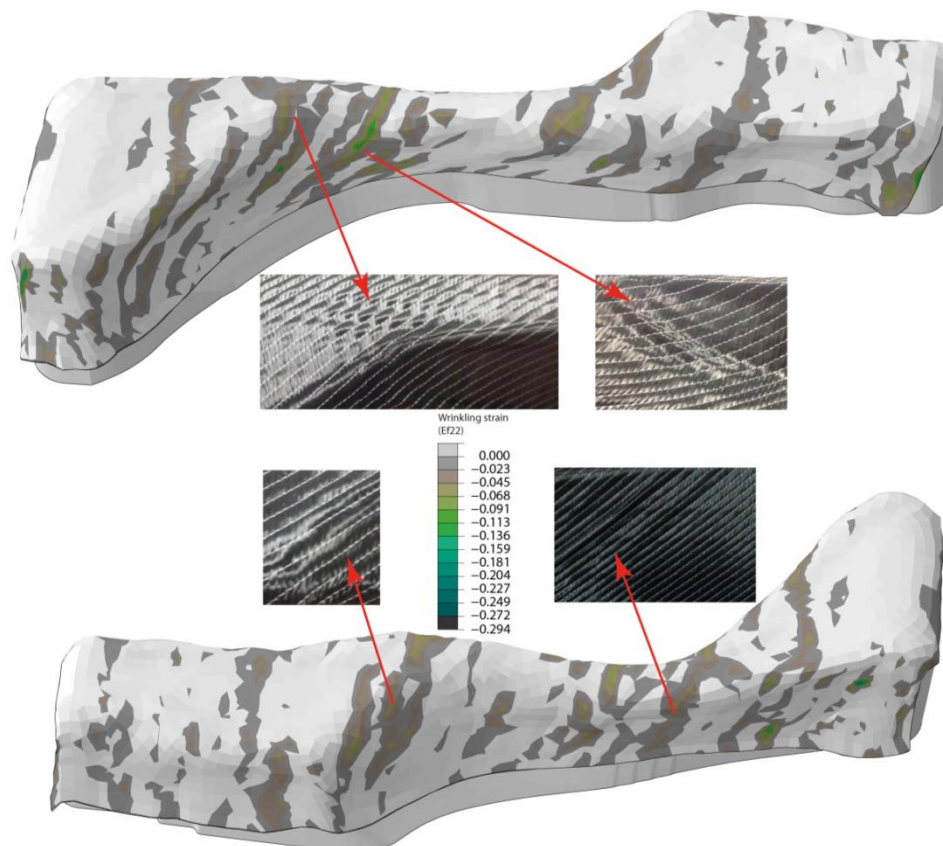


(b) Simulation: Shear angle distribution

Figure 6.9: Comparison of shear angle distribution and experimental geometry for a biaxial $\pm 45^\circ$ ply with 0° stitches, formed by double diaphragm forming.

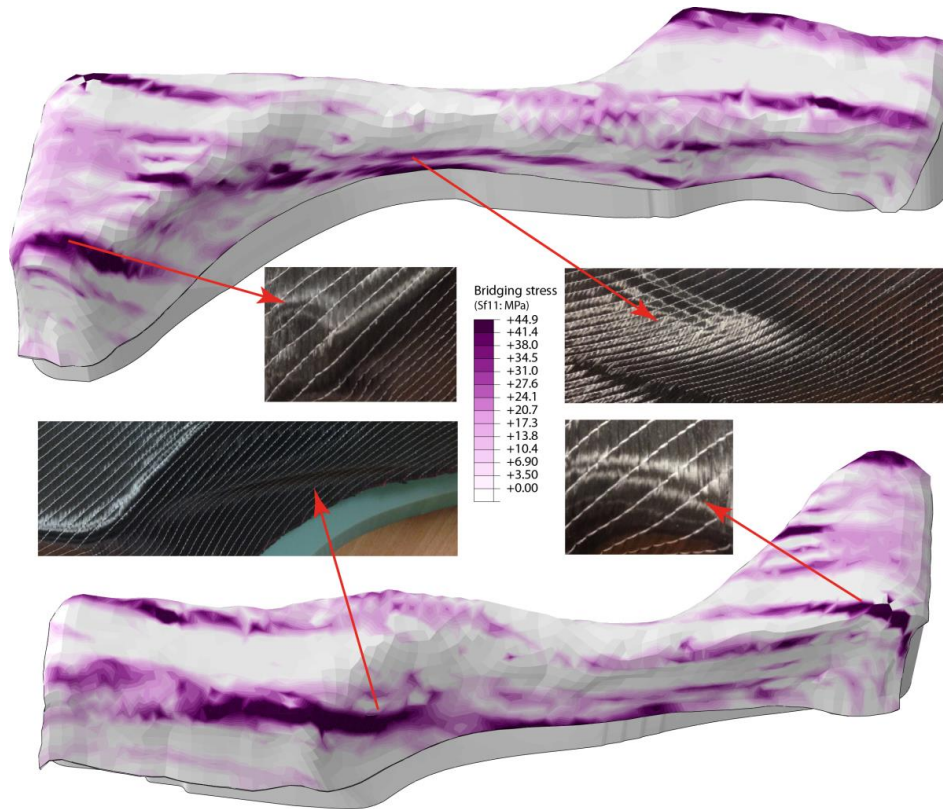


(a) Wrinkling strain along +45° yarns in x-direction

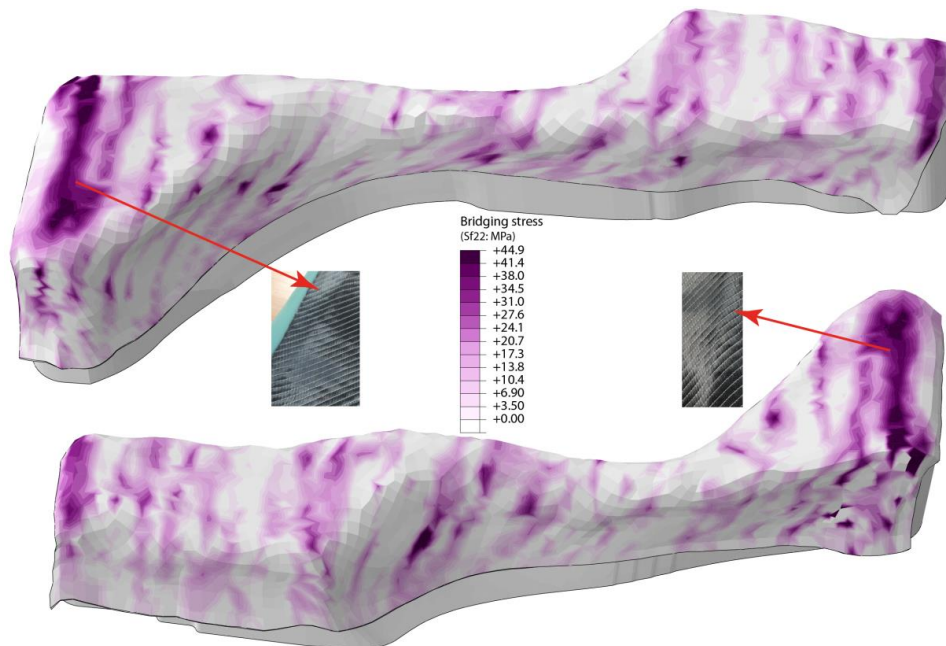


(b) Wrinkling strain along -45° yarns in y-direction

Figure 6.10: Wrinkling strains along two primary yarn directions.



(a) Bridging stress along +45° yarns in x-direction



(b) Bridging stress along -45° yarns in y-direction

Figure 6.11: Bridging stress along the two primary yarn directions.

The shear angle distribution (see Figure 6.9(b)) represents over-shear induced defects, which can cause out-of-plane wrinkling and intra-ply stitch rupture under positive shear (see Section 3.5). In the positive shear areas (shear angles greater than 0°), there are some regions which

experience shear angles of over 50° (see red area in Figure 6.9(b)), indicating that stitch rupture has occurred. This is in agreement with the experiment, as shown by the inset images. In negative shear areas, over-sheared regions (see blue area in Figure 6.9(b)) represent the occurrence of out-of-plane ply wrinkling induced by over-shearing. These wrinkling defects were also observed in the experiment. However, the exact out-of-plane wrinkling shape cannot be precisely predicted using the current material model, since the bending stiffness is not included and the shear angle is only an indicator of macro-scale wrinkling defect.

Wrinkling strains (negative strains along the principal yarns) are plotted along the two primary yarn directions, in Figure 6.10. Wrinkling strains were relatively low (for example in comparison to results from matched tool forming in Section 3.5), therefore mesoscale wrinkling due to yarn buckling (negative strains) was limited to some minor regions on the top surface of the formed part (green contours), as indicated by the photos.

The dominant defect for DDF was observed to be fabric bridging in this study, as shown in Figure 6.11. Bridging was more severe along the 45° yarns in the x-direction (see Figure 6.11(a)) than the -45° yarns in the y-direction (Figure 6.11(b)). Comparisons with the experimental results indicate that the “bridging stress”, where the tensile stress in the direction of the fibre exceeds 35MPa, is an appropriate metric for predicting the likelihood of defects caused by bridging. The bridging stress output from an FE solution can be used to identify the location and orientation of yarns in tension that induce bridging defects, in order to improve the quality of the formed shape.

In addition, some wrinkling defects were observed as a side effect of fabric bridging, due to Poisson’s ratio contraction effects of the diaphragms. As shown in Figure 6.11(a), two significant areas of fabric bridging occurred around the large curvature area as the yarns in the x-direction were in tension. However, the yarns in the y-direction in same areas were unconstrained, and therefore the fabric was more compliant in this direction, inducing wrinkles.

6.4.3 Scenarios for bridging reduction

In order to reduce the fibre bridging defect, the forming mechanism should involve rigid body movement (yarn rotation and slippage) rather than fibre elongation. Shear deformation occurs by rotation of the yarns, which is limited by the phenomenon of shear locking (see

Section 3.5). In DDF, the most effective solution for avoiding bridging is to delay contact between the diaphragm assembly (two diaphragms plus fabric plies) and the tool surfaces. Rigid body movement of the yarns should be generated progressively, as the contact area increases.

In order to increase material draw-in in the present work, darts (local cuts) were added to the optimised ply shape shown in Figure 6.12(a). Darts were positioned to reduce the high tensile stresses in the longitudinal yarns (x-direction), which were the main cause of the severe bridging regions. Darts were cut perpendicular to these yarns in order to minimise the damage to the transverse yarns, as shown Figure 6.12(b). Darts were only permitted on the near vertical sides of the component and not on the top surface, as these fibres coincide with the primary load path. It is important to note that additional plies at different angles would be added to this single ply to manufacture the final component. Therefore the openings created by the darts would be covered by neighbouring plies, or small patches of material, to satisfy secondary load cases.

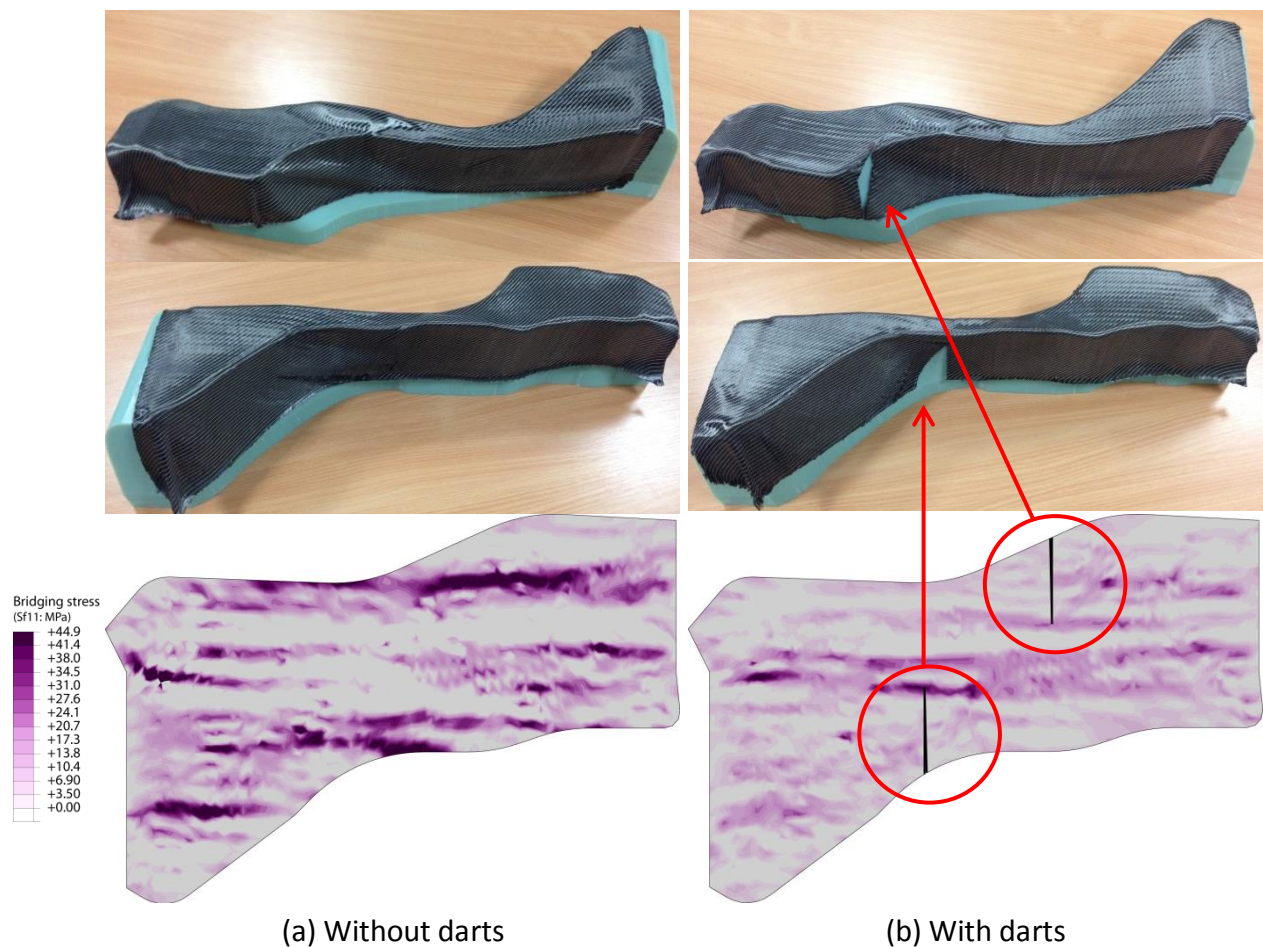


Figure 6.12: Influence of placing local darts on reducing bridging defects.

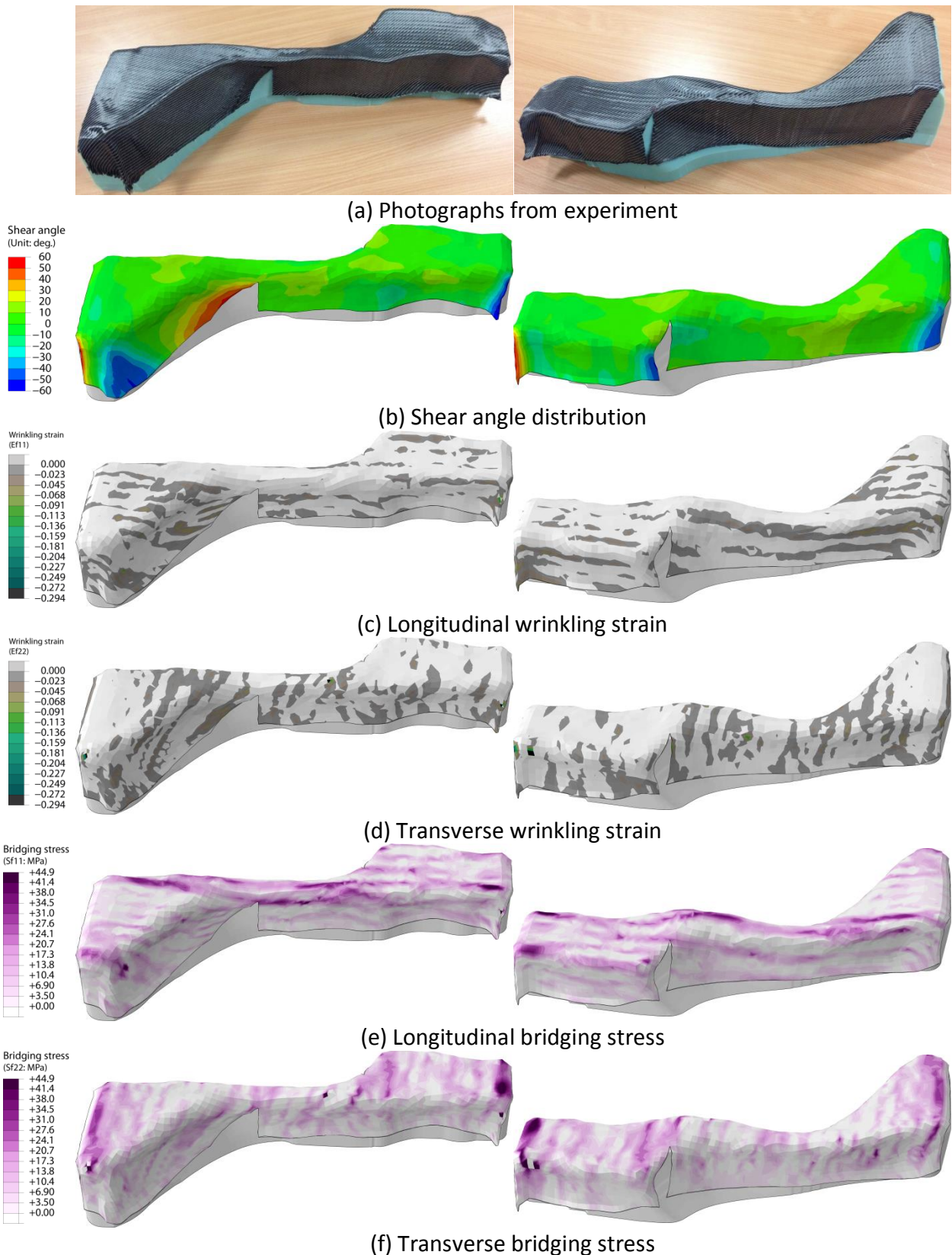


Figure 6.13: Defect detection for preforms with local darts.

Both FE simulations and experiments were conducted using the modified ply shape and results were compared against the case without darts as shown in Figure 6.13. Bridging was effectively reduced by adding darts, compared to the case without darts. The results from the

simulation are in agreement with the experimental data, showing that the model can suitably capture the effect of fabric darts. Furthermore, this study demonstrates that the “bridging stress” is a feasible way of determining potential bridging sites and identifying the yarns responsible. In the present work, placing darts perpendicular to the bridging yarns appears to have had no adverse effect on the surrounding fibre architecture, as seen from the experimental data.

As shown in Figure 6.13, the wrinkling and over-shear induced defects decrease simultaneously as the number of bridging fibres decreases. This indicates that bridging is the dominating defect in DDF, and a reduction of bridging may result in reduction of other forming defects. Applying suitable darts helps to overcome bridging-induced yarn wrinkling and release fabric shear locking, providing better fabric conformity.

6.5 Chapter summary

A forming simulation was developed to model the behaviour of a biaxial non-crimp fabric during double diaphragm forming. The model is used to identify the likelihood of defects occurring during forming of a generic automotive structure, using three different field variables; local shear angle, wrinkling strain and bridging stress. The model indicated that in-plane wrinkling is generally reduced for DDF compared to matched-tool forming, but fabric bridging can occur in large-curvature regions. Bridging is the dominant defect for diaphragm forming, as the forming pressures are relatively low (up to 1 bar) compared to matched tool forming. The fabric gets pinned between two points on the tool by the applied pressure, preventing further rigid body movement such as yarn rotation or inter-ply slippage. The finite element simulation was successfully used to identify feasible locations for darts, in order to alleviate fabric bridging and improve surface conformity, whilst minimising any detrimental effects on the mechanical performance of the component.

Chapter 7 Conclusions

The aim of this chapter is to summarise the primary conclusions drawn from this research. The conclusions are divided into two key areas to follow the outline of the thesis; (I) material characterisation and modelling, (II) process simulation and optimisation.

7.1 Fabric characterisation and modelling

Woven fabric and NCF were characterised based on a non-orthogonal constitutive framework, enabling the orientation of primary yarns to be tracked at the macro-scale. An explicit finite element (FE) algorithm was employed to simulate either symmetric or asymmetric fabric behaviour during preforming and to predict forming-induced defects. Comparisons between simulation results and experimental data indicate:

- i. The non-orthogonal constitutive model is able to replicate realistic fibre re-orientation for both biaxial woven fabrics and NCFs during preforming. Both symmetric and asymmetric material behaviours are precisely simulated and realistic forming defects are captured under this framework, taking into account different fabric types.
- ii. There is a compromise between fabric formability and handleability. Woven fabric shows superior formability, but it is unstable during handling, making automated fibre placement difficult. The architecture of the NCF with pillar stitches is more stable, but the formability is compromised and there is the likelihood of additional manufacturing defects during forming compared to the woven material of the same areal mass.
- iii. Different defect types have been identified for different fabric architectures and different forming processes. In matched tool forming, two types of wrinkling defects have been identified. One is out-of-plane wrinkling (macro-scale wrinkling) induced by excessive shear, while the other is in-plane wrinkling (meso-scale wrinkling) caused by fibre compression. Wrinkling position, mode and mechanism can be determined by correlating the local distributions of shear angle and wrinkling strain, where wrinkling strain (negative fibre strain or compressive strain) represents the occurrence of wrinkling and the shear angle distribution is used to confirm whether the identified defect can be attributed to over-shear induced out-of-plane wrinkling or not. Fabric bridging is the

dominant defect in diaphragm forming, as the forming pressures are relatively low (up to 1 bar) compared to matched tool forming. The fabric gets pinned between two points on the tool by the applied pressure, preventing further rigid body movement such as yarn rotation or inter-ply slippage.

7.2 Process simulation and optimisation

The numerical simulation was employed in process design and optimisation to either improve forming quality, or facilitate automated fabric handling, for different fibre architectures. The process simulation and optimisation results indicate that:

- i. Inter-ply stitches can be introduced to facilitate automatic handling, but local stitch-bonds influence the global shear angle distribution rather than having just a localised effect. Thus, placing stitch bonds is not an intuitive process. Optimised patterns of through-thickness stitches can improve the formability of a multi-ply preform compared with an unstitched benchmark. Load paths are adjusted globally due to strain redistribution through the localised stitches, resulting in a more uniform shear angle distribution.
- ii. Fabric forming behaviour can also be partially controlled by arranging in-plane constraints during matched tool forming, using either a segmented blank holder or a set of spring-loaded clamps. Spring-loaded clamps can effectively homogenise the global shear angle distribution and minimise the local maximum value, but the peak compressive strains are found to be higher than when using a segmented blank holder constraint. Therefore, the application of blank holders contributes to reduce the potential of wrinkling by providing extra resistance in the normal direction.
- iii. The double diaphragm forming process can be used to produce complex net shape preforms. Placing darts is one potential way to overcome manufacturing defects such as fabric bridging. The bridging stress determined from the FE analysis can be employed to identify feasible locations for darts to improve surface conformity, whilst minimising any detrimental effects on the mechanical performance of the component.

References

- [1] Middendorf, P. and C. Metzner, *18 - Aerospace applications of non-crimp fabric composites*, in *Non-Crimp Fabric Composites*, S.V. Lomov, Editor. 2011, Woodhead Publishing. p. 441-448.
- [2] Sköck-Hartmann, B. and T. Gries, *20 - Automotive applications of non-crimp fabric composites*, in *Non-Crimp Fabric Composites*, S.V. Lomov, Editor. 2011, Woodhead Publishing. p. 461-480.
- [3] Mallick, P.K., *Fiber-reinforced composites: materials, manufacturing, and design*. 2007: CRC press.
- [4] Chand, S., *Review carbon fibers for composites*. Journal of Materials Science, 2000. **35**(6): p. 1303-1313.
- [5] Sherman, D., *2012 McLaren MP4-12C - First drive review*, <<http://www.caranddriver.com/reviews/2012-mclaren-mp4-12c-first-drive-review-tech-trickledown-page-2>>. Accessed June 2016.
- [6] Taylor, J., *BMW M3: The Complete Story*. 2014, New York: Crowood.
- [7] Fuchs, H., *Development and Build of the Ford Focus Fcv Light—weight Carbon Fiber Decklid*. New York: SPE Automotive and Composites Divisions, 2007: p. 436-455.
- [8] Lieven, T., S. Mühlmeier, S. Henkel, and J.F. Waller, *Who will buy electric cars? An empirical study in Germany*. Transportation Research Part D: Transport and Environment, 2011. **16**(3): p. 236-243.
- [9] Automotive Council UK. *Automotive technology roadmaps*, <<http://www.automotivecouncil.co.uk/wp-content/uploads/2013/09/Automotive-Council-Roadmaps.pdf>>. 2013.
- [10] Chai, X., H. Mi, C. Zhu, C. He, J. Xu, X. Zhou, and J. Liu, *Low-temperature thermal stabilization of polyacrylonitrile-based precursor fibers towards efficient preparation of carbon fibers with improved mechanical properties*. Polymer, 2015. **76**: p. 131-139.
- [11] Kim, S.Y., S.-Y. Kim, J. Choi, S. Lee, S.M. Jo, J. Joo, and H.-S. Lee, *Two step microwave plasma carbonization including low plasma power pre-carbonization for polyacrylonitrile based carbon fiber*. Polymer, 2015. **69**: p. 123-128.
- [12] Mainka, H., O. Täger, E. Körner, L. Hilfert, S. Busse, F.T. Edelmann, and A.S. Herrmann, *Lignin—an alternative precursor for sustainable and cost-effective automotive carbon fiber*. Journal of Materials Research and Technology, 2015. **4**(3): p. 283-296.
- [13] Mitschang, P. and K. Hildebrandt, *8 – Polymer and composite moulding technologies for automotive applications*, in *Advanced materials in automotive engineering*, J. Rowe, Editor. 2012, Elsevier. p. 210-229.
- [14] Dumont, F., C. Weimer, D. Soulat, J. Launay, S. Chatel, and S. Maison-Le-Poec, *Composites preforms simulations for helicopters parts*. International Journal of Material Forming, 2008. **1**(1): p. 847-850.
- [15] Meyer, B.C., C.V. Katsiropoulos, and S.G. Pantelakis, *Hot forming behavior of non-crimp fabric peek/c thermoplastic composites*. Composite Structures, 2009. **90**(2): p. 225-232.
- [16] Long, A.C., *Introduction*, in *Design and manufacture of textile composites*, A.C. Long, Editor. 2005, Elsevier. p. xiii-xvi.

- [17] Snudden, J., C. Ward, and K. Potter, *Reusing automotive composites production waste*. Reinforced Plastics, 2014. **58**(6): p. 20-27.
- [18] Job, S., *Composite recycling—summary of recent research and development*. Materials KTN Report, 2010: p. 26-42.
- [19] Long, A.C., *Design and manufacture of textile composites*. 2005: CRC press.
- [20] Coupé, D., *Woven reinforcements for composites*, in *Composite reinforcements for optimum performance*, P. Boisse, Editor. 2011, Elsevier. p. 89-115.
- [21] Lomov, S.V., M. Barburski, T. Stoilova, I. Verpoest, R. Akkerman, R. Loendersloot, and R.H.W.t. Thijs, *Carbon composites based on multiaxial multiply stitched preforms. Part 3: Biaxial tension, picture frame and compression tests of the preforms*. Composites Part A: Applied Science and Manufacturing, 2005. **36**(9): p. 1188-1206.
- [22] Lee, J.S., S.J. Hong, W.-R. Yu, and T.J. Kang, *The effect of blank holder force on the stamp forming behavior of non-crimp fabric with a chain stitch*. Composites Science and Technology, 2007. **67**(3–4): p. 357-366.
- [23] Creech, G. and A.K. Pickett, *Meso-modelling of Non-Crimp Fabric composites for coupled drape and failure analysis*. Journal of Materials Science, 2006. **41**(20): p. 6725-6736.
- [24] Long, A.C., *Composites forming technologies*. 2014: Elsevier.
- [25] Hivet, G. and P. Boisse, *Consistent mesoscopic mechanical behaviour model for woven composite reinforcements in biaxial tension*. Composites Part B: Engineering, 2008. **39**(2): p. 345-361.
- [26] Boisse, P., M. Borr, K. Buet, and A. Cherouat, *Finite element simulations of textile composite forming including the biaxial fabric behaviour*. Composites Part B: Engineering, 1997. **28**(4): p. 453-464.
- [27] Hamila, N., P. Boisse, F. Sabourin, and M. Brunet, *A semi - discrete shell finite element for textile composite reinforcement forming simulation*. International journal for numerical methods in engineering, 2009. **79**(12): p. 1443-1466.
- [28] Boisse, P., Y. Aimène, A. Dogui, S. Dridi, S. Gatouillat, N. Hamila, M.A. Khan, T. Mabrouki, F. Morestin, and E. Vidal-Sallé, *Hypoelastic, hyperelastic, discrete and semi-discrete approaches for textile composite reinforcement forming*. International journal of material forming, 2010. **3**(2): p. 1229-1240.
- [29] Boisse, P., B. Zouari, and J.-L. Daniel, *Importance of in-plane shear rigidity in finite element analyses of woven fabric composite preforming*. Composites Part A: Applied Science and Manufacturing, 2006. **37**(12): p. 2201-2212.
- [30] Prodromou, A. and J. Chen, *On the relationship between shear angle and wrinkling of textile composite preforms*. Composites Part A: Applied Science and Manufacturing, 1997. **28**(5): p. 491-503.
- [31] Tam, A.S. and T.G. Gutowski, *The kinematics for forming ideal aligned fibre composites into complex shapes*. Composites Manufacturing, 1990. **1**(4): p. 219-228.
- [32] Boisse, P., *Composite reinforcements for optimum performance*. 2011: Elsevier.
- [33] Li, L., Y. Zhao, H.-g.-n. Vuong, Y. Chen, J. Yang, and Y. Duan, *In-plane shear investigation of biaxial carbon non-crimp fabrics with experimental tests and finite element modeling*. Materials & Design, 2014. **63**: p. 757-765.

- [34] Bel, S., N. Hamila, P. Boisse, and F. Dumont, *Finite element model for NCF composite reinforcement preforming: Importance of inter-ply sliding*. Composites Part A: Applied Science and Manufacturing, 2012. **43**(12): p. 2269-2277.
- [35] Gereke, T., O. Döbrich, M. Hübner, and C. Cherif, *Experimental and computational composite textile reinforcement forming: A review*. Composites Part A: Applied Science and Manufacturing, 2013. **46**: p. 1-10.
- [36] Cao, J., R. Akkerman, P. Boisse, J. Chen, H. Cheng, E. De Graaf, J. Gorczyca, P. Harrison, G. Hivet, and J. Launay, *Characterization of mechanical behavior of woven fabrics: experimental methods and benchmark results*. Composites Part A: Applied Science and Manufacturing, 2008. **39**(6): p. 1037-1053.
- [37] Harrison, P., M. Clifford, and A. Long, *Shear characterisation of viscous woven textile composites: a comparison between picture frame and bias extension experiments*. Composites Science and Technology, 2004. **64**(10): p. 1453-1465.
- [38] Peng, X., J. Cao, J. Chen, P. Xue, D. Lussier, and L. Liu, *Experimental and numerical analysis on normalization of picture frame tests for composite materials*. Composites Science and Technology, 2004. **64**(1): p. 11-21.
- [39] Lomov, S.V., P. Boisse, E. Deluycker, F. Morestin, K. Vanclooster, D. Vandepitte, I. Verpoest, and A. Willems, *Full-field strain measurements in textile deformability studies*. Composites Part A: Applied Science and Manufacturing, 2008. **39**(8): p. 1232-1244.
- [40] Khan, M.A., *Numerical and Experimental Forming Analyses of Textile Composite Reinforcements Based on a Hypoelastic Behaviour*. 2009.
- [41] Boisse, P., N. Hamila, E. Guzman-Maldonado, A. Madeo, G. Hivet, and F. Dell'Isola, *The bias-extension test for the analysis of in-plane shear properties of textile composite reinforcements and preregs: a review*. International Journal of Material Forming, 2016: p. 1-20.
- [42] Kong, H., A.P. Mouritz, and R. Paton, *Tensile extension properties and deformation mechanisms of multiaxial non-crimp fabrics*. Composite Structures, 2004. **66**(1-4): p. 249-259.
- [43] Schirmaier, F.J., K.A. Weidenmann, L. Kärger, and F. Henning, *Characterisation of the draping behaviour of unidirectional non-crimp fabrics (UD-NCF)*. Composites Part A: Applied Science and Manufacturing, 2016. **80**: p. 28-38.
- [44] Krieger, H., A. Schnabel, L. Appel, and T. Gries, *Experimental setup to validate textile material models for drape simulation*. Key Engineering Materials, 2013. **554-557**: p. 456-464.
- [45] Harrison, P., *Normalisation of biaxial bias extension test results considering shear tension coupling*. Composites Part A: Applied Science and Manufacturing, 2012. **43**(9): p. 1546-1554.
- [46] Buet-Gautier, K. and P. Boisse, *Experimental analysis and modeling of biaxial mechanical behavior of woven composite reinforcements*. Experimental mechanics, 2001. **41**(3): p. 260-269.
- [47] Khan, M.A., T. Mabrouki, E. Vidal-Salle, and P. Boisse, *Numerical and experimental analyses of woven composite reinforcement forming using a hypoelastic behaviour. Application to the double dome benchmark*. Journal of materials processing technology, 2010. **210**(2): p. 378-388.
- [48] Badel, P., S. Gauthier, E. Vidal-Sallé, and P. Boisse, *Rate constitutive equations for computational analyses of textile composite reinforcement mechanical behaviour during forming*. Composites Part A: Applied Science and Manufacturing, 2009. **40**(8): p. 997-1007.

- [49] Boisse, P., N. Hamila, E. Vidal-Sallé, and F. Dumont, *Simulation of wrinkling during textile composite reinforcement forming. Influence of tensile, in-plane shear and bending stiffnesses*. Composites Science and Technology, 2011. **71**(5): p. 683-692.
- [50] Kawabata, S., *The standardization and analysis of hand evaluation*. 1980: Textile Machinery Society of Japan.
- [51] Peirce, F.T., *5—the geometry of cloth structure*. Journal of the Textile Institute Transactions, 1937. **28**(3): p. T45-T96.
- [52] *ASTM Standard test method for stiffness of fabrics-ch. D1388-96*. American S. for Testing. 2002.
- [53] De Bilbao, E., D. Soulat, G. Hivet, and A. Gasser, *Experimental study of bending behaviour of reinforcements*. Experimental Mechanics, 2010. **50**(3): p. 333-351.
- [54] Potter, K. and C. Ward, *5 - Draping processes for composites manufacture*, in *Advances in Composites Manufacturing and Process Design*, P. Boisse, Editor. 2015, Woodhead Publishing. p. 93-109.
- [55] Bersee, H.E.N., S. Lindstedt, G. Nino, and A. Beukers, *Diaphragm forming of thermoset composites*, in *16th International Conference on Composite Materials*. 2007: Kyoto, Japan.
- [56] Friedrich, K., M. Hou, and J. Krebs, *Chapter 4 Thermoforming of continuous fibre/thermoplastic composite sheets*, in *Composite Materials Series*, D. Bhattacharyya, Editor. 1997, Elsevier. p. 91-162.
- [57] Pantelakis, S.G. and E.A. Baxevani, *Optimization of the diaphragm forming process with regard to product quality and cost*. Composites Part A: Applied Science and Manufacturing, 2002. **33**(4): p. 459-470.
- [58] Delaloye, S. and M. Niedermeier, *Optimization of the diaphragm forming process for continuous fibre-reinforced advanced thermoplastic composites*. Composites Manufacturing, 1995. **6**(3-4): p. 135-144.
- [59] Alshaharni, H. and M. Hojjati. *Optimum processing parameters for hot drape forming of out-of-autoclave prepreg over complex shapes using a double diaphragm technique*. in *20th Internation Conference on Composite Materials*. 2015. Copenhagen.
- [60] Bian, X.X., Y.Z. Gu, J. Sun, M. Li, W.P. Liu, and Z.G. Zhang, *Effects of Processing Parameters on the Forming Quality of C-Shaped Thermosetting Composite Laminates in Hot Diaphragm Forming Process*. Applied Composite Materials, 2013. **20**(5): p. 927-945.
- [61] Sun, J., Y. Gu, M. Li, X. Ma, and Z. Zhang, *Effect of forming temperature on the quality of hot diaphragm formed C-shaped thermosetting composite laminates*. Journal of Reinforced Plastics and Composites, 2012. **31**(16): p. 1074-1087.
- [62] Dumont, F. and C. Weimer, *19 - Non-crimp fabric: preforming analysis for helicopter applications*, in *Non-Crimp Fabric Composites*, S.V. Lomov, Editor. 2011, Woodhead Publishing. p. 449-460.
- [63] Leutz, D., M. Kluepfel, F. Dumont, R. Hinterhoelzl, K. Drechsler, and C. Weimer. *FE - Simulation of the Diaphragm Draping Process for NCF on a Macro - Scale Level*. in *THE 14TH INTERNATIONAL ESAFORM CONFERENCE ON MATERIAL FORMING*. 2011. AIP Publishing.
- [64] Margossian, A., S. Bel, J. Balvers, D. Leutz, R. Freitas, and R. Hinterhoelzl, *Finite element forming simulation of locally stitched non-crimp fabrics*. Composites Part A: Applied Science and Manufacturing, 2014. **61**: p. 152-162.

- [65] Luby, S. and E. Bernardon, *Design of fabric preforms for double diaphragm forming*, in *Ninth DOD(NASA)FAA Conference on Fibrous Composites in Structural Design*. 1995: Draper (Charles Stark) Lab., Inc.; Cambridge, MA, United States. p. 1175-1184.
- [66] Krebs, J., K. Friedrich, and D. Bhattacharyya, *A direct comparison of matched-die versus diaphragm forming*. *Composites Part A: Applied Science and Manufacturing*, 1998. **29**(1-2): p. 183-188.
- [67] Krebs, J., D. Bhattacharyya, and K. Friedrich, *Production and evaluation of secondary composite aircraft components—a comprehensive case study*. *Composites Part A: Applied Science and Manufacturing*, 1997. **28**(5): p. 481-489.
- [68] Gutowski, T.G., G. Dillon, S. Chey, and H. Li, *Laminate wrinkling scaling laws for ideal composites*. *COMPOSITES MANUFACTURING*, 1995. **6**(3): p. 123-134.
- [69] Bersee, H.E.N. and A. Beukers, *Diaphragm forming of continuous fibre reinforced thermoplastics: influence of temperature, pressure and forming velocity on the forming of Upilex-R® diaphragms*. *Composites Part A: Applied Science and Manufacturing*, 2002. **33**(7): p. 949-958.
- [70] O'Brádaigh, C.M., R.B. Pipes, and P.J. Mallon, *Issues in diaphragm forming of continuous fiber reinforced thermoplastic composites*. *Polymer Composites*, 1991. **12**(4): p. 246-256.
- [71] Hallander, P., M. Akermo, C. Mattei, M. Petersson, and T. Nyman, *An experimental study of mechanisms behind wrinkle development during forming of composite laminates*. *Composites Part A: Applied Science and Manufacturing*, 2013. **50**: p. 54-64.
- [72] Hallander, P., J. Sjölander, and M. Åkermo, *Forming induced wrinkling of composite laminates with mixed ply material properties; an experimental study*. *Composites Part A: Applied Science and Manufacturing*, 2015. **78**: p. 234-245.
- [73] Van Der Weeën, F., *Algorithms for draping fabrics on doubly - curved surfaces*. *International journal for numerical methods in engineering*, 1991. **31**(7): p. 1415-1426.
- [74] Skordos, A.A., M.P. Sutcliffe, J. Klintworth, and P. Adolfsson, *Multi-Objective Optimisation of Woven Composite Draping using Genetic Algorithms*. 2006.
- [75] Pickett, A.K., G. Creech, and P. de Luca, *Simplified and advanced simulation methods for prediction of fabric draping*. *Revue Européenne des Éléments*, 2005. **14**(6-7): p. 677-691.
- [76] Hancock, S. and K. Potter, *Inverse drape modelling—an investigation of the set of shapes that can be formed from continuous aligned woven fibre reinforcements*. *Composites Part A: Applied Science and Manufacturing*, 2005. **36**(7): p. 947-953.
- [77] Robertson, R., T.-J. Chu, R. Gerard, J.-H. Kim, M. Park, H.-G. Kim, and R. Peterson, *Three-dimensional fiber reinforcement shapes obtainable from flat, bidirectional fabrics without wrinkling or cutting. Part 1. A single four-sided pyramid*. *Composites Part A: Applied Science and Manufacturing*, 2000. **31**(7): p. 703-715.
- [78] Robertson, R., T.-J. Chu, R. Gerard, J.-H. Kim, M. Park, H.-G. Kim, and R. Peterson, *Three-dimensional fiber reinforcement shapes obtainable from flat, bidirectional fabrics without wrinkling or cutting. Part 2: a single n-sided pyramid, cone, or round box*. *Composites Part A: Applied Science and Manufacturing*, 2000. **31**(11): p. 1149-1165.
- [79] Rudd, C., A. Long, K. Kendall, and C. Mangin, *Liquid moulding technologies*. Woodhead, Cambridge, 1997. **231**.
- [80] Van West, B., R. Pipes, and M. Keefe, *A simulation of the draping of bidirectional fabrics over arbitrary surfaces*. *Journal of the Textile Institute*, 1990. **81**(4): p. 448-460.

- [81] Long, A. and C. Rudd, *A simulation of reinforcement deformation during the production of preforms for liquid moulding processes*. Proceedings of the Institution of Mechanical Engineers, Part B: Journal of Engineering Manufacture, 1994. **208**(4): p. 269-278.
- [82] Hancock, S. and K. Potter, *The use of kinematic drape modelling to inform the hand lay-up of complex composite components using woven reinforcements*. Composites Part A: Applied Science and Manufacturing, 2006. **37**(3): p. 413-422.
- [83] Long, A. *Iterative draping simulation based on fabric mechanics*. in *4 th International ESAFORM Conference on Material Forming*. 2001.
- [84] De Luca, P., Y. Benoit, J. Trochon, O. Morisot, and A. Pickett. *Coupled pre-forming/injection simulations of liquid composite molding processes*. in *47 th International SAMPE Symposium and Exhibition 2002*. 2002.
- [85] Boisse, P., N. Hamila, F. Helenon, B. Hagege, and J. Cao, *Different approaches for woven composite reinforcement forming simulation*. International Journal of Material Forming, 2008. **1**(1): p. 21-29.
- [86] Tavana, R., S.S. Najar, M.T. Abadi, and M. Sedighi, *Meso/macro-scale finite element model for forming process of woven fabric reinforcements*. Journal of Composite Materials, 2012: p. 0021998312454034.
- [87] Creech, G. and A. Pickett, *Meso-modelling of non-crimp fabric composites for coupled drape and failure analysis*. Journal of materials science, 2006. **41**(20): p. 6725-6736.
- [88] Peng, X. and J. Cao, *A dual homogenization and finite element approach for material characterization of textile composites*. Composites Part B: Engineering, 2002. **33**(1): p. 45-56.
- [89] Peng, X. and J. Cao, *A continuum mechanics-based non-orthogonal constitutive model for woven composite fabrics*. Composites part A: Applied Science and manufacturing, 2005. **36**(6): p. 859-874.
- [90] Xue, P., X. Peng, and J. Cao, *A non-orthogonal constitutive model for characterizing woven composites*. Composites part A: Applied Science and manufacturing, 2003. **34**(2): p. 183-193.
- [91] Hamila, N. and P. Boisse, *Simulations of textile composite reinforcement draping using a new semi-discrete three node finite element*. Composites Part B: Engineering, 2008. **39**(6): p. 999-1010.
- [92] Peng, X. and F. Ding, *Validation of a non-orthogonal constitutive model for woven composite fabrics via hemispherical stamping simulation*. Composites Part A: Applied Science and Manufacturing, 2011. **42**(4): p. 400-407.
- [93] Yu, W.-R., P. Harrison, and A. Long, *Finite element forming simulation for non-crimp fabrics using a non-orthogonal constitutive equation*. Composites Part A: Applied Science and Manufacturing, 2005. **36**(8): p. 1079-1093.
- [94] Yu, W.R., F. Pourboghra, K. Chung, M. Zampaloni, and T.J. Kang, *Non-orthogonal constitutive equation for woven fabric reinforced thermoplastic composites*. Composites Part A: Applied Science and Manufacturing, 2002. **33**(8): p. 1095-1105.
- [95] Cornelissen, B., M.B. de Rooij, B. Rietman, and R. Akkerman, *Frictional behavior of carbon fiber tows: a contact mechanics model of tow-tow friction*. Textile research journal, 2014. **84**(14): p. 1476-1488.
- [96] Akkerman, R., R. Ten Thijs, U. Sachs, and M. De Rooij. *Friction in textile thermoplastic composites forming*. in *Proceedings of the 10th International Conference on Textile Composites-TEXCOMP*. 2010.

- [97] Boubaker, B.B., B. Haussy, and J. Ganghoffer, *Discrete models of woven structures. Macroscopic approach*. Composites Part B: Engineering, 2007. **38**(4): p. 498-505.
- [98] Duhovic, M. and D. Bhattacharyya, *Simulating the deformation mechanisms of knitted fabric composites*. Composites Part A: Applied Science and Manufacturing, 2006. **37**(11): p. 1897-1915.
- [99] Boisse, P., *Meso-macro approach for composites forming simulation*. Journal of materials science, 2006. **41**(20): p. 6591-6598.
- [100] Hamila, N. and P. Boisse, *A meso-macro three node finite element for draping of textile composite preforms*. Applied Composite Materials, 2007. **14**(4): p. 235-250.
- [101] Hamila, N., P. Boisse, and S. Chatel, *Finite element simulation of composite reinforcement draping using a three node semi discrete triangle*. International Journal of Material Forming, 2008. **1**(1): p. 867-870.
- [102] Xue, P., J. Cao, and J. Chen, *Integrated micro/macro-mechanical model of woven fabric composites under large deformation*. Composite structures, 2005. **70**(1): p. 69-80.
- [103] Creech, G., *Mesoscopic finite element modelling of non-crimp fabrics for drape and failure analyses*. 2006, Cranfield University.
- [104] Allaoui, S., P. Boisse, S. Chatel, N. Hamila, G. Hivet, D. Soulat, and E. Vidal-Salle, *Experimental and numerical analyses of textile reinforcement forming of a tetrahedral shape*. Composites Part A: Applied Science and Manufacturing, 2011. **42**(6): p. 612-622.
- [105] Hull, D. and T. Clyne, *An introduction to composite materials*. 1996: Cambridge university press.
- [106] Jones, R.M., *Mechanics of composite materials*. 1998: CRC press.
- [107] Boisse, P., N. Hamila, F. Helenon, Y. Aimene, and T. Mabrouki, *Draping of textile composite reinforcements: continuous and discrete approaches*. Advanced Composites Letters, 2007: p. 125-131.
- [108] Aimene, Y., E. Vidal-Sallé, B. Hagège, F. Sidoroff, and P. Boisse, *A hyperelastic approach for composite reinforcement large deformation analysis*. Journal of Composite materials, 2009.
- [109] Peng, X., Z. Guo, T. Du, and W.-R. Yu, *A simple anisotropic hyperelastic constitutive model for textile fabrics with application to forming simulation*. Composites Part B: Engineering, 2013. **52**: p. 275-281.
- [110] Khan, M.A., W. Saleem, M. Asad, and H. Ijaz, *A parametric sensitivity study on preforming simulations of woven composites using a hypoelastic computational model*. Journal of Reinforced Plastics and Composites, 2015: p. 0731684415613567.
- [111] Gelin, J., A. Cherouat, P. Boisse, and H. Sabhi, *Manufacture of thin composite structures by the RTM process: numerical simulation of the shaping operation*. Composites science and technology, 1996. **56**(7): p. 711-718.
- [112] Sirtautas, J., A.K. Pickett, and P. Lépicier, *A mesoscopic model for coupled drape-infusion simulation of biaxial Non-Crimp Fabric*. Composites Part B: Engineering, 2013. **47**: p. 48-57.
- [113] Duhovic, M., P. Mitschang, and D. Bhattacharyya, *Modelling approach for the prediction of stitch influence during woven fabric draping*. Composites Part A: Applied Science and Manufacturing, 2011. **42**(8): p. 968-978.
- [114] Molnar, P., A. Ogale, R. Lahr, and P. Mitschang, *Influence of drapability by using stitching technology to reduce fabric deformation and shear during thermoforming*. Composites Science and Technology, 2007. **67**(15): p. 3386-3393.

- [115] Ten Thije, R. and R. Akkerman, *A multi-layer triangular membrane finite element for the forming simulation of laminated composites*. Composites Part A: Applied Science and Manufacturing, 2009. **40**(6): p. 739-753.
- [116] Cheruet, A., D. Soulat, P. Boisse, E. Soccard, and S.-L. Poec, *Analysis of the interply porosities in thermoplastic composites forming processes*. International journal of forming processes, 2002. **5**: p. 247-258.
- [117] Harrison, P., R. Gomes, and N. Curado-Correia, *Press forming a 0/90 cross-ply advanced thermoplastic composite using the double-dome benchmark geometry*. Composites Part A: Applied Science and Manufacturing, 2013. **54**: p. 56-69.
- [118] Sidhu, R., R. Averill, M. Riaz, and F. Pourboghrat, *Finite element analysis of textile composite preform stamping*. Composite structures, 2001. **52**(3): p. 483-497.
- [119] Bel, S., A. Margossian, D. Leutz, U. Beier, R. Hinterhoelzl, and K. Drechsler. *Validation of local stitching simulation for stitched NCF ply stacks*. in *The 19th International Conference on Composite Materials* 2013.
- [120] Sjölander, J., P. Hallander, and M. Åkermo, *Forming induced wrinkling of composite laminates: A numerical study on wrinkling mechanisms*. Composites Part A: Applied Science and Manufacturing, 2016. **81**: p. 41-51.
- [121] Sorrentino, L. and C. Bellini, *Potentiality of Hot Drape Forming to produce complex shape parts in composite material*. The International Journal of Advanced Manufacturing Technology, 2015: p. 1-10.
- [122] Lin, H., J. Wang, A. Long, M. Clifford, and P. Harrison, *Predictive modelling for optimization of textile composite forming*. Composites Science and Technology, 2007. **67**(15): p. 3242-3252.
- [123] *Front matter*, in *Non-Crimp Fabric Composites*, S.V. Lomov, Editor. 2011, Woodhead Publishing. p. i-iii.
- [124] Liu, W. and Y. Yang, *Multi-objective optimization of sheet metal forming process using Pareto-based genetic algorithm*. Journal of materials processing technology, 2008. **208**(1): p. 499-506.
- [125] Antonio, C.C. and N.M. Dourado, *Metal-forming process optimisation by inverse evolutionary search*. Journal of Materials Processing Technology, 2002. **121**(2): p. 403-413.
- [126] Chung, J. and S. Hwang, *Application of a genetic algorithm to process optimal design in non-isothermal metal forming*. Journal of Materials Processing Technology, 1998. **80**: p. 136-143.
- [127] Kahhal, P., S.Y.A. Brooghani, and H.D. Azodi, *Multi-objective optimization of sheet metal forming die using genetic algorithm coupled with RSM and FEA*. Journal of failure analysis and prevention, 2013. **13**(6): p. 771-778.
- [128] Skordos, A., C. Monroy Aceves, and M. Sutcliffe. *Drape optimisation in woven composite manufacturing*. in *Proceedings of the 5th International Conference on Inverse Problems in Engineering*. 2005.
- [129] Schmitt, R., T. Furtjes, B. Abbas, P. Abel, W. Kimmelman, P. Kosse, and A. Buratti, *Real-time machine vision system for an automated quality monitoring in mass production of multiaxial non-crimp fabrics*. IFAC-PapersOnLine, 2015. **48**(3): p. 2393-2398.
- [130] Strauf Amabile, M., V. Eckers, and T. Gries, *Draping of non-crimp fabrics for fibre reinforced composites*. International Journal of Material Forming, 2010. **3**(1): p. 647-650.
- [131] Cao, J. *Woven Composites Benchmark Forum*, <http://www.wovencomposites.org>. Accessed September 2013.

- [132] Peng, X. and Z.U. Rehman, *Textile composite double dome stamping simulation using a non-orthogonal constitutive model*. Composites Science and Technology, 2011. **71**(8): p. 1075-1081.
- [133] Yu, X., B. Cartwright, D. McGuckin, L. Ye, and Y.-W. Mai, *Intra-ply shear locking in finite element analyses of woven fabric forming processes*. Composites Part A: Applied Science and Manufacturing, 2006. **37**(5): p. 790-803.
- [134] Ten Thijs, R. and R. Akkerman, *Solutions to intra-ply shear locking in finite element analyses of fibre reinforced materials*. Composites Part A: Applied Science and Manufacturing, 2008. **39**(7): p. 1167-1176.
- [135] Martin, T., G. Christie, and D. Bhattacharyya, *Grid strain analysis and its application in composite sheet forming*, in *Composite Sheet Forming*, D. Bhattacharyya, Editor. 1997, Elsevier. p. 217-245.
- [136] Rice, J., *Mathematical statistics and data analysis*. 2006: Cengage Learning.
- [137] Gumbel, E.J., *Statistics of extremes*. 2012: Courier Dover Publications.
- [138] Forbes, C., M. Evans, N. Hastings, and B. Peacock, *Statistical distributions*. 2011: John Wiley & Sons.
- [139] Long, A., A.A. Skordos, P. Harrison, M. Clifford, and M.P. Sutcliffe. *Optimisation of Sheet Forming for Textile Composites using variable Peripheral Pressure*. in *SAMPE*. 2006. Paris, France.
- [140] Willems, A., *Forming simulation of textile reinforced composite shell structures*. 2008, Katholieke University Leuven.
- [141] Harrison, P., P. Gomes, R. Correia, F. Abdiwi, and W. Yu, *Press forming the double-dome benchmark geometry using a 0/90 uniaxial cross-ply advanced thermoplastic composite*, in *15th European Conference on Composite Materials*. 2012: Venice, Italy.
- [142] O'Sullivan, L., *Characterization and simulation of structural fabrics—Part 2: Evaluating process simulation software in a product development cycle*. Reinforced Plastics, 2015. **59**(6): p. 305-309.
- [143] McGregor, O.P.L., S. Chen, L.T. Haper, A. Endruweit, and N.A. Warrior, *Defect characterisation and selective stitch removal in non-crimp fabrics*, in *International Conference SAMPE Europe*. 2015: Amiens.
- [144] Buckley, C., D. Turner, A. Dorfmann, and R. Muhr, *Application of flexible biaxial testing in the development of constitutive models for elastomers*. Constitutive Models for Rubber. Rotterdam: AA Balkema, 1999: p. 59-64.
- [145] Ogden, R. *Large deformation isotropic elasticity-on the correlation of theory and experiment for incompressible rubberlike solids*. in *Proceedings of the Royal Society of London A: Mathematical, Physical and Engineering Sciences*. 1972. The Royal Society.
- [146] Twizell, E. and R. Ogden, *Non-linear optimization of the material constants in Ogden's stress-deformation function for incompressible isotropic elastic materials*. The Journal of the Australian Mathematical Society. Series B. Applied Mathematics, 1983. **24**(04): p. 424-434.